

# Aberration corrected (S)TEM of Nanoparticle and Atomically Dispersed Catalysts

Michael Robert Ward

A thesis submitted for the degree of  
Doctor of Philosophy

University of York  
Department of Physics

July, 2013



## Abstract

The field of catalysis is of paramount importance. Catalysts allow chemical reactions to be carried out with lower energy than otherwise possible. They play an important role in the reduction of harmful emissions from today's vehicles and are crucial for designing alternative energy sources for tomorrow's vehicles. Many catalysts take the form of nano-sized particles which brings about challenges for their design and characterisation. In this thesis, aberration corrected electron microscopy is utilised for atomically resolved investigations of the structure of catalytically active nanoparticles as freshly produced and to provide insights of deactivation in treated and used catalysts.

Platinum and palladium nanoparticles are used for the reduction of harmful emissions from diesel car exhausts. Here, fresh insights are provided into the loss of activity in genuine road aged diesel oxidation catalysts. They include the segregation of alloys in the bimetallic variant in which the less active palladium moves to the surface where it can more easily form an oxide. Nano-beam diffraction was used in this study as well as for a model platinum system. The seldom used nano-beam diffraction technique was employed to provide additional structural information on very small nanoparticles, including those that contained defects. Using nano-beam diffraction, no oxides were found in the platinum model catalyst and loss of activity was due to sintering.

Ex-situ studies can only provide before and after information. Here, results from the latest developments in environmental scanning transmission electron microscopy are presented with model catalysts, namely atomically dispersed platinum and palladium. Single atoms of the metals were observed at temperatures as high as 500 °C and in O<sub>2</sub> which represents the current state of the art in this field. The limitations of the *Z* contrast technique is also investigated for heavy atoms located on heavy supports, such as atomically dispersed gold on ceria.

Intricacies in the reduction of Co<sub>3</sub>O<sub>4</sub> to CoO are provided using in-situ transmission electron microscopy in H<sub>2</sub> at elevated temperatures. A new fuse wire like transformation is seen in large crystals in addition to dislocations to accommodate strain into the crystal structure.

# Contents

<b>1</b>	<b>Introduction</b>	<b>14</b>
1.1	Importance of Catalysts . . . . .	14
1.2	Need for Electron Microscopy . . . . .	16
1.3	Overview of Thesis . . . . .	16
<b>2</b>	<b>Electron Optics and Electron Microscopy Techniques</b>	<b>18</b>
2.1	Interaction of Electrons with Thin Crystals . . . . .	18
2.1.1	Introduction . . . . .	18
2.1.2	Real and Reciprocal Lattice . . . . .	19
2.1.3	High Energy Electron Diffraction . . . . .	20
2.1.4	Diffacted Intensities . . . . .	22
2.1.5	Double Diffraction . . . . .	24
2.1.6	Moiré Patterns . . . . .	25
2.2	The (Scanning) Transmission Electron Microscope Instrument . . . . .	26
2.3	TEM Mode and Image Contrast . . . . .	28
2.4	(S)TEM Mode and Image Contrast . . . . .	31
2.5	Aberrations . . . . .	34
2.6	Electron Diffraction using (S)TEM . . . . .	36
2.6.1	Selected Area Diffraction . . . . .	36
2.6.2	Diffraction in (S)TEM . . . . .	37
2.6.3	Nano Area Electron Diffraction . . . . .	38
2.7	Environmental (S)TEM . . . . .	39

2.8	Image Analysis and Simulation . . . . .	40
2.9	Other Techniques . . . . .	41
2.9.1	Scanning Electron Microscopy . . . . .	41
2.9.2	Energy Dispersive X-ray Spectroscopy . . . . .	42
2.10	York-JEOL Nanocentre Resources . . . . .	42
2.11	Microscope Methodology . . . . .	43
2.11.1	TEM and HRTEM . . . . .	43
2.11.2	Diffraction Modes and Techniques . . . . .	47
2.11.3	STEM . . . . .	48
2.11.4	E(S)TEM . . . . .	50
<b>3</b>	<b>Structure and Catalytic Activity of Nanoparticle Catalysts</b>	<b>51</b>
3.1	Structures of Metal Nanoparticles . . . . .	51
3.1.1	Nanoparticle Shapes . . . . .	51
3.1.2	Lattice Parameter of small Nanoparticles . . . . .	55
3.1.3	Bimetallic and Alloyed Nanoparticles . . . . .	57
3.1.4	Metal-Support Interactions and Interface . . . . .	58
3.1.5	Structures of Al <sub>2</sub> O <sub>3</sub> . . . . .	59
3.2	Catalytic Activity of Nanoparticles . . . . .	61
3.2.1	Activation . . . . .	61
3.2.2	Heterogenous Catalyst Surface Mechanisms . . . . .	62
3.2.3	Effect of Coordination Number and Size . . . . .	62
3.3	Ageing and Deactivation Mechanisms of Nanoparticle Catalysts . . . . .	67
3.3.1	Introduction . . . . .	67
3.3.2	Ostwald Ripening . . . . .	69
3.3.3	Nanoparticle Migration and Coalescence . . . . .	72
3.3.4	Model Fitting with Power Laws . . . . .	74
3.3.5	Ageing of Bimetallic Systems . . . . .	76

3.4	Pt and Pd Oxides and their Reduction . . . . .	77
3.4.1	Introduction . . . . .	77
3.4.2	Structures and Activity of Pd Oxides . . . . .	77
3.4.3	Structures and Activity of Pt Oxides . . . . .	79
3.4.4	Bimetallic $\text{Pd}_x\text{Pt}_{1-x}\text{O}_y$ . . . . .	80
3.5	Cobalt (Co) Fischer-Tropsch Catalysts . . . . .	81
3.5.1	Structure of Co and its oxides . . . . .	83
3.5.2	Reduction Mechanism . . . . .	84
<b>4</b>	<b>Nanostructural studies of Pt-SiO<sub>2</sub> and Pt-Pd-Al<sub>2</sub>O<sub>3</sub> DOCs</b>	<b>87</b>
4.1	Introduction . . . . .	87
4.2	Specimens and Preparation for Electron Microscopy . . . . .	87
4.2.1	Description of Specimens . . . . .	87
4.2.2	Specimen Preparation . . . . .	90
4.3	Bimetallic DOC Characterisation . . . . .	92
4.4	Pt Only DOC Characterisation . . . . .	100
4.5	Discussion of Results . . . . .	103
4.5.1	Nanoparticle Sizes . . . . .	103
4.5.2	Segregation . . . . .	105
4.5.3	Nanoparticle Morphologies . . . . .	105
4.6	Conclusion . . . . .	106
<b>5</b>	<b>Nanostructural Studies of a Pt-<math>\gamma</math>-Al<sub>2</sub>O<sub>3</sub> Catalyst</b>	<b>108</b>
5.1	Introduction . . . . .	108
5.2	Specimen Preparation . . . . .	108
5.3	Fresh Catalyst . . . . .	109
5.4	Catalysts Treated in air for 3 h . . . . .	116
5.5	Catalysts Treated in air for 15 h . . . . .	121
5.6	Sintering Mechanism Discussion . . . . .	125

5.7	Conclusions . . . . .	127
<b>6</b>	<b>Imaging Single Atoms Using HAADF–STEM</b>	<b>129</b>
6.1	<i>In-situ</i> Environmental HAADF-STEM of Pt-Pd Atoms . . . . .	129
6.1.1	Introduction . . . . .	129
6.1.2	Preparing Atomically Dispersed Specimens . . . . .	130
6.1.3	Minimising Contamination . . . . .	131
6.1.4	<i>In-situ</i> (S)TEM Methodology . . . . .	133
6.1.5	Results: Without Gas or Heat . . . . .	134
6.1.6	Results: Gas without Heat . . . . .	136
6.1.7	Results: Gas and Heat . . . . .	138
6.2	Intensity Analysis . . . . .	141
6.3	CeO <sub>2</sub> . . . . .	142
6.3.1	Background . . . . .	142
6.3.2	Creating the Models . . . . .	146
6.3.3	Simulation Parameters and Preliminary Simulations . . . . .	148
6.3.4	Au Capped Simulation Results . . . . .	151
6.4	Discussion . . . . .	157
6.5	Conclusions . . . . .	157
<b>7</b>	<b><i>In-situ</i> Co<sub>3</sub>O<sub>4</sub> Reduction in H<sub>2</sub></b>	<b>159</b>
7.1	Introduction . . . . .	159
7.2	Specimen Preparation and Characterisation . . . . .	159
7.3	HRTEM and Diffraction Reduction Sequences . . . . .	160
7.4	Simulations . . . . .	166
7.5	The Co <sub>3</sub> O <sub>4</sub> –CoO Grain Boundary . . . . .	169
7.6	Formation of Co at Higher Pressure . . . . .	171
7.7	Conclusions . . . . .	172

<b>8</b>	<b>Model Supported Nanoparticle Systems</b>	<b>173</b>
8.1	Nanostructure of PtPd nanoparticle coated ZnO Tetrapods . . . . .	173
8.1.1	Introduction . . . . .	173
8.1.2	Sample Preparation . . . . .	175
8.1.3	Leg and Core Structure of Small Tetrapods . . . . .	176
8.1.4	HAADF-STEM and HRTEM of Coated Tetrapods . . . . .	178
8.1.5	Conclusions . . . . .	180
<b>9</b>	<b>Summary and Final Remarks</b>	<b>182</b>

# List of Figures

1.1	Catalysis energy diagram . . . . .	15
2.1	Diagram showing reciprocal lattice planes and the Ewald sphere . . . . .	22
2.2	Diffraction shape effects expected for a cubic nanoparticle . . . . .	24
2.3	Lens diagram of a TEM . . . . .	27
2.4	Typical CTFs for uncorrected and corrected HRTEM . . . . .	30
2.5	Lens diagram of a STEM . . . . .	33
2.6	Optic diagram showing the effect of spherical aberrations . . . . .	35
2.7	Graph showing the SAD error as a function of defocus . . . . .	37
2.8	Screenshots of the CEOS aberration correction software . . . . .	46
3.1	Wulff, Winterbottom and the wetting models . . . . .	52
3.2	Diagrams of raft and a cluster . . . . .	52
3.3	Stable Pt nanoparticle shapes below 5 nm . . . . .	54
3.4	Types of alloying mixtures . . . . .	57
3.5	Pt <sub>3</sub> observed and modelled by Sohlberg <i>et al</i> . . . . .	60
3.6	SAD patterns from large $\gamma/\delta$ -Al <sub>2</sub> O <sub>3</sub> crystals . . . . .	61
3.7	CO conversion activity on different nanoparticle shapes . . . . .	64
3.8	Energy states around $E_f$ at atom sites . . . . .	64
3.9	d-band centre – chemisorption relationship for different surfaces . . . . .	65
3.10	Density of states comparison for small nanoparticles with bulk . . . . .	66
3.11	Relation between reaction barrier–desorption energy for Pt nanoparticles . . . . .	66
3.12	Nanoparticle sintering mechanisms . . . . .	70

3.13	Distributions expected for the different sintering mechanisms . . . . .	75
3.14	Activity of Co nanoparticles on C nanowires . . . . .	82
3.15	Structure of $\text{Co}_3\text{O}_4$ , CoO and Co . . . . .	83
4.1	Schematic of a monolith . . . . .	88
4.2	Pictures of the DOC monolith sections . . . . .	89
4.3	HRTEM and HAADF–STEM of the fresh and aged bimetallic DOC . . .	93
4.4	Size distributions for the bimetallic DOCs . . . . .	94
4.5	Nanostructure of nanoparticles on the fresh bimetallic DOC . . . . .	95
4.6	Nanostructure of nanoparticles on the aged bimetallic DOC . . . . .	96
4.7	Alloy segregation in the aged bimetallic DOC . . . . .	97
4.8	NBD and HRTEM of a nanoparticle with defects . . . . .	98
4.9	Graph showing Pt/Pd ratio vs nanoparticle diameter relationship . . . . .	100
4.10	Graph showing core size vs nanoparticle diameter relationship . . . . .	101
4.11	(S)TEM images of the fresh and aged Pt–Only DOC . . . . .	102
4.12	Nanoparticle size distributions in the Pt–Only DOCs . . . . .	102
4.13	Nanostructure of nanoparticles in fresh and aged Pt–Only DOC . . . . .	103
5.1	Wide area views of the fresh catalyst and nanoparticle size distribution . .	110
5.2	HRTEM images showing fresh catalyst nanoparticle structures . . . . .	112
5.3	Typical SAD pattern from the fresh catalyst . . . . .	113
5.4	NBD pattern of a single distorted nanoparticle . . . . .	114
5.5	NBD pattern of a nanoparticle showing shape effects . . . . .	115
5.6	Nanoparticle size distributions for catalysts treated for 3 h . . . . .	117
5.7	NBD of defects in large structures the catalyst treated at 750 °C . . . . .	120
5.8	Nanoparticle size distributions for catalysts treated for 15 h . . . . .	122
5.9	Atoms and clusters in the catalyst treated for 15 h at 250 °C . . . . .	123
5.10	Clusters, but no atoms in the catalyst treated for 15 h at 500 °C . . . . .	125
6.1	HAADF–STEM of specimens with different coating thicknesses . . . . .	130



6.2	HAADF-STEM showing contamination issues on thin-C films . . . . .	131
6.3	HAADF-STEM image showing single atoms and clusters . . . . .	134
6.4	<i>In-situ</i> HAADF-STEM movie frames without gas or heat . . . . .	135
6.5	HAADF-STEM image in H <sub>2</sub> and O <sub>2</sub> without heat . . . . .	136
6.6	Appearance of atoms in H <sub>2</sub> and O <sub>2</sub> with no heat . . . . .	137
6.7	Comparison of resolution with different power supplies . . . . .	138
6.8	Nanoparticles and resolution comparison at higher temperatures . . . . .	140
6.9	Graph showing results from TDS simulations at different temperatures . .	141
6.10	Quantifying single atom intensities . . . . .	143
6.11	Quantifying atom intensities on a nanoparticle . . . . .	144
6.12	HAADF-STEM image showing anomalous atomic column intensities . .	146
6.13	CeO <sub>2</sub> and tetragonal simulation unit cells . . . . .	147
6.14	Screenshots of QSTEM . . . . .	149
6.15	Plain 5x5x4 CeO <sub>2</sub> simulation with a 100x100 probe array . . . . .	150
6.16	Plain 20x20x4 CeO <sub>2</sub> simulation with an 800x800 probe array . . . . .	151
6.17	Intensity difference of Au at difference convergence angles . . . . .	152
6.18	Graph showing the relationship between intensity and $dE$ . . . . .	153
6.19	Montage of QSTEM output images . . . . .	154
6.20	Graph showing intensity differences with Au at different sites . . . . .	155
7.1	Characterisation of the Co <sub>3</sub> O <sub>4</sub> powder . . . . .	160
7.2	<i>in-situ</i> reduction sequence of Co <sub>3</sub> O <sub>4</sub> in H <sub>2</sub> . . . . .	161
7.3	<i>In-situ</i> reduction sequence of a small Co <sub>3</sub> O <sub>4</sub> nanoparticle . . . . .	163
7.4	<i>In-situ</i> SAD pattern reduction sequence of Co <sub>3</sub> O <sub>4</sub> . . . . .	165
7.5	Simulated diffraction patterns of Co <sub>3</sub> O <sub>4</sub> and CoO . . . . .	167
7.6	Effect of tilt on diffraction patterns of Co <sub>3</sub> O <sub>4</sub> . . . . .	168
7.7	Effect of tilt on HRTEM images of Co <sub>3</sub> O <sub>4</sub> . . . . .	169
7.8	Interface like structure between Co <sub>3</sub> O <sub>4</sub> and CoO . . . . .	170

7.9	<i>In-situ</i> reduction HRTEM sequence at higher pressure . . . . .	171
8.1	Low magnification images of ZnO tetrapods . . . . .	175
8.2	HAADF–STEM image of ZnO tetrapod leg . . . . .	176
8.3	HRTEM of ZnO tetrapod leg and core . . . . .	177
8.4	Effect of electron irradiation on ZnO tetrapod structure . . . . .	179
8.5	Nanoparticle coated tetrapods . . . . .	180
8.6	HRTEM of Pt–Pd nanoparticle coated ZnO tetrapod leg . . . . .	181

# List of Tables

2.1	Typical aberration coefficient values for TEM and STEM . . . . .	47
3.1	Wulff shapes . . . . .	53
3.2	Tammann temperatures ( °C) of Pt group metals . . . . .	73
4.1	Metal loadings on the four DOCs . . . . .	90
4.2	XPS measurements from the DOCS . . . . .	91
4.3	Average bimetallic DOC nanoparticle sizes . . . . .	95
4.4	Average Pt–Only DOC nanoparticle sizes . . . . .	101
5.1	$\mu$ , $\sigma$ and $\Gamma$ values obtained for the fresh and heat treated catalysts . . . . .	126
6.1	QSTEM Parameters . . . . .	149
7.1	JEMs simulation parameters . . . . .	167
8.1	Table of Moiré fringe widths and angles . . . . .	178

# Acknowledgements

Personally, I think the PhD is more of a journey than a book and along the way I have met many interesting and wise people, who in many ways are responsible for the work published here.

First I would like to acknowledge the support of my supervisors, Professors Edward Boyes and Pratibha Gai. Their attention to detail, knowledge, approachability and kindness can't go without mention. I would also like to thank the EPSRC for funding.

I would like to thank Dr Mike Walsh for providing good company in the nanocentre as well as for providing wise discussion regarding catalysis, nanoparticles and electron microscopy. A similar thanks goes to Dr Kenta Yoshida and Dr Leonardo Lari whose tuition and company has been invaluable over the years. I also thank Dan and Tom for their good company in the nanocentre.

All experimental HAADF-STEM images in the *in-situ* section of chapter 6 except for Figures 6.1 and 6.2 were taken by Dr Leonardo Lari. Figure 8.2 was taken by Dr Kenta Yoshida.

Finally, I would like to thank my parents and my family for the support and encouragement they have given over the past four years.

# Declarations

I declare that the work presented in this thesis, except where otherwise stated, is based purely on my own research and has not been submitted for a degree in this or any other university. Parts of the work reported in this thesis have been previously published in

M. R. Ward, E. D. Boyes and P. L. Gai, Aberration Corrected (S)TEM and Nano Beam Diffraction (NBD) of Pt and Pd on  $\text{Al}_2\text{O}_3$  Catalysts *Journal of Physics: Conference Series* (Accepted)

M. R. Ward, E. D. Boyes and P. L. Gai, In-situ Reduction of  $\text{Co}_3\text{O}_4$  in  $\text{H}_2$  using Environmental HRTEM *Journal of Physics: Conference Series* (Accepted)

E. D. Boyes, M. R. Ward, L. Lari and P. L. Gai, ESTEM imaging of single atoms under controlled temperature and gas environment conditions in catalyst reaction studies, *Annalen der Physik* **525** (2013) 423-429

M. R. Ward, E. D. Boyes and P. L. Gai, In-Situ Aberration-Corrected Environmental TEM: Reduction of Model  $\text{Co}_3\text{O}_4$  in  $\text{H}_2$  at the Atomic Level, *ChemCatChem* **5** (2013) 2655-2661

M. R. Ward, T. Cook, E. D. Boyes and P. L. Gai, Nanostructural Studies of Fresh and Road-Aged Practical Pt/ $\text{SiO}_2$  and Pt-Pd/ $\text{Al}_2\text{O}_3$  Diesel Oxidation Catalysts by using Aberration-Corrected (Scanning) Transmission Electron Microscopy, *ChemCatChem* **4** (2012) 1622–1631

M. R. Ward, H. Sugiura, K. Yoshida, N. Tanaka, P. L. Gai and E. D. Boyes, Aberration corrected and 3D cryo-tomography HAADF-STEM surface studies of ZnO tetrapods, *Journal of Physics: Conference Series* **371** (2012) 012073

P. L. Gai, K. Yoshida, C. Shute, X. Jia, and M. Walsh, M. Ward, M. S. Dresselhaus. and J. R. Weertman and E. D. Boyes, Probing structures of nanomaterials using advanced electron microscopy methods, including aberration-corrected electron microscopy at the angstrom scale, *Microscopy Research and Technique* **74** (2011) 664–670

Signature

Michael Ward

Date October 28, 2013

# Chapter 1

## Introduction

### 1.1 Importance of Catalysts

The vast majority of all chemical derived products made today have involved the use of catalysts at some point in their manufacture. A catalyst significantly reduces the amount of energy required for a chemical reaction, improves reaction rates and can improve the yield of the desired product. For these reasons, catalysis is a \$100 Billion per year industry and a critical science for reducing the impact of industry on the environment.

Catalysts play a direct role in the reduction of toxic and greenhouse emissions from industrial process. Perhaps the most well known application of a catalyst is in the emissions control of petrol [1] and diesel [2] automobiles by the use of catalytic converters. Another popular topic on the automobile and energy front is the development of catalysts for improving the efficiency of storing energy with alcohol and  $H_2$  fuel cells [3]. Catalysts also make alternative sources of oil viable, including the conversion of natural gas into diesel fuel [4].

The origin of industrial catalysis was arguably born out of the pioneering work of Humphrey Davy and Edmund Davy who discovered that certain reactions could be carried out at lower temperatures than normal in the presence of Pt wire [5,6]. The word catalysis did not appear until Berzelius coined it in 1830 as a general term to describe the sudden increase in reaction rates with catalysts [7]. The precise, scientific definition of a catalyst was not provided until 1896 by Ostwald [7]. According to Ostwald, a catalyst is a material which changes the reaction rate of a chemical reaction without itself being consumed.

Today, catalysis can be explained in terms of energetics. Figure 1.1 is a simplified energy diagram showing how the catalyst provides an alternative reaction route; which

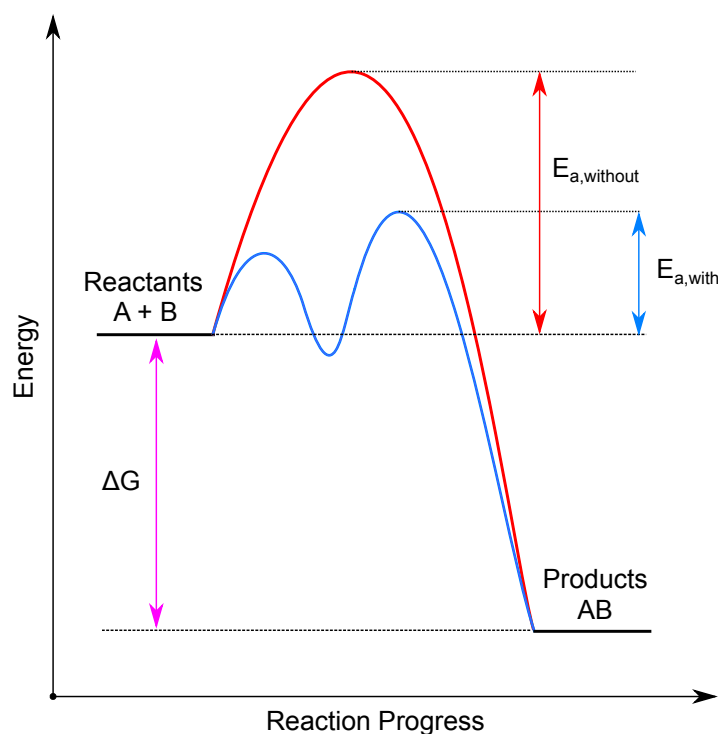


Figure 1.1: Energy diagram showing that catalysis provides an alternative reaction route which requires significantly less energy to activate,  $E_{a,with}$  compared the natural reaction path,  $E_{a,without}$ . The catalysis route may require several processes to occur, such as adsorption, which have their own associated energies. The difference in energy between the products and reactants is known as the free energy  $\Delta G$

requires less energy than the natural reaction route hence the reaction can take place at considerably lower temperatures than is normally possible.

Catalysis is often separated into two branches: heterogenous catalysis and homogenous catalysis. The former catalyses reactants that are in a different phase (state of matter) than itself and the latter is a catalyst which is in the same phase as the reactants. The topic of this thesis concerns solid state heterogenous catalysis.

Catalysts were traditionally bulk quantities of materials in the form of powder or wire, but it was often found that powders were catalytically active at room temperature whereas wires were not. Catalysis is known to occur primarily at the surface of materials, therefore, a catalyst with high surface area is desirable. The use of nanocatalysts in the form of nanoparticles allows the minimal amount of material to be used whilst allowing the highest possible surface area.

The electrical and chemical properties of materials at the bulk scale are well known but when materials are shrunk down below 100 nm in one or more dimensions, the relationship between size and the materials chemical and physical properties is not always



straightforward. Below 10 nm, the nature of the atoms at the surface becomes more important with atoms at steps and kinks often contributing to sudden increases in reaction rates.

As an example, in 1987, Masatake Haruta and his group investigated the catalytic properties of Au nanoparticles [8]. They found that their nanoparticles were remarkably active for the oxidation of CO [8] but only when below 5 nm in diameter. This implied that nanoscale Au could form an Au–O bond despite bulk Au being completely inert. This revelation sparked a surge in nanoparticle research but the exact reason why some nanoparticles are catalytically active is still a hot topic in research [9].

## **1.2 Need for Electron Microscopy**

A problem with nano-catalysts is that they are very small and difficult to see. The presence of nanoparticles in solution can be inferred by its optical properties as Michael Faraday did in 1847 [10]. Conventional optical microscopes provide insufficient resolution to observe nanoparticles below 100 nm let alone deduce their structure. The wavelengths of light are too large to deduce the atomic structure of nanoparticles so alternative techniques must be used. X-rays have been used to deduce the crystal structure of materials but it is largely a bulk technique. High energy electrons on the other hand can be manipulated with magnets to form a small beam suitable for nano-area studies and provide superior resolution. The electron microscope is the most popular electron characterisation technique for nanomaterials.

There are several types of electron microscopes. This thesis primarily concerns the transmission electron microscope (TEM) and the related scanning transmission electron microscope (STEM).

## **1.3 Overview of Thesis**

Despite the advances in electron microscopy resolution and the extensive development of the technique, there are still many unanswered questions surrounding the activity and structural dynamics of nanoparticle catalysts. More recently, nanoparticles are being replaced with very small clusters and atomically dispersed forms. This thesis provides some insights into the reason behind loss of activity in commercial and model nanoparticle sys-

tems in addition to providing new insights of the microscopy of atomically dispersed catalysts using aberration corrected electron microscopy and *in-situ* environmental electron microscopy.

Chapter 2 provides a review of electron diffraction, which is the basic principle behind transmission electron microscopy and provides a critical analysis of the latest techniques relevant to (S)TEM and high resolution TEM (HRTEM). An overview of catalysis with critical analysis of the current state of the art of knowledge in nanoparticle structures and activity is provided in Chapter 3. Chapter 4 reports results from the study of two commercial nanoparticle catalysts, namely diesel oxidation catalysts and more detailed insights than currently available into the loss of activity of these catalysts. Chapter 5 investigates the initial structural changes in treated model nanoparticle catalysts relevant to chapter 4, including the use of the nano-beam diffraction technique. Chapter 6 shows results from the latest state of the art *in-situ* environmental electron microscopy including the observation of single atoms in gases whose intensities are quantified. Also in Chapter 6 is a theoretical study of the presence of heavy single atoms on a heavy support which reveals the shortcomings of the *Z* contrast imaging method in electron microscopy. Chapter 7 is an *in-situ* environmental reduction study of a catalyst precursor where new intricacies of the reduction mechanism are outlined. Chapter 8 provides insights into the structure of Pt-Pd-ZnO model catalysts which may also have technological uses. In the final chapter, Chapter 9, concluding remarks are presented with suggestions for further work.

# Chapter 2

## Electron Optics and Electron Microscopy Techniques

### 2.1 Interaction of Electrons with Thin Crystals

#### 2.1.1 Introduction

In the optical microscope, a light source illuminates a transparent specimen. The transmitted light is then focused and inverted multiple times by a series of lenses to achieve the necessary magnification. If the transmitted light was allowed to travel long enough and the specimen consisted of well ordered slits, then a pattern of light would be formed some distance from the object. The pattern would then be a diffraction pattern.

Diffraction is a phenomenon of waves which occurs when they interact with physical objects. Classically, diffraction can be seen as an apparent change in direction between the incident wave and diffracted wave. However in the context of this work it is best described as the spreading out of waves after interaction with an object and the interference between the resulting waves. The electrons that transmit in an electron transparent specimen interact with the object as a whole but also with the individual atoms. For TEM imaging, the diffraction of electrons by atoms is harnessed by a lens system to form an image.

Assuming that the crystal is very thin, the TEM image contrast will arise primarily from elastically scattered electrons, namely from diffracted electrons. When the crystal becomes thicker, inelastic scattering becomes more important and the image may be dominated by mass/thickness contrast. Regardless of how thick the crystal is, some energy is lost by other inelastic events such as the generation of X-rays. For the special high angle imaging mode of STEM, inelastic scattering dominates the image hence the image shows

mass/thickness contrast.

The diffraction of electrons through a transparent specimen is of great importance for understanding image contrast but the diffraction patterns themselves can also be recorded to yield complementary and unique structural information. In this chapter, conditions for the analysis of diffraction patterns are reviewed with emphasis on diffraction from nanoparticle sized crystals. Following on from the diffraction sections, the (S)TEM instrument and its imaging modes is briefly described and how changing certain parameters can dramatically change the image contrast.

## 2.1.2 Real and Reciprocal Lattice

A perfect crystal is a repetition of a 3D pattern of atoms or ions. The translational symmetry of the crystal can be described mathematically with an array of points called a lattice. The required translational symmetry for 3D lattices is satisfied by 14 lattices called the Bravais lattices [11]. The simplest of these in 3D is the cubic system and its three variants: simple cubic (sc), face centred cubic (fcc) and body centre cubic (bcc). Most precious metals including Pt and Pd are fcc. The crystal is formed by attaching a set of atoms (a basis) to each lattice point so that the same structure is repeated.

The smallest volume that satisfies the translational symmetry of the Bravais lattices is called the unit cell. Each unit cell is defined in terms of unique vectors,  $\mathbf{a}$ ,  $\mathbf{b}$  and  $\mathbf{c}$  that are called the unit cell vectors. The type of lattice dictates the angles between these vectors and the values they can take relative to each other. Any point within a perfect crystal can be described by combinations of these vectors. Atomic coordinates within each cell can be defined in fractions of the unit cell vectors.

An atomic plane is described with miller indices  $(h\ k\ l)$  which are defined as the reciprocal ratio of the plane interceptions respectively with the  $\mathbf{a}$ ,  $\mathbf{b}$  and  $\mathbf{c}$  axis within a unit cell [11]. The notation  $(h\ k\ l)$  describes a specific atomic plane, whereas the notation  $\{h\ k\ l\}$  describes a set of equivalent planes. Crystallographic directions are described as unit vectors in terms of the crystal symmetry. A crystal direction is represented as  $[U\ V\ W]$  and a set of equivalent directions represented as  $\langle U\ V\ W \rangle$  where  $U$ ,  $V$  and  $W$  are integers. For cubic crystals,  $U$ ,  $V$ ,  $W$  and  $h$ ,  $k$  and  $l$  in  $\langle U\ V\ W \rangle$  are interchangeable because the directions are always perpendicular to the plane  $(h\ k\ l)$ .

The periodic properties of a crystal make it suitable for an alternative mathematical

approach in reciprocal space. In the same way a periodic signal in time can be transformed into reciprocal space to produce constituent frequencies, a crystal can be converted into its spatial frequencies. In real space, directions are important in addition to magnitude so the reciprocal frequencies are also expressed as vectors. Any point in reciprocal space is defined by a reciprocal lattice vector,  $\mathbf{g}$ . This vector is expressed in terms of reciprocal lattice vectors  $\mathbf{a}^*$ ,  $\mathbf{b}^*$  and  $\mathbf{c}^*$  which describe the unit cell in reciprocal space. A particular reciprocal lattice vector composed of  $h$ ,  $k$  and  $l$  integers of  $\mathbf{a}^*$ ,  $\mathbf{b}^*$  and  $\mathbf{c}^*$  respectively describes the reciprocal of the vector between atomic planes. The magnitude of  $\mathbf{g}$  is  $1/d$  where  $d$  is a particular atomic plane spacing. For cubic materials,  $\mathbf{g}$  is perpendicular to the atomic plane because the reciprocal lattice vectors remain parallel to the equivalent real lattice vectors.

### 2.1.3 High Energy Electron Diffraction

According to Louis de Broglie, electrons behave as waves. If given sufficient energy, they will have a wavelength a small fraction of the distance between atomic planes. After X-rays were found to diffract experimentally, Lawrence Bragg provided a mathematical model that explained how X-rays constructively interfere as they pass through a crystal [12, 13]. The result was the famous Bragg equation given as [12, 13]

$$n\lambda = 2d \sin \theta_B \quad (2.1)$$

where  $n$  is the diffraction order,  $\lambda$  is the X-ray (or electron) wavelength,  $d$  is the atomic plane separation and  $\theta_B$  is the Bragg angle.  $2\theta_B$  is the angle between the direction of the incident and diffracted wavefront. (2.1) gives the basic conditions necessary for constructive interference of X-rays and electrons. Using crystals, experimental methods are based on fixing one or more of these variables. For a TEM,  $\lambda$  is fixed as is  $d$  for a particular atomic plane. For a 200 kV TEM, the electrons will have wavelength 2.51 pm, which is much smaller than an atomic plane spacing. The relation in (2.1) implies that the angle between the incident and diffracted wavefront will be on the order of  $< 10$  mrad.

The Bragg equation (2.1) does not specify which atomic planes will diffract and which ones will not. Max Von Laue used vectors to show that there is a relationship between the incident wave and diffracted wave when represented as wavevectors  $\mathbf{k}$  and  $\mathbf{k}'$  respectively when travelling through a series of planes described by miller indices. The difference between the two wavevectors is  $\mathbf{K}$  and it must obey the following rules for diffraction to occur

$$\mathbf{K} \cdot \mathbf{a} = h \quad \mathbf{K} \cdot \mathbf{b} = k \quad \mathbf{K} \cdot \mathbf{c} = l \quad (2.2)$$

where the symbols have their previously defined meanings. Using (2.1) and (2.2), it is possible to prove that a particular reciprocal lattice vector  $\mathbf{g}$  is the same as  $\mathbf{K}$  and is related to  $d$  according to

$$K = g_{hkl} = 1/d \quad (2.3)$$

where  $g_{hkl}$  describes a particular reciprocal lattice vector that has miller indices combinations of reciprocal lattice vectors. (2.3) says that  $\mathbf{g}$  is the reciprocal of the atomic plane separation. Therefore, (2.1), (2.2) and (2.3) describe the physical origin of the reciprocal lattice and how it is related to the crystal symmetry and dimensions.

A more convenient way of expressing the relationship between the crystal orientation and diffraction conditions is possible in the form of the Weiss zone law, given as [14, 15]

$$hU + kV + lW = N \quad (2.4)$$

where  $N$  is an integer. The relation in (2.4) is best imagined as a reciprocal lattice plane perpendicular to the electron beam. However, there are many equivalent reciprocal lattice planes stacked on top of each other but (2.1) and (2.2) are not satisfied at all the reciprocal lattice points. Using a construct called an Ewald sphere it is possible to visualise (2.1) and (2.2) in reciprocal space. The Ewald sphere is shown in Figure 2.1. It has radius  $k = k'$  and the edge defines the points at which (2.2) and (2.1) are satisfied. It cuts through each reciprocal lattice plane but only intercepts a fraction of the reciprocal lattice points as shown in Figure 2.1(a). The first intercepted lattice plane is called the zero order Laue zone (ZOLZ) and higher ones are called higher order Laue zones (HOLZ). In 3D, the 3D reciprocal lattice becomes a 2D projection on a diffraction pattern as shown in Figure 2.1(b). The reciprocal lattice sites present in the diffraction pattern are called reflections.

It has been shown that the diffracted intensities do not entirely rely on either the Bragg or Laue conditions. Differences in the intensity of diffracted beams have been observed with minor crystal tilts. A vector used to describe the distance away from the Bragg location is called the excitation error,  $\mathbf{s}$  and is defined as

$$\mathbf{K} = \mathbf{g} + \mathbf{s} \quad (2.5)$$

The value of  $\mathbf{s}$  is pivotal in the contrast of defects [14]. The Bragg and Laue conditions are not met exactly because of the finite size of the crystal. Figure 2.1(c) shows a pictorial definition of  $\mathbf{s}$ . An understanding of how intensities arise in the diffraction pattern are outlined below.

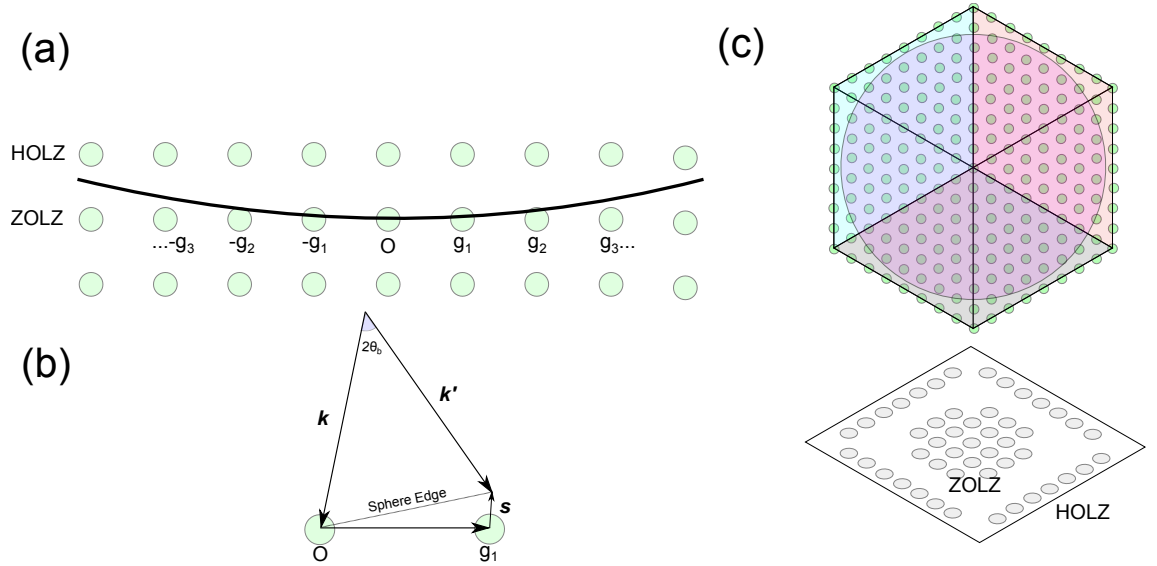


Figure 2.1: Diagram showing (a) how the Ewald sphere intercepts the reciprocal lattice planes and (b) the definition of the excitation error,  $s$  and (c) a 3D view of the Ewald sphere in reciprocal space and the projection of the intercepted reciprocal lattice points into the diffraction pattern below

### 2.1.4 Diffracted Intensities

The Bragg and Laue formalisms explain the symmetry of diffraction patterns from perfect single crystals but do not take into account the underlying diffracting mechanism. A quantum mechanical treatment on the interaction of electrons with atomic potentials lead to the discovery that atoms spherically scatter plane waves. By taking into account the scattering of electrons by atoms it is possible to understand how diffracted intensity arises in the diffraction pattern and how image contrast arises.

Each atomic species scatters a plane wave with different phase and amplitude. The atomic form factor  $f_i(\theta)$  describes the relative scattering amplitude of an atom compared to an electron. Assuming a perfect crystal, it is only necessary to sum up the scattering amplitudes of each atom within a unit cell, taking into account their relative positions. The result is a scattering amplitude for a unit cell, often given the name structure factor. It is expressed as [13, 14, 15]

$$F = \sum_i f_i(\theta) \exp(2\pi i(hx_i + ky_i + lz_i)) \quad (2.6)$$

where  $h$ ,  $k$  and  $l$  are the miller indices of a particular atomic plane and  $x$ ,  $y$  and  $z$  are numbers describing atomic coordinates within a unit cell in terms of  $a$ ,  $b$  and  $c$  respectively.  $f_i(\theta)$  is the atomic form factor of atomic species  $i$ . The diffracted intensity is given by  $|F|^2$ .

The structure factor (2.6) says that particular atomic planes will diffract with different amplitudes compared to others. The relative positions of atoms can also lead to destructive interference causing reciprocal lattice points to be omitted from the diffraction pattern. A well known example are the mixed index terms of fcc materials, such as  $\{1\ 0\ 0\}$  which will destructively interfere and therefore have  $F = 0$ . Such diffracted beams that normally do not appear as per (2.6) = 0 are known as forbidden reflections.

The arrangement of atoms in a crystal is finite. By summing up the amplitudes and phases of atoms in the entire crystal in similar fashion to (2.6) it is possible to deduce that reciprocal lattice points will be shaped in the diffraction pattern [14]. The summation across the whole crystal yields what is called the shape effect. The final appearance of the reciprocal lattice points is governed by how that shape is intercepted by the Ewald sphere. Perhaps the most striking examples are caused by the presence of ultra-thin crystals embedded in large thin film matrices [14].

A general example of shape effects is given in [14, 16] for a rhombus of sides  $N_x$ ,  $N_y$  and  $N_z$  unit cells which will have intensity about  $g$  as

$$I = |F|^2 \frac{\sin(\pi N_x \mathbf{K} \cdot \mathbf{a})^2}{\sin(\pi \mathbf{K} \cdot \mathbf{a})^2} \frac{\sin(\pi N_y \mathbf{K} \cdot \mathbf{b})^2}{\sin(\pi \mathbf{K} \cdot \mathbf{b})^2} \frac{\sin(\pi N_z \mathbf{K} \cdot \mathbf{c})^2}{\sin(\pi \mathbf{K} \cdot \mathbf{c})^2} \quad (2.7)$$

where the symbols have their previously defined meanings. (2.7) is important for (S)TEM specimens because the specimen is thin in one or more directions. If a crystal is tilted slightly, often the reciprocal lattice points will appear stretched in one direction with non zero  $s$  contributing to intensities around the perfect Bragg reflection, these are called *rel-rods*. Examples for discs, rods and spheres can be found in most books (e.g. [14, 15]). In Figure 2.2, the shape effects associated with a cubic nanoparticle are shown. They show that there are intensity oscillations in the directions corresponding to the cube faces. If it is a fcc material, then the oscillations would be in the  $\langle 0\ 0\ 1 \rangle$  directions.

A similar analysis has been applied to X-ray diffraction peaks, which follow similar rules to electron diffraction. It has been shown that X-ray diffraction of small crystals causes the peaks to flatten out into stumpy broad peaks. The average grain size  $d_{av}$  is given by the Scherrer equation [13]

$$d_{av} = \frac{K_{Sch} \lambda}{B \cos \theta} \quad (2.8)$$

where  $K_{Sch}$  is the Scherrer constant related to the shape and index of the crystals,  $B$  is the full width half maximum in radians and  $\theta$  is the angle. This is relevant to electron diffraction because electron diffraction patterns from polycrystalline materials often produce rings. The rings are simply a collection of reciprocal lattice points from many crystals



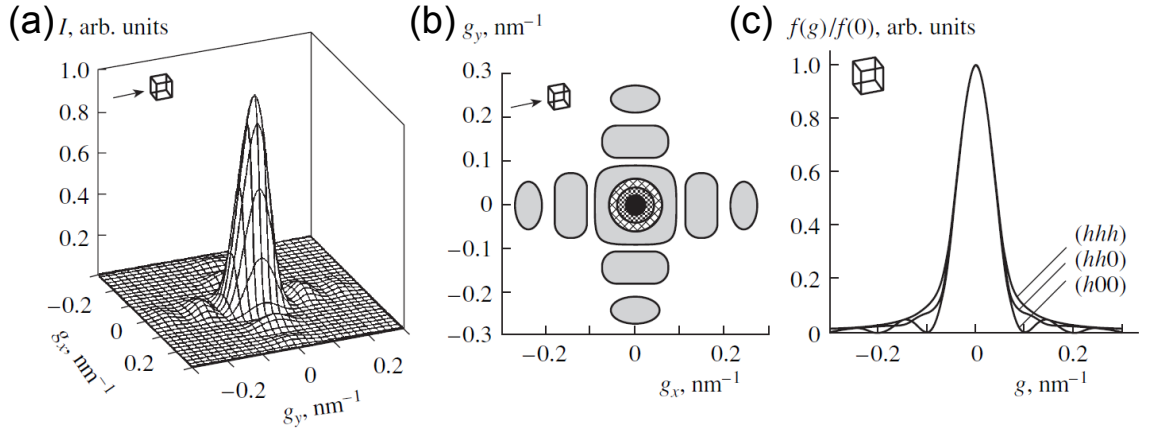


Figure 2.2: A reproduced figure from [16] showing (a) the intensity distribution around a reflection in X-ray diffraction for a cubic nanoparticle viewed along one of its faces (b) as (a) but 2D representation that would appear in an electron diffraction pattern and (c) expected intensity distribution in an X-Ray diffraction pattern

that only share the same vertical axis. A diffraction pattern like this can be analysed in the same way as an X-ray powder diffraction pattern.

There appears to be very little experimental diffraction data regarding these shape effects for small crystals such as nanoparticles. X-ray diffraction is bulk technique so it can't detect the shape of individual nanoparticles unless there is ensemble of identical particles. In electron microscopy, selected area diffraction (SAD) techniques are most commonly used which has similar limitations to X-ray diffraction in terms of scale.

Alloyeau *et al* used nanodiffraction to analyse the structure of bimetallic CoPt nanoparticles approximately 10 nm in diameter. They used this technique to prove the structure of individual nanoparticles and found that there is a structure transition above 3 nm. Cowley and co-workers have perhaps been the most prolific users of nanodiffraction using it to probe the structures of individual nanotubes, particles and other structures [17, 18]. It would seem that nanodiffraction studies are often limited to model catalysts with simple supports. Perhaps nanodiffraction or nanobeam diffraction could yield useful information regarding interface structures between nanoparticle and support. More recently nanodiffraction patterns have been combined with STEM images for diffractive imaging [19].

### 2.1.5 Double Diffraction

Nanoparticles used for heterogenous catalysis applications are often supported on a metal oxide such as  $\text{Al}_2\text{O}_3$  [20]. It is possible for electrons to diffract more than once between the loaded nanoparticles and the support. The structure factor (2.6) states that for fcc materials,

mixed indices atomic planes cannot diffract. If double diffraction were to occur, two allowed indices  $h_1k_1l_1 + h_2k_2l_2$  would generate another allowed  $h_3k_3l_3$  reciprocal lattice point [14, 21]. In this way, reciprocal lattice points associated with a zero structure factor cannot appear in fcc materials with a single atom basis. An exception is in hexagonal materials where the primitive unit cell contains more than one atom of the same species. For example in hexagonal  $[1\ 1\ 0]$  orientation, the normally forbidden  $(0\ 0\ 1)$  can appear because adding up the vectors of two allowed lattice points described by  $\mathbf{g}_1$  and  $\mathbf{g}_2$  gives the new forbidden lattice point at  $\mathbf{g}_3$

$$\mathbf{g}_3 = \mathbf{g}_1 + \mathbf{g}_2 \quad (2.9)$$

To reiterate what was said in the above paragraph, consider the double diffraction of an fcc material of the  $(0\ 0\ 2)$  and  $(1\ 1\ 1)$  planes, this would generate a reciprocal lattice point corresponding to  $(1\ 1\ 3)$  which is an allowed reflection. Genuinely forbidden reflections, corresponding to fractional indices atomic planes have been reported in some thin Au nanoparticles but the presence of these forbidden reflections have been attributed to surface defects [22], stacking faults [23] and thickness effects [24].

Double diffraction can lead to the appearance of reciprocal lattice points not associated with any crystal involved. The effect can be striking if the lattice parameters for each material are different. For example, if the nanoparticle and support are on top of one another then it is possible for the diffracted beam from the nanoparticle to act as a new  $(0\ 0\ 0)$  beam in the support. In this case, it is possible that satellite reciprocal lattice sites will appear in addition to the primary spots of the two crystals [21].

### 2.1.6 Moiré Patterns

Moiré patterns arise from the interference caused when two crystals of different lattice parameter or orientation overlap [14]. The Moiré patterns can appear as extra fringes on the image or can even resemble a new crystal if the two crystals involved are orientated sufficiently. Moiré patterns were once used to highlight dislocations in thin films because early TEMs did not have sufficient resolution to image them directly [25].

For the analysis of nanoparticles on substrates the Moiré effect is particularly important because it is possible to extract useful information from the image (via fast Fourier transform, FFT) if a diffraction pattern cannot be obtained. A general equation that gives the Moiré fringe spacing  $D$  is [14]

$$D = \frac{d_1 d_2}{(d_1^2 + d_2^2 - 2d_1 d_2 \cos \theta)^{\frac{1}{2}}} \quad (2.10)$$

where  $d_1$  and  $d_2$  are the atomic plane spacings of the two lattice fringes observed and  $\theta$  is the rotation angle between the two in radians. The rotation between the two lattice fringes causes the rotation to be magnified in the Moiré pattern.

## 2.2 The (Scanning) Transmission Electron Microscope Instrument

Figure 2.3 shows a lens diagram of a typical (S)TEM. In the figure, the location of important lenses, apertures and image planes are indicated. Correction and deflector coils are not shown because they do not contribute to the critical geometry of the ray diagram and the function of the optical elements. The electron source of the microscope is either a filament, such as  $\text{LaB}_6$  or a field emission gun (FEG). The workings of them are described elsewhere (e.g. [15]) but the most important difference for TEM is that the illumination from FEG instruments is more coherent [26]. For STEM it is the 1000x increase in source brightness. The narrower energy spread is beneficial for both TEM and STEM.

Coherency in the electron source is related to its brightness and effective size. Coherence is a term that describes how well each progressive wave from a source are related to each others phase. A temporally coherent source will produce wave-packets identical to each other in frequency and time. A spatially coherent source is one which electrons will all originate from a single apparent source. A spatially and temporally coherent source will be both bright and very small which allows electrons with the same phase to interact with the specimen. It is therefore possible that phenomena caused by the phase difference of diffracted beams relative to the source will produce additional phase information compared to an incoherent source such as a conventional filament source such as  $\text{LaB}_6$ .

The first lenses under the gun are the condenser lenses; the condenser lenses are responsible for the illumination of the specimen. In combination with the condenser aperture, they determine the convergence angle,  $\alpha$ , of the electron beam at the specimen. By adjusting the crossovers between multiple condenser lenses, the convergence angle can also be controlled. Adjusting the location of the crossover determines the spot size of the electron beam at the specimen.

The pre-objective lens or other mini-lenses may be used for specific modes of operation. TEM requires a nearly parallel beam of electrons whereas convergent and nano beam diffraction (CBD, NBD respectively) are special nano-area probes formed in a TEM

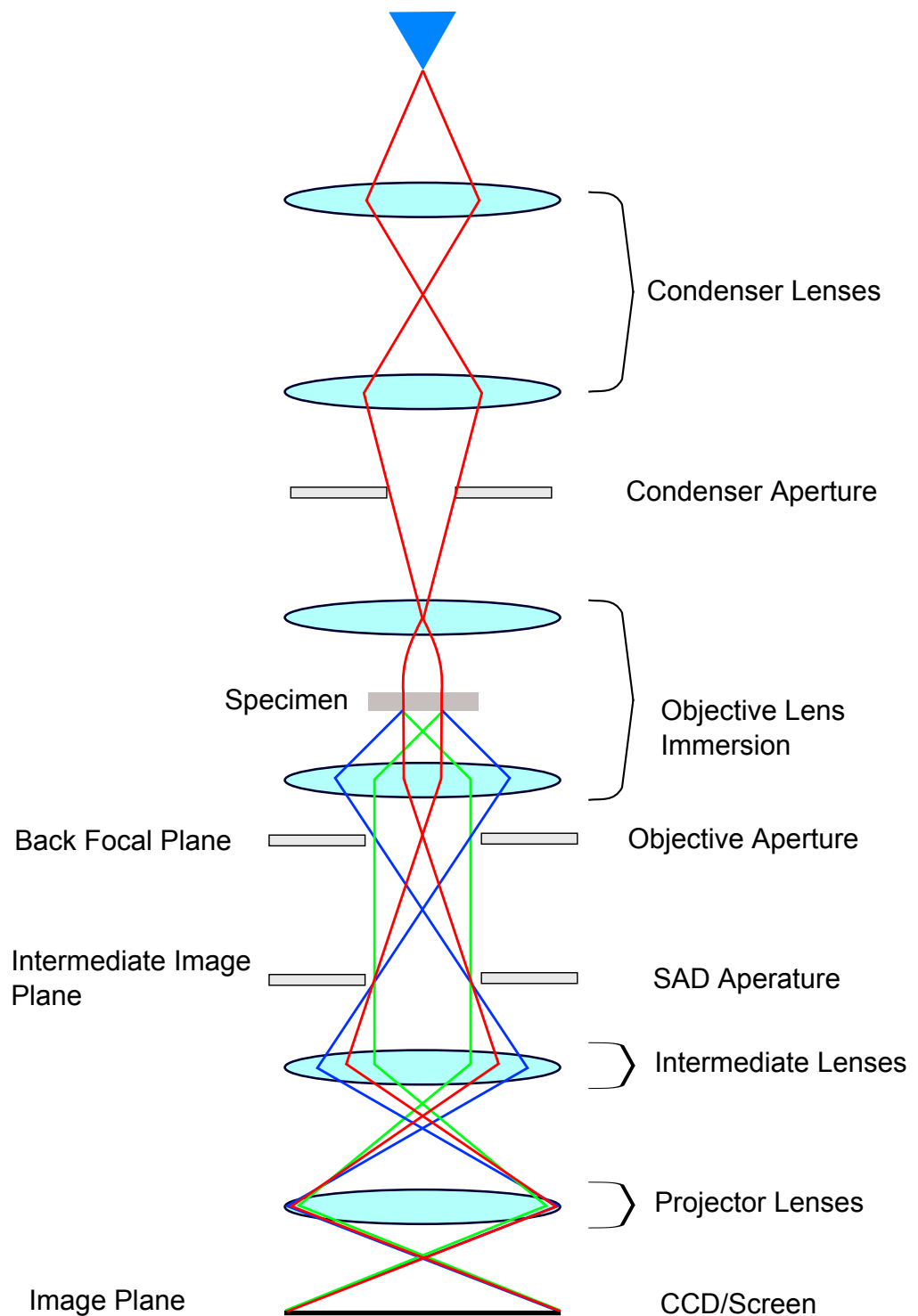


Figure 2.3: A schematic diagram showing the function of the various lenses involved for TEM imaging.

instrument with increased and variable convergence angles.

The post specimen lens in a TEM gathers most of the useful transmitted beams exiting the specimen. The crossover after this lens is the location of reciprocal space (called the back focal plane) and the location of the objective lens aperture. Adjusting the strength of the objective lens causes the back focal plane to shift position and this shift corresponds to a change in the image phase contrast. The objective lens suffers from spherical aberrations which cause wider angle beams to be focused at shorter focal points and this limits resolution. The effect of aberrations are discussed later in more detail.

The intermediate lenses and projector lenses, invert and refocus the electrons to achieve the required magnification and are responsible for switching between imaging and diffraction mode in a TEM. An aperture inserted between the intermediate lenses at the intermediate image plane allows electrons to be selected for diffraction analysis from only a specific area of the specimen. This produces a selected area diffraction pattern (SAD).

A modern (S)TEM may have other features such as an X-ray detector or an in-column energy filter for energy electron loss spectroscopy (EELS). TEM images are normally recorded using a Peltier cooled CCD camera [27].

## 2.3 TEM Mode and Image Contrast

In TEM mode, the specimen is illuminated with an almost parallel beam of electrons. The transmitted electrons are gathered by the post-specimen magnetic field of the objective lens and the intermediate and projector lens display an image of variable magnification on the image screen or CCD camera. The term defocus,  $\Delta f$ , is used to describe the deviation of strength from the imaging lens's gaussian value. Adjusting the defocus ( $\Delta f$ ) means that the back focal plane changes position slightly so the image projected is slightly different.

Contrast from TEM images falls into two main categories: diffraction contrast and phase contrast. Theoretical models explaining the diffraction contrast in materials from a TEM point of view were developed by Hirsch *et al* in the 60s [14]. The basic principle is that the time independent Shrödinger equation is solved for a periodic potential as Bethe originally did in the 1920s. The periodic potential means that the incident wave and diffracted waves split into Bloch waves where there are two principle types. One with maxima at atomic columns and another with maxima between atomic columns. The appearance of the crystal also depends on the orientation of a crystal which relates to the

diffraction conditions of the electrons because it effects how the two types of Bloch waves interact with each other.

The Bloch wave approach requires the knowledge of complex amplitudes for the transmitted beam and for each diffracted beam. It is possible to acquire a two beam case where the transmitted beam  $g_{000}$  and a single diffracted beam  $g_{hkl}$  are the dominant reflections but in reality many beams are strong.

The phase contrast approach is usually described by the phase object approximation developed by Cowley and co-workers [28]. The specimen electron wavefunction,  $\psi(r)$  is given by [29]

$$\psi(r) = \psi_0 \exp(-i\sigma_c \phi_p(x, y)) \quad (2.11)$$

where  $\psi_0$  is the amplitude of the incident wave,  $\sigma_c$  is the relativistic interaction constant given by  $\sigma_c = m/(\hbar^2 k)$ .  $\phi_p(x, y)$  is the atomic potential projected into the  $z$  direction which is given as [29]

$$\phi_p(x, y) = -\frac{8\pi^2 \hbar^2}{m_0} \sum_{j=1}^n \frac{a_j}{b_j} \exp \left[ -\frac{4\pi^2}{b_j} (x^2 + y^2) \right] \quad (2.12)$$

where  $a_j$  and  $b_j$  are fitting parameters. By allowing  $\varphi(x, y) = -\sigma_c \phi_p(x, y)$ , substituting into (2.11) and expanding the sum but ignoring the second order terms (assuming  $\varphi(x, y) \ll 0$ ), then (2.11) becomes

$$\psi(x, y) \simeq 1 + i\varphi(x, y) \quad (2.13)$$

The assumption that second order terms in the expansion of the precursor to (2.13) is called the weak phase object approximation (WPOA). The WPOA is the basis of most HRTEM image theories.

The intensity is  $|\psi|^2$  but this does not include the effect of the microscope optics. A function, called the contrast transfer function is used to describe how one point in the image is transferred into the image. The contrast transfer function is given as [15]

$$T(u) = A(u)E(u)2 \sin(\chi(\mathbf{u})) \quad (2.14)$$

where  $A(u)$  and  $E(u)$  are the aperture and envelope (electron source) terms. The details of  $A(u)$  and  $E(u)$  are described elsewhere but  $E(u)$  adds an envelope term to  $T(u)$  which has the effect of imposing an information limit. The  $\sin \chi(\mathbf{u})$  term is called the phase contrast transfer function and is dependant on the phase function  $\chi(\mathbf{u})$  which is defined as [15]

$$\chi(\mathbf{u}) = \pi \Delta f \lambda u^2 + \frac{1}{2} \pi C_s \lambda^3 u^4 \quad (2.15)$$

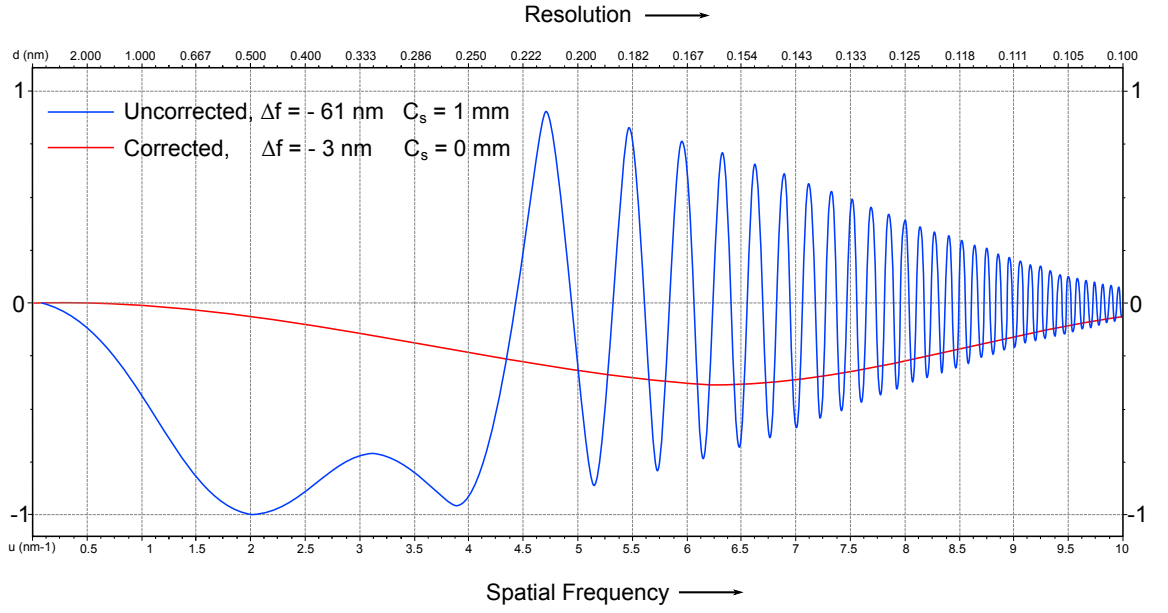


Figure 2.4: Typical CTF for a corrected and uncorrected TEM including  $E(u)$  with the following parameters. Uncorrected:  $C_c = 1.4$  nm and focal spread = 2.60 nm. Corrected:  $C_c = 1.6$  nm and focal spread = 2.98 nm. Both: objective lens stability = 0.5 ppm, energy spread = 0.7 eV, convergence = 0.03 mrad

where all symbols have their previously defined meanings. Figure 2.4 shows a contrast transfer function of an aberration corrected and uncorrected microscope at different defocus values. Without aberration correction, the CTF oscillates at high spatial frequencies therefore limiting resolution. With aberration correction, it does not oscillate meaning the phase of different spatial frequencies is similar. Adjusting the defocus to produce the flat-test curve with a conventional TEM requires the use of a  $\Delta f$  which balances out the  $u^4$  term, this is called the Scherzer defocus.

Another advantage of aberration correction is that the shape of the CTF (Figure 2.4) can be adjusted by changing  $C_s$ . This means that the image contrast can be finely adjusted. Some groups increase the contrast over a particular range of spatial frequencies to image particular details in crystals [30,31]. The negative aberration correction approach results in a negative phase imaging condition (as shown in Figure 2.4 for the corrected microscope). The negative aberration correction, when combined with a positive  $\Delta f$ , results in atomic columns appearing white against a dark background [31].

It is believed that in the negative  $C_s$ , positive  $\Delta f$  imaging mode, the contrast of atomic columns is improved because of increased channelling effects. Channeling occurs when electrons are localised around a particular atomic column, hence their contrast is increased [32]. This usually occurs in a high symmetry zone axis [32]. Chen and Van Dyck have argued that images of materials (such as Si) will show black atomic columns when phase

contrast dominates but white when channeling effects dominate [32]. This phase reversal can also occur due to changes in thickness at a given  $\Delta f$  [32].

With or without aberration correction, several groups have pointed out that HRTEM images may not be accurate enough for sensitive structural analysis [33]. Other aberrations such as coma (beam tilt) and first order astigmatism can effect the image contrast. These aberrations can be corrected, even without an aberration corrector, but misalignments can cause image quality issues. Misalignments with in-column energy filters can also cause image distortion.

Image analysis is often accompanied by the analysis of the images Fourier transform which is accomplished by the fast Fourier transform (FFT) algorithm which produces an artificial diffraction pattern (or optical diffractogram) for analysis of reciprocal space. However, the accuracy of the FFT is dependant on the image quality. Alternative means, namely exit-wave reconstruction, has also been employed to resolve atomic sites at surfaces [34]. This requires the collection of many images and ultimately relies on the alignment of the microscope.

Furthermore, the HRTEM image contrast itself is not without uncertainty. HRTEM simulations over the past few decades have shown that the effect of beam and crystal tilt can play a key role in the appearance of small crystals and can sometimes distort the appearance of crystal planes [35].

Limiting the range of electrons that make up the image can also aid in the analysis of specimens. The objective aperture shown in Figure 2.3 allows a confined range of diffracted electrons to enter the imaging system thereafter. Selecting a single diffracted beam results in an image where the intensity solely arises from that particular diffracted beam. Anything else appears dark, hence dark field. Conversely, selecting the direct (000) beam, is called a bright field image because it shows only effects arising from mass and thickness contrast.

## **2.4 (S)TEM Mode and Image Contrast**

The modern STEM instrument was invented by Albert Crewe and co-workers [36]. Instead of a parallel beam of electrons, the electrons are converged to a point. The focal position of the electron beam is called the electron probe. In many ways, the (S)TEM technique is very similar to the SEM which was invented after the TEM [37]. The STEM was one of



the first instruments to enable the imaging of single atoms [38], with aberration correction, it is now possible to obtain 0.5 Å resolution [39] which is greater than any TEM at the time of writing.

STEM mode is essentially a convergent beam technique. The optic diagram of STEM probe formation is shown in Figure 2.5. The beam is so small that no image can be acquired from a given probe position, instead a Ronchigram is projected [40]. A Ronchigram is a diffraction pattern where virtually every diffracted beam interacts with one another [40,41]. The central region of the Ronchigram when in focus is the infinite magnification image [40].

The probe position is controlled by a set of scanning coils, these are not shown in the diagram. The STEM technique is only dependant on the optics above the specimen, whereas in TEM, the optics of the entire column are important for imaging. The projector and intermediate lenses do nothing to influence the image of a STEM instrument; but they match the collection angle for forward scattered electrons to suitably shaped detectors and energy loss spectrometer (EELS).

A stationary probe formed by a modern STEM is very small (0.1 nm). At each probe position the STEM probe will project a diffraction pattern onto the recording media determined by the camera length similar to TEM diffraction mode. The diffraction pattern may appear as a Ronchigram, a diffraction pattern in which all diffracted beams overlap and interfere with each other. Under-focusing the probe will produce a shadow image [40], which is similar in appearance to a TEM image.

A STEM forms an image by scanning the probe across the specimen and plotting the measured intensities measured by one or more detectors as a function of probe position to form an image. The magnification is set purely by the scanning region and not any lenses. The resolution is limited by the shape, size and the intensity of the probe because the signal originates solely from the atoms influenced by the probe.

The contrast observed in the recorded image depends on which electrons are being collected. The electrons in the direct beam are collected by a detector aligned with the microscope optic axis. These electrons are used to form a bright field STEM image. The technique is called bright field STEM (BF-STEM). The technique is analogous to a conventional TEM image, as opposed to a bright field TEM (BF-TEM) image which only uses the direct beam to form an image. Generally, the BF-STEM image is similar to a TEM image and is composed primarily of diffraction contrast and absorption.

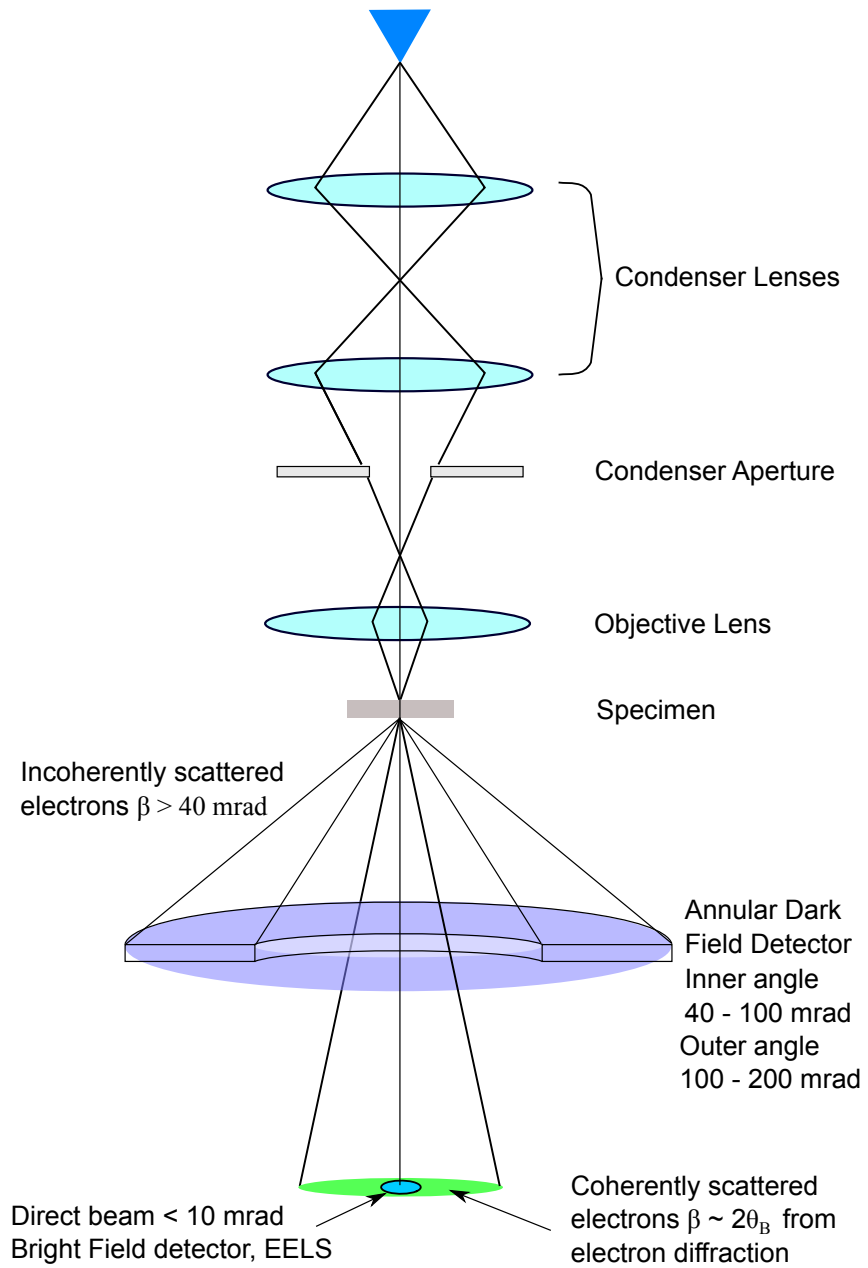


Figure 2.5: Schematic showing the optic diagram of STEM mode. The scanning coils are not shown

The same STEM probe can be used with special detector to collect high angle scattered electrons that originate from electron-nucleus (Rutherford) scattering. The inner angle of the detector is generally  $> 40$  mrad and the outer angle is generally  $< 200$  mrad. Intensity is plotted in similar fashion to the bright field STEM technique except that the detector is annular. In the dark field STEM image intensities are proportional approximately to  $Z^n$  where  $1.5 < n < 2.0$  [38,42,43]. This makes the technique ideally suited for the study of heterogeneous solid state catalysts which often employ high  $Z$  material nanoparticles on low  $Z$  supports [44]. This technique is called high angle annular dark field STEM or HAADF-STEM.

A complication with the HAADF-STEM technique is that the image intensity is not absolute. The detector signal is adjusted by using brightness/contrast settings and during image acquisition, there may be additional processing to assign the full look up table (LUT) values to the images intensities. Several groups have attempted to remedy this problem by expressing the intensities as a function of the initial probe intensity [45,46,47]. Using this technique, it has been possible to assign an atomic column to a number of atoms. Quantitative analysis has been done by calibrating the detector [48] to detect compositional variations in bimetallic nanoparticles [49] and analysing the thickness of MoS<sub>2</sub> crystals [50]. Careful and systematic control over the electronics is required to use the normalised intensities effectively.

## 2.5 Aberrations

The classical axially symmetric cylindrical magnetic lenses are not perfect. They suffer from optic defects called aberrations. Lenses made for photonics (light) optics can be made near perfect by combining convex and concave lens elements. Concave cylindrical magnetic lenses currently do not exist so the aberrations must be dealt with in a different way. Aberrations limit microscope resolution and influence high resolution image contrast, so it is important they are reduced. The spherical aberration is the most important because it cannot be corrected conveniently and it has other effects aside from limiting the microscopes resolution [51,52,53,54]. The most important of these is the convoluted form of the high resolution CFT (see Figure 2.4 on page 30).

Figure 2.6 is a diagram showing the effect of spherical aberrations on electron beams entering the lens on different trajectories. Electrons entering a magnetic lens at higher scattering angles and therefore further away from the centre of the lens are focused at a

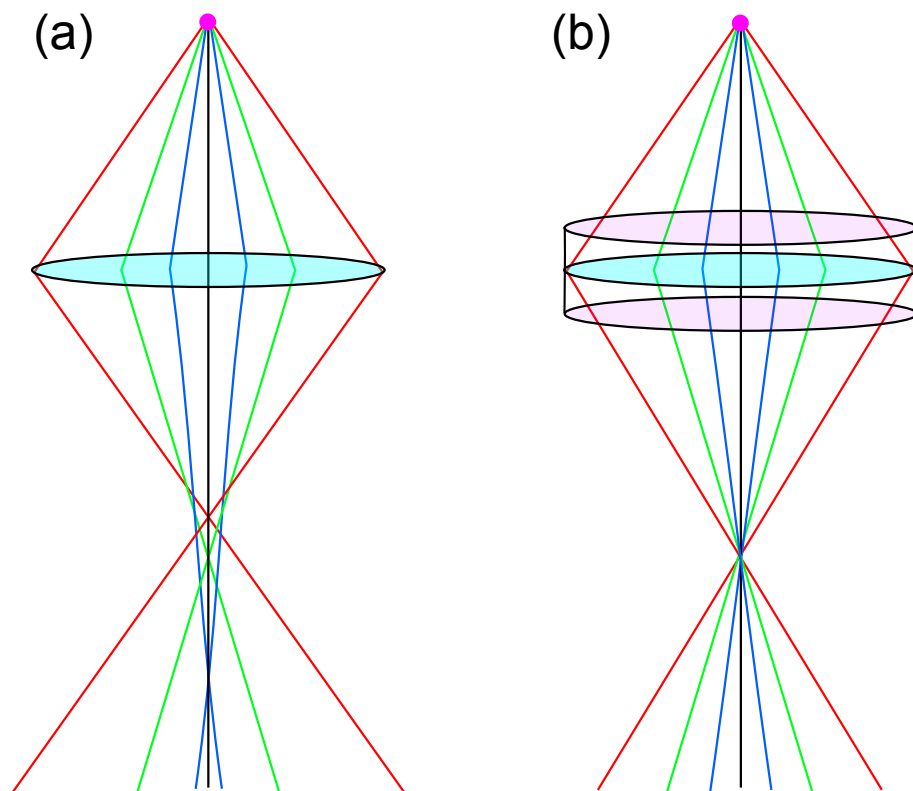


Figure 2.6: A diagram showing the effect of spherical aberration on the focal position of various electrons entering the lens before correction (a) and after correction (b). The black line is the optic axis of the microscope.

different position to those near the centre because the magnetic field is not radially uniform across the gap between the magnets. The aberrations are corrected by a series of multi-pole magnetic lenses which provide asymmetric magnetic fields so in combination the extra lenses act like a single concave lens [52, 53]. The aberration correctors require exceptionally high stabilities and are controlled by sophisticated software which did not exist in Scherzer's day when the idea was first proposed [51].

Objective lens aberrations are corrected using thin amorphous materials such as C because FFTs of the images of such materials are well defined and provide a continuous range of spatial frequencies [55]. Therefore effects of aberrations can easily be seen [53, 56]. In order for the TEM aberration correction software to work,  $\Delta f$  must be 0 but the specimen itself must be underfocused so that the beam converges, this is done by adjusting the specimen height to place it in a small effective negative defocus condition [53]. The methodology associated with this process is described on page 46.

Condenser or probe forming lens aberrations are corrected by using a specimen containing many heavy metal nanoparticles, such as Au, which enable a high amount of counts to be collected on the HAADF-STEM detector. The sharpness of the nanoparticles is

linked to the probe shape and intensity. The correction enables a sharper and more intense probe to be formed allowing the maximum amount of intensity to be plotted with each probe position [57, 58, 59]. The methodology associated with this process is described on page 49.

Another benefit of correcting the spherical aberration is that a wider objective lens pole-piece can be installed without significant compromises in microscope performance. The wider polepiece allows both higher specimen tilt angles and standard heating holders such as the Gatan 628 used during this project.

## 2.6 Electron Diffraction using (S)TEM

### 2.6.1 Selected Area Diffraction

To switch into diffraction mode in TEM, the intermediate lens strength is changed to focus on the back focal plane of the objective lens so that a diffraction pattern is projected instead of an image. The physical size of the projected diffraction pattern is given by [15, 21]

$$Y = \frac{\lambda L}{d} \quad (2.16)$$

where  $Y$  is the distance from the centre of the diffraction pattern (direct beam or  $\{000\}$ ) to a diffracted beam corresponding to atomic plane separation  $d$  on the recording plane.  $\lambda$  is the wavelength and  $L$  is the camera length which is the effective distance between the specimen and the recording plane. The product  $\lambda L$  is often called the camera constant. It refers to the magnification of the diffraction pattern. Use of a small camera constant means that the diffraction pattern appears small but a wider view of reciprocal space is captured. It is possible to calibrate this using materials with a well known lattice parameter and structure.

Aside from limiting the image resolution, there is an impact on the reliability of diffraction patterns in terms of the area selected [60, 61] by a SAD aperture. The area selected by a SAD aperture is determined by projecting the aperture back to the specimen plane. This introduces a displacement between the SAD aperture plane and the specimen plane dependant on the divergence angle,  $\beta$  (twice the Bragg angle,  $\theta_B$ ), spherical aberration and defocus [14, 60, 61]

$$y = C_s \beta^3 + \Delta f \beta \quad (2.17)$$

It is possible to keep the defocus value to a minimum but in a conventional microscope the error can be as large as several  $\mu\text{m}$  because  $C_s$  is large compared to  $\Delta f$ . If  $C_s$  is reduced

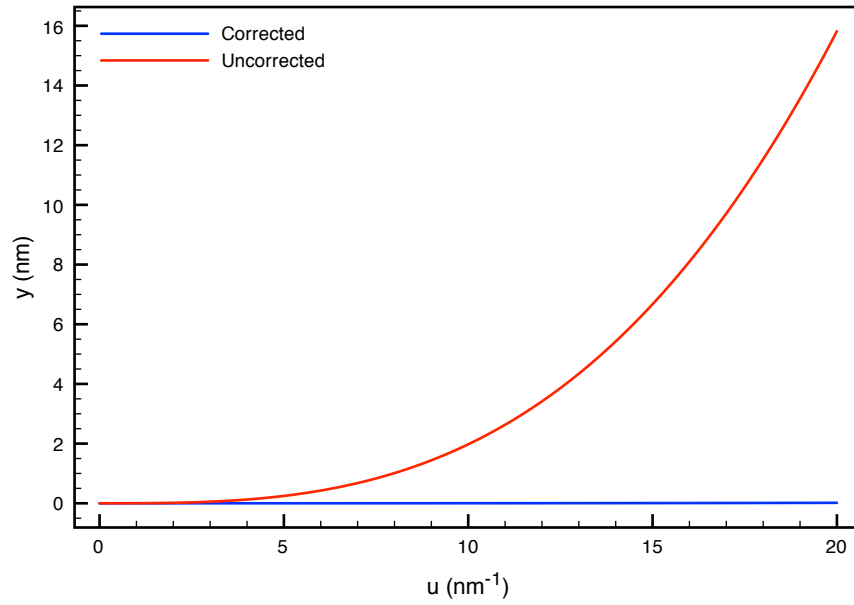


Figure 2.7: A graph showing the relation between reciprocal lattice vectors,  $g$  with increasing spatial frequency and the area uncertainty for a selected area for  $C_s$  values of 1 mm (uncorrected) and 1  $\mu\text{m}$  (corrected). This graph is a remade version of a similar figure in [14] using Pt

by aberration correction from, 1 mm to 1  $\mu\text{m}$  then it is improved by several orders of magnitude. Figure 2.7 shows the area in uncertainty for a conventional microscope and an aberration corrected microscope. For an aberration corrected microscope it can be seen that only the high spatial frequency diffracted beams are displaced. By using a very small aperture, Tanakas group have acquired SAD diffraction patterns from areas as small as 20 nm with virtually no error in an aberration corrected microscope [62].

## 2.6.2 Diffraction in (S)TEM

Correcting the aberrations in a STEM ensures that the probe is as sharp as possible [57]; as defined by probe current density and size. In HAADF-STEM mode, all of the signal originates from the probe, so by correcting the aberrations it is possible to extract the maximum possible amount of signal from the specimen [63]. This is important for imaging small structures with much better contrast than previously possible [57, 58, 64]. Aberrations are corrected by using a specimen with small easily distinguishable crystals such as Au nanoparticles on amorphous carbon. In this case  $\Delta f$  is set to 0 and the specimen as close to focus as possible using the stage height adjustment.

Only the use of a very small aperture will produce a small enough convergence angle for SAD like diffraction patterns in (S)TEM. This technique is dubbed nanodiffraction by

Cowley who pioneered it [18]. Adjusting the focus in STEM mode sets where the probe is focused vertically and this can be used to achieve narrow convergence angle in STEM but this is not suitable for acquiring diffraction patterns from small areas. Either probe size or convergence angle can be minimised but not both together.

### **2.6.3 Nano Area Electron Diffraction**

Generally speaking the vast majority of nanoparticle analysis has been done with HRTEM, BF-STEM and HAADF-STEM. From these images, FFTs have been analysed. In section 2.3, the literature surrounding the accuracy of HRTEM suggested that the FFT approach is not suitable for high sensitivity analysis, particularly small nanoparticles.

There are relatively few studies of nanoparticles with techniques that use a small probe, either parallel or convergent for the study of individual nanoparticles. Generally, information that high angle diffraction modes can extract from materials only applies to thick crystals above 100 nm. The equivalent near-parallel version of CBD is NBD (nano-beam) mode.

There appears to be no detailed literature on the benefits or drawbacks of NBD, perhaps because it requires a small convergence angle to make the diffraction pattern appear much like a SAD spot pattern rather than discs, as is often the case in CBD or STEM.

Alloyeau and co-workers used a nano-area diffraction technique in STEM mode to investigate the lattice parameter of small CoFe nanoparticles [65]. They note that much like (S)TEM images, the crystal needs to be in a zone axis for unambiguous structural analysis. Other groups have studied very small structures including 1 nm Pt nanoparticles on various supports. They generally note that the nanoparticles are amorphous but their analysis is not accompanied by diffraction analysis. Their analysis is reliant on the contrast in the image. NBD has the ability to reveal information even if the nanoparticle is not in the zone axis, even if complete structural analysis is then not possible. Of course, on a thick and complex support, it would be a challenge to distinguish reflections from the nanoparticle and support.

## 2.7 Environmental (S)TEM

Catalysts operate at various temperatures and pressures in different environments. Although (S)TEM can provide structural insights which can infer activity, the vacuum of an electron microscope is not a suitable environment for investigating how the catalyst behaves under the conditions it was designed for.

A branch of electron microscopy deals with the use of high temperature and gaseous environments in the electron microscope. The branch is often referred to as E(S)TEM, short for environmental (S)TEM. Generally, heating is achieved by using specially designed specimen holders for (S)TEM instruments. The heating holders use a heating element to heat the specimen with current provided from outside the microscope. The electrical noise associated with the power supply of these holders is detrimental to resolution, particularly in STEM [66]. Depending on the material the holder is made of, high temperature heating holders cannot be exposed to air while hot because any oxidation would damage the holder. Special holders can be made of oxidation resistant materials. The heating holders tend to be much thicker than regular holders so not all microscopes can accommodate them because the gap between the top and bottom objective lens pole pieces is too narrow. The York-JEOL Nanocentre JEOL 2200FS has an extra large polepiece gap which can accommodate heating holders.

The vacuum of a microscope is generally around  $10^{-5}$  Pa. To allow environmental capacity, specimen holders were specifically designed to act as self contained reaction cells [67]. The holders have electron transparent windows which contain the gas [67]. These can operate at high pressure, up to and above 1 bar. However, the electrons interact with the transparent windows which limits resolution and it also prevents accurate EDX analysis [68].

Another approach is to inject gas into the microscope column around the specimen. Injecting gas into the microscope is potentially risky, because the gas could make its way up to the electron gun and cause damage. There are several approaches to keep the gas around the specimen. The currently used approach is to use a differential pumping system where the gas is rapidly pumped out just above and below the sample [66, 69, 70, 71]. This was originally achieved with a specially designed reaction cell containing differential pumping apertures to prevent the diffusion of gas into the rest of the microscope [69, 70].

Now, a similar cell, called an ECELL, is built into the microscope itself which allows any normal holder to be used [71]. The design essentially allows full TEM capability [71].



This design has been commercialised by FEI [72], and is incorporated into their latest model, the Titan ETEM G2. TEM aberration correctors have been incorporated into this design but not STEM aberration correctors. The design of the E(S)TEM at York is similar but incorporates aberration corrections for both STEM and TEM [72, 73]. Although some microscopes are capable of *in-situ* ESTEM, the resolution obtained is far behind that of conventional ETEM. The developments at York represent the latest developments in the field of ESTEM which have brought forward atomic resolution ESTEM with aberration correction [66].

## 2.8 Image Analysis and Simulation

For image analysis, Gatan Digital Micrograph and the free ImageJ [74] software packages were employed. A Java based electron microscopy simulation package called JEMs [75] was used for crystal visualisation and as an aide for diffraction pattern analysis. Another program, called VESTA [76] was used as an alternative for making and displaying models. JEMS was used for HRTEM simulations whereas a free package created by Chris Koch called QSTEM [77] was used for HAADF-STEM simulations.

The basis behind most (S)TEM simulation software is the multi-slice algorithm originally invented by Cowley and Moodie [28]. The current approach is based off Goodman and Moodie's [78] newer algorithm which can handle many diffracted beams. The multi-slice algorithm takes the structure and splits it into slices of thickness  $\Delta z$ . The initial electron wavefunction is the input and this is diffracted by the atoms in the first slice. The bottom surface of the first slice acts as a Fresnel propagator and the diffracted beams are taken into the next slice and the process continues until the final surface is reached where an exit wavefunction is produced.

Most simulation packages have built in default values for the atomic scattering form factor  $f_i(\theta)$  shown in equation (2.6). In reality, atoms oscillate from their default position because of thermal vibrations so this has the effect of smearing the projected potential of a column of atoms and introduces an absorption term in the electron wavefunction [79, 80, 81]. The electron-phonon interaction gives rise to an increase in higher angle scattering at the expense of lower angle scattering (such as Bragg diffracted electrons) [80]. This effect is often referred to as thermally diffuse scattering.

Simulation packages for now can't take the time lapsed image into account during a single simulation so they use the frozen-phonon model. The frozen phonon approach

randomly shifts each atom once by an amount dictated by the atom's Debye-Waller factor. Detailed discussion on the calculation of Debye-Waller factors can be found elsewhere, see for example [55]. The physical worthiness of the frozen-phonon model was argued by Van Dyck [81] who showed that it is equivalent to a full quantum mechanical treatment of electron-phonon scattering sufficient for quantitative simulations. To include the effects of absorption, QSTEM was used for HAADF-STEM simulations instead of JEMs.

During image acquisition over a period of several seconds, the atoms will vibrate many times and therefore a single frozen-phonon calculation may not be sufficient for quantitative HAADF-STEM image simulations [82]. Hence, some simulation packages can perform many frozen-phonon calculations and take an average to produce a single final output.

## **2.9 Other Techniques**

### **2.9.1 Scanning Electron Microscopy**

A scanning electron microscope (SEM) is much like a low voltage version of a STEM but its intended targets are the surfaces of electron opaque specimens which can be in bulk form. An image is acquired by scanning a specimen surface and collecting any ejected electrons or X-rays. The most commonly used imaging techniques are with back scattered electrons and secondary electrons [83].

Back scattered electrons (BSE) are scattered at high angles with a significant fraction of the incident electron energy that formed the probe. The electrons are scattered by the nuclei of the atoms in the specimen, thus BSE images are sensitive to  $Z$  [83] and typically originate from depths of  $0.1 - 1 \mu\text{m}$ .

Secondary electrons are generated by collisions between the incident beam and loosely bound electrons. The secondary electrons emerge from the specimen at a wide range of angles but their detectable origin is limited close to the surface because their escape range is limited to approximately  $5 \text{ nm}$  [83]. Thus the secondary electrons provide spatial resolution but they are not so sensitive to the atomic species present. The atomic species of the specimen influences the probe electrons below the surface, heavier elements such as Pt limit the electrons to those closer to the surface, whereas light elements such as Si result in larger interaction volumes limiting the spatial resolution for a given accelerating voltage. In addition, some secondary electrons are generated by backscattered electrons producing

a wider background signal. However the primary factors determining is associated with secondary electron image resolution are the incident electron voltage, probe size and the  $< 5$  nm escape range [83].

### **2.9.2 Energy Dispersive X-ray Spectroscopy**

Electrons will lose some energy in electron-electron collisions. An incident electron will cause an electron in a given atomic energy level to be excited into a higher energy state. The hole left behind will be immediately filled by another electron in a higher energy state and that too will leave behind a hole and so forth causing a cascade of transitions. These transitions will each emit an X-ray equal to the difference between energy states. The transitions follow rules based on several quantum numbers and their probability is dictated by Fermi's golden rule [15].

The X-ray is called a characteristic X-ray because such transitions have unique energies associated with energy level transitions in each atomic species. Useful characteristic X-rays are between 0.2 – 20 keV so a (S)TEM is capable of exciting the whole spectrum from an area selected by the incident electron beam. Energy dispersive X-ray spectroscopy (EDX) cannot directly distinguish between the different chemical states associated with the same element.

The formation of X-rays causes an apparent spread in the beam within the specimen, especially in thick materials [83]. This is because the X-ray signal has a relatively low spatial resolution compared to the electron signals, especially for bulk samples due to the large excitation volume into the sample for X-ray generation and escape. Using thin films limits the lateral spreading.

## **2.10 York-JEOL Nanocentre Resources**

The SEM used during this project was a FEI-Sirion equipped with a field emission gun. The microscope can usefully operate between 5 – 30 kV. A new Thermo silicon drift detector was used for EDX analysis. The SEM was equipped with a secondary electron detector and offer a resolution of 2 nm.

A conventional TEM in the form of a JEOL 2011 (upgraded JEOL 2010) with a LaB<sub>6</sub> filament was used principally for sample screening and tasks that did not require the use of

the aberration corrected TEM. This TEM has a resolution of about 0.2 nm. It has a variety of convergent beam modes in the form of EDX, CBD and NBD modes which are useful for small area diffraction. A conventional Thermo liquid N<sub>2</sub> cooled Si(Li) thin window EDX detector was used for chemical analysis. The CCD was a Gatan Multiscan 794 with 1024x1024 image resolution. A standard JEOL single tilt holder and a JEOL double tilt holder were compatible. Maximum tilt range was 25° in the *X* and *Y* axis with a standard JEOL double tilt specimen holder in the narrow gap ultra high resolution objective lens.

The Schottky FEG equipped aberration corrected (S)TEM was a first generation JEOL 2200FS equipped with CEOS aberration correctors on the probe forming and post specimen objective lens with an Omega in-column electron energy loss spectrometer (EELS) and imaging energy filter. A Thermo Si(Li) window EDX detector for chemical mapping and X-ray spectroscopy was also available. This particular 2200FS had an extra wide pole piece gap which allowed a Gatan 628 single tilt heating holder to be used in addition to the default JEOL single and double tilt holders. Aberration correction preserved the < 0.1 nm resolution. This microscope was modified by Professors Boyes and Gai such that environmental (S)TEM is possible [72, 84]. The modifications are described elsewhere [73]. The camera used was a Gatan Multiscan 894 with 2048x2048 image resolution.

## **2.11 Microscope Methodology**

### **2.11.1 TEM and HRTEM**

The JEOL 2200FS was aligned each morning using a reference sample in the form of Au nanoparticles on thin C films. The thin-C films were prepared by Mike Walsh [85]. Thin-C (2 nm) films are prepared by floating the mica supported thin films (Agar 116-1) on distilled water. The floating films are then fished out with a holey-C grid held by tweezers. This causes the holes in the grid to be coated by the thin C film. A diluted suspension of Au nanoparticles were then deposited onto the grid. The thin-C minimised background noise from the film, maximising the resolution of the nanoparticles to aid the alignment of the microscope. Detailed studies of this model catalyst can be found elsewhere [9]. The JEOL 2011 was aligned during the session with ordinary samples, which in the case of this thesis largely contained holey-C films. The alignments below describe a general alignment procedure which is relevant for both the 2200FS and 2011. Differences in alignment procedure between the two microscopes are outlined where required.

The specimen was first put into focus by using the height controls. When in focus, the image showed minimal contrast. It was important that this alignment was done with  $\Delta f = 0$ , i.e. at the default objective lens current. On the 2200FS, the standard focus button was pressed to ensure this. On the JEOL 2011 no such button exists but there is a DV value which represents how far away from standard current the objective lens is. The defocus knob was adjusted so that DV went to 0. The magnification was then switch to and from one magnification to another. This caused  $\Delta f$  to reset to zero whilst DV remained 0.

Before describing more alignment procedures, it is important to note that between each set of lenses there are a series of deflector coils which tilt and shift the beams at various points. They are not shown in Figure 2.3. Only the alignment coils above the specimen plane are described here in detail since they effect the resolution of the microscope. These are referred here to as the gun alignment coils (beneath the gun) and beam alignment coils (beneath the condenser lenses). These are required because the physical alignment of the lenses in the microscope is not perfect. A lateral shift cannot be directly induced in an electron beam hence it must be deflected first by a tilt coil at an angle to the shift coil which then introduces lateral shift, after which a reciprocal tilt restores the beam direction to the axis.

Gun and energy filter alignment was maintained by Dr Leonardo Lari on the JEOL 2200FS. On the JEOL 2011, sometimes the gun needed realignment. This was done by converging the beam to a point using the largest spot size. The beam shift coils were then neutralised and if needed, the beam was shifted to the centre using the gun shift controls. The filament current was then turned down so the filament was visible. When aligned, it should look like a symmetrical cats eye, when it wasn't it was adjusted using the gun tilt controls. The filament was then resaturated. The smallest spot was then selected whilst the beam converged. If it was not centred then the shift coils were used to centre it. The oscillation to the smallest and largest spot size was repeated until the beam at both spot sizes were in the centre of the screen.

The converged beam was occasionally elliptical due to the presence of condenser astigmatism (especially after the above alignment). This was adjusted by using the condenser astigmator coils to make the beam round again. After this, the alignment of the condenser aperture was checked. The beam was repeatedly converged and expanded by adjusting the final condenser lens current (often called brightness) and when it did not expand concentrically from the centre, then the aperture position was adjusted. If the beam went off centre when converged, it was beam shifted to the centre. This was repeated many times

until the beam remained stationary in the centre of the screen and optic axis during focus.

Another important alignment was the synchronisation of the beam tilt and shift coils, this alignment is sometimes called the pivot point alignment. The tilt adjustments ensures that the beam alignment coils tilt axis is aligned with the sample plane so the beam does not move whilst tilting. The shift adjustment ensures that the beam does not tilt during shifting. For the tilt adjustment, the TEM beam was converged at 400K. The tilt wobbler was activated in the  $X$  direction first. The beam would split into two if the alignment was not good. If required, the two beams were merged into one by adjusting the tilt shift and deflector coils for  $X$ . The same was repeated for  $Y$ . The shift compensator alignment is similar but is done in diffraction mode instead. In diffraction mode, the spots should appear sharp and rounded. This was checked by obtaining a diffraction pattern from an amorphous area or over a hole to ensure a crystal did not influence the diffracted spot shapes. In the case the central spot looked elliptical, the intermediate lens astigmatism was corrected using the intermediate astigmator controls.

To ensure there is no rotation caused by changes in accelerating voltage, the voltage centre is then aligned. The voltage centre was aligned by enabling the objective lens wobbler. If not aligned then one side of the beam would rotate more so than the other. It was adjusted by using the deflectors to ensure the rotation centre was at the optic axis. Following on from this, the beam tilt was adjusted to ensure the beam was parallel to the specimen. This was done with the aid of the HT wobbler. If the specimen is not illuminated with a parallel beam then the image contrast would oscillate in one direction to another meaning the beam tilt was not parallel. This was adjusted by using the upper-beam deflector controls (labelled Bright Tilt) to minimise the image contrast oscillations. When entirely parallel, the image contrast will still adjust but it is as if  $\Delta f$  is being changed only. This alignment is useful for dark field imaging [15] where the Dark Tilt button can be used to achieve a slightly different tilt condition to the normal alignment in order to position a selected diffracted beam on the optic axis and allows convenient switching between bright and dark field imaging modes.

Astigmatism in the objective lens was corrected using the CEOS aberration correction software on the JEOL 2200FS. This was done manually using the arrow keys. The correction allows the objective lens current to remain constant throughout the process reducing the likelihood of reintroducing stigmatism. On the JEOL 2011, astigmatism was corrected using the astigmator coils. In both cases, a region of amorphous C was imaged at magnification of 400 K. When in focus, the FFT of the amorphous carbon should appear

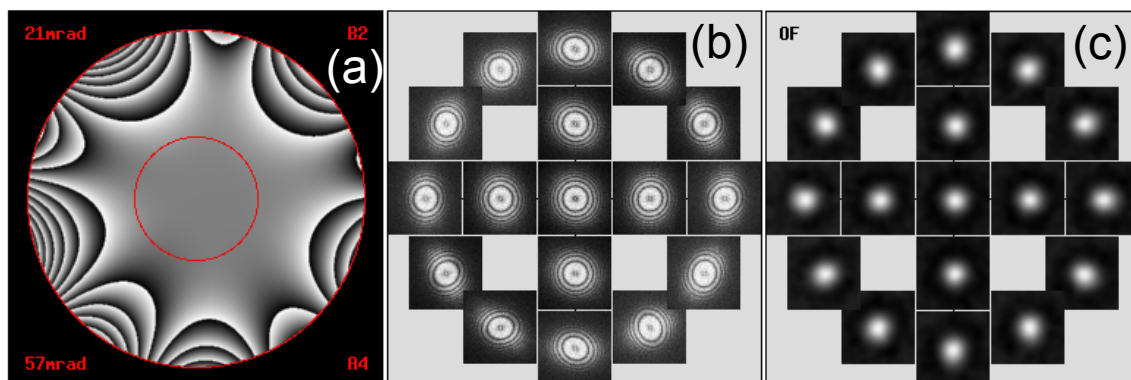


Figure 2.8: CEOS aberration correction software screenshots showing (a) the phase transfer, (b) TEM FFT tableau and (c) HAADF-STEM overfocused probe tableau. Upper and lower LHS values in (a) correspond to the inner and outer angle respectively and the upper and lower RHS values in (a) are the recommended corrections needed to improve the inner and outer angles respectively

as a diffuse circle but this is sometimes difficult to see. It is best to have the C slightly out of focus to see the rings. This is done using the specimen height controls. It is preferable to adjust the FFT when underfocused so that the beam converges and in this case increasing  $\Delta f$  will bring the film into focus.

The reference sample was used to correct the objective lens aberrations in combination with the CEOS software on the JEOL 2200FS. The CEOS software required that the FFT of the amorphous carbon show approximately five rings for accurate correction. The electron beam at this point must converge so the sample needed to be underfocused but at  $\Delta f = 0$  to ensure that the objective lens current remained constant through the process. The specimen height was adjusted to generate at least five well defined rings on the FFT which corresponded to approximately  $-200 - 300$  nm effective defocus.

The CEOS aberration correction software corrects aberrations by acquiring and processing a tableau of FFTs, each at a slightly different beam tilt. This is shown in Figure 2.8(b). A phase plate is generated from this tableau as shown in Figure 2.8(a). The phase transfer should appear flat in its centre and should be symmetrical. The software recommends two corrections (one for inner and one for outer angle) by displaying certain aberration coefficients in the phase plate image. The respective button is pressed to correct the astigmatism. A continuous image of the FFT was then used to correct any astigmatism introduced by this correction and the tableau process was repeated. This process was repeated over several iterations to achieve a flat phase transfer and a good inner and outer angle such as the one shown in Figure 2.8(a). The aberrations were corrected such that the aberrations had values similar to Table 2.1 upon recommendation from CEOS

Table 2.1: Typical aberration coefficient values for TEM and STEM

Aberration Coefficient	Aberration Name	Recommended Value
$A_1$	Astigmatism (Two-fold)	$< 5 \text{ nm}$
$A_2$	Astigmatism (Three-fold)	$< 20 \text{ nm}$
$A_3$	Astigmatism (Four-fold)	$< 1 \text{ }\mu\text{m}$
$B_2$	Coma (two fold)	$< 20 \text{ nm}$
$B_3 = S_3$	Coma (three fold)/ Star	$< 1 \text{ }\mu\text{m}$
$C_1$	Defocus	$< 5 \text{ nm}$
$C_3 = C_s$	Spherical Aberration	$\approx -1 \text{ }\mu\text{m}$

and with a symmetric phase transfer. The aberration coefficient labels follow the Haider notation [86].

During operation, care was taken not to adjust the magnification unnecessarily because changes in the lens configuration can often introduce astigmatism. On the JEOL 2200FS a rotation occurred at 800K and 1M. On the 2011, the rotation occurred at 120 K. These rotations cause the image to be rotated with respect to the diffraction pattern but this was taken into account by using a reference sample in the form of  $\text{MoO}_3$  crystals. The crystals grow long along  $[001]$ .

Typical exposures when recording TEM images were approximately 1 s to minimise the effects of specimen drift if present. Diffraction patterns were recorded with a wide range of exposures but usually not greater than 10 s to prevent radiation damage to the CCD. SAD patterns from large crystals were recorded with exposures less than 1 s. Dark field TEM images were recorded with long exposures up to 60 s depending on the intensity of the diffracted beam of interest.

High magnification calibration was done by Leonardo Lari and was carried out by imaging Si dumbbells in  $[110]$  (see for example [32]). Lower magnifications were calibrated by JEOL engineers.

### 2.11.2 Diffraction Modes and Techniques

Aside from intermediate astigmatism already described, it may be possible that the projector lens deflectors occasionally needed adjusting. Misalignment here caused the diffraction pattern to be projected off the optic axis of the microscope.

Diffraction mode has its own focus adjustment. This is done by inserting an objective aperture such that the outline of the aperture can be clearly seen and adjusting the bright-



ness (convergence of the beam) such that the diffraction pattern shows clear, sharp spots. This process was essential for high quality dark field TEM imaging since it ensures that the objective aperture is focused onto the back focal plane (reciprocal space).

SAD (and NBD) patterns were calibrated by using an Al calibration specimen which consists of polycrystalline Al thin films which produced a well defined ring pattern. The diffraction patterns at a given camera length can be calibrated by comparing to diffraction patterns of the Al calibration sample which has well known lattice parameter (0.405 nm) and hence spatial frequencies.

NBD mode is essentially the same as TEM mode but there is more control over the convergence angle of the converged beam. Switching from TEM to NBD often required a dedicated alignment as described above. The most dramatic alignment is the adjustment of the beam tilt which often required several turns in coarse mode of the deflectors. Spherical aberrations cannot be corrected in this mode but astigmatism can. Once NBD was aligned, switching to and from NBD to TEM was straightforward but after a few days of non-use NBD mode requires realigning. To achieve a parallel beam suitable for individual nanoparticle analysis, the smallest condenser aperture was used. The small aperture introduces Fresnel fringes into the image of the aperture and it can be quite difficult to see nanoparticles.

### 2.11.3 STEM

On the York JEOL 2200FS, switching to TEM and STEM required alignment and it does not reach full stability for a few days. For this reason, the 2200FS was operated in TEM or STEM for weeks at a time with dedicated time for switching. This was done by Leonardo Lari, who also maintained most of the major alignments such as gun alignment. STEM alignment required that TEM mode was reasonably aligned too. Aberrations (spherical, astigmatism etc) were corrected daily by the user as described below.

A dedicated alignment sample was used which was prepared by Mike Walsh [85]. It is a standard holey-C grid coated with a pre-made solution of nanoparticles to produce a densely populated specimen. Ligands in the solution prevented build up of the nanoparticles.

To align STEM and correct aberrations, a Ronchigram was generated. This was done by removing any condenser aperture and focusing the specimen by adjusting the specimen

height at  $\Delta f = 0$  to ensure the probe forming lens remains at its default value. At slight underfocus, the shape of the Ronchigram is well defined and it shows an infinite magnification image at its centre which can often show the nanoparticles crystal structure [41,63].

Aberrations are first corrected manually using a slightly underfocused Ronchigram at  $> 1$  M. The round nanoparticles on the alignment specimen allow aberrations such as astigmatism and coma (beam tilt) to be detected easily by eye. If coma aberration ( $B_2$ ) was present the Ronchigram would appear lopsided. It was corrected using the bright tilt controls.

If the nanoparticles appeared elliptical or stretched when near focus this meant there was astigmatism ( $A_1$ ). This was corrected manually using the CEOS aberration correction software. This step and the previous step required several iterations since adjusting  $B_2$  effects  $A_1$ .

Higher aberrations were corrected using the CEOS aberration correction software.  $\Delta f$  was set to 0 if required and the specimen adjusted as necessary so the Ronchigram was in focus. Also, the values for the bright tilt lens settings were synchronised with the corrections by pressing the DP12 button in the CEOS aberration correction software window. Magnification was set to 600 K and condenser aperture 4 was inserted. A scan was initiated using the CEOS aberration correction software with the HAADF detector in place using a camera length of 30 cm.

The software is similar to the TEM version but instead of acquiring FFTs, probe images were acquired. The overfocused probe image tableau is shown in Figure 2.8(c). Residual astigmatism or small adjustments to the focus were made by using the aberration correction software when viewing continuous overfocused and underfocused images of the probe. Higher order aberrations were computed by acquiring both an underfocused and overfocused probe tableau. After this, the software generated a phase transfer for inspection. The process from here was similar to the TEM correction method described in the previous section. After a few iterations of correcting the aberrations, the phase transfer should ideally appear symmetrical with an inner angle of at least 19 mrad and an outer angle of at least 50 mrad. An example is shown in Figure 2.8.

Typical corrected aberration coefficients were similar to TEM and are shown in Table 2.1 on page 47. STEM images were taken using either 512x512 or 1024x1024 scans. Pixel dwell times were approximately 10  $\mu$ s although this was adjusted *in-situ* depending on the magnitude of specimen drift which is described below. Assuming a 1024x1024

image at 10 M magnification, typical step sizes were 0.014 nm, at 6 M, typical step sizes were 0.023 nm. In the 10 M case, approximately ten pixels corresponded to the width of the FWHM of a typical line scan from a single Pt atom (see chapter 6).

#### 2.11.4 E(S)TEM

To achieve maximum resolution, spherical aberrations and higher order aberrations are corrected using the reference samples in the standard tilt holder in vacuum. Operating wise, aside from injecting the gas, E(S)TEM is virtually identical to ordinary (S)TEM but there are a few extra challenges described below.

Specimens in the heating holder were held by two washers, one above and one below but its internal components and the TEM grid itself heat up during operation and expand. This introduces significant specimen drift. Therefore, when a specific temperature was reached, at least 10 minutes was required for it to stabilise. Specific heating experiments are described in more detail in chapters 6 and 7 but the temperature of the heating holder was set by adjusting the current flowing through it. The Gatan power supply was used in chapter 7 for ETEM but an alternative was used as described in chapter 6 for ESTEM.

The temperature of the heating holder had been calibrated in vacuum and in H<sub>2</sub>. Using the default Gatan Power supply, which also shows the temperature readings, the current was increased gradually (over 2-5 minutes) to a specific current. Temperatures had been calibrated with respect to the current flowing through the holder by recording the temperatures measured by the Gatan power supply. This was repeated in H<sub>2</sub>. The temperatures were recorded after several iterations of increasing the current to ensure that the temperatures are genuine. It is believed that the gas will cool the specimen and also the holder, so the readings at a given current in gas are slightly less than recorded in vacuum. The calibrations allowed another power supply to be used since the temperature is known at a given current setting.

Gas was inserted at different points in the experiment as described in chapter 6 and 7. The gas system was prepared before the *in-situ* experiment began such that the gas lines had been purged. The gas lines were pumped out for 10 minutes before use.

# Chapter 3

## Structure and Catalytic Activity of Nanoparticle Catalysts

### 3.1 Structures of Metal Nanoparticles

#### 3.1.1 Nanoparticle Shapes

As with any physical system, a nanoparticle will want to be in the lowest possible energy state, therefore it will attempt to shed its free energy. Free energy is usually defined in terms of the Gibbs free energy  $G$  which is given by [87]

$$G = PV - TS \quad (3.1)$$

where  $P$  is the pressure,  $V$  is the volume,  $T$  is the temperature and  $S$  is the entropy. Volume and pressure are fixed since a nanoparticle of a given size will occupy a given volume thus the minimisation of  $G$  comes from the  $TS$  term. In physical terms, the Gibbs free energy is the amount of energy that is available to do work in a system at constant temperature and pressure. A negative free energy implies that a reaction is spontaneous and will release energy.

Over 100 years ago, Wulff equated the free energy to a shape comprised of multiple facets each with their own surface energies, such a shape became known as the Wulff construction [89]. The basic concept behind the Wulff construction is that the surface energy density of a facet  $\gamma_i$  is related to the distance between it and the centre of the nanoparticle  $h_i$  according to the relationship

$$\gamma_i/h_i \quad (3.2)$$

which is the result for a nanoparticle with anisotropic surface energies. If it were isotropic, then nanoparticles would be perfect spheres. The angle at which the nanoparticle makes

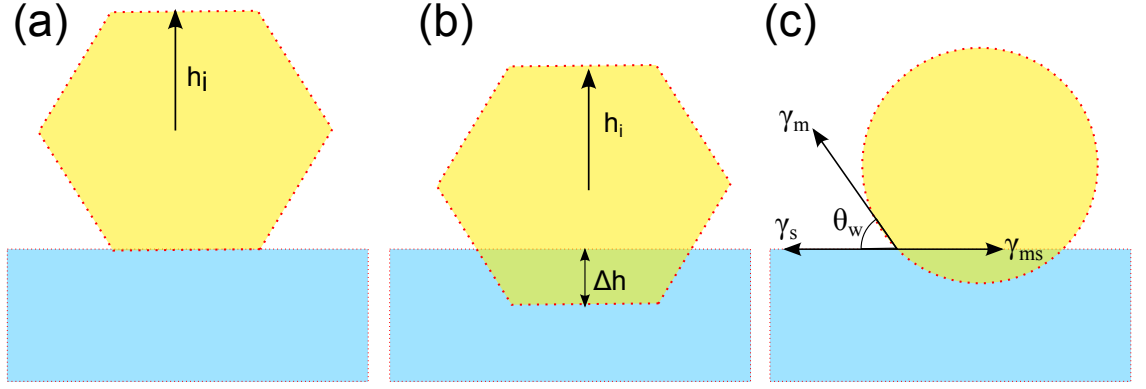


Figure 3.1: Diagrams showing the (a) Wulff construction concept, (b) Winterbottom/Wulff-Kaischew construction and (c) the wetting concept. These diagrams are based on the equivalent diagrams in Henry's nanoparticle morphology review paper [88]

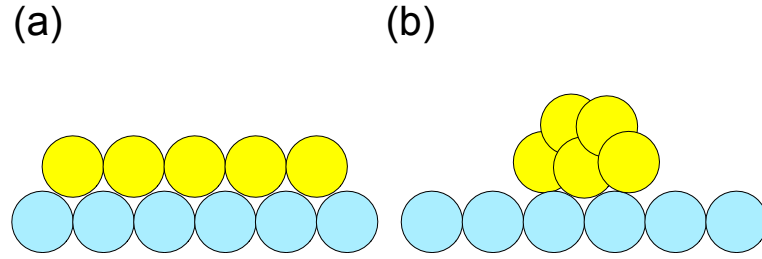


Figure 3.2: Schematic diagrams showing the difference between the 2D raft structure (a) and a conventional 3D cluster (b)

contact with the support at equilibrium is defined as the contact angle  $\theta_w$  which is defined by Young's equation as [88]

$$\gamma_s = \gamma_m \cos \theta_w + \gamma_{ms} \quad (3.3)$$

where  $\gamma_s$ ,  $\gamma_m$  and  $\gamma_{ms}$  are the surface energies of the support, metal and metal-support interface. These energies can be related to the adhesion energy  $E_{ad}$  which is the energy (work) required to form a particular surface and is the same as the amount of energy required to hold one surface to another.  $E_{ad}$  is defined as [88]

$$E_{ad} = \gamma_s + \gamma_m - \gamma_{ms} \quad (3.4)$$

By combining (3.3) and (3.4) it is possible to derive a link between  $E_{ad}$  and  $\theta_w$  to yield

$$E_{ad} = \gamma_m(1 + \cos \theta_w) \quad (3.5)$$

which is known as the Young-Dupré equation. A nanoparticle that is a perfect sphere on a support is then said to be a droplet like object on a non-wetting surface because the contact angle is 0. A nanoparticle that has a contact of  $180^\circ$  on the other hand will have spread into a 2D arrangement of atoms sometimes called a raft [59, 90, 91, 92, 93]. Figure 3.2 shows the difference between a raft like cluster and an ordinary one.

Table 3.1: Examples of Wulff equilibrium shapes and the type and number of enclosing faces

Shape	$\{111\}$ Faces	$\{001\}$ Faces	$\{110\}$ Faces
Tetrahedron	4	0	0
Octahedron	8	0	0
Truncated Octahedron	8	6	0
Cuboctahedron	8	6	0
Cube	0	6	0
Truncated Cube	8	6	0

The Wulff model predicts a truncated octahedron as the default equilibrium shape for any fcc metal nanoparticle where the surfaces energies follow the order  $\gamma_{110} > \gamma_{001} > \gamma_{111}$  [94]. Table 3.1 tabulates some of the expected equilibrium shapes and the number of facets each one has.

The Wulff model does not take into account the free energies associated with corner and edge atoms and assumes an unsupported nanoparticle. Various modifications were made to the Wulff model to account for the support. One such modification is the Wulff-Kaischew model which models the interface between the support and nanoparticle as equivalent to a truncated face as shown in Figure 3.1(b). In this model the relation between surface energy and distance to the centre of the nanoparticle is more complicated [88]:

$$\Delta h/h_i = E_{adh}/\gamma_i \quad (3.6)$$

where  $\Delta h$  is the distance from the symmetric outline of the nanoparticle to the truncated surface at the interface (shown in Figure 3.1(b)) and  $E_{adh}$  is the adhesive energy between the nanoparticle and support which is equivalent to the amount of energy required to separate the nanoparticle from the support at infinite distance [88]. The Wulff-Kaischew model (3.6) assumes that the support and the nanoparticle have the same structure. Another, more refined model was proposed by Winterbottom [95] by introducing the wetting concept which is shown in Figure 3.1(c).

The Wulff and Winterbottom constructions are consistent with observed nanoparticles larger than 10 nm [20]. Observed Pt shapes include: truncated octahedra, octahedra, tetrahedron, cuboctahedra, cubes and truncated cubes [96, 97]. Pd nanoparticles are observed to be similar if they are larger than 10 nm [98, 99].

Below 10 nm, additional structures not predicted by the normal Wulff and Winterbottom models have been observed [20]. Shapes such as icosahedra, decahedra and other twinned structures have been reported [20, 88, 100, 101, 102, 103, 104]. The appearance of such structures have often been attributed to the importance of edge and corner atoms [20].

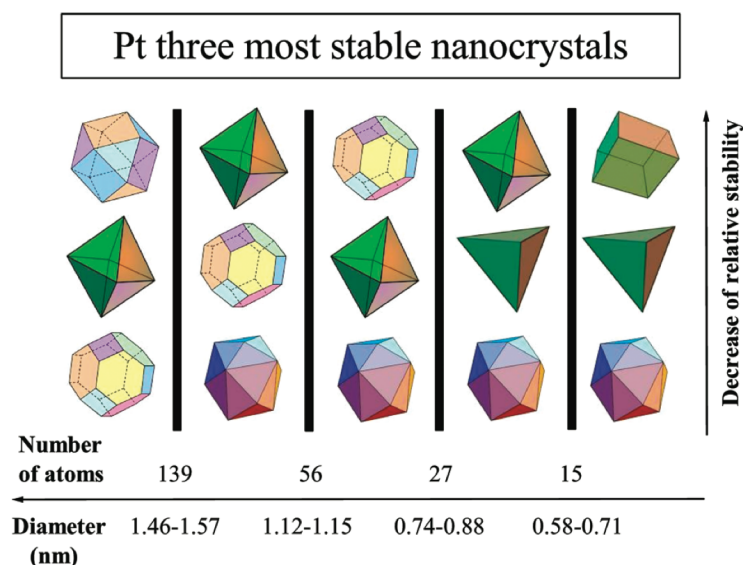


Figure 3.3: Diagram showing the most stable Pt nanoparticle shapes as predicted by Chepulskii *et al* [108]

Perhaps the most profound example of exotic nanoparticle structures was the five fold twinned Au nanoparticles discovered by Ino and Allpress [100] and Sanders [105] using TEM. Nanoparticles that contain more than one twin are often called multiply twinned particles (MTPs).

A model for MTPs was proposed by Yang by modelling the nanoparticle as an arrangement of multiple tetrahedral units [101]. The tetrahedral units however did not fit together so a small gap was left as predicted thermodynamically. It is believed that the nanoparticle fills this gap by inducing strain in the structure so the the gap is filled and the nanoparticle is bound by  $\{111\}$  facets [106]. The nanoparticle does not have sufficient energy to remove the twins, so they remain at the expense of some free energy to form the shape. As a result, decahedral and icosahedral nanoparticles are stable structures [101, 107].

Modern density functional theory (DFT) calculations suggest that the equilibrium shape of very small nanoparticles can take a wider variety of nanoparticle shapes [108]. For example, Chepulskii *et al* demonstrated that in the size range 1.12 – 1.57 nm Pt nanoparticles are more likely to form tetrahexahedron, octahedra or truncated octahedra. Below 1 nm, the tetrahexahedron is most stable, followed by the octahedron and cube. The most stable shapes proposed by Chepulskii *et al* are shown in Figure 3.3. They note that bulk surface energies are only relevant for nanoparticles larger than approximately 1.5 nm.

There does not seem to be any reports, either experimentally or theoretically of small (< 5 nm) twinned Pt nanoparticles although advanced synthesis techniques have encour-

aged the formation of twins leading to branched Pt structures [109]. Pd twinned nanoparticles have also been synthesised [99]. During heating, Pd nanoparticles are known to form twins [88] but there are no detailed reports on twinning trends in Pt nanoparticles during thermal treatment.

A twin is a grain boundary that may have been formed by a deformation or transformation event or during the crystal's growth. A deformation twin arises when homogenous shear causes one part of a crystal to be shifted such that it is in a different orientation than the other but it still retains its original crystal structure [110]. A transformation twin occurs when a crystal is subjected to a sudden change in temperature or pressure.

Twins can also arise during crystal growth [111]. This can occur when a new crystal is grown on-top of an existing crystal. The atoms of the growing crystal may share the lattice of the original crystal and may be in a slightly different orientation leading to a twin. Typical growth twins include contact twins and penetration twins [111].

Pt and Pd have considerably higher stacking fault energies than Au [112] and they are more likely to stabilise full dislocations as opposed to partial dislocations (such as either side of a stacking fault) [112]. Consequently, Pd and Pt have higher surface energies than Au and Ag. According to Cai *et al*, the stacking fault energy of Pt is reduced by atom relaxation but the effect is not significant in other metals [113]. Despite the high stacking fault energy, stacking faults (and twins) have been observed in small Pt nanoparticles, perhaps influenced by the expanded interatomic distances [114].

In the simplest fcc case, a twin boundary is like a mirror. Deformation twins are more likely to form in materials with low stacking fault energies such as in Au and Ni [112]. For fcc materials, the preferred twinning plane is  $\{111\}$ .

### 3.1.2 Lattice Parameter of small Nanoparticles

Various groups report that the lattice parameters of fcc metal nanoparticles less than 10 nm in size are different to those at bulk scale. The general consensus is that the lattice parameter of fcc metals contracts at the nanoscale including Ag, [115, 116, 117], Au [118, 119], Pt [119, 120] and Cu [120] but for Pd the lattice parameter has been reported to increase with decreasing size [121, 122].

The expansion of lattice parameter in most metals has been attributed to the effect of surface stress [123] but Lamber *et al* reported a contraction in lattice parameter for Pd



using electron diffraction and suggested an alternative mechanism [124]. They believe that previous reports of an expansion (of Pd) was due to the uptake of impurities into the Pd structure [124]. Li *et al* reported a contraction for 5 nm fcc Au nanoparticles but a expansion at higher temperatures [125].

Du *et al* found using HRTEM that surface Pt atoms are strained [114] with the inter-atomic Pt-Pt distances elongated but atoms on surface steps were closer to each other in Pt nanoparticles supported on amorphous C. They utilise the HRTEM images for lattice parameter investigations suggesting that the lattice has expanded by 1.3 – 4.8 % but in different directions suggesting a tetragonal distortion [114]. They believe this is because O is adsorbed on the surfaces from synthesis [114].

It is believed that surface stress plays a key role in nanoparticle equilibrium shapes and it has been incorporated into the Wulff model by many groups. In a more recent simulation of Pt nanoparticle shapes, Chepulskii and co-workers reported a strong dependance on lattice parameter for nanoparticles below 3 nm because of surface tension [108] through *ab-initio* DFT calculations. These simulations did not include effects of edge or corner atoms. From this work they found that the most stable structure at 1.57 nm was the octahedron but between 1.46 – 1.57 nm the more exotic tetrahexahedron becomes the most stable shape as shown in Figure 3.3.

Another simpler model has been proposed by Qi *et al* that models the free energy of a spherical contracting sphere [126]. The result of their model is the lattice change  $\Delta a$  is related to the nanoparticle radius  $r$  according to the relation

$$\frac{\Delta a}{a} = \frac{(1 - \epsilon)r - r}{r} \quad (3.7)$$

where  $\epsilon$  is a constant which is given by [126].

$$\epsilon = \frac{1}{1 + \frac{2G_s}{\gamma} \cdot R \cdot \alpha_{Qi}^{\frac{1}{2}}} \quad (3.8)$$

where  $\gamma$  is the surface free energy,  $\alpha_{Qi}$  is a constant which takes into account the non-spherical nature of the nanoparticles shape and  $G_s$  is the shear modulus.

Investigations of nanoparticle lattice parameter have been primarily done with XRD using unsupported metal powders [125, 127] and electron diffraction (mainly SAD) using C film supported nanoparticles [124, 127]. Some groups have used HRTEM techniques to investigate lattice parameters but some believe that this method can be unreliable (see page 31).

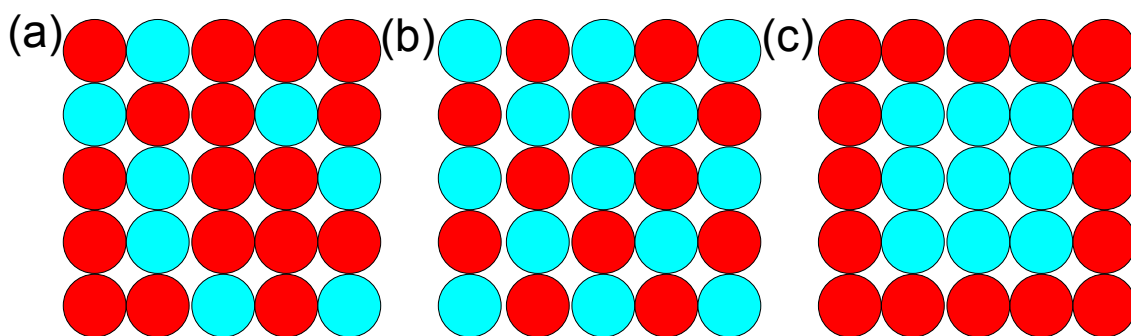


Figure 3.4: Ball models showing the arrangement of two metals in a bimetallic system with (a) being random, (b) ordered and (c) core-shell mixtures

### 3.1.3 Bimetallic and Alloyed Nanoparticles

In general, the structure of bimetallic nanoparticles depends on the alloy. Pt–Pd are in the same group in the periodic table and nanoparticles have virtually identical structures to their monometallic counterparts. Pt–Sn nanoparticles on the other hand can display a range of different structures because of the different groups the two materials are in.

An additional factor in describing their structure is the arrangement of their constituent elements. There are three main solutions/alloy types: random, ordered and core-shell which are shown pictorially in Figure 3.4.

Strain is introduced in alloys depending on the size of the two mixing atoms. In the case of Pt and Pd, their atomic radii are 138 pm and 137 pm respectively. Nanometre sized alloys of Pt and Pd have been observed to retain their fcc structure with the bimetallic structures almost identical in terms of atomic plane separations to their monoatomic counterparts [128]. In general, Pt–Pd nanoparticles are reported as having virtually identical structures to their monometallic counterparts.

There is considerable literature on bimetallic nanoparticles for use in magnetic applications. Alloyeau and co workers have found that shape in addition to size plays a role in the order to disorder of CoPt nanoparticles [129]. This group used a variant of NBD to analyse over 100 nanoparticle diffraction patterns. Their experiments and associated Monte-Carlo simulations indicate that decreases in nanoparticle diameter leads to a decrease in the order-disorder temperature.

Vegards law predicts that an alloy's lattice parameter will increase linearly with increasing composition of one element, mathematically, it is given by the formula for an

alloy of type  $A_xB_{1-x}$  ( $x$  is %) [130]

$$a_{AB} = xa_A + (1 - x)a_B \quad (3.9)$$

where  $a_A$  and  $a_B$  are the lattice parameters of material  $A$  and  $B$  respectively. In the case of Pt-Pd, the lattice parameters are so similar that it will be difficult to detect any changes in composition using diffraction. However, the law could be used to find anomalies in alloy compositions.

Tsen and coworkers investigated the practicality of HRTEM for investigating the lattice parameters of alloys and bimetallic nanoparticles [131]. They used a conventional 400 kV TEM with multi-slice simulations to deduce that 3 nm diameter nanoparticles could have their composition deduced to within  $\pm 3$  % as long as the constituent element lattice parameters were within 3 % of each other. They conclude that the accuracy of this procedure relies on statistics and that more accurate results can be achieved by taking more specimens. The nanoparticle specimens in this case were a set of three specimens: Au and Pt,  $\text{Au}_{90}\text{Pd}_{10}$  and  $\text{Au}_{10}\text{Pd}_{90}$  and finally  $\text{Au}_{80}\text{Pd}_{20}$  and  $\text{Au}_{20}\text{Pd}_{80}$ .

Both Pt and Pd have slightly different chemistry with regard to reactions with O so quantifying the distribution of both metals in a nanoparticle is important especially at the surface [128]. The similar size of Pt and Pd means that random distributions of both are most likely [128]. However, special synthesis methods can lead to core-shell nanoparticles [132, 133]. The latter reference reports synthesising predominant Pt shells surrounded by a thin Pd layer.

### 3.1.4 Metal-Support Interactions and Interface

Nanoparticle catalysts rarely exist on their own. When nanoparticles are loaded onto a support, often a metal-oxide, such as  $\text{Al}_2\text{O}_3$  or  $\text{SiO}_2$ , bonds form between the nanoparticle and support. A term dubbed the metal-support interaction is used to express the chemical and physical changes the support induces in the nanoparticle. This interaction is important because it influences nanoparticle morphology, activity and ageing mechanisms [134, 135, 136, 137, 138].

The most widely reported metal-support interaction is that with cubic  $\text{TiO}_2$ , originally reported in detail by Tauster [139]. Unlike  $\text{SiO}_2$  and  $\text{Al}_2\text{O}_3$ ,  $\text{TiO}_2$  is reducible. Tauster *et al* reported that only reduced  $\text{TiO}_2$  was able to migrate onto the metal nanoparticle surfaces with no indication that nanoparticle size played a role in this migration. They did find that

the surfaces on the nanoparticles needed to be flat [139]. Another group timed that it took just 120 s to cover a 0.3 nm thick Pt film with a monolayer of  $\text{TiO}_x$  [140].

Various groups have reported different activities for the same metal loaded on different substrates [137]. For example, using XPS, Fleisch *et al* reported that Pd nanoparticles loaded on  $\text{La}_2\text{O}_3$  displayed signs of electronegativity with increasing particle size leading to changes in the chemical state of the Pd nanoparticle [136]. On  $\text{SiO}_2$  the same group did not observe the same trends [136]. This effect has been linked to the exchange of charge between larger nanoparticles and support on  $\text{Al}_2\text{O}_3$  [141] but not for smaller nanoparticles.

It is believed that nanoparticles supported on acidic supports (such as  $\text{Al}_2\text{O}_3$ ) are electron deficient because of interactions at specific sites between the nanoparticle and the support [91]. This causes nanoparticles to acquire a net positive charge but only if the size of the nanoparticle is small (approximately 1 nm) [91]. Large nanoparticles do not exhibit a similar deficiency because there are too many atoms to share out the excess positive charge. It is believed that the acidic nature of the support gives rise to the oxidation resistant properties of some small loaded metal nanoparticles because there are not enough electrons to absorb O onto their surface [91]. Other groups, using band energy arguments, suggest that specific interactions lead to the removal of electrons from the metal nanoparticle, thus removing electrons from being able to form bonds. Therefore, it is believed that small nanoparticles will be resistant to oxidation.

$\gamma\text{-Al}_2\text{O}_3$  has surface defects. Several groups have observed single atoms of Pt and 2D clusters located on the supports composed of this material [142, 143]. Sohlberg *et al* believes that  $\text{Pt}_3$  primers attach to O terminated  $\gamma\text{-Al}_2\text{O}_3$   $\{1\ 1\ 0\}$  around a cation vacancy [143]. Figure 3.5 shows their HAAD-STEM image and corresponding models. Kwak *et al* believe that unsaturated  $\text{Al}^{3+}$  centers on the  $\gamma\text{-Al}_2\text{O}_3$  surface are responsible for the stability of Pt rafts [92].

### 3.1.5 Structures of $\text{Al}_2\text{O}_3$

$\text{Al}_2\text{O}_3$  in its natural form is often called corundum but it is not popular as a catalyst support because it has low surface area. This form is known as  $\alpha\text{-Al}_2\text{O}_3$ . High surface area forms of  $\text{Al}_2\text{O}_3$  can be easily produced. The most common high surface area form is  $\gamma\text{-Al}_2\text{O}_3$ . It is widely used as a catalyst support in a variety of applications including automobile exhaust control [144, 145] and the chemical industry [146, 147].  $\gamma\text{-Al}_2\text{O}_3$  also has the lowest surface energy of all  $\text{Al}_2\text{O}_3$  phases [148, 149] and for certain reactions it is acidic

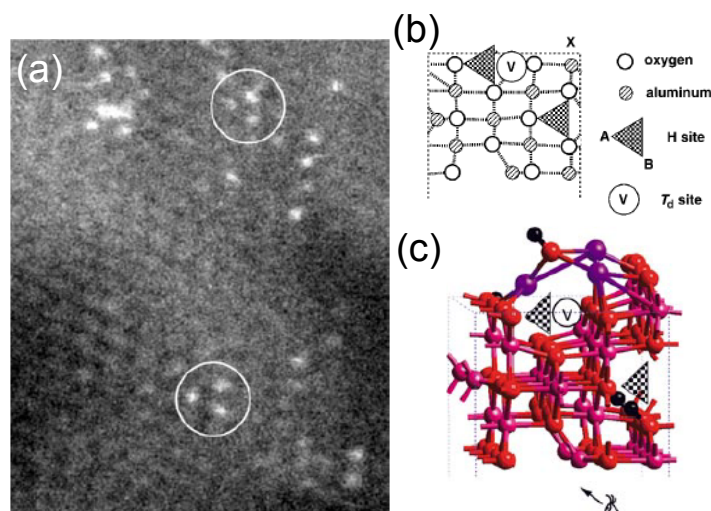


Figure 3.5: Reproduced images from [143] showing (a) HAADF-STEM image of  $Pt_3$  primers, (b) edge view of the  $\gamma\text{-Al}_2\text{O}_3$   $\{110\}$  surface and (c) a 3D model. The  $T_d$  label refers to a perfect cation vacancy and the triangle refers to the location of H bonded preferentially to O atoms. The X denotes where the surface is O terminated

[91].  $\gamma\text{-Al}_2\text{O}_3$  is usually prepared by dissolving a precursor such as boehmite ( $\text{AlOOH}$ ) and calcining afterwards [150] to form the desired  $\text{Al}_2\text{O}_3$  phase.

Assuming  $\gamma\text{-AlOOH}$  is the precursor, then the  $\gamma$ ,  $\eta$ ,  $\delta$  and  $\theta$  phases could coexist depending on the precursor treatment temperature and time [150,151]. The  $\gamma$  phase is usually described as cubic [150,151,152]. However, some groups report that the  $\gamma$  phase can have tetragonal distortion when prepared from  $\gamma\text{-AlOOH}$  [153,154,155]. The  $\delta$  phase is described as tetragonal [156] or orthorhombic but there is debate as to whether the tetragonal  $\delta$  phase actually exists or if there is another intermediate phase such as the  $\gamma'$  phase proposed by Paglia *et al* [157]. The  $\theta$  phase is orthorhombic [150] and it has been confirmed as a separate phase. Variations of the  $\theta$  phase,  $\theta'$  and  $\theta''$  have been identified but these have been found only by using different synthesis techniques. The hexagonal  $\alpha$  phase (corundum) is formed only at 1200 °C.

In general, the  $\gamma$  and  $\eta$  phase is described as a defect spinel structure ( $\text{MgAl}_2\text{O}_4$ ) where vacancies occupy cation sites. There is some debate (experimental and theoretical) about where the vacancies are located: tetrahedral sites [156], octahedral sites [158,159,160] or a mixture of both [161]. In addition, there are reports of pentahedral cations by a few groups [161,162]. Repetitions of the different vacancies in different directions is believed to be responsible for the complex structure of  $\text{Al}_2\text{O}_3$  phases. Paglia *et al* have proposed that  $\gamma\text{-Al}_2\text{O}_3$  has 1 nm scale structure suggesting that a given 1 nm sized area will consist of multiple structures [163].

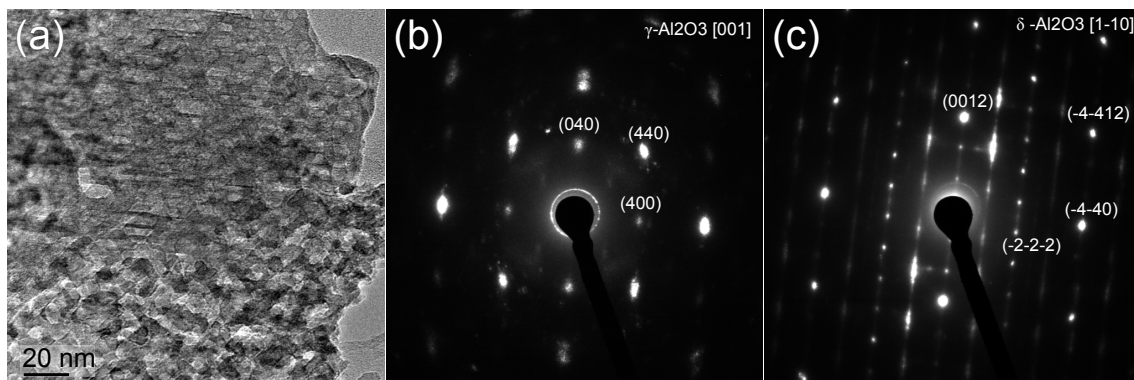


Figure 3.6: Examples of SAD patterns from large crystals of a  $\gamma$ - $\text{Al}_2\text{O}_3$  catalyst. The lower crystal in the TEM image in (a) is indexed as  $\gamma$ - $\text{Al}_2\text{O}_3$   $[001]$  in (b) but the upper crystal in (a) is indexed as  $\delta$ - $\text{Al}_2\text{O}_3$   $[1\bar{1}0]$  in (c)

Regarding  $\gamma$ - $\text{Al}_2\text{O}_3$ , there are several types of distinct reflections that can be observed in an electron diffraction pattern. As described by [153], the first type are the  $h + k + l = 2n$  reflections which originate from Al in tetrahedral positions. These are diffuse and often streaked. The  $h + k + l = 4n$  reflections are sharp and originate from the O sub-lattice. The  $h + l = \text{even}$  reflections are diffuse and originate from a mixture of tetrahedral and octahedral Al. Similar rules are observed for the  $\delta$  phase.

Figure 3.6 shows some examples of SAD patterns of two joint  $\text{Al}_2\text{O}_3$  crystals. The first diffraction pattern is indexed as  $\gamma$ - $\text{Al}_2\text{O}_3$   $[001]$  and the second is indexed as  $\delta$ - $\text{Al}_2\text{O}_3$   $[1\bar{1}0]$ . The reflections in the  $\delta$  pattern are well defined whereas the ones in the  $\gamma$  pattern are broad. Various groups have noted that  $\delta$  is more ordered than  $\gamma$  [153, 157].

Deducing nanoparticle-support relationships using  $\gamma$ - $\text{Al}_2\text{O}_3$  supports is a challenge because it is difficult to deduce the local structure of the support. Commercial  $\gamma$ - $\text{Al}_2\text{O}_3$  tends to be composed of smaller crystallites which often form porous agglomerates [164]. Although there have been many studies on Pt and Pd- $\gamma$ - $\text{Al}_2\text{O}_3$  systems, the support structure, especially on the scale of small nanoparticles  $< 5$  nm, is rarely studied in detail. The use of nano-area techniques could be used to probe local variations in support structure.

## 3.2 Catalytic Activity of Nanoparticles

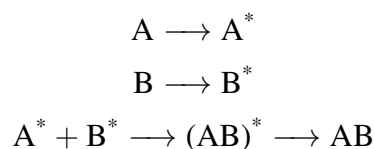
### 3.2.1 Activation

Catalysts are usually synthesised from a catalyst precursor. The catalyst precursor is chemically sturdier making it more suitable for transport. A particular process, such as exposure

to H<sub>2</sub> and calcination, can be used to prepare the final catalyst. The process by which the catalyst is prepared ultimately determines its activity because the process is responsible for the final chemical and physical state. Catalysis is almost exclusively carried out on surfaces so the structure of the nanoparticle determines its chemical properties. This section reviews current knowledge of the origin of catalytic activity of nanoparticles and their structure.

### 3.2.2 Heterogenous Catalyst Surface Mechanisms

Heterogenous catalysis occurring over a solid surface in the presence of gaseous reactants has been long studied over the past century [7]. Reactions take place when one or more reactants are adsorbed (not absorbed) onto a solid surface [165]. The first being the Langmuir-Hinshelwood mechanism and the second being the Elley-Ridely mechanism [165]. The Langmuir-Hinshelwood mechanism for heterogenous catalysis occurs when both reactants are adsorbed onto a solid surface which can then diffuse across the surface and eventually meet and react with each other. The subsequent bond formation between the two reactants causes the final product to desorb. A general equation can be written as [165]



where the \* denotes that the gaseous species has been adsorbed. The final product is desorbed from the surface back into the gas phase. The Elley-Ridely mechanism is similar to the Langmuir-Hinshelwood mechanism but only one reactant is adsorbed onto the surface. A further mechanism, called the Mars and Van Krevelen mechanism works like the previous mechanisms but it requires a lattice vacancy [166].

### 3.2.3 Effect of Coordination Number and Size

Nanoparticles, particularly those of Pt group metals including Pt, Pd and Au, are known to possess a range of structures at the nanoscale. There are many different reports on the activity of different size and shape metal nanoparticles for different reactions involving Pt [167, 168, 169] and Pd [170, 171, 172, 173]. The role of size and structure has been the

subject of dedicated studies because identity and chemical nature of the active sites and surfaces has often been ambiguous.

Somorjai and Blakely were amongst the first to propose that sites responsible for H-H, C-H and C-C breaking on Pt surfaces were imperfections located on low symmetry atomic surfaces such as the  $\{\bar{5}57\}$  and  $\{\bar{6}79\}$  faces [174]. They suggested a link between the catalytic activity and the coordination number (number of nearest neighbours) identifying that a kink would have a coordination number of 6 whereas an atom in a close packed  $\{111\}$  surface would have a coordination number of 9 [174].

Li *et al* reported that smaller Pd nanoparticles were more active at catalysing the reaction between phenylboronic acid and iodobenzene (Suzuki reaction) [175]. They found that the smallest (3.0 nm) nanoparticles were less active than 3.9 nm particles. They found 3.9 nm nanoparticles to be the most active and 6.6 nm nanoparticles to be the least active. The group totalled up the number of surface atoms and edge and vertex atoms. They found a correlation between conversion rate and the number of edge and corner atoms. However, they believe that the decrease in activity seen in the smallest nanoparticle is because the reactants become too strongly adsorbed to the surface which results in catalyst poisoning. Other groups, in similar types of reactions, report a similar correlation [176, 177]. Therefore at least in organic molecule catalysis the active sites appear to be edge, corner and kink atoms i.e. low coordination atoms.

The role of low coordination sites for the oxidation of CO has been investigated theoretically and experimentally. Grass *et al* reported that small Rh nanoparticles are more active for CO oxidation than larger ones. They attribute the increased activity to the ability of low coordination atoms to encourage the formation of surface oxides [178]. They concluded that the rapid increase in activity at small sizes was linked to an equivalent decrease in activation energy. Joo *et al* on the other hand, report the opposite trend with Ru nanoparticles [179]. They report that 6 nm nanoparticles have as much as eight-fold improvement in activity than 2 nm nanoparticles suggesting that the larger nanoparticles encourage the formation of the active oxide surface layer.

Recently, Wang *et al* have shown that spherical Pd nanoparticles, with low symmetry facets which contain kinks, have higher CO oxidation activities than cubic and polyhedral shaped crystals [170]. Figure 3.7 shows this graphically. It is interesting that there is almost no activity at temperatures below 200 °C for cubic and polyhedral nanoparticles.

Lopez *et al* reported a direct correlation between coordination number and binding en-



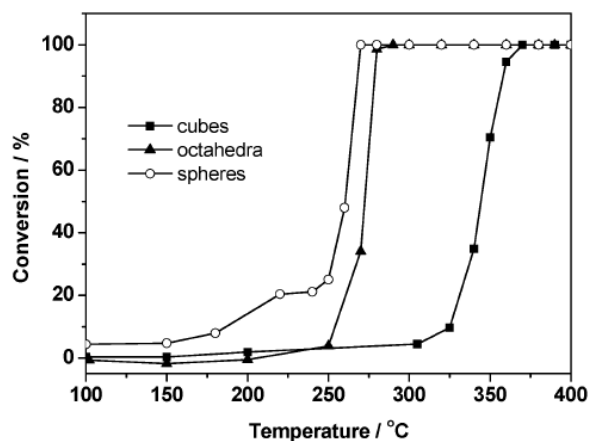


Figure 3.7: A reproduced graph from Wang *et al*s paper [170] showing CO conversion activity over three different Pd nanoparticle shapes. Note that the spherical nanoparticle offers almost 20 % activity at 200 °C whereas the other shapes have virtually no activity at this temperature

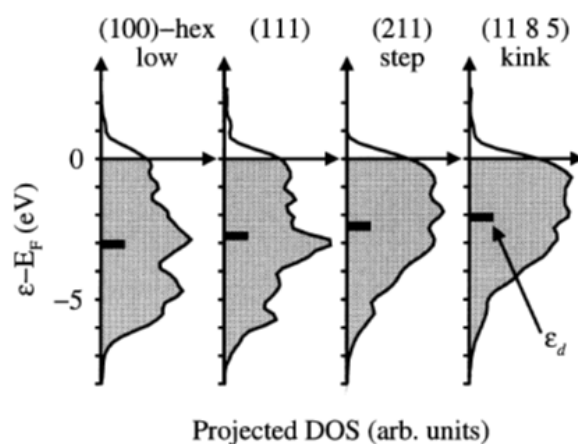


Figure 3.8: A reproduced graph from [181] showing difference in available energy states around  $E_F$  because of the shift in the d band of differently coordinated atoms

ergy [180] and a direct correlation between CO oxidising activity and size; with nanoparticles above 5 nm having virtually no activity [180] agreeing with previous experiments [8].

Despite there being some debate about the precise origin of the catalytic activity of different nanoparticles, there is a correlation between low coordination atoms and high activity. Hammer and Norskov *et al* unearthed an important link between activity and the location of the d band centre [182]. The d band is very important in metals because the Fermi energy,  $E_f$  is often located within it. The Fermi level is the energy of the electron in the highest energy state at absolute zero. In other words, it is the highest energy state occupied in the systems ground state [11]. Electrons around the Fermi energy can hop to higher energy states in the d band at room temperature hence why bulk metals conduct at room temperature. If the d band and the band above it should be separated, then the metal

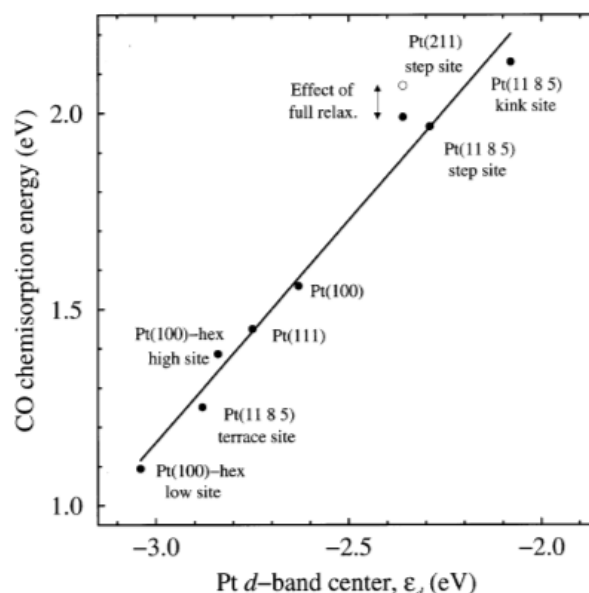


Figure 3.9: A reproduced graph from [181] showing the relationship between the change in chemisorption energy and the d band centre shift for various Pt surfaces

would behave more like a semi-conductor.

According to Hammer *et al* [181], the d band centre moves towards the Fermi level as the coordination number of the atom decreases as shown pictorially in Figure 3.8. In Figure 3.8 there are fewer energy states around  $E_f$  for atoms located on hexagonal  $\{001\}$  surfaces compared to ones at  $\{11\bar{8}5\}$  kink sites. In the latter case, this means that there are more electrons available for forming new bonds. Hammer *et al* further went on to show a linear relationship between the change in chemisorption strength and the d band centre  $\epsilon_d$  which is shown in Figure 3.9. DFT calculations by Lopez *et al* give a similar result for Au [180].

The electronic properties of entire nanoparticles have now been simulated. Sun *et al* employed DFT to calculate the band structure of a 1 nm nanoparticle with fcc structure and an amorphous variant [132]. They found that the fcc nanoparticle had highly localised hybrid d and sp bands leading to a bandgap with no electrons occupying conducting states at the Fermi energy, as shown in Figure 3.10(a). Their amorphous nanoparticle on the other hand had overlapping orbitals resulting in the merging of several bands as shown in Figure 3.10(b). The results from Wang *et al* further support the validity of the d-band model for nanoparticles.

Using the d band model, many groups have shown that the strain which may be induced by the support [183] causes a similar effect [184, 185, 186, 187] to the d band centre resulting in improved catalytic activity.

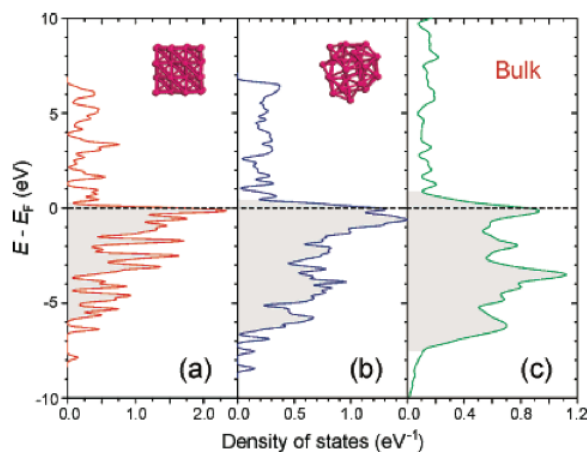


Figure 3.10: A reproduced graph from [132] showing that the available density of states diminishes in very small Pt nanoparticles relative to bulk

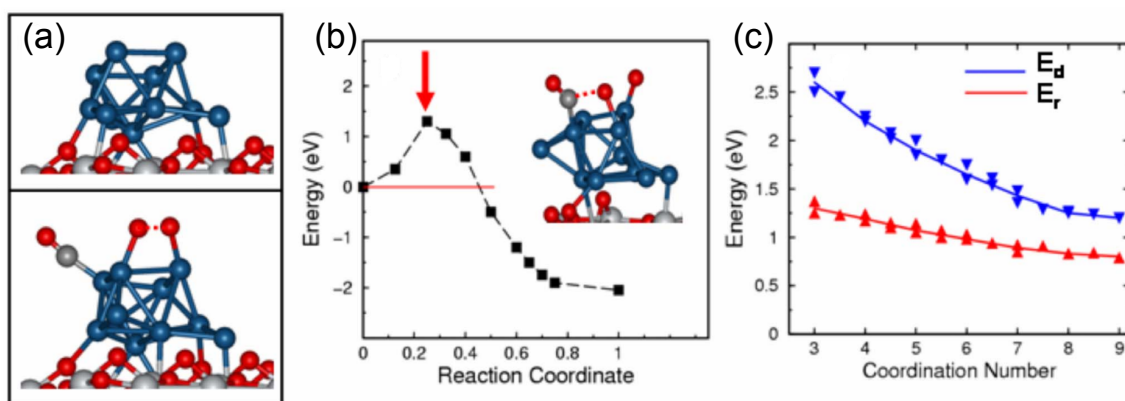


Figure 3.11: A reproduced figure from [189] showing (a) their models for CO and O<sub>2</sub> adsorbed on the Pt nanoparticle surface (blue/grey), (b) the energy required for CO and O to form a bond and (c) the reaction barrier energy  $E_r$  and  $E_d$  desorption energy plotted against coordination number

Another factor in nanoparticle activity, particularly for CO oxidation, is the O adsorption energy. Bilgaard *et al* calculated O adsorption energies for a variety of metals using density functional theory techniques [188]. Adsorption energies for Pd and Pt were calculated to be  $-1.20$  eV and  $-2.17$  eV respectively. For comparison, from the same paper, the energy for Au was calculated to be  $0.54$  eV. The negative energies for Pd and Pt imply an exothermic process meaning that O adsorption is spontaneous whereas for Au it is endothermic which implies Au will not adsorb O [188].

Rashkeev *et al* used density functional theory to investigate the role of size in the absorption of O<sub>2</sub> and CO for Au and Pt nanoparticles on a TiO<sub>2</sub> (110) slab [189]. Figure 3.11(a) shows their model for O<sub>2</sub> and CO<sub>2</sub> adsorbed on a Pt cluster on TiO<sub>2</sub>. They demonstrated that low coordination Pt sites have strong, rigid Pt-Pt bonds resulting in high reaction energy barriers because any absorbed molecule will find it difficult to move.

The results from Rashkeev *et al* show that for Pt a decrease in catalytic activity is expected for small Pt particles because the O binds too strongly to the low coordination atoms resulting in catalyst poisoning. DFT by Sun *et al* implies a similar result [132]. However, Pt nanoparticles will be always catalytically active because as the coordination number increases  $E_r$  remains almost a constant. In contrast, the Au-Au bond weakens making it easier for absorbed molecules to move on the surface and the reaction barrier  $E_r$  decreases rapidly for low coordination Au atoms but increases around a coordination number of 5 implying that larger nanoparticles containing fewer low coordination sites will lose their activity [189]. Hvolbæk *et al* used DFT to obtain a similar result [190]

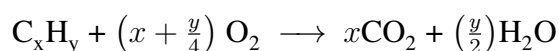
### 3.3 Ageing and Deactivation Mechanisms of Nanoparticle Catalysts

#### 3.3.1 Introduction

Thermal treatment of nanoparticle catalysts has shown that nanoparticles will grow in size. An increase in size leads to a decrease in the total surface area of the nanoparticle population, the bulk:surface atom ratio and the number of active sites.

Nanoparticles have been used in automobile catalysts since the 1970s. The nanoparticles were often Pt and Pd. As technology has progressed, petrol and diesel car engines and fuels have become more complex to meet the requirements of modern emissions targets. Diesel cars are becoming more popular in part thanks to their superior fuel economy and lower CO emissions per km. However, there are some unique challenges with regard to the reduction of harmful emissions from diesel automobiles.

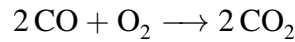
The source of energy in an internal combustion engine is the release of energy from complete combustion of hydrocarbon  $C_xH_y$ , which is written as



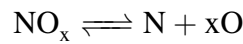
where  $x$  and  $y$  are integers describing a hydrocarbon molecule. For petrol engines,  $x$  is around 6 but for diesels,  $x$  is around 16. The heavier diesel fuel does not mix with air as easily as petrol and as a result, regions in the engine where there is not enough available air encourages the production of CO via incomplete combustion. CO is very toxic. To minimise the occurrence of incomplete combustion, modern diesels use a lean burn cycle, which means there is always an excess of  $O_2$  in the engine.

Despite this, a small amount of CO is always produced. The excess of O<sub>2</sub> in the engine combined with N<sub>2</sub> in the air encourages the formation of NO and NO<sub>2</sub> which are also toxic. In addition, long-chain hydrocarbons sometimes pass through unburnt and are expelled as soot to which dangerous chemicals such as esters, carboxylic acids and others can attach themselves.

In petrol engined automobile exhausts, it is possible to oxidise CO to CO<sub>2</sub> according to the equation



and to reduce NO<sub>x</sub> according to



with the same catalyst; often Pd nanoparticles supported on an O<sub>2</sub> storage support such as CeO<sub>2</sub> [1]. The petrol exhaust catalysts are hence called three way catalysts. However, the same catalyst cannot be used in a diesel exhaust because the excess of O<sub>2</sub> discourages the simultaneous reduction of NO<sub>x</sub> and oxidation of CO and unburnt hydrocarbons. For that reason, diesel exhaust catalysts are often a combination of three separate catalysts linked together which include a particulate filter, a diesel oxidation catalyst and a nitrogen storage and removal catalyst. The diesel oxidation catalyst (DOC) is responsible for the oxidation of CO and hydrocarbons.

The majority of DOCs used today employ Pt [191] nanoparticles supported on a wash-coat loaded onto a monolithic (honeycomb like) structure. Pt is one of the most expensive naturally occurring metals and therefore there is motivation to improve the efficiency of DOCs with as little Pt as possible. Manufacturers are now combining Pt with other metals such as Pd to reduce metal costs and improve stability. Pd alone cannot be used because it is easily poisoned by S and P which are intrinsic impurities in diesels derived from crude oil.

Despite the wealth of literature surrounding the thermal ageing of nanoparticles, there are few studies of road aged DOCs. Winkler *et al* reported nanoparticle morphology differences between a fresh DOC aged in a muffle oven and a laboratory engine aged Pt-Al<sub>2</sub>O<sub>3</sub> DOC [192]. Using TEM they found nanoparticles had grown in size and that nanoparticle morphologies varied between the inlet and outlet [192] with faceted particles appearing more often at the outlet.

Wiebenga *et al* investigated using TEM and TPR [193] a bimetallic Pt-Pd-Al<sub>2</sub>O<sub>3</sub> DOC. They showed that nanoparticles increased in size from the inlet to the outlet end of the monolith and they suggest temperature variations during particulate filter regeneration is the cause, with the outlet being hotter than the inlet. They also compared the NO<sub>x</sub> reduction activity of the road aged DOC to various model catalysts aged between 2-72 h at temperatures between 750 – 950 °C and found that it agreed with the model catalyst aged for 24 h at 700 °C. The compositional variations in the bimetallic nanoparticles were not reported in detail.

The manner in which the nanoparticles have grown in application aged systems is debated. Commercial catalysts will often contain a mixture of nanoparticle morphologies, support structures and contamination from the manufacturing process. This sometimes makes nanoparticle ageing mechanisms to be elusive in commercial systems. Typically, model systems are used to represent the real catalyst under controlled conditions [194].

Experiments on model systems have yielded two main nanoparticle sintering mechanisms: Ostwald ripening and coalescence. Figure 3.12 shows a schematic of Ostwald ripening and particle migration/coalescence.

### 3.3.2 Ostwald Ripening

The Ostwald ripening process describes the phenomenon where smaller nanoparticles lose atoms in favour of larger nanoparticles [195, 196]. Figure 3.12(a-c) shows a schematic of the Ostwald ripening process. It's physical description originates from the Kelvin effect [195]. This describes the size dependant behaviour of solute drops on a surface in terms of surface-tension of the solution-surrounding environment interface (see for example [197]). Ostwald ripening of nanoparticles has attracted a great deal of theoretical and experimental attention because it is a fundamental ageing process that is particularly important for catalysts used at high temperatures in oxidising environments such as DOCs.

The basic principle behind Ostwald ripening is that atoms in regions of high chemical potential will prefer to move into regions of lower chemical potential to be in a lower energy state. Nanoparticles are often modelled as wetted (see Figure 3.1) spherical segments resting on a support [198]. The chemical potential at the surface of a spherical nanoparticle of radius  $r$  is given by [196, 198]

$$\mu(r) = \mu_0 + \frac{2\gamma_m\Omega}{r} \quad (3.10)$$

where  $\mu_0$  is the bulk chemical potential,  $\gamma_m$  is the surface free energy of the nanoparticle

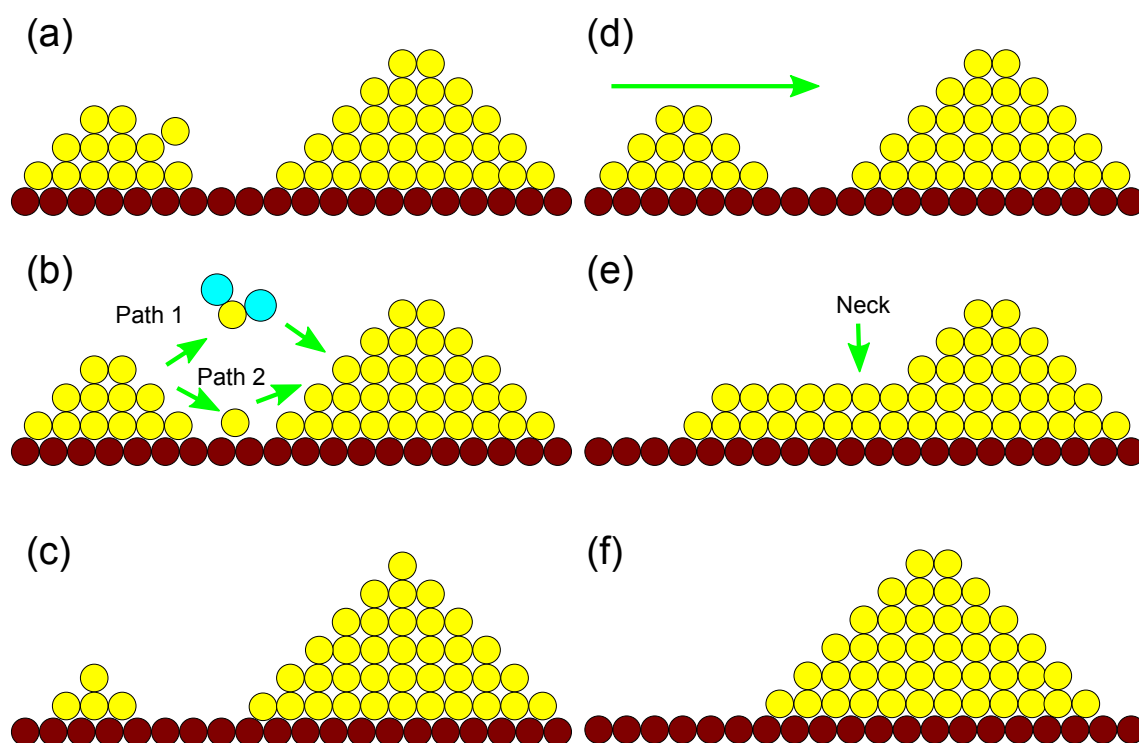


Figure 3.12: Schematic diagrams showing important parameters in (a-c) Ostwald ripening, (d-f) particle migration and coalescence. In Ostwald ripening an atom at the surface is able to (a) detach itself from the nanoparticle and (b) migrate across the surface or through the gas phase (perhaps via the formation of a molecule), over time the smaller nanoparticle will shrink but the larger one will grow. In coalescence, atoms on the surface move and drag the nanoparticle across the surface, eventually the two nanoparticles meet and a neck is formed (e) and finally they completely coalesce and form a larger single nanoparticle

metal and  $\Omega$  is the atomic volume of the bulk metal. Virtually all models are based on (3.10). Atoms on the edge that can diffuse are sometimes called monomers. In general, the diffusing atoms cannot diffuse through the support itself but they can diffuse across their surfaces.

The ability for an atom to move into a region of lower chemical potential depends on two factors: (a) the ability of atoms to detach from nanoparticles and (b) the ability of atoms to diffuse. These two mechanisms are referred to interface control and diffusion control respectively [195, 199, 200]. In most models, the nanoparticles are fixed and the density of atoms diffusing onto the surface of nanoparticles is constant within a certain distance.

Using *ex-situ* TEM and *in-situ* environmental TEM many groups have reported Ostwald ripening by observing the disappearance of small nanoparticles and the growth of larger ones. Lee *et al* suggested Ostwald ripening was responsible for the re-dispersion of  $> 5$  nm Pt nanoparticles on  $\text{Al}_2\text{O}_3$  below  $600^\circ\text{C}$  in  $\text{O}_2$  [201]. Their chemisorption data suggested that atoms diffused across the surface of the support in a  $\text{PtO}_2$  phase [201]. They observed that there was no such re-dispersion on Pt- $\text{SiO}_2$  suggesting the support plays a key role in inhibiting diffusion. They believe under certain conditions the  $\text{PtO}_2$  molecule can be stabilised by forming a metal-complex with the support structure. Some other groups observed a dual peak particle distribution in their  $\text{O}_2$  treated Pt- $\text{Al}_2\text{O}_3$  catalyst suggesting Ostwald ripening was the dominant mechanism supporting a mixture of shrunken and expanded nanoparticles. The general consensus is that the presence of  $\text{O}_2$  enhances Ostwald ripening [202].

Simonsen *et al* have reported observations of  $\text{O}_2$  induced Ostwald ripening of Pt nanoparticles using *in-situ* TEM [203, 204, 205]. The nanoparticles were supported on amorphous  $\text{Al}_2\text{O}_3$  which was loaded onto a  $\text{Si}_3\text{N}_4$  thin window TEM grid. The catalyst was exposed to 10 mbar air at  $650^\circ\text{C}$ . The group notes that the thin, flat surface of the amorphous  $\text{Al}_2\text{O}_3$  avoids complications with cliffs and defects that are normally present on commercial crystalline  $\text{Al}_2\text{O}_3$  supports. It was observed that during exposure to  $\text{O}_2$  the shapes transformed from faceted to rounded structures. The nanoparticle size distribution initially had log-normal shape but gradually changed into a Gaussian and finally a Lifshitz-Slyozov-Wagner shape [203, 204]. Other groups have observed similar results [206].

Clearly the support plays a key role in the sintering mechanism. Liu *et al* reported that Ostwald ripening (and coalescence) of Pd nanoparticles on  $\alpha\text{-Al}_2\text{O}_3$  was only significant at  $600^\circ\text{C}$  in air and  $700^\circ\text{C}$  in steam. They used TEM to study various *ex-situ* reacted



catalysts including steam and air environments at 500 mTorr [207]. Okumura compared the growth of Pt crystallites on  $\alpha$  and  $\gamma$ -Al<sub>2</sub>O<sub>3</sub> using atomic force microscopy and found that particles grew much larger on the  $\alpha$  phase support [208]. They believe that surface defects on  $\gamma$ -Al<sub>2</sub>O<sub>3</sub> are responsible for inhibiting Ostwald ripening and coalescence. Baker *et al* reported using environmental *in-situ* TEM that nanoparticles shrunk on  $\gamma$ -Al<sub>2</sub>O<sub>3</sub>, the authors believed that an unstable PtO<sub>2</sub> molecule was formed during diffusion [209], a similar effect was reported by Chen and Schmitt using SiO<sub>2</sub> although the latter group imply that both coalescence and ripening take place [210]. Flynn *et al* on the other hand suggest that metal or a metal-oxide diffuses onto the substrate and eventually meets another larger particle [211]. Interestingly, at 600 °C Chen and Schmitt report that 20 % of the Pt nanoparticles were twinned.

### 3.3.3 Nanoparticle Migration and Coalescence

Nanoparticles are known to be able to migrate and demonstrate Brownian motion. The nanoparticles are able to meet and eventually collide and coalesce to form single energetically favourable structure. Figure 3.12(d-f) shows a diagram of the migration and eventual coalescence process.

Old models regard migration and coalescence as a single thermally activated grain-boundary diffusion process [212]. The process is believed to activate at the Tammann temperature. Table 3.2 gives the Tammann temperature of the Pt group [191]. Note that Au has a low Tammann temperature compared to Pt which is one reason why Pt is preferred for use in exhaust catalysts. The general consensus in the literature is that nanoparticles can coalesce at lower temperatures [213] because their melting points are lower than that at bulk [214,215,216].

More recent experimental and theoretical evidence suggests that the coalescence process is not a continuous process and has several steps at which an energy barrier must be overcome [217]. The original models cannot take into account the detailed microstructure of the nanoparticles whereas the newer models can [213,217]. For example, Molecular dynamics simulations show that the initial neck formation leads to a release of energy leading to a local temperature rise and acceleration of the coalescence process [213].

The coalescence process occurs because the two merging nanoparticles have higher surface energy so a single large particle is energetically preferred as confirmed in a series of papers by Lehtinen and Zachariah [218, 218, 219, 220]. From the same work, it is

Table 3.2: Tammann temperature of some metals used in heterogeneous catalysis

Metal	Atomic Number	Tammann Temperature °C
Ru	44	990
Rh	45	845
Pd	46	640
Ag	47	345
Pt	78	750
Au	79	395

believed that there is a size limit for coalescence because as the nanoparticle size increases it becomes more difficult to melt, so that the coalescence of two large nanoparticles will only partly coalesce. Observations by Jose-Yacaman *et al* support this [221].

Liu *et al* observed that nanoparticle migration took place at temperatures much lower than the Tammann temperature during catalyst regeneration. They attributed this to a build up of gasified carbon molecules surrounding the Pd nanoparticles and promoting migration [207]. Compared to Pt, Pd is more resistant to sintering [222, 223].

Theory developed by Gruber concerning the coalescence and migration of bubbles in solids is applicable to nanoparticles. The theory assumes that nanoparticles are spheres and do not wet the surface of a substrate [224]. In this model, the speed of diffusing atoms is on the order of  $\sqrt{(D_s t)}$  where  $D_s$  is the diffusion coefficient of the atoms on the surface.  $D_s$  is given as [224]

$$D_s = D_0 \exp\left(\frac{-Q}{RT}\right) \quad (3.11)$$

where  $D_0$  is a constant,  $Q$  is the activation energy for surface diffusion,  $R$  is the gas constant and  $T$  is the temperature. The particle diffusion constant is related to (3.11) according to [224]

$$D_p = 0.301 D_s \left(\frac{2r_a}{R}\right)^4 \quad (3.12)$$

where  $r_a$  is the atomic diameter and  $d$  particle diameter. The 0.301 arises from the effect of fcc structure. It is possible to show that a nanoparticle will undergo Brownian motion with a random walk displacement of [224]

$$X_c = 2\sqrt{D_p t} \quad (3.13)$$

where  $t$  is time. The model outlined here does not take into account the faceted nature of most nanoparticles. Willertz and Shawmon show that (3.12) becomes exponential with dependence on the surface energy of an edge atom [225].

It has been observed that when bubbles meet, they will coalesce which means that two or more spheres will clump together and restructure to form a single structure [226]. Nichols reported that the process consists of several steps: (1) formation of a neck between the two spheres (2) neck removal (where one particle elongates) and finally (3) when a new equilibrium shape is attained. Each of these steps has an associated relaxation time [226]. It is believed that the time it takes for restructuring to occur in both particles scales with size [227].

Using aberration corrected HAADF-STEM, Asoro *et al* confirmed the above sequence but at the atomic level for 2.8 nm Pt supported on C [228]. They observed the transformation *in-situ* using electron beam heating. Their observations agree with those at larger scale in terms of morphology but the timescale involved is different. Molecular dynamics simulations for Au by Arcidiacono *et al* agreed with macroscopic theory down to 2 nm but below this size, they suggest that the relative orientation between smaller nanoparticles plays a key role [213].

Theissmann *et al* investigated the role of orientation between two nanoparticles [217]. They found using *in-situ* (heating) TEM that Au nanoparticles on amorphous C would rotate slightly before beginning the coalescence process and that structures became stable during elongated periods of constant temperature [217]. They reported that the coalescence process (formation of neck) took just 0.04 seconds. They stopped their heating experiment at 800 °C and allowed it to cool rapidly and observed mismatch between some atomic planes suggesting that these nanoparticles are loosely held together as opposed to coalescence [217]. They concluded that their own simulations matched experimental observations that nanoparticles that are orientated differently to each other will not coalesce.

There seems to be some debate as to whether Pt nanoparticles below 5 nm predominantly coalesce/migrate as opposed to ripen [200, 208]. Harris *et al* observed extremely large nanoparticles that were unexplained but found nanoparticles below 5 nm coalesced [229]. Baker *et al* reported using *in-situ* TEM that nanoparticles below 2.5 nm remain stationary in O<sub>2</sub> at temperatures up to 900 °C [230].

### 3.3.4 Model Fitting with Power Laws

The majority of models used to describe the growth of nanoparticles are based on (3.10) [198, 200]. The original models proposed by Wynblatt and Gjostein were based on the nucleation theory of spheres, called Lifshitz-Slyozov-Wagner theory (LSW) [198, 200].

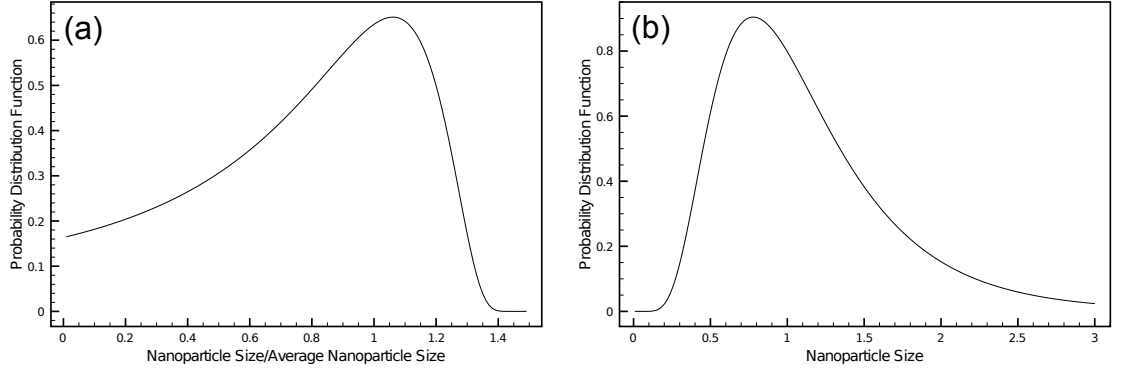


Figure 3.13: Evolution of nanoparticle size distributions expected for (a) Ostwald ripening and (b) Coalescence. The distributions final form corresponds to the LSW and log-normal distribution respectively

The end result of their derivation is a relation of the form

$$\frac{dr}{dt} = \frac{\kappa}{R} \left( \frac{r}{r^*} - 1 \right) \quad (3.14)$$

where  $r$  is the nanoparticle radius,  $r^*$  is the critical radius and  $\kappa$  is a constant which takes different values depending on the system and whether the system is interface or diffusion limited. The ratio  $r/r^*$  defines whether the derivative  $dr/dt$  is positive or negative which equates to an increase and decrease in nanoparticle size respectively.  $r^*$  is an equilibrium radius for a given nanoparticle concentration but it is also the average of  $1/r$  [195].

(3.14) is referred to as a power model. A more general form is

$$\left( \frac{r^*}{r_0^*} \right)^n = 1 + \frac{\kappa t}{r_0^*} \quad (3.15)$$

where  $r_0^*$  is the average nanoparticle size at  $t = 0$ . A more convenient way of expressing (3.15) is

$$n \log \frac{r^*}{r_0^*} = \log \left( 1 + \frac{\kappa t}{r_0^{*n}} \right) \quad (3.16)$$

Campbell and coworkers have argued that below 3 nm, the free energy of a nanoparticle increases dramatically [196]. The general consensus is that small nanoparticles have higher free energies than larger ones because of the increased contributions from surface tension [20]. Campbell's modifications to the original theory by Wynblatt has resulted in a more complex expression which takes into account the non-constant size-free energy relationship of small nanoparticles. It is of the form [196, 231]

$$\frac{dr}{dt} = \frac{\kappa}{R} \left( \exp \left[ \frac{-E_{tot}}{k_b T} \right] \right) \left[ \exp \left[ \frac{2\gamma_m \Omega}{k_b T r^*} \right] - \exp \left[ \frac{-2\gamma_m \Omega}{k_b T r} \right] \right] \quad (3.17)$$

where  $E_{tot}$  is the metals sublimation energy [231].

Many of the groups cited here have used the shape of the final nanoparticle size distributions to infer the dominant ageing mechanism [204, 206, 232]. The two expected distributions are shown in Figure 3.13. However, some groups believe that it is not possible to do this [233]. Datye and coworkers argue that virtually any nanoparticle size distribution can be fitted with a log-normal distribution. Wanke *et al* also suggest that to acquire a LSW requires much more time than is practically possible using model systems [234]. Datye and coworkers also propose from TEM that with changes in environmental conditions such as a change from oxidative to reductive atmospheres (e.g.  $H_2$ ), nanoparticles will predominantly undergo migration and coalesce because with the gas environment the ability of atoms to diffuse is inhibited [233]. In a diesel exhaust, the oxidative atmosphere may change briefly during operation and during filter regeneration it may switch to a reductive atmosphere.

### 3.3.5 Ageing of Bimetallic Systems

Bimetallic nanoparticles have been reported to have excellent resistance to sintering [93, 235, 236]. For Pd-Pt nanoparticles it is reported that the presence of Pd inhibits the formation of  $PtO_2$ , discouraging Ostwald ripening [93, 235, 236]. Due to differences in bulk energies between constituent atoms that alloys will gradually segregate over time. The current theoretical consensus in the case of Pt-Pd is that Pd will segregate to the surface, leaving behind a Pt enriched core. However, there is some evidence that size plays a key role in the formation of a core. Barcaro for example, found that Pt will form patches on  $\{111\}$  surfaces in small nanoparticles [237].

Experiments involving the ageing of nanoparticles over long periods of time generally agree with this [236, 238, 239, 240]. HAADF-STEM is ideally suited for the analysis of bimetallic nanoparticles but it has rarely been applied to application aged ones, instead HAADF-STEM has been extensively used to characterise as prepared catalysts.

The segregation of Pt and Pd leads to the formation of PdO [236, 240, 241, 242]. The activity and structure of PdO is reviewed below.

## 3.4 Pt and Pd Oxides and their Reduction

### 3.4.1 Introduction

When metals are exposed to O<sub>2</sub> rich atmospheres oxides can be formed. The metals of Pt and Pd are not very reactive at room temperature with O<sub>2</sub> but at sufficiently high pressure and temperatures they will form oxides. Many groups report the formation of Pt and Pd oxides when loaded onto oxide supports. The formation of oxides on Pt and Pd nanoparticle systems changes their catalytic properties. There are few detailed crystallographic studies of Pt oxides formed in the nanoparticle context.

### 3.4.2 Structures and Activity of Pd Oxides

Pd is known to form a tetragonal PdO phase [243] which is stable at room temperature. Lattice parameter measurements seem to vary by about 5 % between the different methods used [244], they are approximately  $a = 3.01 \text{ \AA}$  and  $c = 5.31 \text{ \AA}$ . Kumar and Saxena, using TEM and SAD found PdO as tetragonal but they also found two additional Pd oxides: the first being cubic PdO and a cubic Pd<sub>2</sub>O [245]. There is little information on the thermodynamic stability of such structures, but most groups who use TEM to analyse PdO find it to be beam sensitive; often losing its structure.

In addition to the above structures, 2D metal oxide structures can exist. It is believed that these 2D forms are precursors or intermediate stages during the formation of bulk PdO [246]. A  $\sqrt{5} \times \sqrt{5} R 27^\circ$ -Pd(101)-O structure has also been confirmed to exist by LEED. Currently, there appear to be no reports in the literature about the presence of these 2D oxides using TEM and SAD. Perhaps given surfaces of sufficient size, it may be possible to detect the presence of such surface oxides using NBD and SAD by searching for additional reflections that may arise from deviations of the expected structure factor (2.6) rules.

Rodriguez *et al* reported that Pd is converted to PdO above 300 °C on SiO<sub>2</sub> and Al<sub>2</sub>O<sub>3</sub> in 1 atm O<sub>2</sub>. They observed using *in-situ* TEM that the PdO crystals spread because of wetting effects [247]. Interaction with the support was also observed as was discussed in the previous section. Chen and Ruckenstein also reported a similar phase change [248].

There is much literature on the reduction and reformation of PdO because of its widespread use in methane oxidation catalysts. Farautto *et al* investigated the hysteresis of PdO-Pd formation on different supports [249]. They found that the PdO → Pd decomposition

is inhibited on  $\text{Al}_2\text{O}_3$  at temperatures below 600 °C. They also observed that  $\text{Al}_2\text{O}_3$  did not adsorb any  $\text{O}_2$  [249]. Following on from this research, other groups have probed the nanostructure during the  $\text{PdO} \rightarrow \text{Pd}$  transformation.

Datye and coworkers used TEM, XRD and XPS to investigate phase transformations (*ex-situ*) of a  $\text{Pd}-\theta\text{-Al}_2\text{O}_3$  [250]. Once treated in air they found that initially spherical Pd nanoparticles had transformed into PdO which often contained no facets. Other groups have reported that Pd nanoparticle faces will become irregular and the nanoparticle will often become rounded [251]. Datye and coworkers report that PdO decomposes at 700 °C with the transformation occurring at the surface generating patches of Pd which increase the decomposition rate [250]. They observed that the Pd clusters formed can be easily re-oxidised in air and that complete transformation produces single crystals. They also observed that some nanoparticles had Pd shells surrounding PdO nanoparticles and some PdO crystals were surrounded by an amorphous layer which they attribute to  $\text{PdO}_x$  which was initially suggested by Farrauto *et al* [249]. At high temperature they observed sintering of Pd metal but not PdO suggesting it is unable to move on the support surface.

Penner *et al* used HRTEM and SAD to investigate the structural changes in epitaxially grown 5 – 7 nm Pd nanoparticles supported on  $\text{SiO}_2$ . They suggest that PdO formation begins (during  $\text{O}_2$  treatment) at temperatures as low as 350 °C and is complete at 400 °C which almost puts its formation within the DOC operating temperature of 200 – 300 °C. They observed the transformation by the appearance of PdO rings in the SAD pattern. As with Chen and Ruckenstein [248], Penner *et al* observed the formation of pits and cavities often forming distorted doughnut shapes because they were oxidised [252]. They believe that PdO forms as a cluster on Pd and will move towards the support. They also note that the PdO is epitaxial to the original Pd nanoparticles. Penner *et al* used CO as a reducing agent and observed that PdO started to reduce at 273 °C and that the Pd nanoparticles formed were partially aligned which agrees with the previous observations.

Baldwin *et al* and Farrauto *et al* found that treating  $\text{Pd}-\gamma\text{-Al}_2\text{O}_3$  in  $\text{O}_2$  lead to an increase in methane oxidation activity [249, 253]. Farrauto identified the active phase as PdO. However, some groups report that metallic Pd is the active phase in methane oxidation.

Hirvi *et al* have investigated the CO oxidation abilities of PdO surfaces using density functional theory [254]. They found that of the most stable surfaces, the (001) surfaces are almost inert but the (101) surface is able to adsorb CO strongly enough such that the Lingmuir-Hinshelwood mechanism can take place. They note, as with other authors, that

the Elley-Ridely mechanism also takes place on (1 0 1) surfaces.

### 3.4.3 Structures and Activity of Pt Oxides

Galloni and Roffo used the Jorgensen method to produce what they identified as bcc  $\text{Pt}_3\text{O}_4$  [255] but Waser and McClanahan described a bcc  $\text{NaPt}_3\text{O}_4$  structure [256]. This disagreement has led to an argument about the structure of Pt oxide synthesised by this method [256, 257]. Galloni and Busch in the same paper [257] believe that the hexagonal symmetry observed in a diffraction pattern in their previous work was  $\text{PtO}_2$  [257]. Moore and Pauling used XRD and identified a tetragonal phase which they attribute to  $\text{PtO}$  [243] but their argument is based on its similarity to  $\text{PdO}$ , so its existence has not been proven conclusively; as Waser *et al* [256] have argued.

Characterising Pt oxides from commercially available specimens have yielded conclusive data for hexagonal  $\alpha\text{-PtO}_2$  [258]. Muller and Roy reported the presence of an additional orthorhombic phase called  $\beta\text{-PtO}_2$  [258] and a tetragonal  $\text{Pt}_3\text{O}_4$  [258].  $\beta\text{-PtO}_2$  was also found by Shannon [259] using high pressure synthesis techniques. A further expanded lattice  $\beta'\text{-PtO}_2$  phase was reported by Herrero Frandez and Chamberland but like  $\beta\text{-PtO}_2$  it exists only at high pressure [260].

Kumar and Saxena synthesised their own Pt oxides by treating Pt nanoparticles of various sizes on amorphous  $\text{SiO}_2$  and  $\text{Al}_2\text{O}_3$  in  $\text{O}_2$ . Using TEM and SAD, they report additional cubic phases:  $\text{PtO}$  and  $\text{Pt}_2\text{O}$  [245]. The work by Kumar and Saxena suggests that size plays a key role in the structure of Pt oxides but interfaces with the support may also play a key role.  $\text{PtO}_3$  may not be observed often because according to DFT calculations by Seriani *et al*, it is thermodynamically stable only at temperatures above 627 °C [261]. Comparing  $\text{PtO}$  prepared in bulk using chemical methods may not agree with nanoscale preparation methods, but the current consensus appears to be that Pt oxides are poor crystals and may simultaneously form multiple phases with variable lattice parameters. See for example, the list of Pt oxide phases listed in [258] and [245].

Literature surrounding the activity of Pt oxides mostly revolve around  $\alpha\text{-PtO}_2$ . Using density functional theory, Pedersen investigated the CO oxidation abilities of oxidised Pt and  $\alpha\text{-PtO}_2$  [262]. They found that the hexagonal  $\{001\}$  and  $\{100\}$  surfaces had the lowest energy and the (001) facets are poor for CO oxidation via the Langmuir-Hinshelwood mechanism. Furthermore a defective surface containing O vacancies (allowing a reaction to occur via the Mars van Krevelen method) had a high reaction barrier of 1.4 eV. There-



fore,  $\text{PtO}_2$  (0 0 1) are inert [262]. However, they did show that on  $\{1\ 0\ 0\}$  surfaces the reaction barrier for CO oxidation is small and therefore it offers a level of activity. The work here agrees with the work by Hendrickson *et al* who investigated the activity of Pt surfaces in  $\text{O}_2$  [263].

In addition to bulk phases, there is considerable research interest in the formation of amorphous  $\text{PtO}_2$  films often referred to as  $\alpha\text{-PtO}_2$  [264]. Generally speaking, these films have been produced by reactive sputtering and by careful control over the sputtering parameters it has been possible to synthesise the rather elusive form of PtO and the well known phases of  $\text{PtO}_2$  [265, 266]. Annealing of some  $\alpha\text{-PtO}_2$  films in air at 420 °C by Kreider *et al* resulted in weak  $\alpha\text{-PtO}_2$  peaks in the otherwise amorphous XRD graphs but the annealed films still displayed poor crystallinity [267].

There appear to be only a few TEM studies of  $\text{PtO}_2$  and other Pt oxides. Zhensheng *et al* [268] prepared  $\alpha\text{-PtO}_2$  by the fusion method and found that it had needle like morphology with lengths up to 50 nm and diameters up to 6 nm. This seems to agree with current XRD data: the data show  $\alpha\text{-PtO}_2$  is a poor crystal in the  $c$  axis.

In many applications,  $\text{PtO}_2$  is reduced to Pt metal. The metal is the active phase in some applications therefore it is important to understand its reduction mechanism. McKinney reported using XRD that dried  $\text{PtO}_2$  is reduced easily by CO at 25 °C and 40 °C with induction periods of 2 h and 30 minutes respectively [269]. In the presence of excessive  $\text{O}_2$  however, he reports that  $\text{PtO}_2$  is not reduced at 80 °C and believes that  $\text{PtO}_2$  catalyses the oxidation of CO. Upon reduction of  $\text{PtO}_2$  the Pt metal was observed to become active at 184 °C in excess  $\text{O}_2$  but with excess CO there was little activity. Reduction of  $\text{PdO}_2$  by  $\text{H}_2$  has been reported to form Pt nanoparticles [270].

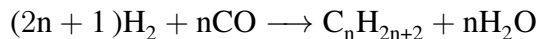
### 3.4.4 Bimetallic $\text{Pd}_x\text{Pt}_{1-x}\text{O}_y$

Dianat and coworkers (including Seriani) investigated bimetallic versions of the PdO,  $\text{PtO}_2$  and  $\text{Pt}_3\text{O}_4$  structures using DFT [271]. They predict that bimetallic oxides are stable at temperatures below 272 °C which would make their presence unlikely in a DOC application. However, they predict at intermediate temperatures of 300 – 500 °C oxides of PdO coexist with  $\text{PtO}_2$  and  $\text{Pt}_3\text{O}_4$ . Above 500 °C the group report that bimetallic metal alloys are formed but if the bimetallic oxide is Pd rich then PdO forms with Pt domains. The formation of Pt domains on PdO has been experimentally observed on model PtPd/ $\text{Al}_2\text{O}_3$  systems that have undergone  $\text{O}_2$  treatment but also PdO model catalyst where Pt has been

added [271].

### 3.5 Cobalt (Co) Fischer-Tropsch Catalysts

An emerging field of catalysis that is receiving much attention is that regarding Fischer-Tropsch synthesis of diesel fuels. The Fischer-Tropsch (FT) reaction is



but the whole FT process involves many reactions including hydrogenation and gasification. The whole purpose of the FT process is to synthesise diesel from alternative sources such as coal, gas and biomass instead of directly from crude oil.

Catalysis employed in FT synthesis are often Co, Ni and Cu. Co has been found to be highly active in the Fischer-Tropsch reaction but often the catalyst is prepared by pre-treating readily available oxides such as  $\text{Co}_3\text{O}_4$ . Fischer-Tropsch processes are popular research topics in the oil and chemical industry because it allows the production of fuel without the need for crude oil [4]. In 1980 there were only a handful of large scale Fischer-Tropsch facilities throughout the world [272] but now they are much more widespread because of the recent interest in gas to liquids technology [273].

Gas to liquids (GTL) technology; the conversion of natural gas into diesel, has the Fischer-Tropsch process at its heart. It has become attractive because of the discovery of new natural gas reserves, the need to minimise the flaring of natural gas and the need to make remote sources of natural gas viable sources of energy.

In GTL technology, the first step is to produce syngas which is a mixture of CO and  $\text{H}_2$ . The next step is to convert the syngas into the desired product followed by hydroprocessing to remove  $\text{H}_2\text{O}$ . In the Fischer-Tropsch reaction, a polymerisation reaction occurs in which adsorbed CO is hydrogenated causing methylene ( $\text{CH}_2$  with two spare electrons) species to form chains with the newly formed alkyl groups on the catalyst surface [272].

The Fischer-Tropsch process requires a catalyst primarily to allow control over the process output. Fe based catalysts have been found to be selective for alkanes in the  $\text{C}_{1-4}$  range at high temperature ( $340^\circ\text{C}$ ) and pressure (25 bar) [274]. More recently, Co based catalysts have been used because they offer a better compromise between cost, efficiency and selectivity at low temperature ( $225^\circ\text{C}$ ) [275, 276]. The Co catalysts have been found

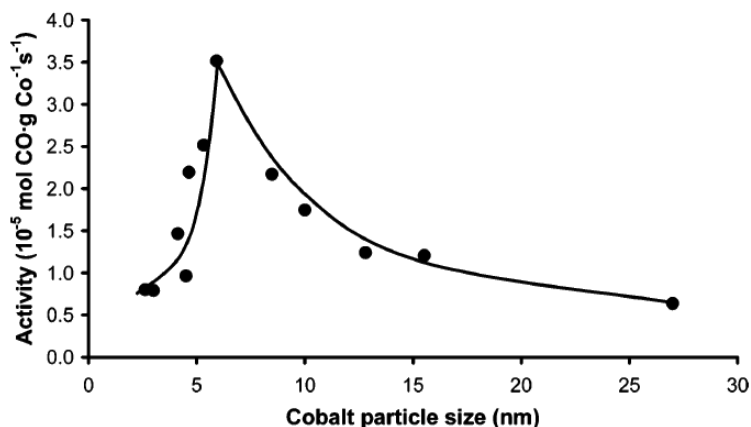


Figure 3.14: Reproduced graph from [283] showing the relationship between activity and Co nanoparticle size when supported on inert C nanowires

to be highly selective towards  $C_{5+}$  hydrocarbons which is beneficial for the synthesis of diesel [276].

The active sites in the Fischer-Tropsch process has been proven by Iglesia and co-workers to be  $Co^0$  (Co metal) [275, 276, 277, 278]. Typical catalysts use Co nanoparticles on supports such as  $Al_2O_3$  but the metal loading is often above 33% to encourage a worthy level of activity as well as selectivity [279].

It has been verified by many groups that Co catalyst activity is not dependent on the size of nanoparticles suggesting an active site invariance [280, 281, 282], but these studies were with larger nanoparticles ( $> 7$  nm). Model Co on C-nanowires suggest that the specific activity for  $C_{5+}$  molecules drops as the nanoparticle size is decreased below 7 nm with an increase in  $C_{1-3}$  molecule selectivity [283]. The same group have noted that the support is inert whereas more common supports such as  $Al_2O_3$  can form mixed oxides with the nanoparticle species supported [284].

It has been reported that re-oxidation (via  $H_2O$ ) of Co will deactivate 6 nm nanoparticles under realistic operating conditions [285, 286, 287]. On the other hand, calculations have shown that bulk Co cannot be influenced by  $H_2O$  [288]. There is still some debate as to the origin of activity in smaller Co nanoparticles [273].

Co is rarely available as a pure metal for the development of catalysts. Instead, an oxide, usually  $Co_3O_4$  [4, 289], is reduced by pre-treatment with  $H_2$  and  $N_2$ . The reduction of the oxide ultimately determines the range of reduced/oxidised Co species and the resulting structure/shape of the catalyst. If Fischer-Tropsch processes are to reach cost parity with the crude oil approach to diesel production then the functionality of the catalyst must be fully understood. The reduction mechanism of  $Co_3O_4$  will be reviewed in this section but

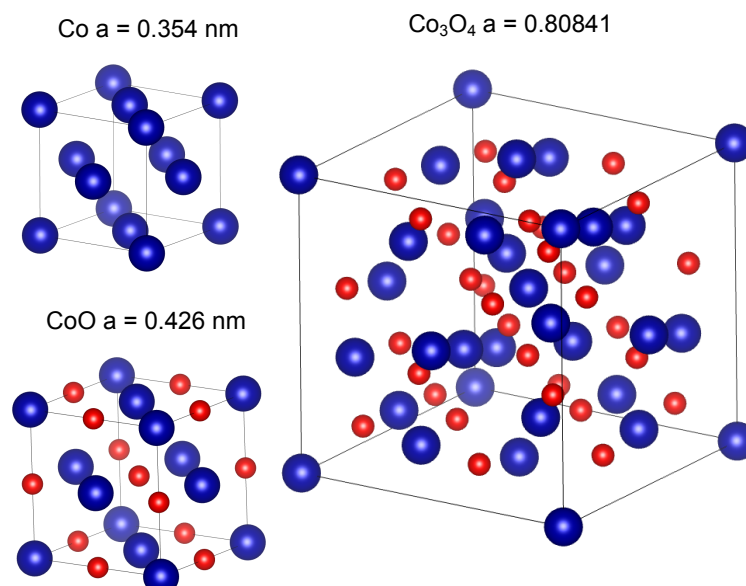


Figure 3.15: Ball models showing the crystal structures with corresponding calculated electron diffraction intensities of spinel  $\text{Co}_3\text{O}_4$ , rocksalt  $\text{CoO}$  and fcc  $\text{Co}$ . The diagrams are approximately to scale to each other

first a summary of known Co and Co oxide phases is presented.

### 3.5.1 Structure of Co and its oxides

Figure 3.15 shows the three common structures associated with the reduction of  $\text{Co}_3\text{O}_4$ .  $\text{Co}_3\text{O}_4$  forms in the fcc spinel structure where  $\text{Co}_2^+$  occupy the tetrahedral sites and  $\text{Co}_3^+$  the octahedral sites. The O atoms form an almost perfect cubic close packed sub-lattice.

$\text{Co}_3\text{O}_4$  has low spatial frequency  $\{1\ 1\ 1\}$  reflections and its  $n\{0\ 0\ 2\}$  ( $n$  odd) reflections are forbidden according to the structure factor (2.6). The  $\{4\ 4\ 0\}$  and  $\{0\ 0\ 4\}$  reflections are the brightest followed by the  $\{0\ 2\ 2\}$  and  $\{1\ 1\ 1\}$  reflections. Casas-Cabanas and coworkers observed anomalous intensities in their  $\{1\ 1\ 1\}$  and  $\{0\ 2\ 2\}$  XRD peaks from their low temperature precipitated  $\text{Co}_3\text{O}_4$  powders and showed that they could be explained by Co atoms occupying non-ideal positions at interstitial sites [290]. Upon heating, the defects were removed with the displaced Co atoms moving into their standard positions. Their works suggests that diffraction intensities can be used to detect structural anomalies.

$\text{CoO}$  is often found in a fcc rocksalt ( $\text{NaCl}$ ) phase. In this form,  $\text{Co}_3^+$  is located on octahedral sites and  $\text{Co}_2^+$  at tetrahedral sites. In this structure, O atoms are in a fcc sublattice displaced by  $1/2\ 1/2\ 1/2$  in the Co unit cell. The  $\{0\ 0\ 2\}$  reflections are the most intense followed by the  $\{0\ 2\ 2\}$  reflections. The  $\{1\ 1\ 1\}$  reflections are weak.

Two additional phases have also been identified: hexagonal wurtzite (like ZnO) [291, 292] and a fcc zincblende phase [292]. According to simulations by Grimes and Lagerlof, the rocksalt phase is the most stable followed by the wurtzite and zincblende phase [292]. The wurtzite structure has been shown to transform into the rocksalt phase at approximately 378 °C [293].

According to Grimes and Lagerlof, the zincblende and wurtzite forms have only been observed between 290 – 310 °C [292] and the rocksalt form forms above 320 °C from the thermal decomposition of Co oxide precursors (e.g. cobalt acetate) [292], so it may not be relevant to the reduction of Co<sub>3</sub>O<sub>4</sub>.

Co exists in fcc and hcp phases with the fcc taking dominance during high temperature (> 350 °C) synthesis [294]. A unique simple cubic  $\eta$  phase has been reported using certain wet preparation techniques [295] but this cannot be prepared from the reduction of Co oxides.

### 3.5.2 Reduction Mechanism

*Ex-situ* and *in-situ* studies have come to a general consensus that the following reduction occurs [296, 297, 298]

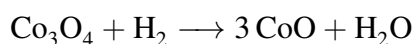


where Co is generally observed in its fcc phase. HRTEM has shown that the reduction process is epitaxial with the directions being equivalent in each different structure e.g. Co<sub>3</sub>O<sub>4</sub>{1 1 1} to CoO{1 1 1}.

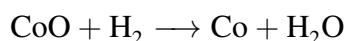
Potoczna-Petru and coworkers used HRTEM with specimens reacted *ex-situ* to investigate the changes in structure of unsupported Co<sub>3</sub>O<sub>4</sub> [298]. They investigated the reduction mechanism of differently sized Co<sub>3</sub>O<sub>4</sub> nanoparticles of 5.3, 12.1, 20.3 and 42 nm. They found that at 300 °C the smallest nanoparticles had completely reduced to Co. With increasing size, the nanoparticle became more resilient to reduction. The largest nanoparticles remained as Co<sub>3</sub>O<sub>4</sub> at 300 °C and 500 °C whereas mixed metal-oxides were observed at the intermediate sizes and temperatures. They report that CoO was only observed in trace quantities for the 20.3 nm nanoparticles at 400 °C. In the same paper, they indicated that the synthesis temperature of Co<sub>3</sub>O<sub>4</sub> changed its initial reduction temperature from 175 °C to 230 °C [298]. There appears to be no explanation for this although other groups have indicated a slight change in defect structure in Co<sub>3</sub>O<sub>4</sub> [290].

The particle morphologies also change according to Potoczna-Petru and coworkers [298]. They believe that CoO and Co forms at the top of the crystals causing stacking faults and empty spaces (voids) to appear in the middle of Co<sub>3</sub>O<sub>4</sub> structures. They believe that these voids are formed during CoO to Co reduction because the Co unit cell has less volume than the CoO unit cell. Since this experiment was done *ex-situ* there appears to be no consensus on how these stacking faults relate to the reduction mechanism. In-fact, a paper written by Dieckman in 1984 stated that there was no reliable data on the defect structure of Co<sub>3</sub>O<sub>4</sub> [299] so it raises the question whether surface defects can form in very small nanoparticles.

Lin and co-workers have combined TPR data and kinetic models in an effort to deduce the reduction mechanism of Co<sub>3</sub>O<sub>4</sub> and CoO [296]. They believe the reduction mechanism is



and



The activation energy for these two steps is calculated to be 94.43 kJmol<sup>-1</sup> and 82.97 kJmol<sup>-1</sup> respectively.

Supported Co<sub>3</sub>O<sub>4</sub> has also been investigated. Jacobs *et al* investigated the reducibility of Co<sub>3</sub>O<sub>4</sub> on Al<sub>2</sub>O<sub>3</sub>, TiO<sub>2</sub>, SiO<sub>2</sub> and ZrO<sub>2</sub> [300]. On Al<sub>2</sub>O<sub>3</sub> and TiO<sub>2</sub> they report a strong interaction between the support with larger crystals behaving like bulk Co<sub>3</sub>O<sub>4</sub> but smaller crystals being more resilient to reduction. On SiO<sub>2</sub> they report virtually no differences between the reduction process as a function of Co loading.

*In-situ* reduction using H<sub>2</sub> TPR has been done on unsupported and supported (on  $\gamma$ -Al<sub>2</sub>O<sub>3</sub>) Co<sub>3</sub>O<sub>4</sub> using XRD by Bulavchenko *et al* [297]. They reported that reduction began at  $\pm 10$  °C about 200 °C in the unsupported samples with complete reduction occurring at 350 °C. XRD peaks for CoO and Co appeared at 180 °C and 260 °C respectively in the supported sample. Their *in-situ* experiments suggest that reduction takes place in one step in pure H<sub>2</sub> but in two steps in a H<sub>2</sub>-He mixture. A two stage process has been observed in *in-situ* experiments which use lower pressures (< 5 mbar) [301].

In pure H<sub>2</sub> at 1 bar they found that unsupported Co<sub>3</sub>O<sub>4</sub> reduced in one step (to hexagonal Co) and Al<sub>2</sub>O<sub>3</sub> supported Co<sub>3</sub>O<sub>4</sub> reduced to CoO and then to cubic Co. They believe

that a metal-support interaction occurs on the supported catalyst leading to the formation of a reduction resilient Co-Al mixed oxide.

To summarise,  $\text{Co}_3\text{O}_4$  has been found to reduce to CoO at approximately 360 °C with reduction beginning as low as 200 °C but the reduction temperature is dependent on crystal size.

## Chapter 4

# Nanostructural studies of Pt–SiO<sub>2</sub> and Pt-Pd–Al<sub>2</sub>O<sub>3</sub> DOCs

### 4.1 Introduction

Diesel oxidation catalysts (DOCs) are used for the oxidation of CO and any unburnt hydrocarbons in a diesel automobile exhaust. The primary active components in DOCs are metal nanoparticles (usually Pt) loaded onto a thermally stable support such as  $\gamma$ -Al<sub>2</sub>O<sub>3</sub> [2] and SiO<sub>2</sub> [302]. Pd is now being added to Pt nanoparticle DOCs because bimetallic Pt-Pd nanoparticles are more resistant to sintering [303] but it does introduce the complication of segregation. There are very few previous reports on the nanostructure of technological bimetallic DOCs [192, 193]. Previous investigations into structural changes in bimetallic and monometallic nanoparticles have been carried out primarily on model catalysts in controlled ageing environments [93, 247, 303]. Here, fresh and aged Pt-Pd-Al<sub>2</sub>O<sub>3</sub> and Pt-SiO<sub>2</sub> DOCs are compared to gain new insights into the possible influence of the nanostructure on reaction mechanisms using aberration corrected (scanning) transmission electron microscopy (AC-(S)TEM).

### 4.2 Specimens and Preparation for Electron Microscopy

#### 4.2.1 Description of Specimens

In modern times, most DOCs are monolithic catalysts [2, 304]. The monolithic catalyst is composed of three primary components: the monolith itself, the washcoat and the active catalysts [304]. Figure 4.1 shows a cross-section of a typical DOC. The monolith itself is



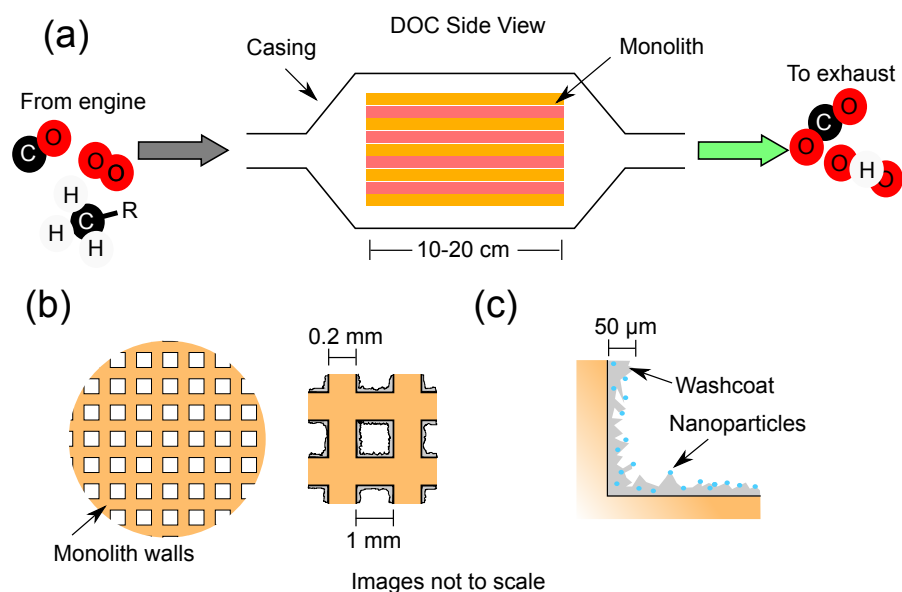


Figure 4.1: Diagram showing the typical structure of a monolithic DOC with (a) the DOC as a whole, (b) close ups of the monolith channels and (c) close up of the washcoat layer containing the catalyst support and catalytically active nanoparticles. Typical sizes (based off [306]) of such structures are indicated

usually made from a chemically inert material such as cordierite [304,305], which in pure form has formula  $(\text{MgFe})_2\text{Al}_3(\text{Si}_5\text{AlO}_{18})$ . The monolith structure ensures good gas flow in operation by containing channels as shown in Figure 4.1(b). The monolith also maintains the structural integrity of the weaker materials loaded upon it [305].

The monolith is coated with high porosity materials that increase the effective surface area of the monolith catalyst [306]. The coating is called the washcoat, it can be seen in the monolith channel closeup in Figure 4.1(b) and (c). The latter shows the nanoparticles loaded onto the washcoat. The washcoat is primarily composed of a high surface area and thermally stable materials such as  $\gamma\text{-Al}_2\text{O}_3$ ,  $\text{SiO}_2$  and zeolites [305,306]. Additionally, the washcoat must be able to support nanoparticles, ideally with high dispersion [2, 305]. The washcoat is applied during manufacturing by dipping the monolith into a gel or slurry and leaving it to dry [306].

The washcoat is generally not catalytically active for CO oxidation [305]. The washcoat is therefore impregnated with the catalytically active species, usually Pt nanoparticles [2, 305, 306]. This is achieved by dipping the wash-coated monolith into a solution of various precious metal precursors, usually metal salts [306]. The wet monolith is then dried and may undergo thermal treatment to catalytically activate the nanoparticles [306].

In this chapter, fresh and road aged monolith sections of two types of DOC were

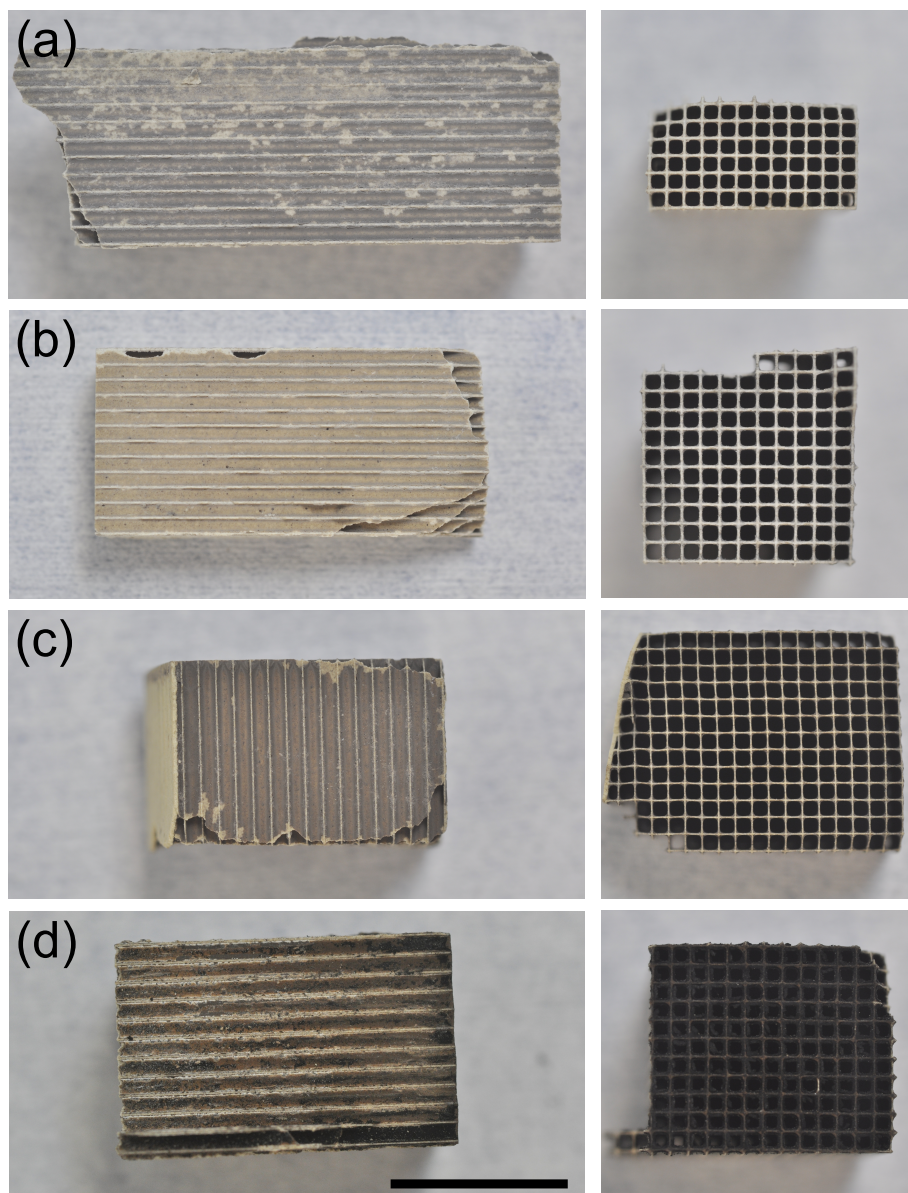


Figure 4.2: Pictures of the monolith sections (as received) showing side and top views of (a) Pt-Only Fresh, (b) Pt-Only Aged, (c) Bimetallic Fresh and (d) Bimetallic Aged monolith sections. Scale bar is 1 cm

investigated. Monolith sections cut from the main structure were supplied by Johnson Matthey but the manufacturer of the DOCs is unknown. A Pt-Pd-Al<sub>2</sub>O<sub>3</sub> DOC and Pt-SiO<sub>2</sub> DOC variants were supplied. The aged Pt-Pd-Al<sub>2</sub>O<sub>3</sub> and Pt-SiO<sub>2</sub> DOCs were supplied as road-aged for 40,000 and 36,000 miles respectively. The DOCs will be referred to as Bimetallic-DOC and Pt-Only DOC respectively hereafter. Figure 4.2 shows images of the as received monolith sections. According to SEM data from Johnson Matthey [241], the washcoats on the Bimetallic-DOC and Pt-Only DOCs are 50  $\mu\text{m}$  and 25  $\mu\text{m}$  thick respectively when measured at the straight parts of the monolith channels. The washcoats are between about 25 – 50  $\mu\text{m}$  thicker at the monolith channel corners in both cases [241].

Table 4.1: Metal loadings by atomic weight on the four DOCs provided by Johnson Matthey [241]

DOC	Pt (%)	Pd (%)
Bimetallic Fresh	0.89	0.46
Bimetallic Aged	0.72	0.36
Pt Only Fresh	0.34	trace
Pt Only Fresh	0.29	trace

Table 4.1 shows the metal loadings in the two different DOC systems determined with infrared chromatography by Johnson Matthey [241]. Johnson Matthey did not manufacture the monoliths but they helped with the wider analysis (SEM, XRD) as referenced. The quantities are atomic weights. The amount of Pt and Pd varies from area to area on the nanoscale. The majority of Pt:Pd ratios recorded were between 5:1 and 1:5 by atomic weight. Overall Pt:Pd ratios were observed from approximately 40:1 to 1:20 (see for example Figure 4.9 on page 100). The readings for the large ratios were often accompanied by large errors since small broad peaks in the EDX spectrum are more difficult to distinguish from background noise and other nearby peaks as determined by the NSS software. These measurements suggest that during manufacture, the Pt and Pd metals are not evenly distributed on the nanoscale. The overall metal loading in the fresh and aged DOCs suggest the loss of some metal during their use and this is discussed in the following sections. Observations from bulk indicate that a 2:1 ratio (by atomic weight) of Pt:Pd is present in both the fresh and aged samples in the Bimetallic DOC [241]. The overall metal loading is different between the Pt-Only and Bimetallic DOCs. Table 4.1 shows that the metal loading in the Bimetallic DOC is twice that of the Pt-Only DOC in both fresh and aged cases.

XPS data provided by Johnson Matthey is summarised in Table 4.2 for the Bimetallic DOCs and the Pt-Only DOCs. The XPS measurements show that in the aged DOCs, very small amounts P and S (from the diesel fuel) are present [241]. Other species such as Ca may originate from lubricants and engine parts. Significant concentrations of S and P can form compounds with Pd-PdO in the Bimetallic DOC and may lead to a reduction of the catalytic activity [223].

#### 4.2.2 Specimen Preparation

The aim of the study here was to examine the structure of the nanoparticles which are primarily located on the washcoat material (see Figure 4.1 on page 88). The cordierite

Table 4.2: XPS measurements of the four DOCs [241]

Name	Peak Binding Energy ( eV)	FWHM ( eV)	FWHM (%)	Peak Binding Energy ( eV)	FWHM ( eV)	FWHM (%)
	Fresh Bimetallic DOC			Aged Bimetallic DOC		
Si <sub>2p</sub>	103.60	2.54	6.17	103.60	2.40	6.25
Al <sub>2s</sub>	120.35	3.17	30.44	119.99	3.03	25.24
O <sub>1s</sub>	532.28	3.16	57.78	532.17	3.14	54.78
Cl <sub>s</sub>	285.59	3.14	4.93	284.39	4.27	12.36
P <sub>2s</sub>	-	-	-	192.69	3.21	0.26
S <sub>2s</sub>	-	-	-	233.76	3.55	0.53
	Fresh Pt Only DOC			Aged Pt Only DOC		
Si <sub>2p</sub>	154.74	2.58	27.72	154.87	2.58	29.99
Al <sub>2s</sub>	119.80	2.64	1.18	120.40	2.71	1.19
O <sub>1s</sub>	532.98	1.89	64.39	533.11	1.88	64.81
Cl <sub>s</sub>	285.07	2.28	6.34	258.01	2.38	5.92
Ca <sub>2p</sub>	-	-	-	348.56	1.67	0.12
P <sub>2s</sub>	-	-	-	192.68	0.34	0.20
S <sub>2s</sub>	-	-	-	234.88	0.18	0.29

itself and the other materials were not of interest in this study. (S)TEM specimens were prepared as follows. Separately, each monolith section was further sectioned using Cu wire of approximately 1 mm diameter to saw (manually) through the channels of each monolith. This was done on filter paper using a fresh sheet for each monolith section. The sectioning process generated debris in the form of powder and small chunks of monolith which were collected into a bottle. The debris from the top layers of the monolith were not used to prepare (S)TEM specimens to minimise contamination arising from the initial monolith cutting process which was done prior to receivership.

The debris and powder was dispersed in ethanol in a small glass bottle. Approximately 25 mg of debris was used. The bottle was shaken by hand and was then placed in an ultrasonic bath for 240 s. The resulting suspension for the fresh DOCs gave a beige colouration to the ethanol. The aged variants however, gave a grey-black solution with some sign of liquid separation suggesting the presence of oils. A disadvantage of this method was that the specimen was populated by large (often > 1  $\mu\text{m}$ ) diameter cordierite crystals. It was found that imaging the cordierite caused it to deteriorate under the beam after a short while preventing practical analysis of the washcoat and the nanoparticles loaded upon it.

Therefore, further effort was required to encourage the washcoat to separate from the cordierite. The same powder mentioned above was exposed to ultrasonic frequencies for longer durations (approximately 10 minutes). This broke up the specimen even more,

resulting in more separated washcoat and cordierite crystals allowing for more extensive and convenient analysis of the nanoparticles loaded upon the washcoat.

(S)TEM specimens were made by dispersing the powder solutions on a TEM grid. Single or multiple 2.5  $\mu\text{l}$  drops were deposited onto a TEM grid held by crossover tweezers. The TEM grids chosen for (S)TEM work were holey-C (Agar 163-8) and lacey-C films (Agar 166-3) supported by Cu grids. Most regions studied here were over the holes on the support meaning that interference caused by the amorphous C background was minimised thus improving the possible resolution.

Despite the aged specimens originating from the dirty environment of a car exhaust there were few contamination issues. Only prolonged exposure to convergent probes (such as STEM and NBD) resulted in detrimental deposition or agglomeration of hydrocarbon contamination. This suggests that organic materials were either washed off by the ethanol or were stabilised on the support material. Generally, any contamination observed was worse on the C films suggesting that the TEM grids themselves contained surface contaminants which could diffuse.

### 4.3 Bimetallic DOC Characterisation

Figure 4.3 shows HAADF-STEM and TEM images of the fresh and aged Bimetallic DOC. Coverage of nanoparticles on the  $\gamma\text{-Al}_2\text{O}_3$  support is high and is consistent between different regions on the (S)TEM specimens regardless of support structure/shape variations. HAADF-STEM was able to show the smallest nanoparticles and clusters because of the large difference between  $Z$  of the Pt-Pd nanoparticles and light  $\text{Al}_2\text{O}_3$  support. However, HAADF-STEM was unable to resolve the atomic structure of the smallest nanoparticles directly and the support rarely showed any structure. This could be because the nanoparticles may not be sufficiently orientated and the signal received from the support is relatively low compared to the nanoparticles and it contains vacancies.

HRTEM resolved the atomic structure more often than HAADF-STEM in ordered particles, this may be because the image is comprised of diffraction and phase contrast. The support also showed crystal structure most of the time, again because although  $\text{Al}_2\text{O}_3$  may contain vacancies, it still can strongly diffract electrons hence the appearance of lattice fringes. It was virtually impossible to resolve the smallest (and presumably disordered) clusters from the support hence why HRTEM was not used for nanoparticle size analysis.

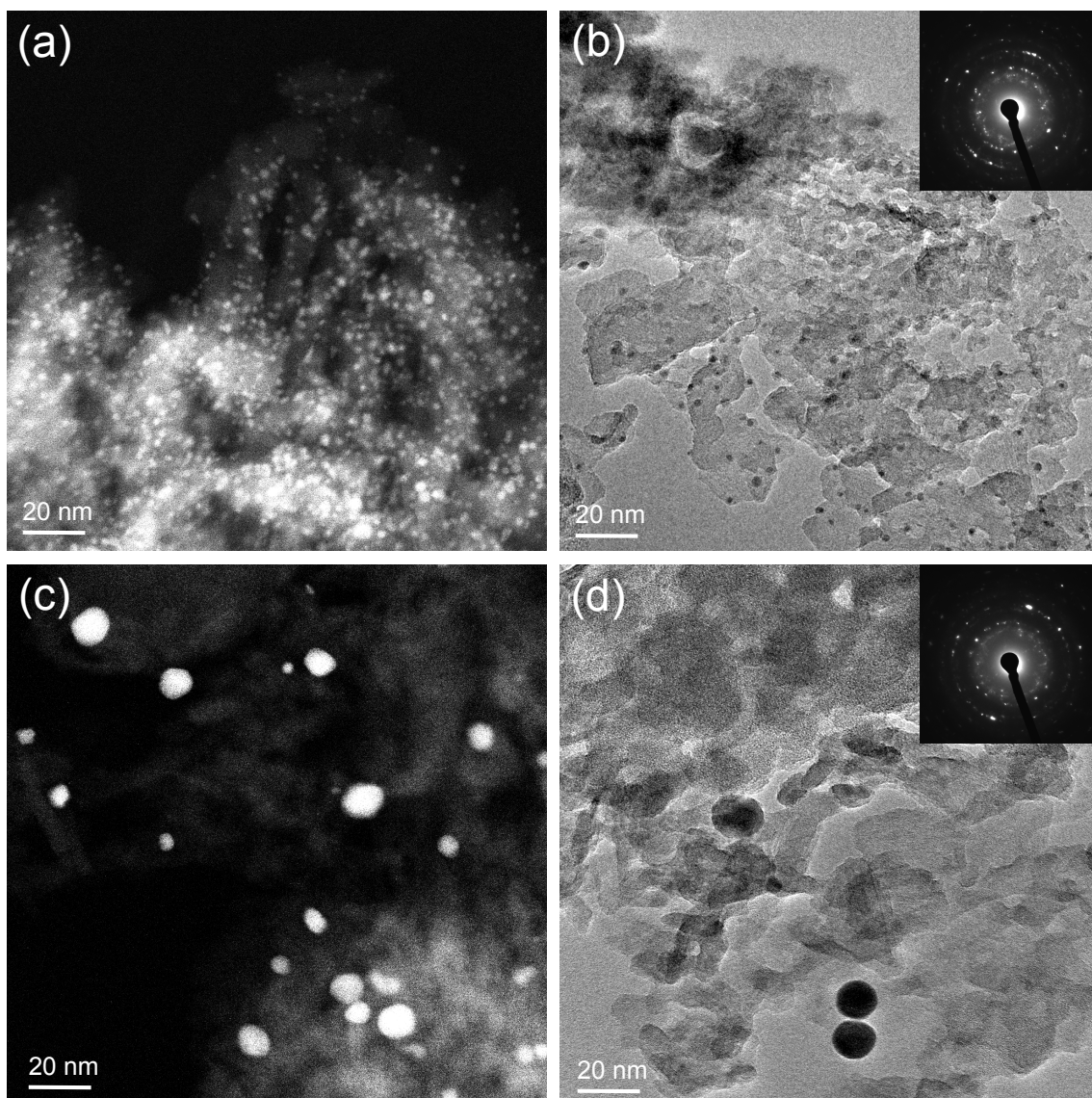


Figure 4.3: HAADF-STEM and TEM images of different areas on the fresh (a-b) and aged (c-d) Bimetallic DOC providing wide views typical for these specimens. The HAADF-STEM images clearly show the morphology of the nanoparticles but the HRTEM images show the morphology and structure of the support. The inset SAD patterns are dominated by the  $\gamma$ - $\text{Al}_2\text{O}_3$   $\{004\}$  and  $\{440\}$  rings



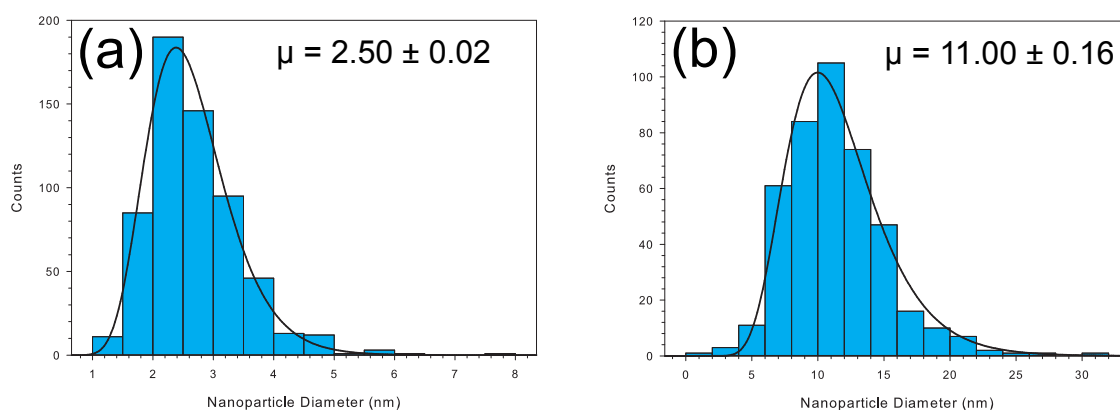


Figure 4.4: Nanoparticle size distributions of the (a) fresh and (b) aged Bimetallic DOC. The black lines are the the log-normal distribution fit

The  $\gamma$ - $\text{Al}_2\text{O}_3$  washcoat was in the form of flake and rod like crystals which are reported shapes for the  $\gamma$  and  $\delta$  phases [151]. SAD analysis of the support showed dominant  $\gamma$ - $\text{Al}_2\text{O}_3$   $\{004\}$  and  $\{440\}$  reflections from most areas as shown in Figure 4.3. XRD data from crushed monolith sections taken by Johnson Matthey suggest the dominant phase is a tetragonal phase,  $\delta$ - $\text{Al}_2\text{O}_3$  [241]. Several groups have reported that  $\gamma$ - $\text{Al}_2\text{O}_3$  can be tetragonally distorted [155] perhaps because of the presence of an alternate  $\gamma$  phase [155].

Nanoparticles sizes were determined by measuring the largest dimension of a individual nanoparticles using HAADF-STEM. It was difficult to distinguish small nanoparticles from the support in TEM hence why HAADF-STEM was used. Nanoparticles that could not be distinguished as a single entity were not counted. A mixture of low and high magnification images were used to provide an adequate sampling (600 nanoparticles) of the nanoparticle sizes. It is possible to use a semi-automatic threshold technique (in ImageJ or Digital Micrograph) that outlines nanoparticles based on their intensities. However, it was found this method was unsuitable because contrasting thick and thin regions of the support in addition to the presence of low and high  $Z$  materials made determining a consistent threshold value across the whole field of view impractical for purpose.

Figure 4.4 shows the resulting nanoparticle size distributions of the fresh and aged Bimetallic DOCs. The distributions have tails towards the smaller sizes, suggestive of a log-normal distribution as shown in Figure 3.13 on page 75. A log-normal curve fit was applied in Sigmaplot. Sigmaplot returned values for the constants in the distribution equation, including the mean nanoparticle diameters. Errors in the mean were determined from the standard error of the returned variables from SigmaPlots log-normal curve fit.

Individual errors of nanoparticles were estimated by the change in  $\Delta f$  required to bring out of focus nanoparticles into focus in the HAADF-STEM images. In a given

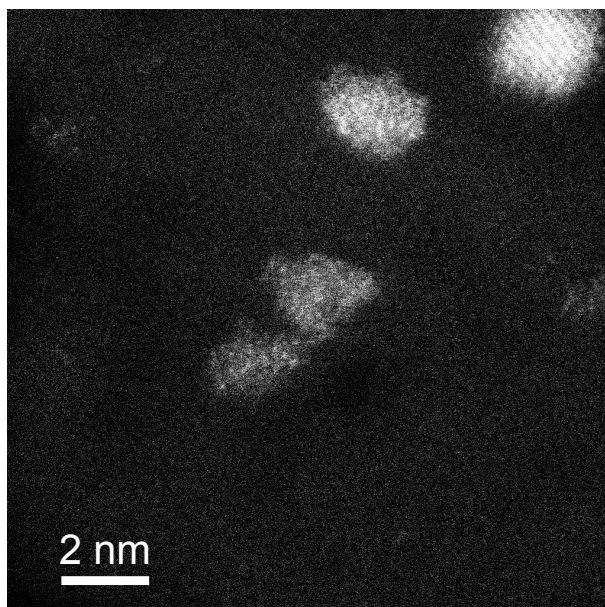


Figure 4.5: High magnification HAADF-STEM image of nanoparticles on the fresh Bimetallic DOC

Table 4.3: Mean Bimetallic DOC nanoparticle diameters determined by HAADF-STEM and XRD

DOC	$\mu$ nm	Error nm
Bimetallic Fresh (STEM)	2.50	0.02
Bimetallic Fresh (XRD)	n/a	n/a
Bimetallic Aged (STEM)	11.00	0.16
Bimetallic Aged (XRD)	7	n/a

HAADF-STEM image, all nanoparticles are not simultaneously in focus because the support structure height varies. Nanoparticles generally appear larger and rounded when out of focus because their shape outline becomes diffuse. A variety of different magnifications were used to provide a good coverage of different nanoparticle sizes. The error in a single measurement was estimated from HAADF-STEM images such as the ones found in Figure 4.3(a) and (c) such that the error in a single nanoparticle diameter measurement is 0.3 nm.

The results from the nanoparticle size distributions are tabulated in Table 4.3 along with complementary XRD data provided by Johnson Matthey [241]. According to the HAADF-STEM data, the mean size of nanoparticles have increased in size from the fresh to aged state by over 400 %. The XRD analysis could not provide a reliable measurement for the fresh catalyst. There is a 3 nm discrepancy between the smaller XRD and larger HAADF-STEM nanoparticle size measurements in the aged sample which is discussed later.



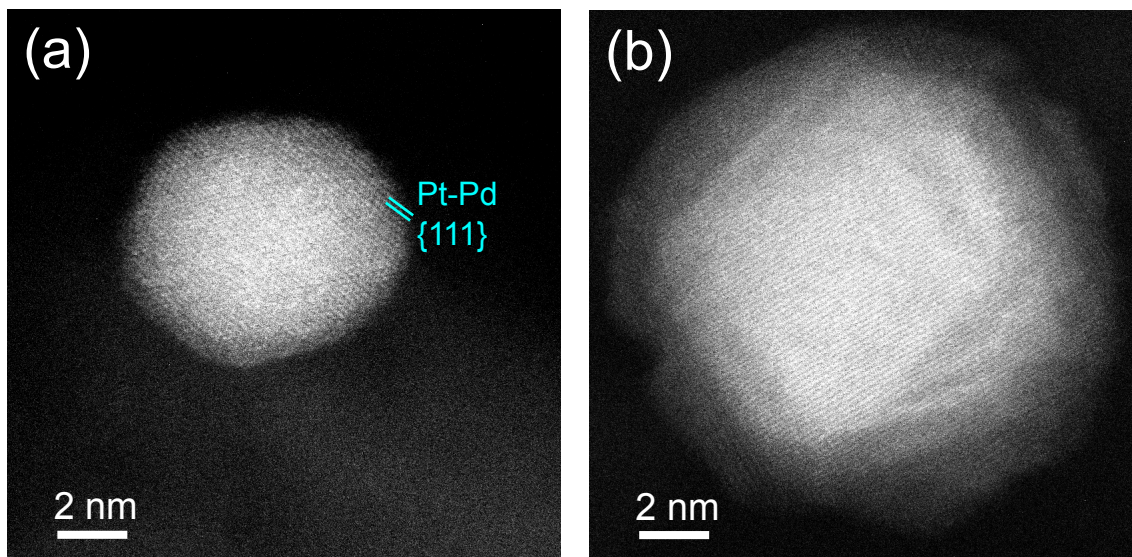


Figure 4.6: High magnification HAADF-STEM images of nanoparticles on the aged Bimetallic DOC showing (a) a rounded nanoparticle and (b) faceted nanoparticle showing signs of core-shell structure

Nanoparticle morphologies were investigated primarily with HAADF-STEM because the high  $Z$  nanoparticles are more easily distinguished from the support compared to HRTEM. Figure 4.5 shows some HAADF-STEM images at high magnification which reveal the presence of small nanoparticles and clusters. Virtually all of the nanoparticles observed with HAADF-STEM are rounded in shape comprising of multiple irregular low symmetry facets. Intensity variations in the clusters in Figure 4.6 suggest that the Pt-Pd alloy is a random mixture of both elements. No core-shell nanoparticles, or nanoparticles with segregated Pt-Pd regions were observed in the fresh Bimetallic DOC.

In contrast, in the aged Bimetallic DOC, nanoparticles display a wider range of morphologies. Many nanoparticles retain their rounded shapes but are larger, as illustrated in Figure 4.6. Many nanoparticles above 20 nm were observed to be faceted along multiple directions with some resembling equilibrium shapes such as truncated octahedra bound by  $\{111\}$  and  $\{200\}$  faces. Such truncated octahedra have been experimentally and theoretically reported in amorphous carbon supported model systems of monometallic Pt and Pd nanoparticles [20, 108] and bimetallic PtPd nanoparticles [307].

HAADF-STEM reveals complex intensity variations in some of the nanoparticles. Figure 4.7 illustrates a HAADF-STEM image at the atomic level of a larger faceted nanoparticle in  $[110]$  zone axis exhibiting intensity variations within its structure. EDX analysis (along the lines in Figure 4.7(a)) from the nanoparticle show compositional variations indicating that the outer layers are very rich in Pd whereas the core is Pt enriched. The boundaries with different contrast indicate distinct compositional regions with the lower

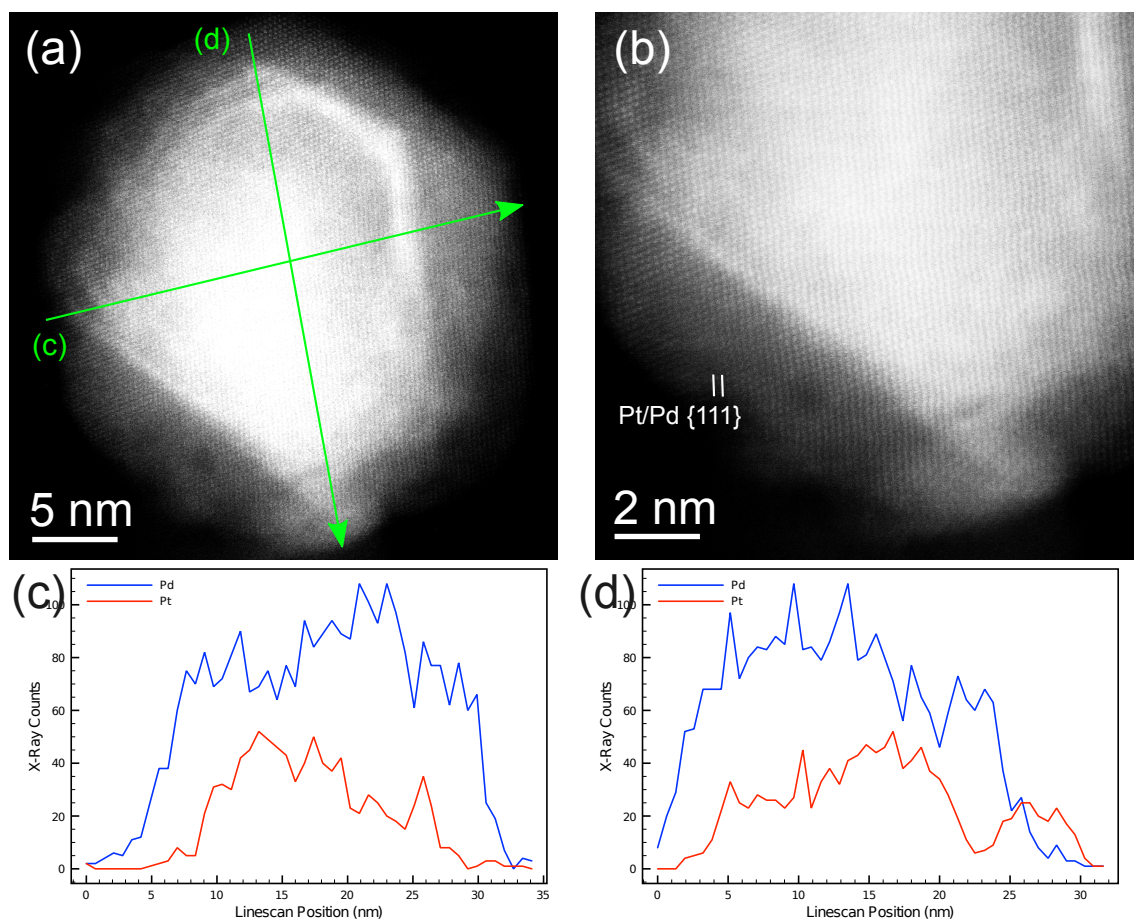


Figure 4.7: A HAADF-STEM image of a large nanoparticle displaying signs of alloy segregation with (a) showing the entire nanoparticle (b) a closeup of the bottom edge and (c) and (d) EDX line spectra corresponding to those labelled in (a). This nanoparticle is Pt-Pd

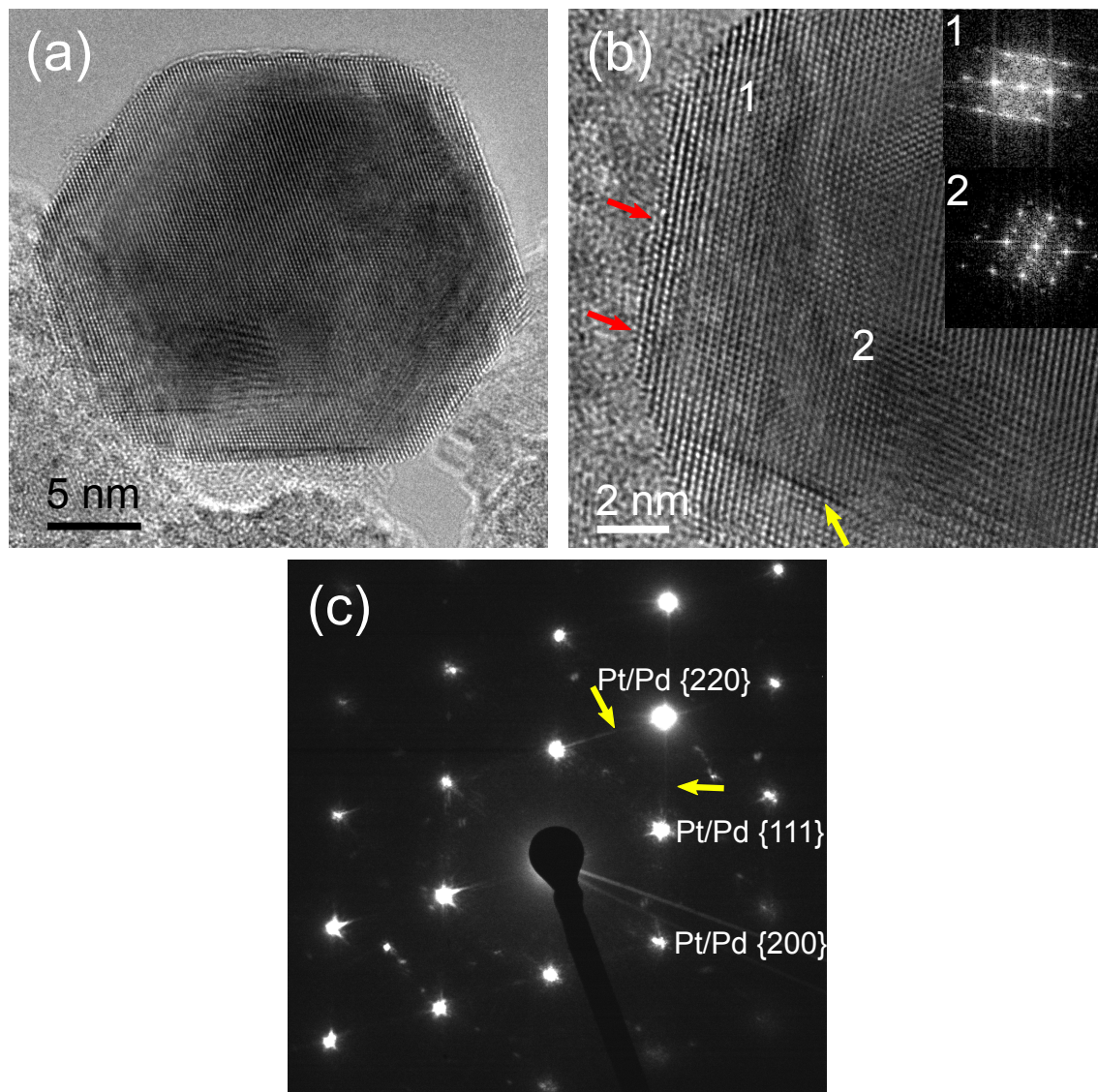


Figure 4.8: HRTEM images (a,b) with inset FFTs in (b) and NBD diffraction pattern (c) of a nanoparticle close to the  $[1\ 1\ 0]$  zone axis with (b) showing contrast from an angled interface. The NBD diffraction pattern is from the whole nanoparticle and reveals streaking caused by the shape effects associated with the angled interface

boundary being a (200) internal boundary between the Pt rich and Pd rich regions as shown at higher magnification in Figure 4.7(b). The line scan in Figure 4.7(c) shows a high concentration of Pt in the lower part of the nanoparticle suggesting that the coalescence of a Pt rich particle has occurred.

AC-HRTEM and NBD of a nanoparticle on the aged DOC shown in Figure 4.8 have revealed defect structures. NBD indicates the nanoparticle is close to a  $\langle 1\ 1\ 0 \rangle$  zone axis. EDX point and line (Figure 4.7) spectra have confirmed that the outer layers are Pd rich and the core is Pt enriched. The streaked reflections shown in FFT 1 are likely caused by the distortion of the Pt spatial frequencies due to the presence of the  $\text{Al}_2\text{O}_3$  support. The additional reflections in the FFT 2 are possibly interference fringes caused the presence of



an angled interface with another crystal. The Moiré fringes can be more clearly seen in the lower magnification image in (a).

Diffuse streaks along  $\langle 111 \rangle$  in the NBD pattern in Figure 4.8(c) can be attributed to shape effects caused by the presence of stacking faults [308], thin tilted interfaces [21] or by the presence of a very thin crystal [14, 21]. It may be possible that a thin sheet/disc shaped PdO crystal has formed on the nanoparticle facet in the region of FFT 2. The contrast may be complicated by thickness effects as well. It can be seen that the contrast near the region labelled 2 is inverted (black atomic columns) with respect to the edge of the crystal (white atomic columns).

Previous observations of Pt-Pd alloys under heat and in oxidative atmospheres [239, 309] imply that in the complex operating conditions of DOCs the segregation of Pd to the surface results in lattice mismatch of about 1 % between Pt and Pd. There are no reports on the formation of stacking faults caused by this mismatch. In other alloys, such as in freshly prepared Au-Pd bimetallic nanoparticles, the presence of stacking faults bound by partial dislocations resulting from the difference in lattice parameter of about 4% between the constituent atomic species has been reported [310].

The nanoparticles observed at the same time as those in Figure 4.7 and 4.8 contained more Pd than Pt. Following these initial observations, using a converged TEM beam, Pt:Pd ratios were plotted against nanoparticle diameter to determine if there was any correlation. The nanoparticle diameters were determined in the same fashion as before and the metal element weights determined in NSS using the standard-less quantitative analysis tool. Figure 4.9 shows the results of this study. There appears to be no link between the amount of Pd and the size of the nanoparticle. It is not known how the DOC was made but it is a bulk scale item and here, using TEM, the nanoscale is reported, so it is possible in some areas more Pt and Pd precursors were mixed producing a non-uniform distribution.

In addition, to investigate if there was any link between core shell size and nanoparticle diameter, using HAADF-STEM images the core was measured along the same line that was used to measure the overall nanoparticle diameter. There is some degree of error here because some cores are not well defined and not all nanoparticles had matching spectra. The result was plotted in Figure 4.10. The graphs show that there is an approximate linear relationship between core and shell size. The  $x$  error in both Figures 4.9 and 4.10 originate from the error in diameter measurement described previously. The  $y$  errors in Figure 4.9 were obtained from the NSS EDX software. The error in  $y$  on Figure 4.10 was estimated from intensity differences taken from a pure Pt nanoparticle and similarly sized core-shell

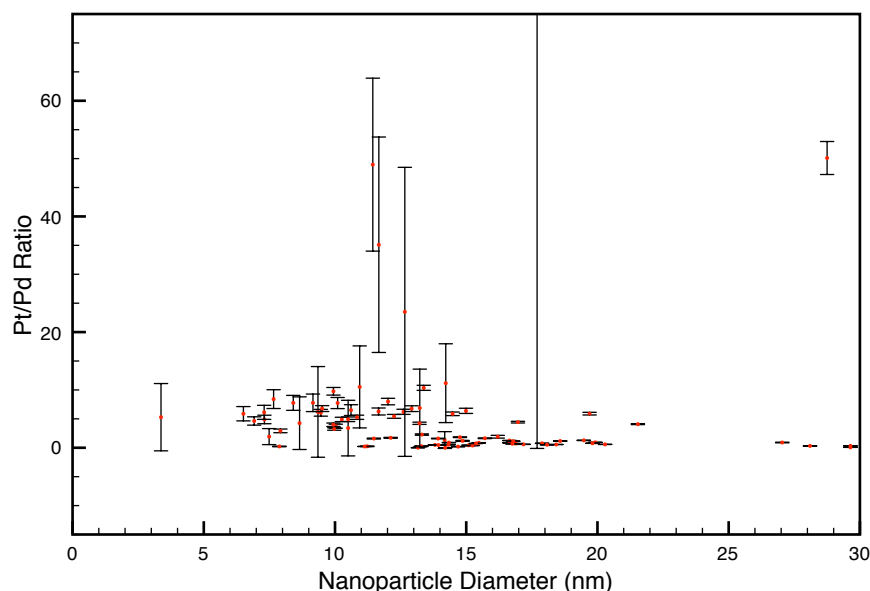


Figure 4.9: Graph showing that there is no relationship between the size of nanoparticles and their relative Pt and Pd content, note that extreme values are cut-off for presentation purposes but their error bars can be seen

bimetallic nanoparticle to distinguish between alloy segregation and thickness effects. The error in this was approximately 1 nm.

Core-shell nanoparticles were observed in a minority of particles (30 %) and almost exclusively in particles above 20 nm. Clear segregation along atomic planes was not observed in most nanoparticles. This is because most nanoparticles were not in an appropriate zone axis. The  $[1\ 1\ 0]$  zone axis has the  $\{1\ 1\ 1\}$  and  $\{2\ 0\ 0\}$  planes perpendicular to the beam which reveals segregation much more clearly than a lower symmetry zone axis such as  $[1\ 0\ 2]$  where the  $\{1\ 1\ 1\}$  and  $\{0\ 0\ 2\}$  are not perpendicular to the beam. Analysis here has suggested that  $\{1\ 1\ 1\}$  and  $\{0\ 0\ 2\}$  are the preferred segregation planes.

## 4.4 Pt Only DOC Characterisation

Figure 4.11 shows some TEM and HAADF-STEM images of the fresh and aged Pt-only DOC. In the fresh version, the  $\text{SiO}_2$  support is comprised mostly of spheres which have amorphous structure. Diffraction patterns from region such as those in Figure 4.11(a) and (b) show only Pt rings. Nanoparticle coverage across different areas of the fresh Pt-Only DOC was inconsistent. Some  $\text{SiO}_2$  spheres were coated with only a few small nanoparticles whereas some were covered by up to 50. The support morphology in the aged version, shown in Figure 4.11(c) and (d), was largely unchanged. Some regions contained soot in

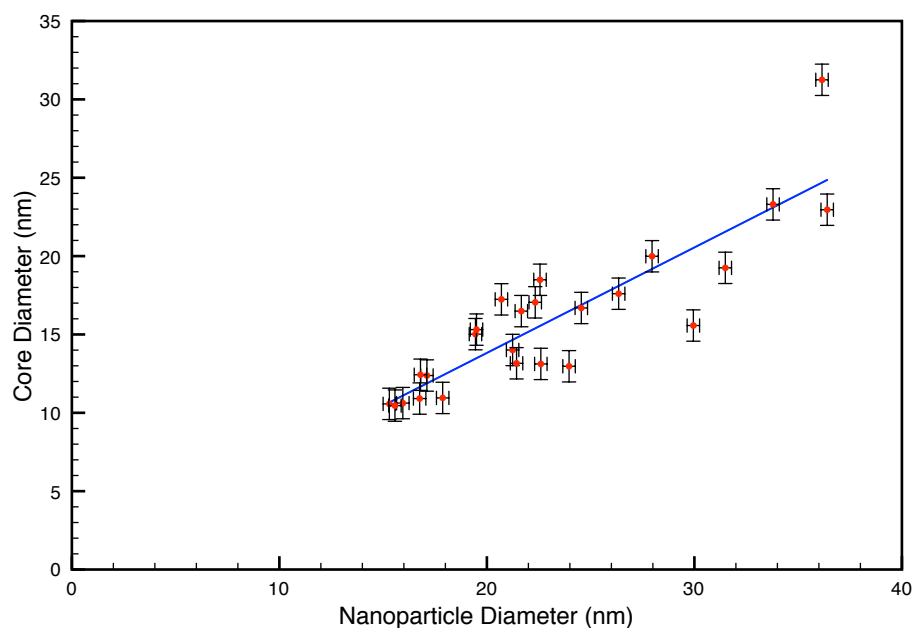


Figure 4.10: Graph showing that there is an approximate linear relation between core size and overall diameter

Table 4.4: Mean Pt Only DOC nanoparticle diameters determined by HAADF-STEM and XRD

DOC	$\mu$ nm	Error nm
Pt Only Fresh (STEM)	3.06	0.03
Pt Only Fresh (XRD)	4	n/a
Pt Only Aged (STEM)	6.60	0.04
Pt Only Aged (XRD)	9	n/a

between the  $\text{SiO}_2$  spheres and sometimes the soot was coated in nanoparticles suggesting that the nanoparticles could be mobile during use. On the aged variant, the nanoparticle coverage is poor with only one or two large Pt nanoparticles per  $\text{SiO}_2$  sphere.

Using the same method as the Bimetallic DOC case, nanoparticle diameters were measured. Figure 4.12 shows the nanoparticle size distributions of the fresh and aged Pt Only DOCs. A log-normal curve fit was used for both because they both have long trailing tails. The values returned for the mean and those determined from XRD are given in Table 4.4. It is interesting that on the fresh variant that there are already nanoparticles larger than 10 nm. XRD analysis of crystal sizes by Johnson Matthey return values of 4 and 9 nm for the fresh and aged Pt-only DOC respectively. The results differ for the aged variant but the XRD analysis is done using a bulk specimen whereas the HAADF-STEM measurements presented here are nanoscale. The discrepancies are discussed later on page 103

In Figure 4.11 it can be seen that the majority of the nanoparticles on the fresh and aged version are spherical or rounded and only seem to differ in size. However, using

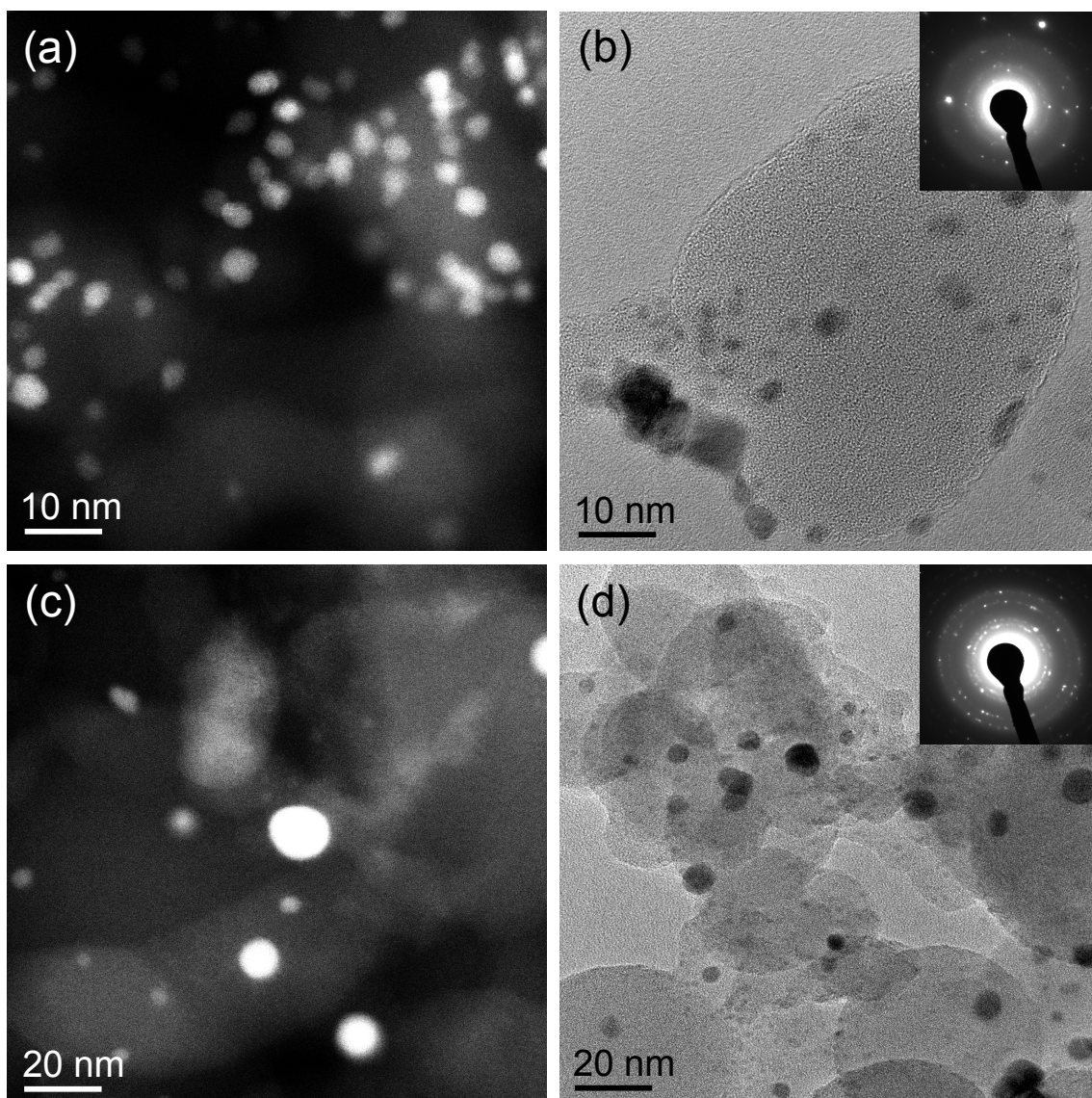


Figure 4.11: (S)TEM and TEM images of the (a),(b) fresh and (c),(d) aged Pt Only DOC providing wide views typical for these specimens. The insets in (b,d) are SAD diffraction patterns which show faint Pt rings

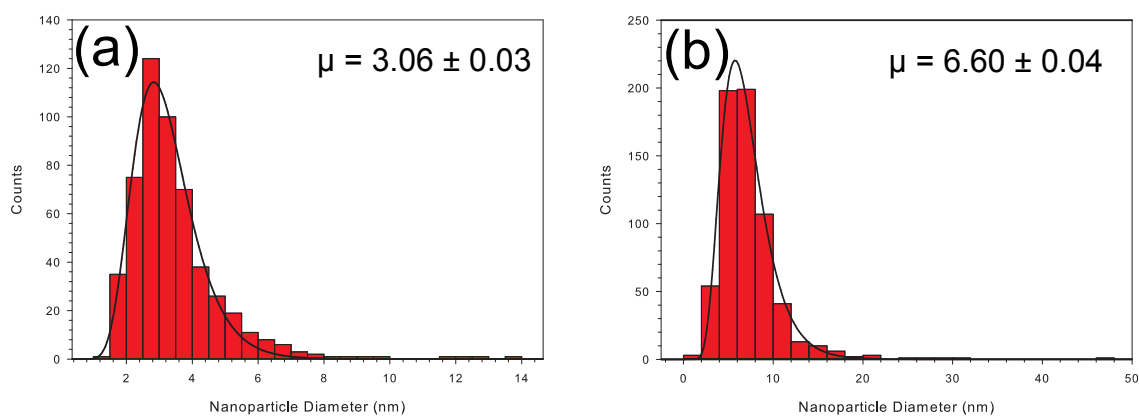


Figure 4.12: Nanoparticle size distribution of the (a) fresh and (b) aged Pt-Only DOC. The black lines are the log-normal distribution fits

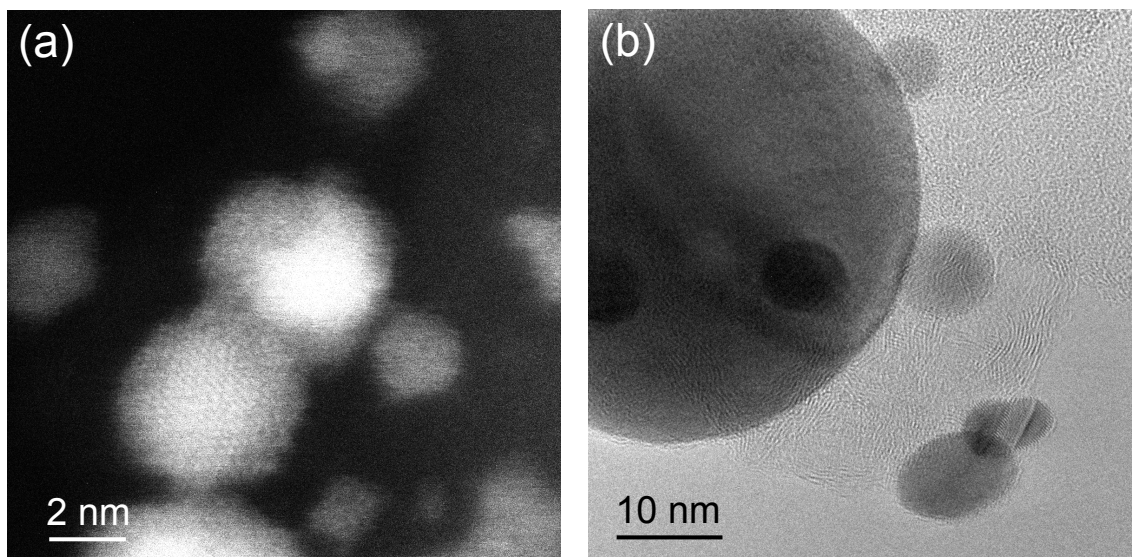


Figure 4.13: Nanoparticle morphologies/structure on the (a) fresh and (b) aged Pt Only DOC. (a) is a HAADF-STEM image and (b) is a HRTEM image. HRTEM was unable to show Pt clusters or very small nanoparticles on thick regions of the  $\text{SiO}_2$  support whereas HAADF-STEM could

HAADF-STEM on the fresh version reveals the presence of small Pt nanoparticles that would be missed in an HRTEM image. Figure 4.13(a) shows an aberration corrected HAADF-STEM image of a cluster of nanoparticles. Note that under the electron beam, the two central nanoparticles had coalesced into one. It can be seen clearly that virtually all of the nanoparticles are rounded but weak intensities in between the nanoparticles may suggest the presence of clusters. HAADF-STEM of the  $\text{SiO}_2$  often resulted in the charging of the specimen, leading to a loss in resolution. Figure 4.13(b) shows a HRTEM image of a group of nanoparticles on the aged version. The large nanoparticle is joined by smaller nanoparticles, some of which contain defects. Out of the many nanoparticles observed, only approximately 1% of the particles were defective and the rest were primarily single crystals. In addition, of the nanoparticles with defects, approximately 50 % were larger than 20 nm, i.e. the biggest sizes.

## 4.5 Discussion of Results

### 4.5.1 Nanoparticle Sizes

The average sizes of the fresh and aged nanocatalysts in the two DOCs reveal significant differences between the fresh and aged systems. The nanoparticles have grown in diameter, by almost 400 % in the bimetallic DOC, but only by 200 % in the Pt-only DOC . The most significant factor contributing to this large difference is the relative loadings of



the two systems (see Table 4.1). In general, it has previously been reported that metal dispersion is better on  $\text{Al}_2\text{O}_3$  than  $\text{SiO}_2$  supports [311]. The Bimetallic DOC has over twice the amount of metal and (S)TEM observations revealed that nanoparticle coverage was constant and dense on the Bimetallic DOC but varied on the Pt-only DOC. In the two systems, the observed higher concentration of nanoparticles below 2 nm in the bimetallic DOC presumably have a larger number of low coordination surface atoms resulting in higher surface energies and are more likely to be unstable and probably more active chemically initially. The removal of low coordination surface atoms to minimise the surface energy and transport of the atoms between particles leads to faceting and then sintering which has been observed in detail by Walsh *et al* with Au-C [312].

Comparing the size distributions in the Pt-only to those in the bimetallic DOC, presented in Figure 4.4 and Figure 4.12, respectively, there is a much broader range of nanoparticle sizes in the former. Both distributions have long tails towards the larger nanoparticles. Datye *et al* have pointed out that no-one so far has a clear explanation to why there is always such a tail in certain nanoparticle catalyst systems after sintering [233].

The loss of low coordination atom sites is likely to result in a loss of activity. The observations of the Bimetallic DOC suggest that the higher metallic content, the morphology of the support and the presence of small nanoparticles contribute to the nanostructural changes and sintering behaviour in contrast to the low-loaded fresh Pt-only variant which has larger nanoparticles. There is a much broader range of nanoparticle sizes in the aged Pt-only DOC. This suggests that the surface is smooth, allowing relatively easy diffusion of nanoparticles across the  $\text{SiO}_2$  spheres in contrast with the jagged surfaces of the  $\text{Al}_2\text{O}_3$  in the bimetallic DOC.

The measurement of nanoparticle size measurements differ depending on which technique was used. On the Pt-only catalyst, XRD returns a larger value than HAADF-STEM whereas the opposite is true on the aged bimetallic DOC. The HAADF-STEM nanoparticle size measurements were made directly using the images by selecting a nanoparticle's largest dimension as described earlier. XRD measures crystal size as opposed to nanoparticle size with the latter potentially containing more than one crystal segment. The Debye-Scherrer equation ((2.8)) was used to ascribe the broadening of the metal peaks to the crystal size of the nanoparticles. In the fresh bimetallic case, the nanoparticles were too small to provide a suitable XRD peak for measurement. In the aged case, as with SAD patterns taken in TEM mode, the intensity within the diffraction pattern is dominated by the support, namely the  $\{004\}$  and  $\{044\}$  peaks from  $\gamma\text{-Al}_2\text{O}_3$  and equivalent reflections in

$\delta$ -Al<sub>2</sub>O<sub>3</sub>. In the Pt-SiO<sub>2</sub> there is significant signal from the thick amorphous support which could broaden the Pt diffraction peaks thus resulting in a larger crystal size measurement. To summarise, the influence of the support is the primary reason for the discrepancy between XRD and HAADF-STEM nanoparticle size measurements with the latter generally being more reliable for these reasons.

### 4.5.2 Segregation

The results observed here in real world commercial systems generally agrees with the current literature on the segregation of Pd and Pt. The majority of the particles observed were Pd rich and only the larger nanoparticles showed the formation of a Pd enriched shell. This agrees with simulations by Barcaro *et al* [237] and experimental work by van den Oetelaar who further reported the segregation of Pd to the surface is enhanced by O environments [239]. The same group suggested that smaller particles with a near 1:1 ratio of Pt:Pd would form alternating patchy regions of the different elements but this was not directly observed in this work [239] perhaps because to be visible it requires the nanoparticle to be in a particular orientation.

Segregation observed here was most striking when the nanoparticles were oriented near the  $[1\ 1\ 0]$  zone axis such as in Figure 4.7. In general, bands of Pt and Pd could be observed principally along the  $\{0\ 0\ 1\}$  and  $\{1\ 1\ 1\}$  planes which correspond to the lowest surface energy surfaces of fcc materials [20, 307]. In smaller nanoparticles, this was not observed possibly because of the differences in overall surface energies of smaller bimetallic nanoparticles [237, 307]. It is possible that PdO can fix the position of Pd atoms in a nanoparticle leading to a separate PdO region as suggested by experimental evidence from Datye and co-workers [242, 250]. Previous studies of PdO suggest that the morphology of PdO particles are generally rounded [240, 242, 252, 313]. It is possible that in some of the images here, some of the rounded surfaces may be composed of PdO.

### 4.5.3 Nanoparticle Morphologies

Nanoparticle morphologies on the aged Pt Only and Bimetallic DOCs were observed to vary. In general, the observed nanoparticles on the Pt Only sample were spherical. Spherical nanoparticles are believed to be more active in the oxidation of CO than polyhedral nanoparticles [169, 170], as they are made up of many low symmetry atomic planes with steps and kinks on the surface with a higher proportion of active sites [174, 236]. For the

oxidation of CO, density functional theory calculations have indicated that the activity of Pt nanoparticles is size dependent although less sensitive than for Au nanoparticles [189].

A majority of the observed nanoparticles were spherical in the aged Bimetallic DOC and did not exhibit core-shell formation but as previously discussed in the section above, it may be because the nanoparticles are insufficiently orientated to see the core-shell structure. However, approximately 30 % were faceted and were larger in size ( $> 20$  nm). Compositional analysis of these larger faceted nanoparticle has shown the segregation of Pd to the surface, and outer surfaces are Pd-rich. In the order of higher to lower activity, Pt  $\{110\}$ ,  $\{111\}$  and  $\{100\}$  faces are believed to be the most catalytically active for the CO oxidation [94] and for Pd the order is reported as  $\{100\}$ ,  $\{111\}$  and  $\{110\}$  [314]. CO is expected to bind more tightly to Pd [315]. We believe that the observed surface segregation of Pd in the larger particles in the aged Bimetallic DOC is beneficial for the CO oxidation activity particularly at higher concentrations of the gas because the CO will eventually block the active sites on the surface. In contrast, Pt can be poisoned by high CO concentrations. XPS data indicate the presence of very small concentrations of P and S in the aged DOC systems, but not in the fresh variants probably due to the S and P content in the diesel fuels. However with considerable reductions of S content in the current diesel fuels the incorporation of Pd in technological bimetallic DOC systems is feasible.

In addition, PdO can form at operating temperatures of DOCs ( $200 - 300$  °C) in the oxidising environment [252]. PdO itself is thought to be inactive in the oxidation of CO and that PdO<sub>x</sub> layers can inhibit O and CO absorption [316]. In general we did not observe significant PdO formation in our studies. This is consistent with the report that PdO can be reduced to Pd metal in CO/NO<sub>x</sub> atmospheres [316] so there may be a balance between the formation of and reduction of PdO in DOC operating conditions.

## 4.6 Conclusion

The nanostructure, chemical composition and surface segregation in fresh and road aged technological diesel oxidation catalysts (DOCS), namely Pt-SiO<sub>2</sub> (Pt-Only DOC) and PtPd-Al<sub>2</sub>O<sub>3</sub> (Bimetallic DOC) systems were studied using aberration corrected (S)TEM along with complementary analysis with EDX, XRD, XPS and infrared chromatography. Comparisons of XRD and HAADF-STEM data of the fresh and aged DOCs have revealed atomic structural changes as a result of sintering. Nanoparticles on the fresh Pt-only catalyst were found to be rounded below 50 nm. Significantly, the direct atomic scale aber-

ration corrected HAADF–STEM observations of the aged bimetallic DOC reveal that a majority of the nanoparticles do not display segregation and have varying amounts of Pt and Pd intermixed. Only a minority (30 %) of nanoparticles have core-shell like structures. The core-shell structures were always observed to have a Pd rich shell and a Pt enriched core. These core-shell nanoparticles were larger than 20 nm and often were faceted by  $\{111\}$  and  $\{200\}$  atomic planes. The essentially spherical morphology of nanoparticles on the Pt-only DOC reveal low symmetry facets with atomic steps which can contribute a higher number of active sites in the oxidation of CO and hydrocarbons based on observations here and previous studies on model systems [222, 303, 317]. These changes in nanostructure have been attributed to metal loading, particle sizes in the fresh catalysts and the type of support. Fundamental insights into the practical catalyst nanostructures and stabilities have important implications for the design of technological DOCs.

## Chapter 5

# Nanostructural Studies of a Pt- $\gamma$ -Al<sub>2</sub>O<sub>3</sub> Catalyst

### 5.1 Introduction

Pt-Al<sub>2</sub>O<sub>3</sub> is a well studied catalyst but there are few aberration corrected studies. With aberration correction, in HRTEM, it is possible to deduce intricacies in the surface structure of the nanoparticles on the fresh catalyst, allowing fresh insights into their catalytic activity. However, many nanoparticles that have been studied in commercial Pt-Al<sub>2</sub>O<sub>3</sub> catalysts often appear to display no ordered structure in HRTEM or HAADF-STEM images but this is likely because they are in a low symmetry zone axis. Here, HRTEM and HAADF-STEM is used to probe the nanostructures of nanoparticles on a fresh Pt-Al<sub>2</sub>O<sub>3</sub> catalyst in addition to heat treated catalysts. Insights into the stability of nanoparticles during sintering are provided by HAADF-STEM. NBD was used to shed light on the presence of epitaxy between the support and nanoparticle and to investigate how certain defects may arise during sintering. The use of NBD has not been used on a specimen such as these having only been used on a model (thin film) Pt-Al<sub>2</sub>O<sub>3</sub> specimen [318].

### 5.2 Specimen Preparation

The catalyst was provided by Johnson Matthey as a grey-black powder. No crushing was necessary because the powder was fine. (S)TEM specimens were prepared by suspending 2 mg of the catalyst powder in ethanol in a small glass bottle. The suspension was placed in an ultrasonic bath for 240 s to break up any large Al<sub>2</sub>O<sub>3</sub> particles. Single or multiple 2.5  $\mu$ l drops were deposited onto a TEM grid held by crossover tweezers. The TEM grids

chosen for (S)TEM work were holey-C (Agar 163-8) films supported by Cu grids.

Thermal treatment of the catalyst powder was kindly carried out in a furnace in the Department of Chemistry at the University of York by Natalie Pridmore. Approximately 20 mg of the provided catalyst powder was placed into an  $\text{Al}_2\text{O}_3$  crucible. Each run was carried out separately with air at atmospheric pressure. Treatments were carried out for 3 h at 250 °C, 500 °C and 750 °C. Treatments carried out for 15 h were at 250 °C and 500 °C. The 750 °C variant at 3 h represents the rapid ageing of the catalyst. The use of high temperature to deliberately promote sintering is common amongst groups that study thermally treated nanoparticle catalysts.

Specimens were found to contaminate due to the formation of additional C layers in (S)TEM. This was particularly troublesome in the NBD studies where the NBD beam acted as a spray, covering regions in thick C layers after a few seconds. Based on trials with empty C films, the contamination observed arises both from the C film and from hydrocarbons and other chemicals contained in the powder suspension. The contamination was generally worse in the heat treated specimens, particularly the 750 °C variant. All (S)TEM specimens were plasma cleaned in air for 30 s at 10 % power. It is possible that plasma cleaning in air may have introduced some slight rounding to the nanoparticles due to the presence of adsorbed  $\text{O}_2$  but there was no evidence to suggest that the plasma cleaning changed the nanoparticles morphologies at the low power levels used. Despite the contamination, it was still possible to image at high magnification in HAADF-STEM after beam showering. Beam showering is described in chapter 6 on page 133. The areas suspended over a hole, away from the C film were found to be relatively contamination free relative to the C film.

### 5.3 Fresh Catalyst

TEM and HAADF-STEM observations of the fresh catalyst show that the nanoparticle morphologies are varied. Generally speaking, the nanoparticles have at least one well defined facet, usually the  $\{111\}$  or  $\{002\}$  faces. Observations suggest that no particular shape dominates but this may be because of the random orientation of the supported nanoparticles with respect to the electron beam direction. The observation of facets suggests the presence of standard Wulff structures such as cubeoctahedra that have interfaced with the support to form structures described by the Winterbottom model [20, 88, 108]. Most nanoparticles were measured to be larger than 2 nm in at least one dimension as

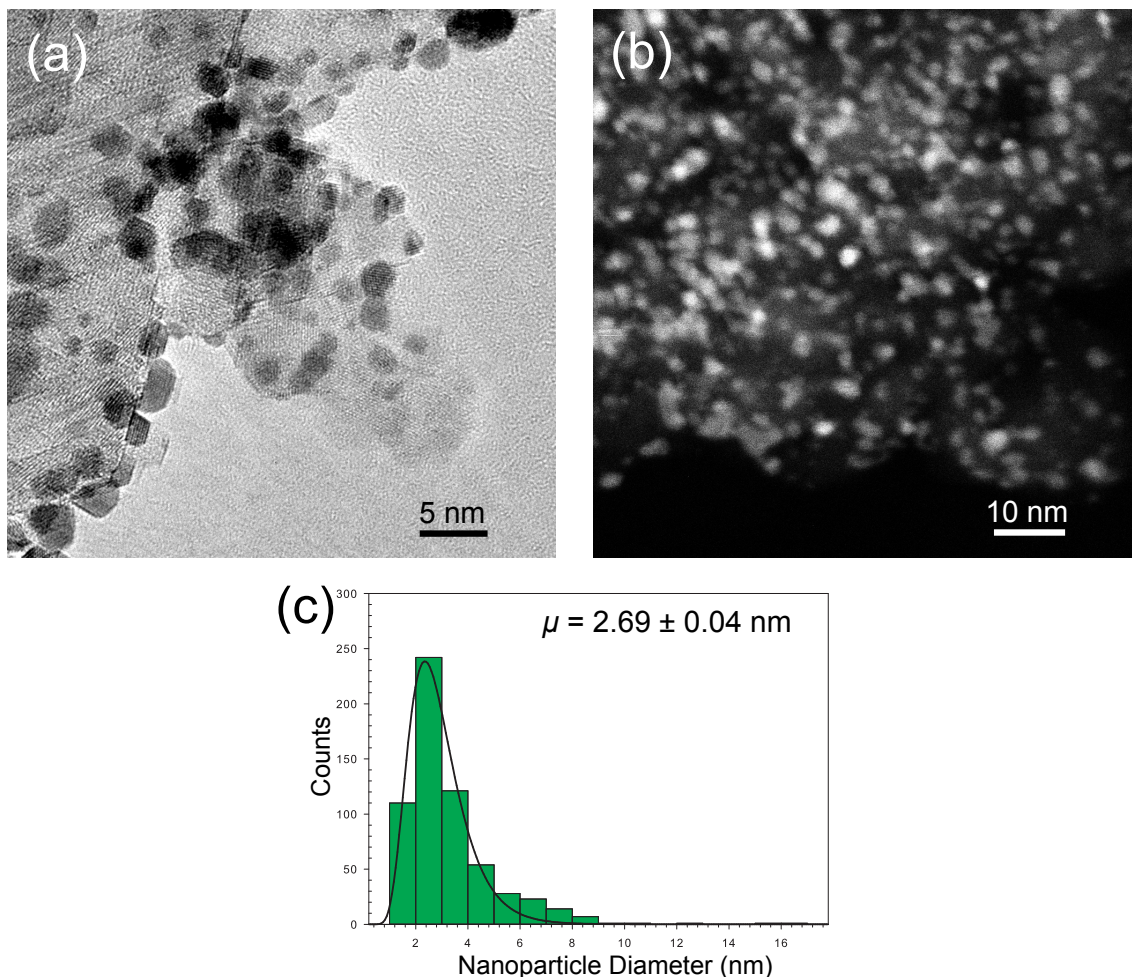


Figure 5.1: TEM image (a) and HAADF- STEM image (b) of the fresh Pt-Al<sub>2</sub>O<sub>3</sub> catalyst. The nanoparticle size distribution is shown in (c)

shown in Figure 5.1. The majority of nanoparticles were observed to be faceted on at least one side. The morphology of the nanoparticles in these catalysts are different compared to the Bimetallic DOC nanoparticles presented in chapter 4. This is probably because of the differences in manufacture which may have involved the use of different Pt precursor salts such as Pt(NH<sub>3</sub>)<sub>4</sub>Cl<sub>3</sub> [97, 319] which can lead to a wide variety of nanoparticle shapes [97, 320].

Structures with size around 1 nm were generally observed to be rounded but rarely showed signs of structural order. However, given the poor crystallinity of the support and the random orientation of larger particles, it is likely that the smallest nanoparticles are also randomly orientated. From the HAADF-STEM and HRTEM images alone it is not possible to deduce if they have structure or not but several groups believe that the structure and stability of small clusters are heavily influenced by the presence of surface defects on the support surface [91, 142]. Through development in (S)TEM diffraction techniques, it may be possible to elucidate the support structure at the nanoscale.

Figure 5.1(a) shows a TEM image that demonstrates the diverse range of nanoparticle morphologies present on the fresh catalyst. The regions of the support with large facets were generally coated with faceted nanoparticles with flat interfaces between the nanoparticle and support which would result in expected Winterbottom/Wulff shapes. The  $\text{Al}_2\text{O}_3$  on the left hand side of Figure 5.1(a) has been indexed as  $\gamma\text{-Al}_2\text{O}_3$ , about  $6^\circ$  out of the  $[101]$  zone axis with the dominant set of reflections being  $\{22\bar{2}\}$ . This means that the nanoparticles in the lower left region of the TEM image are supported on the  $\gamma\text{-Al}_2\text{O}_3$   $\{131\}$  face. The HAADF-STEM image shows an example of a typical region containing nanoparticles. Taking EDX spectra from entire  $\text{Al}_2\text{O}_3$  crystals revealed that the Pt by atomic weight was between 0.5 % and 10 % indicating that the metal is unevenly dispersed through the catalyst and this is considered typical of real world materials.

HAADF-STEM was carried out at various magnifications to provide a worthy sampling of the different nanoparticle sizes. The large area view seen in Figure 5.1(b) appears to be out of focus because the edges of some of the nanoparticles are blurry. This can be explained in terms of variations in height of the support structure which are beyond the microscope's depth of focus. This can lead to the assumption that the nanoparticles are rounded but multiple through focus images were taken to ensure as many nanoparticles as possible were resolved in-focus. The nanoparticle diameters were determined as previously described in chapter 4 (page 94). The error of the mean indicated in Figure 5.1(c) (and later in Figures 5.6 and 5.8) are small and are beyond the microscope's resolution limit. This is due to the large number of samples taken. Individual errors in each measurement were estimated in similar fashion as described in chapter 4 on page 95. Using a typical HAADF-STEM image shown in Figure 5.1(b), it was found that changes in  $\Delta f$  as large as 25 nm were required to bring some nanoparticles into focus. The error in the size of nanoparticles is then 0.3 nm using the methodology described in chapter 4.

Large agglomerates of nanoparticles were observed in the catalysts here but these were not counted because they did not represent the true size of the individual nanoparticles. HAADF-STEM at higher magnification revealed the presence of cluster features on the  $\text{Al}_2\text{O}_3$  surfaces but no single atom features were observed. Generally, nanoparticle catalysts are calcined or heated after the nanoparticles are loaded onto the support [145]. It is possible that any single atoms present during the synthesis have migrated and either formed clusters or have been absorbed into larger structures.

The TEM image in Figure 5.1 was taken using a conventional TEM. The nanoparticles appear much darker and the support shows greater contrast compared to images taken with



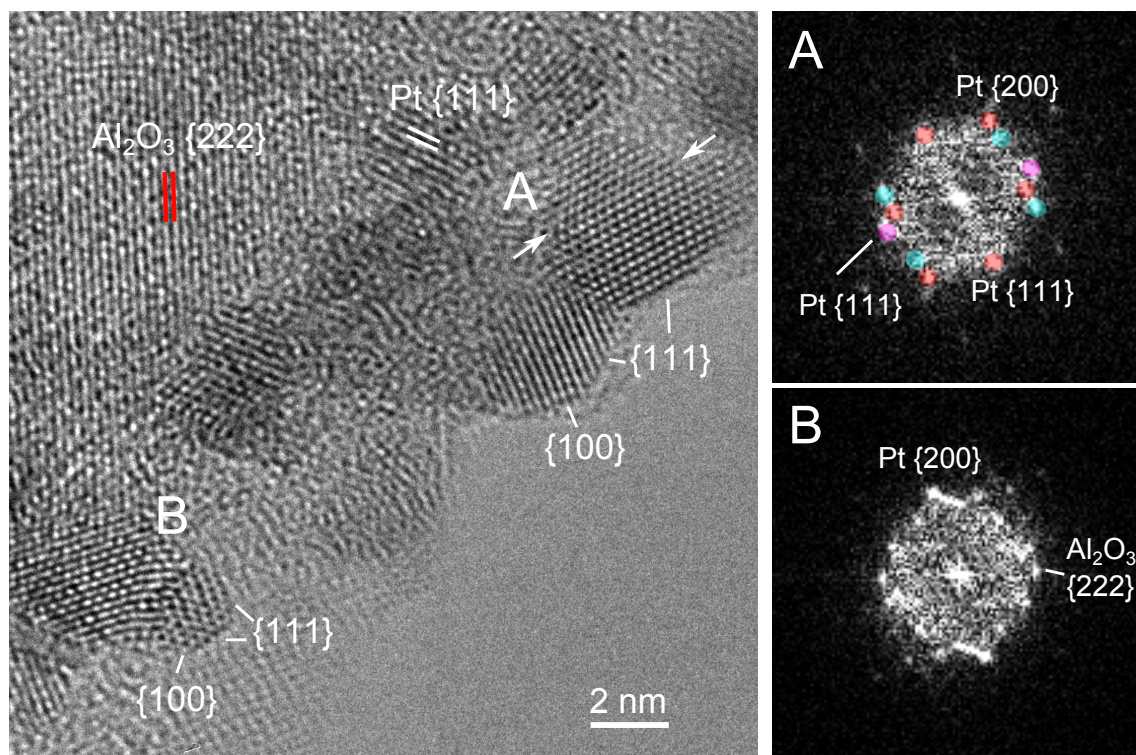


Figure 5.2: HRTEM image showing some of the typical morphologies of nanoparticles on the fresh catalyst, the FFTs correspond to the labeled areas A and B with A showing the presence of a poly-crystal nanoparticle. The arrows around nanoparticle A show the presence of a grain boundary

AC-HRTEM. This is because the CTF (Figure 2.4 on page 30) is flatter on the AC machine but it extends to higher spatial frequencies whereas the conventional TEM will have a sudden sharp peak and trough at lower spatial frequencies resulting in greater contrast in the image. The resolution limits of the conventional TEM however prevent the accurate analysis of their surface structure including the identification of low coordination atoms which are believed to be beneficial for CO oxidation. For detailed nano-structural studies, AC-HRTEM was needed.

Figure 5.2 shows a typical HRTEM image of a 25 nm wide region of the fresh catalyst. Approximately 95 % of the nanoparticles displaying lattice information were single crystals, the rest contained defects such as dislocations, stacking faults or grain boundaries. Twinned Pt nanoparticles are relatively rare compared to Au nanoparticles of similar size. The presence of such defects in nanoparticles can lead to the introduction of strain [9] and the presence of additional low coordination atoms [9,312]. From the HRTEM image and its FFT in Figure 5.2 it would seem that nanoparticle A is twinned. Most of its surfaces are  $\{111\}$  faces but the region interfacing with the support contains many steps. The angle between the grain boundary (arrowed in the image) and the lower part of the crystal is  $70^\circ$  as expected for an fcc twin but the upper region is at an angle of  $64^\circ$  suggesting that

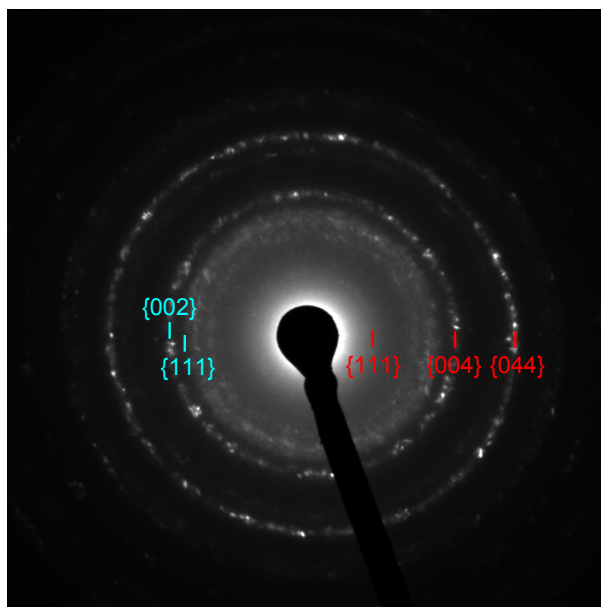


Figure 5.3: Typical SAD pattern from a 100 nm diameter region of the fresh Pt-Al<sub>2</sub>O<sub>3</sub> catalyst showing poorly defined Al<sub>2</sub>O<sub>3</sub> rings. The RHS labels indicate the positions of some Al<sub>2</sub>O<sub>3</sub> (assuming  $\gamma$  phase) reflections. The LHS labels indicate the locations of the expected Pt reflections.

this grain boundary is not a twin but rather an angled interface. The contrast in the upper region is different to the bottom one. In the bottom grain, the atomic columns are mostly white but on its right side, the columns are dark. The upper region appears to be a mixture of black and white columns suggesting that the nanoparticle is not uniformly thick and the crystals either side of the grain boundary are not orientated exactly in the same zone axis. It is possible that this grain boundary has developed during the nanoparticle crystal growth.

The FFT of nanoparticle B indicates that it is strained. It resembles the coalescence of a large nanoparticle with a smaller one. The effect of phase reversal can be seen clearly here, with the atomic columns of the smaller nanoparticle appearing black whereas the ones in the larger one are predominately white. The FFT shows that the  $\{200\}$  reflection is stretched which corresponds to the bending of the lattice at the point where the two nanoparticles join. The coalescence of nanoparticles during the initial synthesis of the catalyst will greatly reduce the available surface area of the nanoparticles and ultimately lead towards a loss of low-coordination atoms which are required for reaction.

The fresh Pt-Al<sub>2</sub>O<sub>3</sub> catalyst contains flake like crystals of Al<sub>2</sub>O<sub>3</sub> which vary in size and shape but they are generally faceted. Figure 5.3 shows a typical SAD pattern from a 100 nm area of the support. The bright rings are the  $\{004\}$  and  $\{044\}$  type reflections originating from  $\gamma$ -Al<sub>2</sub>O<sub>3</sub>. Depending on the phase of any one crystal, the indexing of the

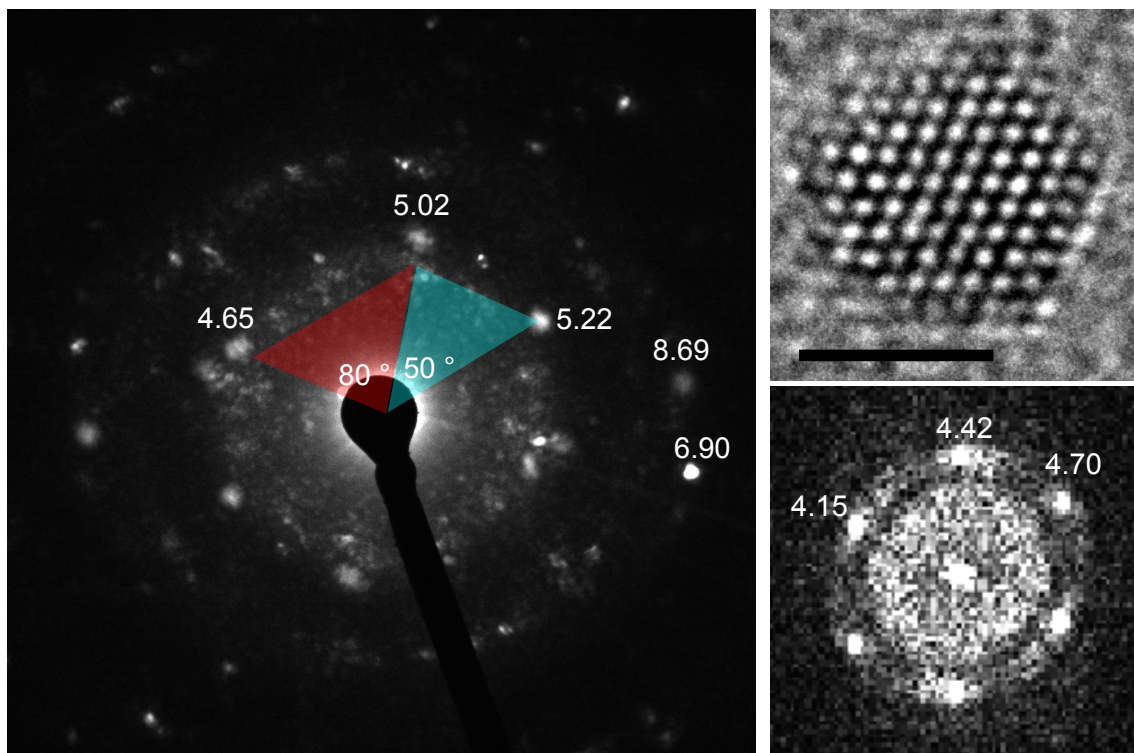


Figure 5.4: NBD pattern of a distorted nanoparticle on poor crystalline support region with HRTEM image and FFT. Scale bar is 2 nm. Coloured region shows approximate unit cell. The FFT resembles  $[1\ 1\ 0]$  but the angles or the spatial frequencies do not match Pt suggesting that the lattice has been distorted. Measurements are in  $\text{nm}^{-1}$  in the diffraction pattern and FFT

two reflections is different but in general, the  $\theta$ ,  $\delta$  and  $\eta$  phase share the same high intensity reflections corresponding to the cation positions [157]. The  $\text{Al}_2\text{O}_3$  crystal in Figure 5.3 has low Pt coverage, so the Pt  $\{1\ 1\ 1\}$  reflections are not well defined in this diffraction pattern. TEM observations of the support here are similar to those by Tilley and Eggleton [321] who reported that the support displayed poor crystallinity. The SAD diffraction pattern reported in [321] by Tilley and Eggleton appears to be virtually identical to  $\gamma$  phase SAD patterns but Tilley and Eggleton describe the presence of the  $\eta$  phase. The SAD pattern shows that the nanostructure of individual nanoparticles cannot be accurately determined from such diffraction patterns hence the requirement for nano-area diffraction techniques. SAD of nanoparticle catalysts, which typically encompass  $> 50$  nm diameter regions, usually generate ring patterns so it is difficult to isolate one nanoparticle, even with dark-field TEM, if the nanoparticle is small and has poor long range order. Furthermore, especially on large support crystals, the dominant reflections in such diffraction patterns tend to originate from the support. NBD allows nanoparticle by nanoparticle (1 – 20 nm depending on microscope settings) structural analysis although it also includes diffraction from the support.

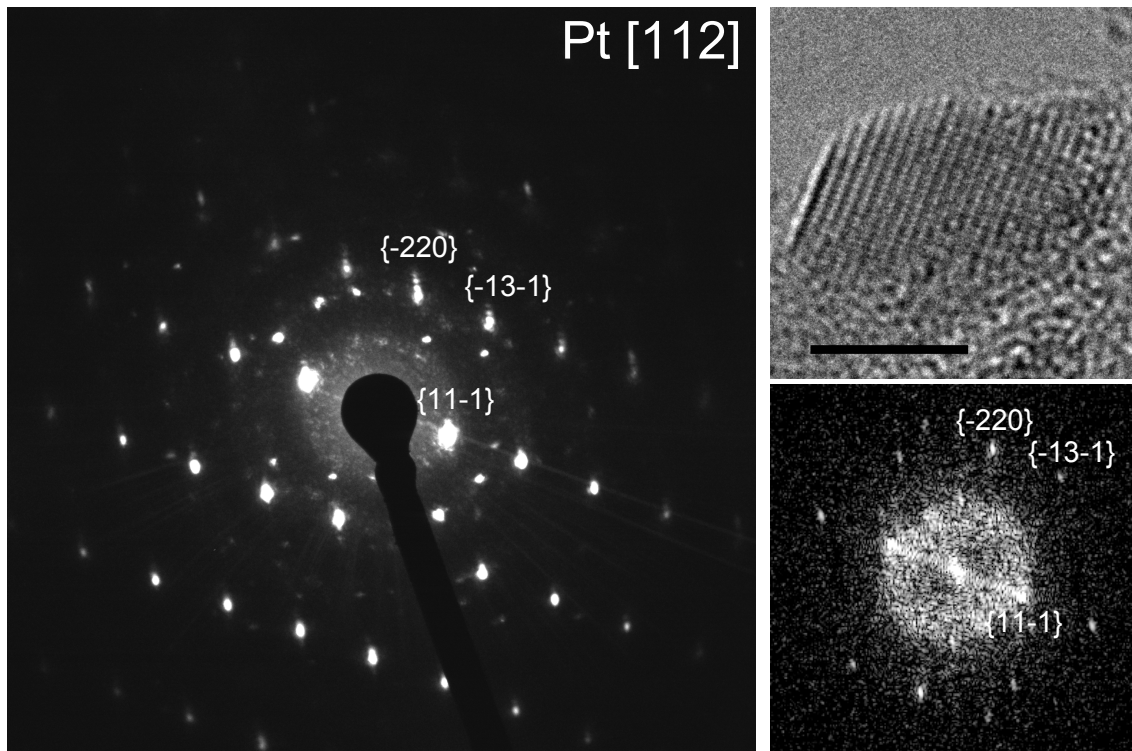


Figure 5.5: NBD pattern of a small nanoparticle displaying diffraction phenomena not observed in the FFT, namely the appearance of additional reflections around the upper row of Pt reflections. Scale bar is 2 nm

Figure 5.4(a) shows an NBD pattern of a 2.5 nm nanoparticle on an amorphous region of  $\text{Al}_2\text{O}_3$ . The nanoparticle appears to have no definite shape but it has many steps and kinks at its surface. The FFT and the diffraction pattern show that the spatial frequencies for this nanoparticle are approximately  $\pm 10\%$  of their expected values for Pt in  $[1\ 1\ 0]$ . It cannot be in  $[1\ 1\ 1]$  because the angles are not  $60^\circ$ . The lattice of the nanoparticle is sufficiently distorted that it is not fcc. The NBD pattern implies that the support is weakly crystalline with some stronger reflections approximately parallel to the atomic planes of the nanoparticle which suggests that the region of the support in contact with the nanoparticle may display different order compared to the surrounding support structure. Strain induced by this could change the catalytic properties of the nanoparticle [184, 322]. The FFT shows different spatial frequencies to those in the diffraction pattern which has been calibrated (see page 48) but they are all approximately the same difference out (about  $0.5 - 0.6\text{ nm}^{-1}$ ) suggesting that the image may require calibration. However, it is possible that the distorted structure of the small Pt nanoparticle could lead to ambiguous spatial frequencies in the FFT as Biskupek *et al* have suggested [33].

Figure 5.5 shows a HRTEM image of a nanoparticle located at the edge of an  $\text{Al}_2\text{O}_3$  crystal. The NBD pattern shows Pt in the  $[1\ 1\ 2]$  zone axis. What is striking about this diffraction pattern is the additional features on the upper  $\{1\ 1\ 3\}$  and  $\{2\ 2\ 0\}$  reflections.



The additional reflects appear more clearly in the upper reflections but it can be seen that all of the reflections in the diffraction pattern are streaked along the same direction. Van Dyck [308] has shown using optical masks that additional reflections, similar in appearance to those reported here, can be produced by linear defects or grain boundaries in an array of spots provided the array is sufficiently small. The analogy is made that a small crystal containing a translation, such as a stacking fault, will display similar characteristics [308]. Here, the image shown in Figure 5.5 does not show such a translation in the nanoparticle structure however, so the origin of the features observed must be because of another phenomenon.

Shevchenko *et al* [16] have shown theoretically that sufficiently small nanoparticles will cause fine structure to appear in the reflections of small nanoparticles. In comparison to their example for a cube, the additional reflections here would suggest that the nanoparticle is wedge shaped because the reflections extend in the  $[\bar{3} 1 1]$  direction.

An additional feature in the diffraction pattern in Figure 5.5 is a faint streak connecting the two  $\{1 1 1\}$  reflections. The same streak appears in the FFT. The origin of this streak is the sudden dark contrast seen at the left hand side of the nanoparticle in the HRTEM image. This type of contrast is believed to be caused by the Al termination of the support structure which in this image, suggests that the  $\text{Al}_2\text{O}_3$  may have formed a thin epitaxial layer on the nanoparticle's side.

## 5.4 Catalysts Treated in air for 3 h

Figure 5.6 shows the nanoparticle size distributions for the catalysts aged for 3 h in air at 250 °C, 500 °C and 750 °C. In all cases, a log-normal fit was applied to each distribution. The mean was extracted from the resulting log-normal distribution and its error was given as a standard error in Sigmaplot. The images and the histograms imply that the majority of particles remain unchanged. The tail in the 500 °C and 750 °C are much larger than the 250 °C variant which itself is very similar to the fresh distribution. The 750 °C variant contains a wide range of nanoparticle sizes, some larger than 50 nm. The sudden increase in the range of nanoparticle sizes clearly indicates that the temperature of 750 °C is an unsuitable temperature for using Pt- $\text{Al}_2\text{O}_3$  type catalyst with high metal loading in a oxidative environment.

The nanoparticle size distributions for the 250 °C and 500 °C are contradictory to what has been observed by other groups (see for example [233]). The histograms and log-

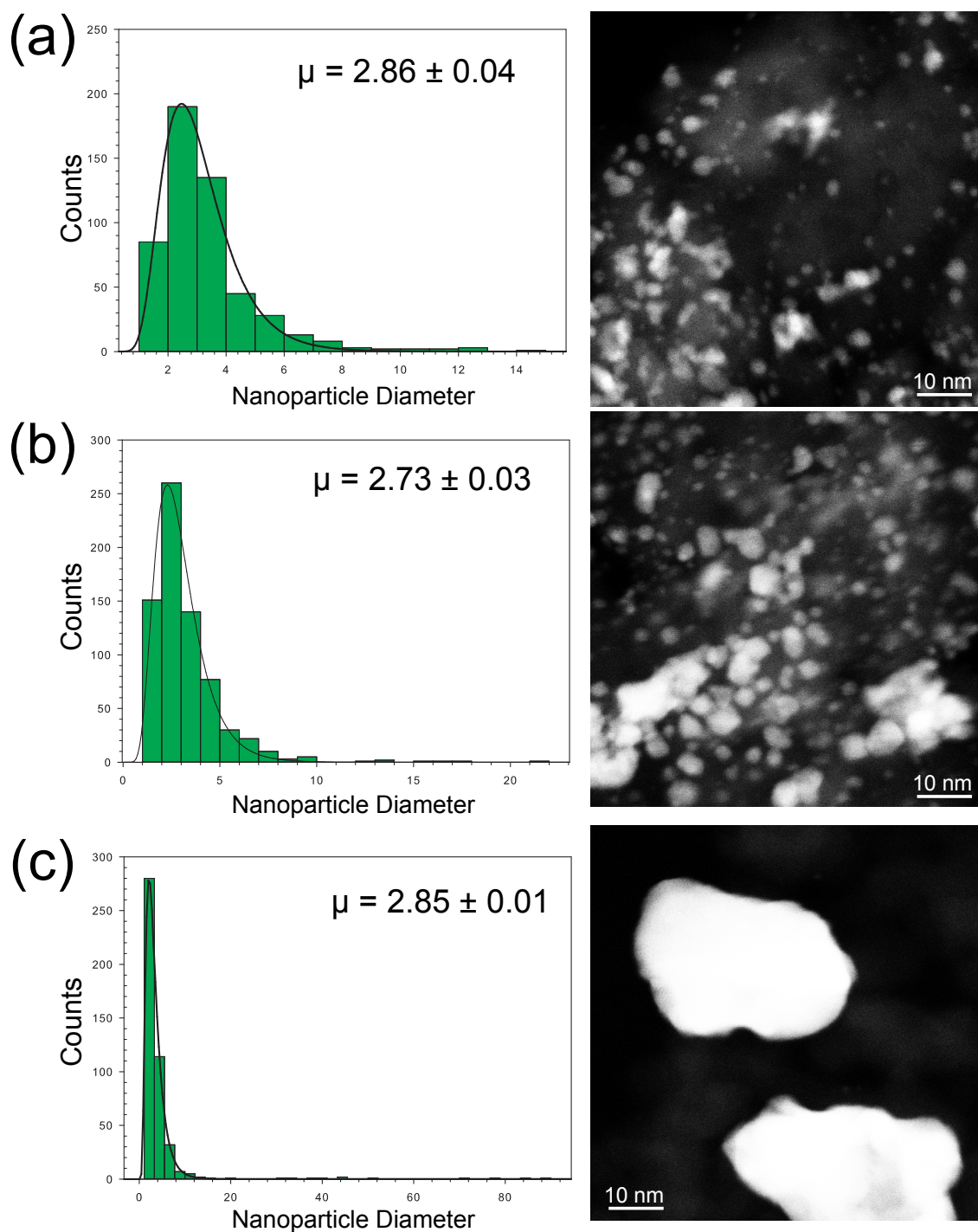


Figure 5.6: Nanoparticle size distributions and example HAADF-STEM images of the catalysts treated in air for 3 h at (a) 250 °C, (b) 500 °C and (c) 750 °C. Note that, although the image in (c) shows large nanoparticles the vast majority of nanoparticles counted were similar in size to those shown in (a) and (b)

normal distribution fits here imply that the majority of nanoparticles have decreased in size as indicated in Figure 5.6. This could imply that Ostwald ripening has occurred resulting in the smaller nanoparticles shrinking at the expense of the growing larger nanoparticles, causing the distribution's tail to tend towards even larger values compared to the fresh catalyst. Simonsen *et al* [203] reported that Ostwald ripening had taken place on a Pt-SiO<sub>2</sub> model catalyst at a pressure of 10 mbar at 650 °C which is  $1/_{100}$  atmospheric pressure.

HAADF-STEM and HRTEM of the catalysts treated at 250 °C and 500 °C revealed no major differences in terms of nanostructure compared to the fresh catalyst. Figure 5.6(a) and (b) show examples of HAADF-STEM images taken from these catalysts. Nanoparticles at the edges however, which are more clearly resolved, did show some slight rounding of their edges suggesting the presence of adsorbed O<sub>2</sub> on the surface which has lead to a change in surface energy. On the 500 °C variant, a minority of particles had appeared to have formed a neck which is a sign of coalescence.

The nanostructures in the catalyst treated at 750 °C shows considerable evidence of sintering in many areas. Nanoparticles larger than 20 nm such as those shown in Figure 5.6(c) were observed which did not exist in the fresh catalyst. The morphology of the nanoparticles was varied and there were fewer nanoparticles/clusters below 2 nm than on the fresh catalyst suggesting that these clusters have been re-dispersed because of particle migration. However, a large number of nanoparticles similar in size to the fresh catalyst still remained hence the log-normal distribution shown in Figure 5.6(c). Large faceted nanoparticles were generally observed in relative isolation compared to rounded ones. This is suggestive that once sintering has largely stopped due to lack of metal, the nanoparticle will aim to loose its free energy by forming a Wulff shape. In regions of high metal content, the reshaping of the nanoparticle will be hindered by continuous coalescence and ripening, leading to irregular surfaces. The irregular surfaces could be more beneficial for the oxidation of CO because of the presence of low co-ordination surface atom sites at steps and kinks at the surface.

Unlike the smaller ones, approximately 30 % of structures larger than 20 nm were observed to contain defects. The high temperature, which is likely to cause rapid Ostwald ripening and coalescence, will cause the nanoparticles to align, form necks and coalesce. It is believed that for two nanoparticles to form a neck they must be in similar orientations [213]. In such circumstances, the strain induced by the coalescence of two nanoparticles with different orientations is likely to result in the formation of defects.

Figure 5.7 shows a HRTEM image (with dark field TEM image inset) and correspond-

ing nano-area diffraction patterns taken from different areas of the nanoparticle. The nano-area patterns were taken with a converged TEM beam using the smallest condenser aperture. The specimen was found to contaminate rapidly so the switch to NBD mode was avoided. The resulting diffraction patterns with a beam diameter of approximately 2 nm have a slightly larger convergence angle than the NBD patterns taken in Figures 5.4 and 5.5 but they can still be interpreted like a normal SAD pattern.

The nanoparticle shown in Figure 5.7 is not a single crystal. It is approximately 40 nm wide. The regions A and C are at the opposite sides of the nanoparticle and differ in orientation to each other. The contrast observed across the central region (region B) implies that there is a sudden thickness change around this region suggesting that the crystal is a complex 3D shape. The inset in the HRTEM image shows a dark field TEM image taken from the entire crystal. The dark field image shows that the crystal is actually two overlapping nanoparticles each approximately 20 nm in diameter measured at their widest point horizontally. The HRTEM is an image of the top region of these nanoparticles.

The angles in diffraction pattern in A are similar to Pt  $[2\ 1\ 3]$  but the spatial frequencies in the diffraction pattern are too small. Instead, it is more likely a highly distorted Pt  $[1\ 1\ 2]$  diffraction pattern. Diffraction pattern B is an overlap of A and C. Some of the extra reflections seen in B could arise from the double diffraction of A and C. A similar diffraction pattern to B was observed by Elechiguerra *et al* [104] in Ag 100 nm decahedral nanoparticles caused by the overlap of the  $[1\ 1\ 0]$  and  $[1\ 1\ 2]$  zone axis diffraction patterns.

The diffraction pattern corresponding to region C is Pt  $[1\ 1\ 0]$  and it is very close to this zone axis hence the high resolution in this area. An interesting property of these three diffraction patterns is that the  $[\bar{1}\ 1\ \bar{3}]$  direction in region C is approximately aligned with  $[1\ 1\ 1]$  direction in region A suggesting that there is a twist boundary.

The diffraction pattern in B contains faint streaking along  $[1\ 1\ \bar{1}]$  (with respect to C). This suggests that there may be an ordered interfacial region between the two overlapping nanoparticles. A thin interfacial region could generate the streaks or additional periodic reflections in the diffraction pattern [21] because such a region would be thin hence it may have its own shape effects.

The presence of large nanoparticles was not observed in every area. Some regions were observed to be very similar to the fresh catalyst despite the treatment at high temperature. The nature of particle size distributions requires that the nanoparticles be measured from each image, smaller particles will be numerous in the average HAADF-STEM image of



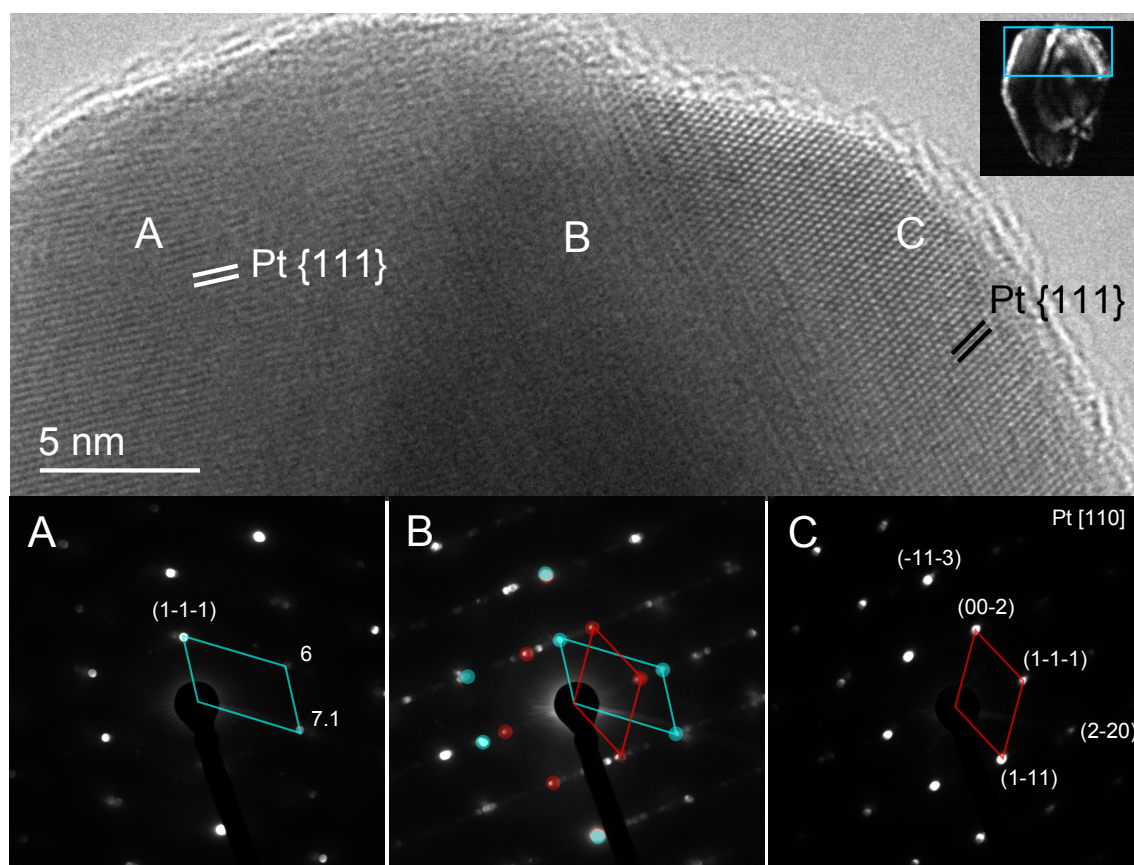


Figure 5.7: Example of a large structure on the catalyst treated for 3 h at 750 °C. Nano-area diffraction reveals the presence of additional diffraction phenomena including double diffraction and diffuse streaks possibly caused by the presence of a tilted grain boundary between two 20 nm nanoparticles which are resolved in the inset dark field TEM image. Measurements are in  $\text{nm}^{-1}$  in diffraction pattern A

the treated Pt-Al<sub>2</sub>O<sub>3</sub> specimen whereas there would only be a few large nanoparticles in one area.

A well known problem with (S)TEM is that the image is a 2D projection of a 3D material [323]. The HAADF-STEM images show in some areas that there is minimal sintering despite the close proximity of the the projected images of the nanoparticles. From the images it is impossible to deduce the height location of the nanoparticles relative to each other but given that considerable changes in  $\Delta f$  are required to bring certain nanoparticles into focus is suggestive that some nanoparticles are located on the other side of the support.

According to Ono [324, 325], for stable surface Pt oxides to form, O<sub>2</sub> needs to dissociate into atomic O. This can only be achieved at high temperatures. Aside from studies on model catalysts [245], there do not appear to be any reports of the presence of stable crystalline Pt oxides related to nanoparticle catalysts where the nanoparticles are below 10 nm. PtO<sub>2</sub> and other phases have been found primarily on very large crystals, namely electrodes, that have large, extended {1 1 1} and {0 0 1} facets [324, 325]. However, it has been reported that XPS measurements have shown that PtO<sub>x</sub> species do exist in Pt nanoparticle contexts [324].

## 5.5 Catalysts Treated in air for 15 h

Figure 5.8 shows the nanoparticle size distributions for the catalysts treated in air for 15 h. Similarly to the catalysts treated for 3 h, the mean values for the nanoparticle diameters do not agree with previous studies on similar Pt-Al<sub>2</sub>O<sub>3</sub> catalysts [233, 303]. The distributions imply that the nanoparticles in the catalyst aged at 500 °C on average have decreased in size relative to those treated at 250 °C. Similar to the case for the 3 h variants, the tail in the log-normal distribution is much longer signifying the presence of large particles that did not exist in the fresh catalyst. The large nanoparticles are likely to arise from the migration and eventual coalescence of nanoparticles as has been suggested by *in-situ* studies on model catalysts [312].

Figure 5.9 shows a HAADF-STEM image that contains very small features which are consistent with individual atoms in addition to larger structures. Atoms have been previously been reported on similar freshly prepared Pt [142] and Pt-Rh [323] Al<sub>2</sub>O<sub>3</sub> catalysts. Bradley *et al* [326] reported that individual atoms and clusters were observed on pre-oxidised Pt-Al<sub>2</sub>O<sub>3</sub> (0.36 %Pt) catalyst but only clusters on the *ex-situ* reduced at 700 °C.

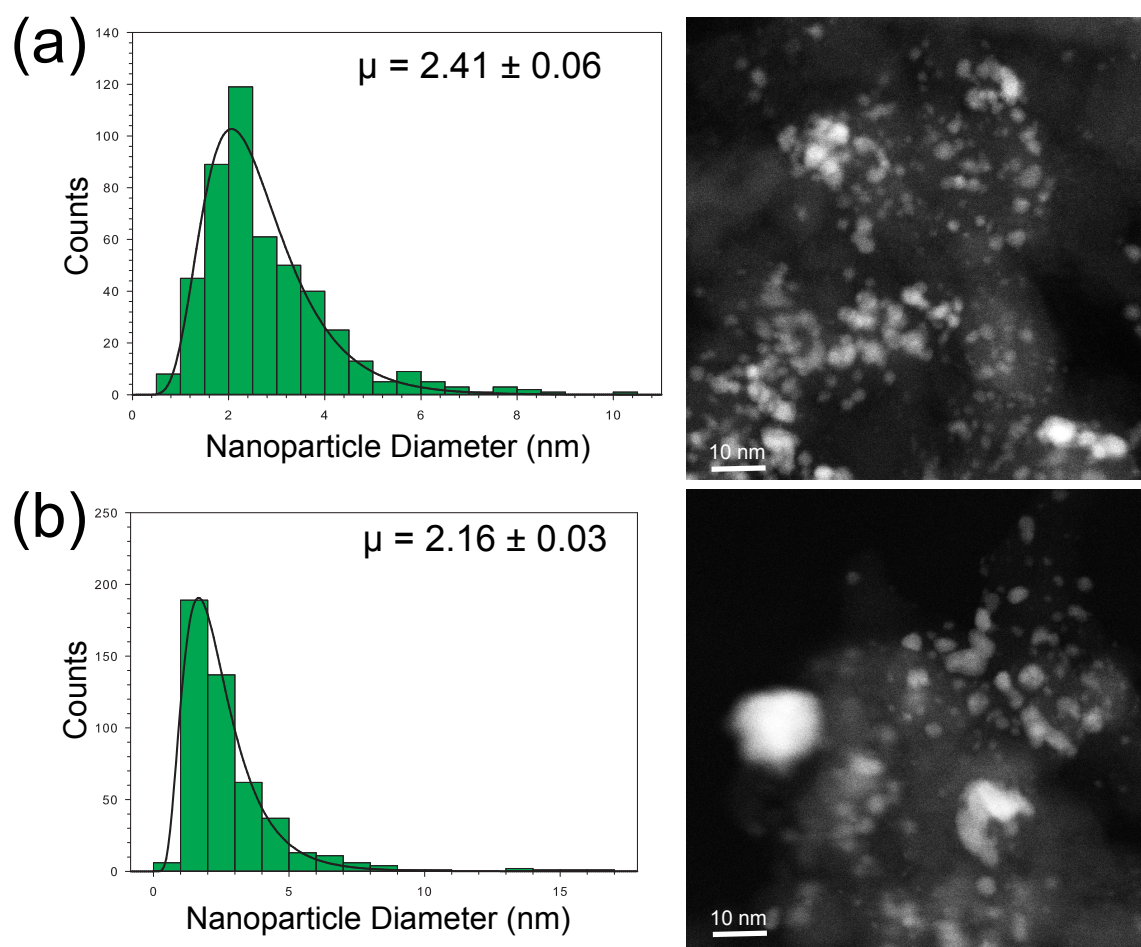


Figure 5.8: Nanoparticle size distributions and HAADF-STEM images for the catalysts treated in air for 15 h at (a) 250 °C and (b) 500 °C



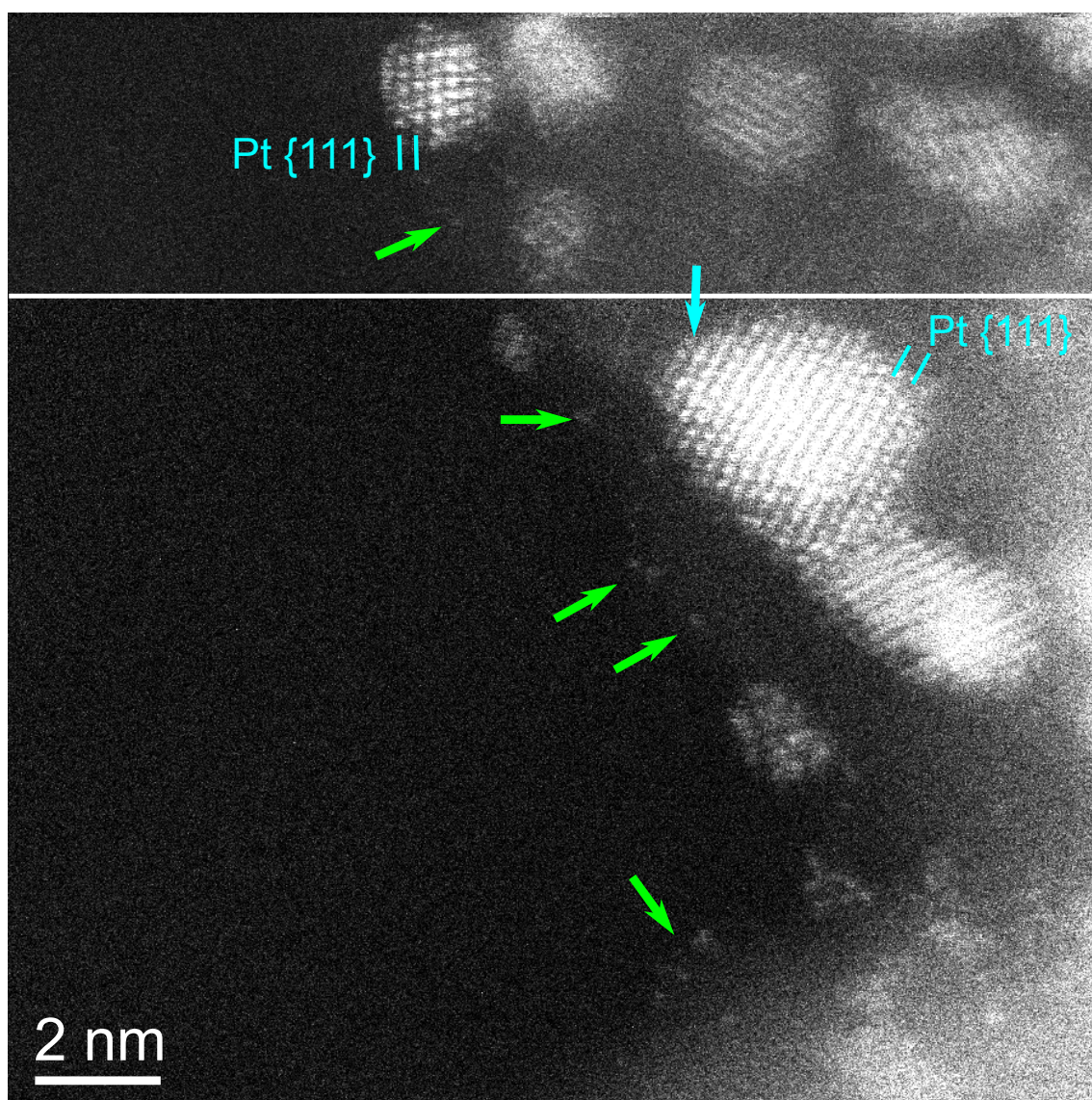


Figure 5.9: HAADF-STEM image of the Pt-Al<sub>2</sub>O<sub>3</sub> catalyst treated in air for 15 h at 250 °C. The upper part of the image was taken with a different defocus to the bottom part. Intensity measurements are taken from the bottom part only. The green arrows point to individual atoms located on the surface and edge of the Al<sub>2</sub>O<sub>3</sub> support. Amorphous clusters, distorted nanoparticles and ordinary nanoparticles can be seen in this image plus the formation of a neck in the central region. The blue arrow on the central nanoparticle denotes the row from which intensities are measured. The contrast has been adjusted for viewing purposes

Given that the  $\gamma$  and related  $\eta$ ,  $\delta$  and  $\theta$  phases of  $\text{Al}_2\text{O}_3$  are likely to contain surface defects, it is possible that the atoms are located in the cation vacancies as suggested by Sohlberg *et al* [143]. The HAADF-STEM images here, do not show Pt tri-clusters that were observed by Sohlberg *et al* [143]. Extraordinarily bright features the size of an atom, were observed by Nellist *et al* [142] who suggested that these are two Pt or Rh in close proximity. The image here does not show such bright isolated features.

In addition to the single atoms, clusters can be observed which are less than 1 nm and have no obvious shape. The clusters reported by other groups are sometimes referred to as rafts [142] because they are believed to be 2D structures based on intensity measurements [66, 142]. To investigate whether the observed structures here are 2D or 3D, the intensity profiles of the features are examined as follows.

The average intensity for the atomic features located in the thin region of the support is  $I_{Atom} = 67044 \pm 997$  and the background intensity around those regions is  $I_{thin} = 48351 \pm 1870$ . Measuring atoms in the row of atoms labelled in the nanoparticle results in  $I_{NPAtom} = 147881 \pm 1394$  and the background intensity of the thick region of the support is  $I_{thick} = 87220 \pm 2520$ . Removing background intensities from the respective locations of the atoms yields  $I'_{atom} = 18693 \pm 2266$  and  $I'_{NPAtom} = 60661 \pm 2879$ . Crewe [38] and LeBeau *et al* [47] have shown that the number of atoms in each column is proportional to the measured intensity although LeBeau *et al* point out that the Debye-Waller factors that govern their thermal vibrations are not the same as the bulk value at the surface of nanoparticles [47]. This can reduce their intensity [47]. Assuming a proportional relationship, this means that assuming the atomic features at the edge of the thin support region are truly single atoms then the atomic columns at the edges of the nanoparticles are approximately 3 atoms tall. The centre of the nanoparticle is approximately 15 atoms tall. Applying the same principles to the clusters seen at the edge of the support reveals that they are between 2-5 atoms thick. Typical errors for these measurements are  $\pm 2$  atoms. This measurement implies that these features are not rafts but are 3D clusters with very limited or no order.

Figure 5.10 shows two HAADF-STEM images from the catalyst treated for 15 h at 500 °C. In frame (a), a sparsely populated area can be seen. In this area, atoms and clusters smaller than 2 nm are present in addition to structurally ordered nanoparticles. There is some evidence of nanoparticle migration because nanoparticles display the formation of necks with neighbouring structures. Frame (b) on the other hand shows a densely populated region with many large nanoparticles that have clear structure. In these areas of high metal content, clusters and atoms were almost never observed suggesting that all mo-

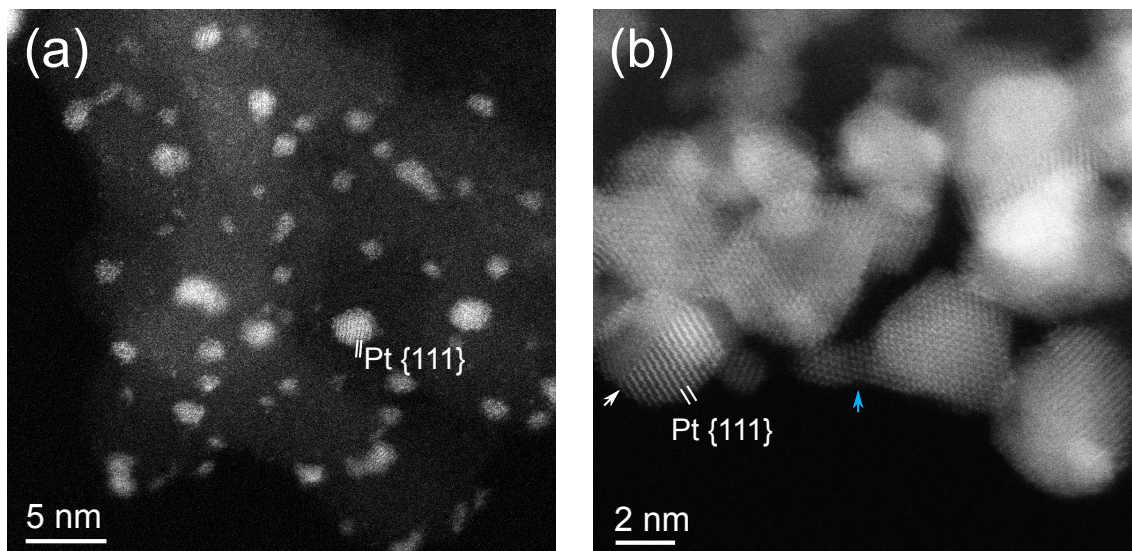


Figure 5.10: HAADF-STEM image of the Pt- $\text{Al}_2\text{O}_3$  catalyst treated in air for 15 h at 500 °C. The image in (a) shows that there are still some very small clusters remaining on the support but in regions of higher metal content such as (b), there is evidence of neck formation (blue arrow) and no observable clusters below 2 nm or single atoms. A polycrystalline nanoparticle containing a grain boundary is indicated with a white arrow in (b)

ble structures have coalesced into the large structures seen here. In these regions where nanoparticles coalesce en-masse, defects within the structures can be observed. In (b), an atypical twinned nanoparticle can be seen. The inclusion of defects during coalescence is generally not understood but the strain associated with the orientation difference between structures could lead to further defects as the coalescence process continued.

## 5.6 Sintering Mechanism Discussion

The nanoparticle size distributions returned  $\mu$  values that did not suggest a straight-forward relationship between treatment time and temperature. The Pt- $\text{Al}_2\text{O}_3$  catalyst nanoparticle density was found to be inconsistent from area to area. During the electron microscopy sessions, five different areas were selected to shed light on the metal content across the catalyst. It has been assumed that the largest observed nanoparticles originated where the density of nanoparticles was large so that coalescence was rapid, particularly at 750 °C. The long tail and inconsistent mean nanoparticle size is attributed to non-uniform distribution of Pt.

Regarding the treated catalysts, the main difference between them is the length of the tail in the log-normal distributions. A statistic that could be used to shed some light on



Table 5.1:  $\mu$ ,  $\sigma$  and  $\Gamma$  values obtained for the fresh and heat treated catalysts

Catalyst	$\mu$	$\sigma$	$\Gamma$
Fresh	$2.69 \pm 0.04$	$0.37 \pm 0.01$	1.21
250 °C 3 h	$2.86 \pm 0.04$	$0.39 \pm 0.01$	1.28
500 °C 3 h	$2.73 \pm 0.03$	$0.42 \pm 0.01$	1.40
750 °C 3 h	$2.85 \pm 0.01$	$0.55 \pm 0.01$	1.99
250 °C 15 h	$2.42 \pm 0.06$	$0.40 \pm 0.02$	1.32
500 °C 15 h	$2.16 \pm 0.03$	$0.51 \pm 0.01$	1.79

this is the skewness which is given as

$$\Gamma = (\exp \sigma^2 + 2) \sqrt{\exp \sigma^2 - 1} \quad (5.1)$$

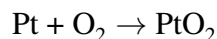
where  $\sigma$  is the standard deviation. The skewness is a quantity that describes how much of the distribution leans to one side of the mean,  $\mu$ . Table 5.1 displays the values of  $\mu$ ,  $\sigma$  and  $\Gamma$  for the fresh and heat treated catalysts. The skewness increases as the temperature is increased for catalysts treated for 3 h and the same is observed for the 15 h variants.

Datye *et al* reported that the sintering of Pt was much more rapid in air than in  $H_2$  and concluded that Ostwald ripening was the dominant process at temperatures above 700 °C [233]. They observed few clusters below 1 nm in their specimens at this temperature. Despite this, all of their treated catalysts were fitted to log-normal distributions, even those aged for over 100 h. Ezekoye *et al* observed extraordinarily large particles (up to 1  $\mu m$ ) on their catalysts treated at 900 °C in  $O_2$  rich atmospheres. Their box plots show that the catalysts treated at high temperature results in a wide range of nanoparticle sizes. Perhaps the box plot is a better way to represent nanoparticle size distributions with non-uniform metal loading. These studies are generally on  $\gamma-Al_2O_3$  resembling commercial catalysts but other groups, using model systems (including amorphous  $Al_2O_3$ ), observe the formation of LSW distributions [203].

The results here imply that nanoparticle size distributions are unreliable for deciphering the dominant sintering mechanism on commercial catalysts which not only have varied metal loadings but also varied support structures. A further complication in using nanoparticle size distributions is that the background theory also makes many assumptions. For example, in Ostwald ripening, it is assumed that nanoparticles are stationary but *in-situ* (S)TEM studies clearly show that it is not the case [312]. Furthermore, nanoparticles with the critical radius,  $r^*$  are believed to remain at that size. The nanoparticle distributions here, regardless of temperature and time, do suggest that nanoparticles in the range of 2 – 3 nm generally remain. This could imply that they are relatively immobile compared to their smaller and larger brethren.

Although the *ex-situ* studies cannot directly imply a size-mobility relationship, *in-situ* studies by other groups seem to imply that the size-mobility relationship is also not solved with some groups suggesting that smaller nanoparticles or clusters are more stable than larger ones. More recent studies on  $\gamma$ -Al<sub>2</sub>O<sub>3</sub> systems using DFT do seem to imply that small clusters are more likely to be stabilised on the support [92].

It is generally believed that in oxidising environments, Pt is likely to sinter by the formation of PtO<sub>2</sub>. According to Harris [202], the enthalpy change for the reaction



is 175 kJmol<sup>-1</sup> whereas the sublimation energy for Pt is 565 kJmol<sup>-1</sup> and the energy required to transfer an atom from the nanoparticle to substrate is 527 kJmol<sup>-1</sup>. In Figure 5.9, single spots of intensity, which are likely to be single Pt atoms, have been detected. If indeed PtO<sub>2</sub> is formed, it is possible that it may be stabilised by vacancies in the support surface. Although Pt is very heavy compared to Al<sub>2</sub>O<sub>3</sub>, it is not possible to distinguish between Pt and PtO<sub>2</sub> directly from the image. The atoms observed here were found to be less mobile than Pt atoms on amorphous-C which is reported extensively in chapter 6 on page 129.

It was observed that clusters remained on the catalyst even after exposure to air for 15 h at 500 °C. Additionally, the majority of the observed nanoparticles were close to the original  $\mu$  in the fresh catalyst which suggests that particles around that size are stable on the  $\gamma$ -Al<sub>2</sub>O<sub>3</sub> support.

## 5.7 Conclusions

The atomic structure of a Pt-Al<sub>2</sub>O<sub>3</sub> has been studied by aberration corrected HRTEM and HAADF-STEM. Faceted nanoparticles resembling Wulff constructions dominated the structures observed on the fresh catalyst, particularly in regions where there were well defined Al<sub>2</sub>O<sub>3</sub> support surfaces.

Heat treated catalysts in air were also studied to investigate the onset of sintering at different temperatures after 3 h and 15 h. Virtually no differences between the 3 h and fresh catalyst were observed except for the 750 °C variant where particles larger than 20 nm were frequently observed. Single atoms were found on the catalyst aged for 15 h at 250 °C and 500 °C suggesting that Ostwald ripening has occurred. Furthermore, clusters



were still present on these catalysts suggesting they are either stabilised by the support or are generated as an intermediate state. A future *in-situ* study could resolve this matter.

NBD was used for analysing nanoparticle structures with a complex support. NBD patterns allowed calibrated aberration free measurements to be taken directly, allowing the structure of some nanoparticles to be determined with certainty. Additionally, NBD was used to provide additional insights into the nature of defects located in some crystals on the heat treated catalysts.

The support in this catalyst is complex and from area to area the nanoparticle loading and the support quality varied. A question which this study raises is whether clusters and atoms are truly stable on a support with surface defects. Detailed *in-situ* studies in O<sub>2</sub> could shed more light on this as would the study of a model Al<sub>2</sub>O<sub>3</sub> support loaded with atomically dispersed Pt. Such studies are proposed as future work.

# Chapter 6

## Imaging Single Atoms Using HAADF-STEM

### 6.1 *In-situ* Environmental HAADF-STEM of Pt-Pd Atoms

#### 6.1.1 Introduction

Individual atoms are the smallest form that active catalysts can possibly take. Imaging single atom catalysts under controlled atmospheres and temperatures would represent the state of the art in environmental electron microscopy [66]. This section represents part of the work to quantify the direct study of Pt and Pd atoms under different gases at different temperatures. A well known issue of studying single atoms is the threat of contamination.

Contamination on C grids is a well known nuisance and comes in many forms. The C films are usually produced by depositing carbon via arc-evaporation of graphite onto a plastic coated support grid [327]. The plastic is then removed by heat treatment leaving behind the C film [327]. Contamination in the form of graphite or carbyne sheets has been reported [327, 328, 329] but in the context of the work described here it is easy to avoid such structures. Generally, the holey and lacey variants of C film used during this thesis have contained such structures. Continuous C films were considerably worse and hence were not used.

Another type of contamination takes the form of molecule layers which cannot be easily observed in TEM or HRTEM because of the contrast from the amorphous C film. Molecules are usually hydrocarbons [330] which can originate from the C film fabrication process or be deposited *in-situ* by remnants of oils from pumping systems in electron microscopes. The hydrocarbons become highly mobile during exposure to electrons [330].

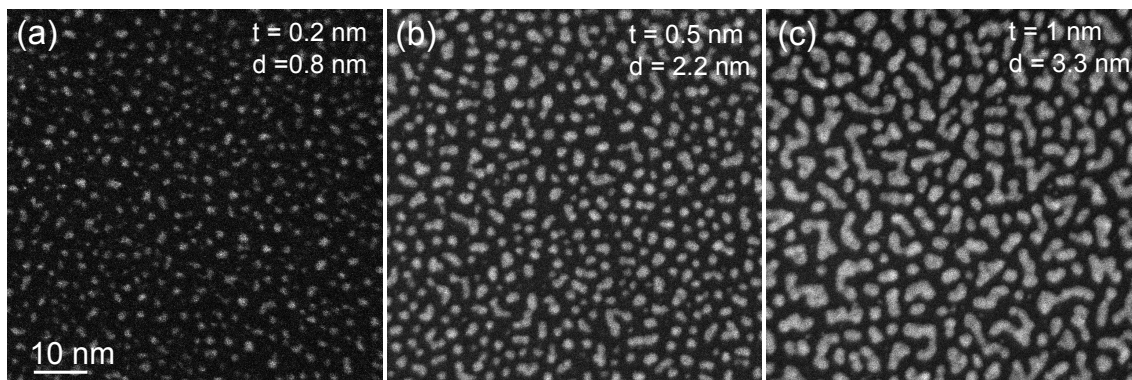


Figure 6.1: HAADF-STEM images of Pt-Pd coverage on C using coating thickness settings of (a) 0.2 nm, (b) 0.5 nm and (c) 1 nm. Approximate average sizes are indicated in the top right corner. These display little contamination because they have been beam showered

In HAADF-STEM, the hydrocarbons are collected by the electron probe and are deposited as spheres around the probe when stationary [331].

### 6.1.2 Preparing Atomically Dispersed Specimens

All specimens relevant to this section were prepared using the high resolution coater described on page 42. Using holey-C grids (Agar 168-3), trials were carried out to determine the coating thickness and beam current to generate specimens that contained primarily small clusters and individual atoms. Every specimen was checked using HAADF-STEM. Figure 6.1 shows a series of HAADF-STEM images of a selection of prepared samples using different deposition machine thickness settings. Settings of 20 mA with a 0.2 nm coating thickness produced the best specimens for purpose.

Study of all of the specimens prepared for preliminary investigations were all found to contaminate very quickly in HAADF-STEM. Generally speaking, the rate at which each specimen contaminated was consistent. A typical high speed scan (512 x 512) at 8 M magnification lasting 0.5 s is sufficient to produce noticeable contamination on the specimen. Zooming out would reveal a bright square where contamination had been deposited. Leaving the probe stationary for more than one second with condenser aperture 3 (24 mrad) would generate a sphere of contaminants similar to those reported by McGilvery et al [331].

In addition, during the trials, holey-C coated with 2 nm thin C films were also used. These were prepared by dipping the mica supported films into distilled water to separate the scored films (approximately 3 mm<sup>2</sup> grids using scalpel) from the mica. A holey-C Cu

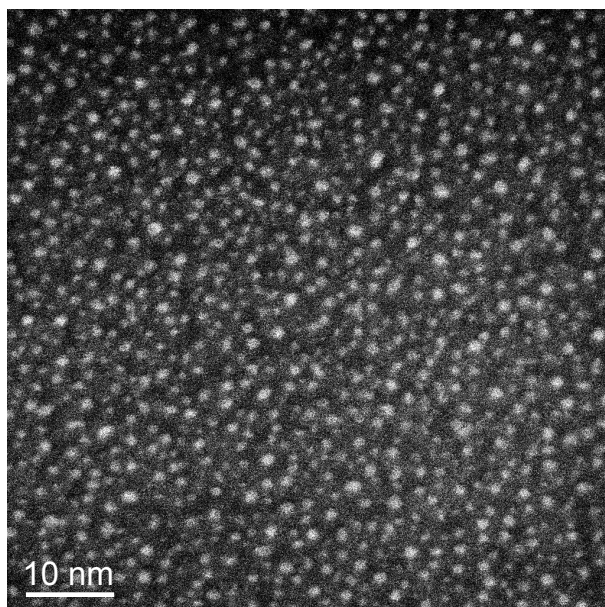


Figure 6.2: HAADF-STEM of a thin-C film. The image shows that there are distinct background features which are unique to the thin-C regions. EDX spectra suggests that the background intensities may originate from Fe and Ni compounds associated with mica

TEM grid was dipped into the water and the film was forced onto the grid upon lifting the grid out through the film. The grids were then left to dry. This method has been previously used for HRTEM and HAADF-STEM studies by others [9, 38, 312]. Contamination on these specimens was considerably worse but only in the thin film regions. Figure 6.2 shows an example HAADF-STEM image of the thin-C region showing noticeable background intensity which is not observed in regions where the thin-C is broken or on ordinary holey-C films.

The thin-C films were baked using the heating holder in a optical baking rig (described elsewhere [332]) at 300 °C prior to metal deposition. The process did not resolve the issue. Using ethanol to remove the contamination also made it considerably worse. For this season, thin-C was not used for these studies despite successes with the films for HRTEM by others [9, 38, 312].

### 6.1.3 Minimising Contamination

To minimise contamination of the final specimens for individual atom imaging using HAADF-STEM, the following sequence of events proved the most successful: plasma cleaning the Pt-Pd target and the depositing machine components, plasma clean grids, plasma clean specimen holder, optical baking [38] and finally beam showering *in-situ*. The details for each step are described below in separate paragraphs. Air was used during

plasma cleaning in all instances.

To minimise contamination from the deposition, the internals of the depositing machine (stage, mounting ring, source cover) were all wiped with a filter cloth to remove any dirt. The target, mounting ring and the target cover were then plasma cleaned for 300 s at 75 % power.

Cu grid supported holey-C films were used for the specimens to be used in the experiments. The grids were plasma cleaned at 10 % power for 40 s. Continuous exposure at 20 % for more than 20 s caused the holes to grow larger and the film to destabilise and tear. Using higher powers for short periods created nanoparticles which are presumably crystalline forms of C compounds. The newly formed nanoparticles were too beam sensitive to deduce their structure. Improvements in contamination here are generally consistent with those reported by McGilvery et al [331] but the specimens were still not suitable for purpose without using other techniques to reduce contamination.

The specimen holders and washers were plasma cleaned for 300 s at 75 % power but without the specimen in place. For the heating experiments, the Gatan 628 heating holder was not plasma cleaned as a whole because of the presence of plastic wire covers, but the washers were plasma cleaned for 300 s at 75 % power.

The specimen was placed (fresh from Pt-Pd coating) straight into the heating holder and placed into an optical baking device. The device was built by Jeremy Mitchell and details of it can be found in his thesis [332]. Essentially, the device emits white light and the heat from the bulb reaches 60 °C in vacuum. The specimen was left in for at least 10 hours overnight. Generally, during the trials, it was found that this procedure did not remove the contamination sufficiently. Regardless, specimens were kept in this device overnight for vacuum storage before the experiment. The unit had an oil-free dry high vacuum pumping system.

Beam showering the specimen *in-situ* prior to detailed HAADF-STEM imaging for 20 minutes greatly assisted in the acquisition of high quality images of single atoms. The beam showering process does not remove the contamination but it stabilises it. Continuous scans did build up contamination over time but it was possible to image the same area for at least 5 minutes with no deterioration in quality caused by contamination.

During *in-situ* environmental experiments beam showering was done prior to the injection of gas. It was found that at moderate temperatures from room temperature up to 200 °C contamination was significantly worse. This is because the gas reacts with the con-

taminants on the surface of the specimen making them mobile again. The specimen when heated to 300 °C removed most of the contamination if allowed to cool but it was found that even in gas ( $H_2$ ) at pressures up to 10 Pa, imaging at 300 °C was greatly improved.

It was concluded that in all cases the main contamination was attributed to the specimen or holder components and once cleaned specimens could be examined for extended times. The dry pumped microscope itself was already adequately clean.

#### **6.1.4 *In-situ* (S)TEM Methodology**

Aberrations were corrected prior to the injection of gas using a reference sample, with Au nanoparticles on a Cu grid supported holey-C film. Beam showering was achieved by enabling free lens control and adjusting the setting for CL1 to be 6000 and then setting the defocus to  $-22000$  nm. The smallest SAD, objective and EELS apertures were inserted to minimise any signal reaching the detectors to prevent any damage. After the beam shower, first order astigmatism was corrected using the ronchigram approach [41].

The gas system was expunged prior to the experiment for 10 minutes to remove residual gas from the pipelines. The inlet gas pressure was set to 1.3 mbar for each *in-situ* environmental experiment using  $H_2$ . Beam showering was repeated in gas when the heating holder was not used.

It was found during the experiments that the default power supply for the Gatan heating holder produced considerable electrical noise preventing the imaging of individual nanoparticles. An alternative solution was devised by Professor Ed Boyes which involved the use of a separate power supply connected to a series of resistors to prevent too much current being sent to the heating holder.

Note that most images in this section have been smoothed but linescans have been taken from unmodified images to preserve the original intensities. The images were smoothed in Gatan Digital Micrograph or ImageJ using the smoothing tool. Smoothing replaces the intensity of a pixel by the average intensity of pixels surrounding it. This is applied across the entire image like a moving average, resulting in more uniform intensity variations across the image i.e. less noise.

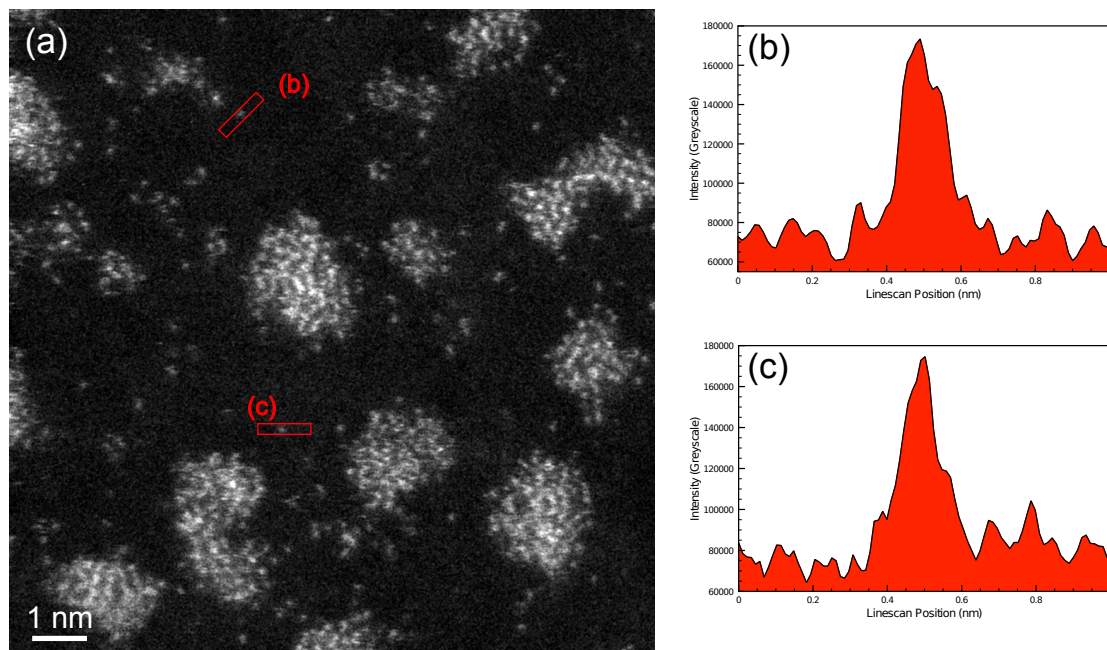


Figure 6.3: HAADF-STEM image of a dispersed Pt-Pd specimen showing both atoms and clusters in (a). Some line scans of the indicated atoms are shown in (b) and (c)

### 6.1.5 Results: Without Gas or Heat

Figure 6.3 shows a HAADF-STEM image of one of the Pt-Pd specimens. The image shows clearly that the larger structures are akin to clusters as opposed to fcc nanoparticles. Individual atoms can also be observed with excellent clarity. Line scans of individual atoms are shown in Figure 6.3. The background noise is less than 100,000 arbitrary units whereas a single Pt is approximately 200,000 arbitrary units. The nominal background is consistent across many different images so the sudden bright peak must be either Pd or Pt. Given the strength of the signal expected from Pt vs Pd and the dominance of Pt in the source material (86 % Pt), it is more likely that the brightest peaks like those in Figure 6.3 are Pt rather than Pd.

It can be seen in both Figures 6.3 and 6.4 that dimmer spots can be seen along with the bright ones. Pd has  $Z = 46$  and Pt has  $Z = 78$ . Based on the approximate HAADF-STEM intensity rule where  $I \propto Z^2$  [38,42,43], the intensity of a Pd atom should be 35 % that of a Pt atom. For a probe size of 0.1 nm it would take 169 atoms of C to produce the same intensity as a Pt atom. It was found that on the original specimens during contamination reduction trials that the nanoparticles became almost indistinguishable from the background suggesting that the deposition of contamination is rapid, at least several nanometers per second. However, this intensity relationship is not absolute after the inclusion of the image processing of the HAADF-STEM detector and data are normalised within each frame.

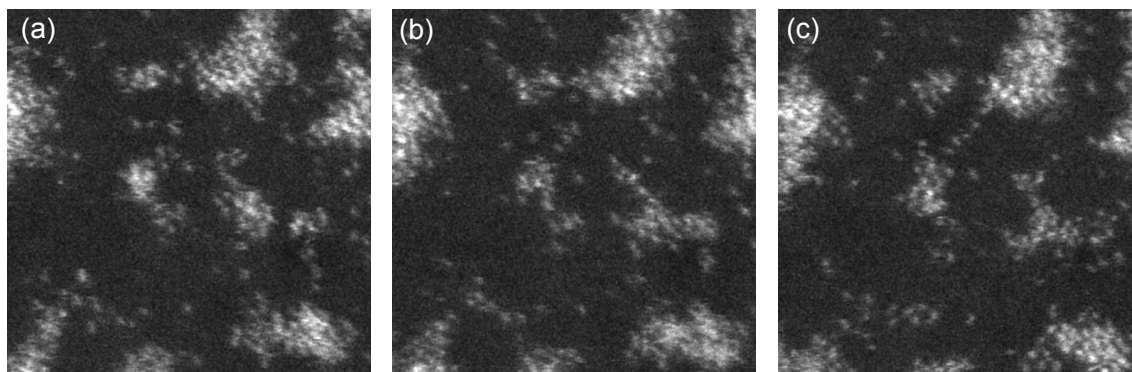


Figure 6.4: Frames from movies taken *in-situ* with no gas or heat showing the dynamics of atoms under the influence of the electron beam, the time taken between each frame is approximately 2 s. Dimension of each frame is approximately 7 nm. The most dramatic changes can be seen in the centre of the image where a cluster is undergoing constant structural flux and atoms are being exchanged to and from the larger cluster on the top right

In addition to images, movies were also recorded because it is necessary to deduce the effect of the electron beam so that heating effects and the effects of exposure to gas can be distinguished. Frames from these movies are shown in Figure 6.4. The movies clearly show that the atoms move around very quickly. It is possible that some of the apparent low intensity atoms seen in Figures 6.3 and 6.4 are atoms that are on the move as they are scanned. Dwell times per pixel were 10  $\mu\text{s}$  in this case. Asoro *et al* observed similar behaviour of Pt nanoparticles [228] although less atom diffusion was observed possibly because the nanoparticles in their work contained more ordered structures and hence the atoms on their surface are more stable than those reported here. Similar results have been observed for Au [57, 333] and U [334] atoms on C supports. Bals *et al* [335] observed that C supported 2D Ge clusters would form 3D structures when heated under the electron beam. There have been no reports on the segregation of alloys in bimetallic systems at the atomic level perhaps because the clusters are inherently unstable under the electron beam and would require *in-situ* HAADF-STEM. Bradley *et al* [326] observed that Pt atoms on  $\text{SiO}_2$  irradiated by the electron beam display similar behaviour to that presented here and by Batson *et al*.

The clusters are also unstable in agreement with previous electron irradiation studies of Pt clusters [38, 228] and other heavy metals [57, 333, 335]. There is a constant exchange of atoms between the different clusters and each one seems to compete against the other. It is assumed here that the dynamics observed here are solely because of the effects of electron beam irradiation as has been verified by other groups studying nanoparticle stability under the electron beam [57, 228, 334]. Some very small clusters were observed to explode sending atoms in all directions towards other nanoparticles perhaps with each atom constantly



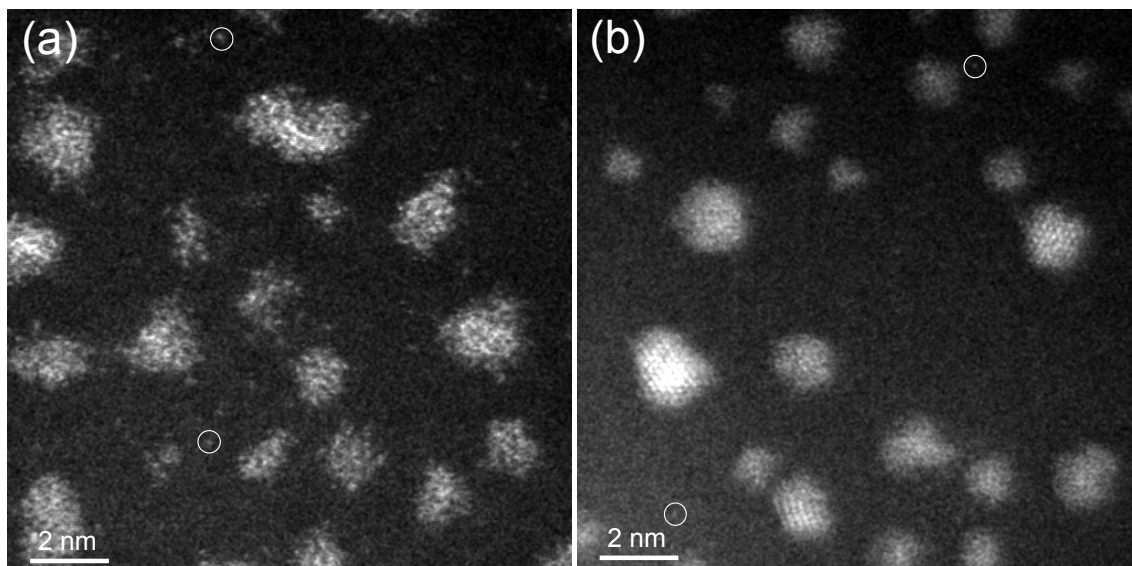


Figure 6.5: HAADF-STEM images at room temperature of Pt–Pd atoms and clusters in (a)  $\text{H}_2$  and (b)  $\text{O}_2$ . Note the contrast is poor compared to Figures 6.3 and 6.4 because the specimen is continuously contaminating, the effects of this are seen towards the bottom of the images where contamination has been built up during the scan. Circles in (a,b) show two atoms whose intensities are analysed in Figure 6.6

seeking the lowest energy state possible. Despite recording several movies, the effect of the electron beam alone is not enough to encourage the formation of stable nanoparticles with ordered structures which have been observed to form with heating [312].

### 6.1.6 Results: Gas without Heat

Figure 6.5 shows a HAADF-STEM image of one of the Pt–Pd specimens in  $\text{H}_2$  and  $\text{O}_2$ . Imaging in gas was challenging because contamination became an issue again despite beam showering prior to the gas. It was found that beam showering within the gas aided in acquiring images but only for the first few scans. It is likely that the injection of gas onto the specimen with the electron beam active has made previously immobile contaminants mobile again upon reaction with  $\text{H}_2$  or  $\text{O}_2$ . Generally, contamination in  $\text{O}_2$  was considerably worse than that in  $\text{H}_2$ .

Despite the issues of contamination, single atoms were still imaged. In  $\text{H}_2$ , the atoms generally appeared as bright as in vacuum but not sharp. In  $\text{O}_2$  on the other hand, single atoms appeared as blurry dots with no sharp peak. A possible explanation is that the heavier  $\text{O}_2$  atoms in the gas spread out the beam and the contribution from diffuse scattering from the gas is greater than in the lighter  $\text{H}_2$  gas but extensive further work is required to resolve these issues.

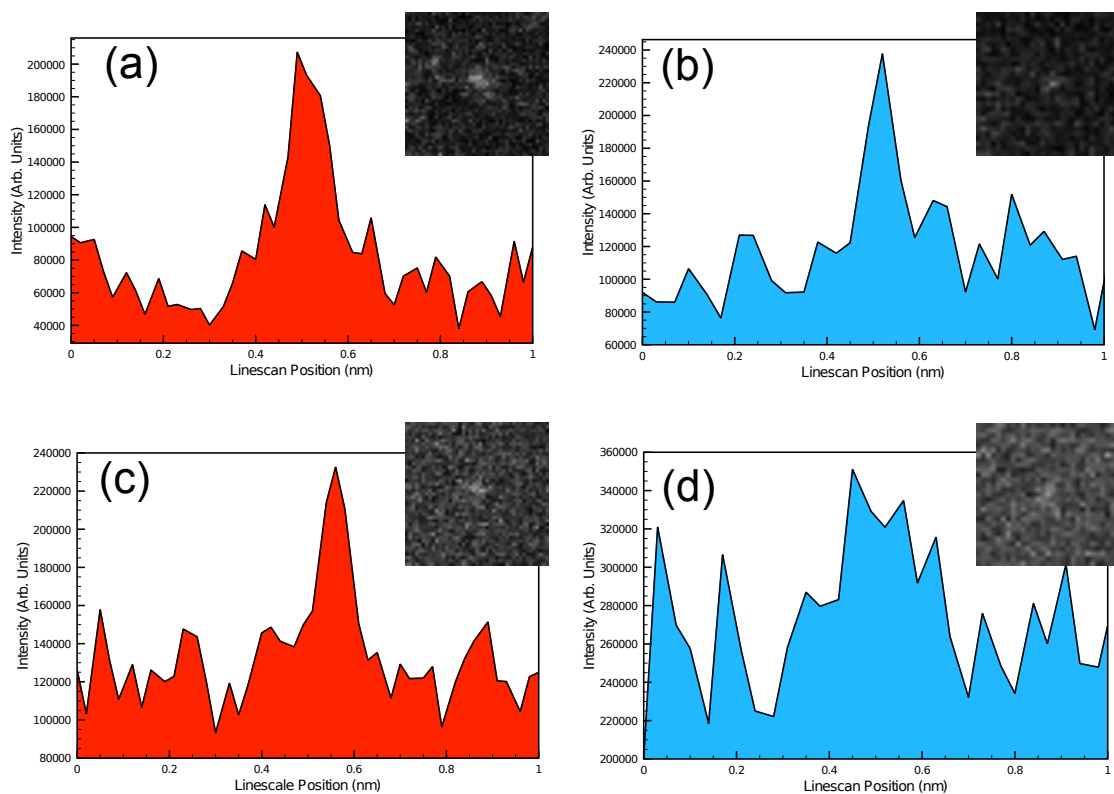


Figure 6.6: Examples of linescans taken from atoms in HAADF-STEM images in (a,c) H<sub>2</sub> and (b,d) O<sub>2</sub> with corresponding image insets with approximate dimensions of 1 nm. (a) and (b) are from the top of the image where contamination is almost unnoticeable but (c) and (d) are taken where the contamination has built up at the bottom of the image

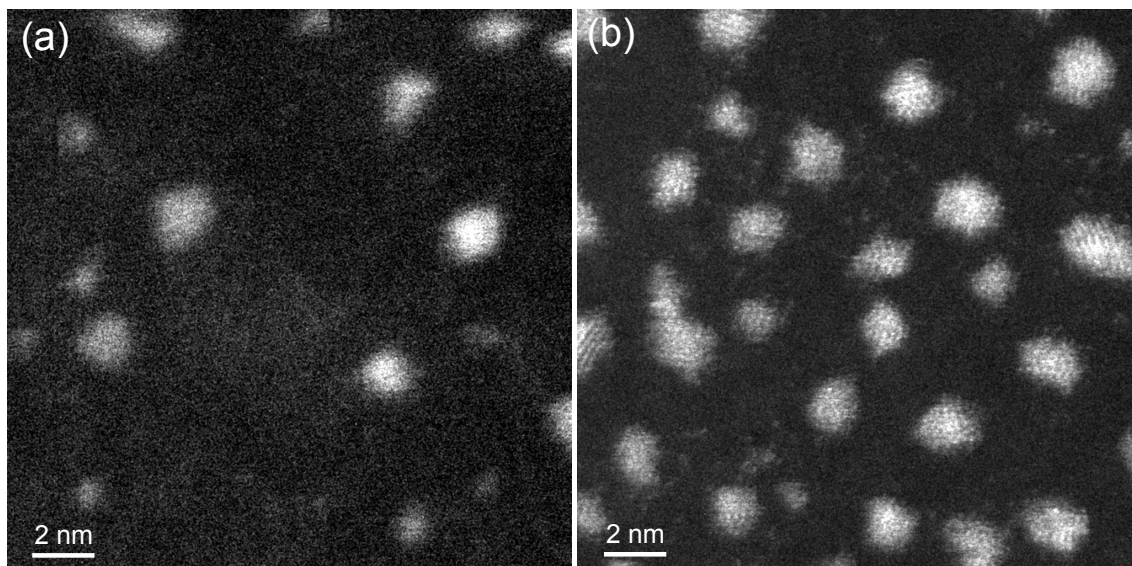


Figure 6.7: HAADF-STEM image of Pt-Pd atoms and clusters in  $\text{H}_2$  at  $300^\circ$  using (a) default Gatan heating holder supply and (b) an alternative supply described in the text. Note how the resolution is insufficient to observe atoms or atomic columns in (a) because of detrimental electric noise but this is absent in (b)

Figure 6.6 shows examples of linescans of atoms in  $\text{H}_2$  and  $\text{O}_2$  at room temperature. The two linescans in each gas were taken from the same image at different locations. This is contamination built up at the bottom of the image where the contaminants have diffused; carried along with the beam.

Movies were also recorded but the contamination build up prevented detailed analysis of cluster and atom behaviour. It was observed that the clusters were unstable as in the case of the electron irradiation experiment in vacuum suggesting that any changes observed in cluster morphology are primarily electron beam driven. The deposition of layers of contamination reduced the ability of the clusters to move with each successive frame.

### 6.1.7 Results: Gas and Heat

The resolution obtainable in HAADF-STEM was found to be dependant on the heating holders power supply. Figure 6.7 shows HAADF-STEM images recorded in  $\text{H}_2$  at  $300^\circ\text{C}$  using two different power supplies. The particular Gatan heating holder power supply introduced several types of scanning noise to the STEM images although TEM images with  $< 0.1\text{ nm}$  were previously recorded with it [85]. The alternative power supply (Keithley 2614B) on the other hand makes virtually no difference to the resolution allowing atoms, clusters and nanoparticles to be studied successfully under the influence of gas. The temperatures in  $\text{H}_2$  and  $\text{O}_2$  were calibrated as described on page 50.

Figure 6.7 represents two separate experiments using the two different power supplies but the procedure followed in both was the following: the specimen was gradually heated over 5 minutes to 300 °C in H<sub>2</sub>. This was done by gradually turning up the current to the required value for the desired temperature, this was determined from the calibrations described on page 50. 300 °C was used for the heating holder power supply test because at this temperature contamination was minimised as described on page 133 and therefore provided a more suitable test to determine the effects of the two different power supplies on image resolution. Following on from the heating stage, the specimen was allowed to settle for 5 minutes to minimise specimen drift before imaging commenced.

Heating at 300 °C without the beam did not result in any observable morphological changes. Furthermore, atoms were still visible immediately after switching on the beam as shown in Figure 6.7(b) suggesting that the atoms are stable on the support at 300 °C.

Figure 6.8 shows several HAADF-STEM images of two *in-situ* experiments which show the evolution of nanoparticle structure and morphologies over longer periods of time with the electron beam switched off at 500 °C and 600 °C. Figure 6.8 shows two separate experiments. In (a) the specimen was heated up to 500 °C over the space of 5 minutes in the same way described in the previous paragraph. H<sub>2</sub> was then added at this temperature. The specimen was then left for 30 minutes to stabilise and to encourage faceting, particle migration and coalescence. Figure 6.8(b), the same procedure was repeated but the temperature was further increased to 600° over the space of 5 minutes. The specimen was allowed a further 5 minutes stabilise and to further encourage the nanoparticles to facet. Figure 6.8(b) represents the current resolution limits of the current set up.

Nanoparticles had coalesced *in-situ* without the aid of the electron beam and the number of atoms on the support had decreased as shown in Figure 6.8(a). Any atoms later observed were believed to originate from nanoparticle-nanoparticle atom exchanges activated by the electron beam. The nanoparticles had not only become larger but they had become internally well-ordered and externally faceted.

The temperature was further increased in another experiment to 600 °C and an image is shown in Figure 6.8(b). The image is not as good quality as 500 °C. There is again some evidence of nanoparticle faceting as shown in the top left corner and no atoms could be resolved after immediately switching on the beam suggesting that any loose atoms have been absorbed into the larger clusters and nanoparticles. Further imaging did not yield any detectable atoms, this may be because of the lower resolution at this temperature.

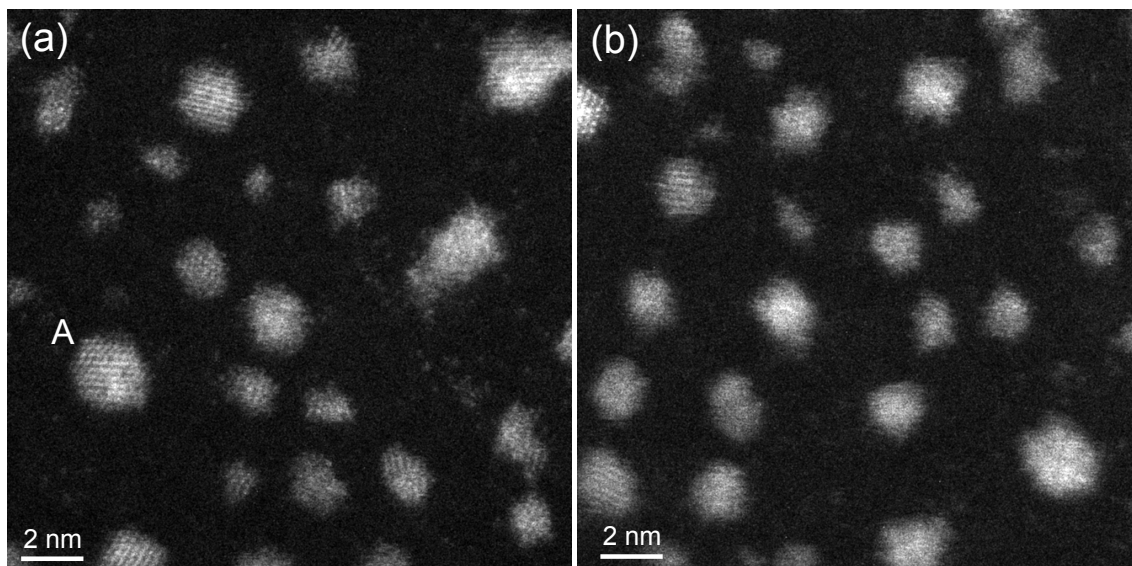


Figure 6.8: HAADF-STEM images of Pt-Pd heated for 30 minutes in  $\text{H}_2$  at (a) 500 °C and (b) after 5 minutes more heating at 600 °C. Note how the nanoparticles have become more faceted relative to room temperature and 300 °C but the resolution is not as great at 600 °C

A possible reason for the lower resolution relative to 500 °C is that at this temperature the C support is not as stable as it was at lower temperatures. Another possible cause could be because of the fundamental properties of thermally diffuse scattering (TDS) which says that at higher temperature, atoms can be displaced more from their default positions in the lattice. To initiate an investigation into this, QSTEM was used to simulate Pt orientated into the  $[1\ 1\ 0]$  zone axis which is a common orientation for C supported nanoparticles. QSTEM itself is described in detail in the next section. Here, the default unit cell of Pt was used but it was tilted by 45° into the appropriate zone axis. TDS was included in the simulation with 30 iterations. Probe array was set to the default 400x400 and the pixel array was 100x100. The  $z$  potential position was adjusted so that there was one atom per slice for the most efficient calculation. Temperatures between 50 °C and 1050 °C were set in 50 °C steps so the temperatures corresponded to those of the heating experiments.

The results from the simulation shown in Figure 6.9 in terms of the standard deviation  $\sigma$  of the randomly measured intensities of 5 atomic columns in each image. There is no relationship between intensity deviations of atomic columns and temperature with any differences less than 5 % of the intensities of the atomic columns. In terms of mean intensities between the output images, the simulations did show that there is an insignificant 2 % increase in calculated intensities for the atomic columns measured at 1300 °C compared to room temperature. This suggests that at higher temperatures the thermal motion of atoms slightly enhances the inelastic scattering contribution to the HAADF-STEM

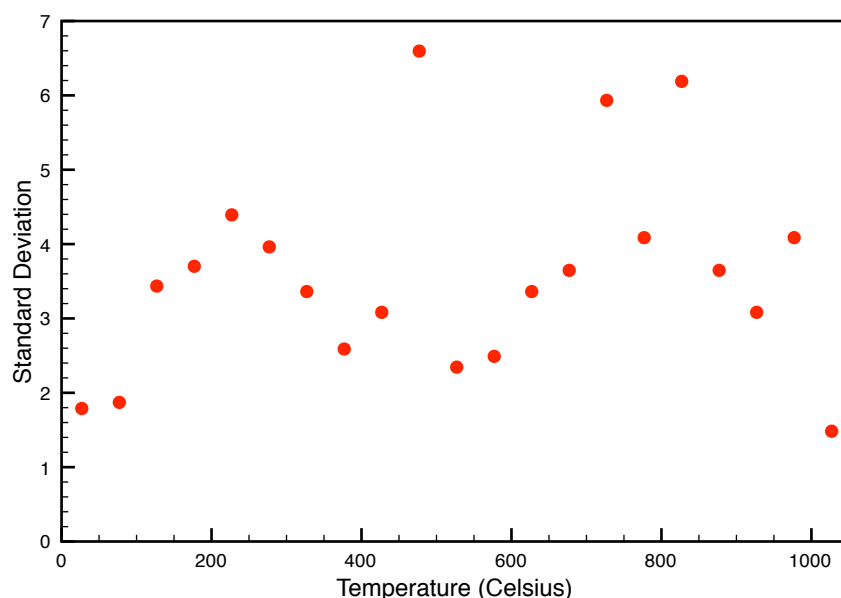


Figure 6.9: Graph showing the results of the simulations at different temperatures showing that there is no relation between temperature and the standard deviation of the Pt atom column intensities. The largest standard deviation value corresponds to approximately 5 % of the intensities of the atomic columns

image. However, this cannot account for the loss in resolution shown in Figure 6.8(b).

A similar *in-situ* ESTEM experiment could not be repeated with  $O_2$  because at the time of writing, only a single non-oxidation resistant holder was available. It would be an interesting experiment to compare the sintering of similar specimens because it is believed that  $O_2$  encourages Ostwald ripening by forming  $PtO_2$  [202]. This is identified as a useful piece of future work.

## 6.2 Intensity Analysis

The intensities in the images shown in Figures 6.3 and 6.7 were analysed in detail to provide a quantitative measurement for the background, single atom and cluster/raft intensities.

This was achieved by measuring mean values of squares 3x3 or 6x6 pixels wide at magnifications between 8 M and 12 M. Images taken with 512x512, the 3x3 square was approximately the same size as the bright atomic columns and single atom features. In the 1024x1024 images, a 6x6 square was used. Intensities from 120 squares randomly positioned over the empty regions of the specimen (where there was only amorphous carbon) were measured using the measure tool in ImageJ. 120 samples were then taken from

features believed to be single atoms, these were generally the features located in isolated areas or at the very edge of nanoparticles and clusters. 120 squares were taken from random points in random nanoparticles. Only 70 samples from single atoms were taken on the image taken at 500 °C in H<sub>2</sub> because there were fewer of these features at this temperature. Figure 6.10 shows the results from this analysis which shows that the intensities from the background and support are quantised.

The nanoparticle indicated as A in Figure 6.8(a) was subject to intensity measurements such that a 3x3 square was placed at intervals along a horizontal row to measure the intensity of the atomic columns. The trough to trough movement in Figure 6.11 represents a transition from the edge of one side of the nanoparticle to the other. Each new row moves further toward the bottom of the nanoparticle. The intensity variations in the nanoparticle shown in Figure 6.11 indicate that the nanoparticle is a 3D object as opposed to a raft because the intensities of the atomic columns increases towards the centre. By setting the intensities of single atoms in Figure 6.10(a) and (c) to be normalised to the same level, it is possible to estimate the number of atoms in an atomic column since the same graph also includes random measurements from the same nanoparticle. A linear intensity relationship was assumed much like Crewe *et al* originally used in their initial experiments [38] (i.e. two atoms in a column is approximately twice as intense as a single atom). The second *y* axis in Figure 6.11 on the RHS represents the approximate number of atoms in each column in the nanoparticle. The nanoparticle has between 1-2 atoms per column at its edge and approximately 6 at its centre. The measurements indicate that once heated sufficiently, 2D clusters will eventually meet, coalesce and stabilise to form 3D nanoparticles.

## 6.3 CeO<sub>2</sub>

### 6.3.1 Background

CeO<sub>2</sub> is an important material valued for its catalytic properties. CeO<sub>2</sub> and other oxides such as ZrO<sub>2</sub> are crucial materials in three-way catalysts (TWC) and some DOCs [336]. They have been in widespread use since the 1980s and the TWC/DOC application is the largest market that uses the rare earth metal oxides [336]. In the TWC context, CeO<sub>2</sub> can act as a promotor by supplying O atoms to the Pt or Pd nanoparticles loaded onto it [337]. In addition, CeO<sub>2</sub> stabilises Pd nanoparticles. Pt is not as widely used in TWCs because of its expense despite its superior catalytic properties [191]. Au is not used in automobile catalysts because it sinters at much lower temperatures than Pd and Pt. However, the

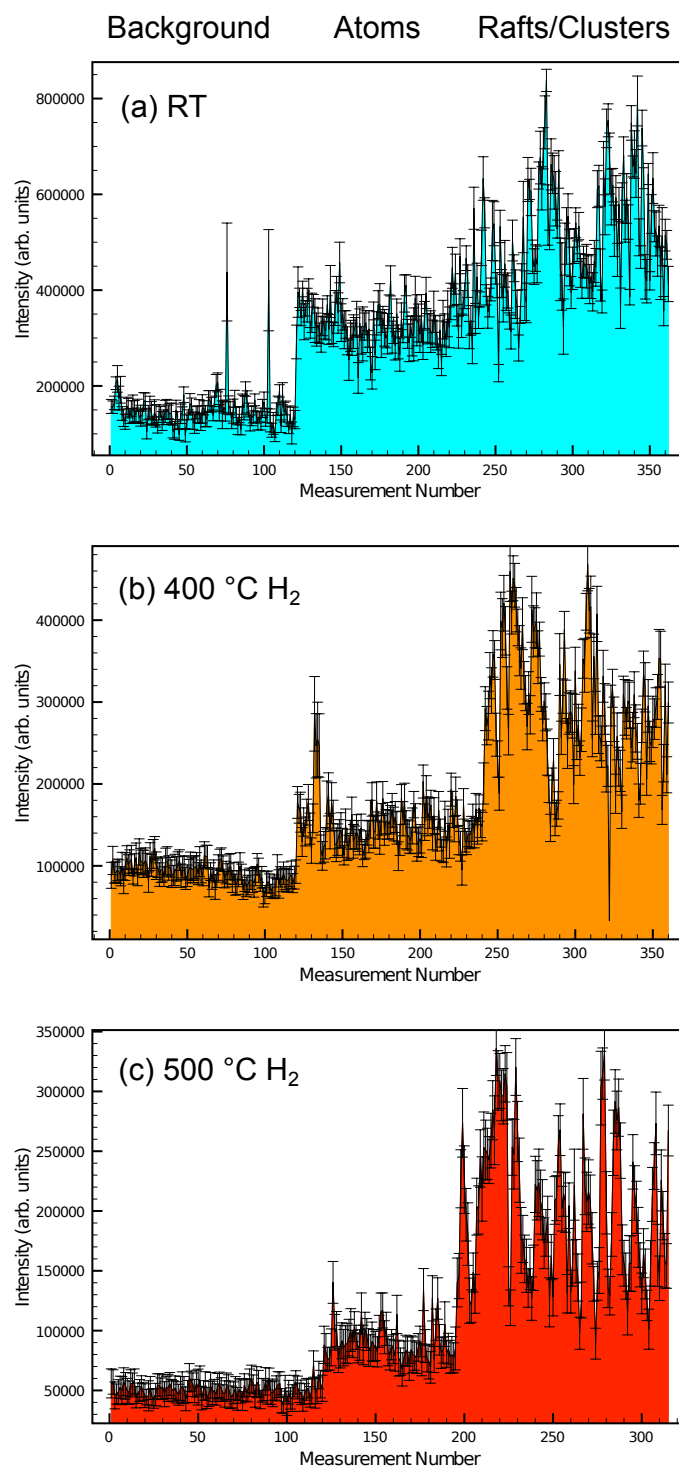


Figure 6.10: Three graphs showing the intensities of the measured features in (a) RT and vacuum, (b) 400 °C and H<sub>2</sub> and (c) 500 °C and H<sub>2</sub>. There are clearly quantised intensities associated with each feature, the measurements over nanoparticles vary because they are different sizes and thicknesses



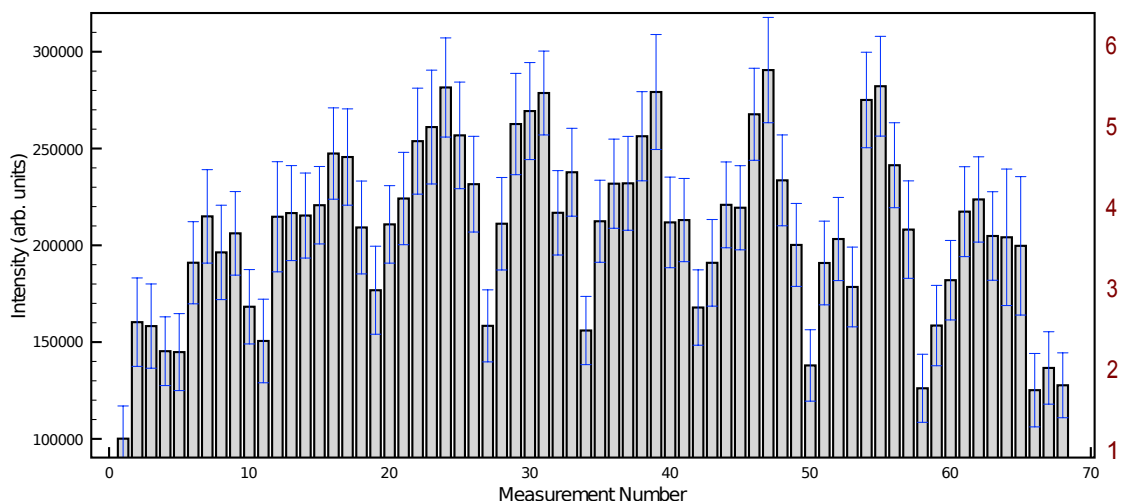
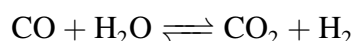


Figure 6.11: A graph showing intensity measurements from a single nanoparticle measured from approximate atomic column positions along each row. The first peak (trough to trough) represents the first row of atoms seen in the nanoparticle labelled as A in Figure 6.8(a). The second Y axis on the RHS indicates normalised intensities based on the intensities measured in Figure 6.10 and converted into atoms per column

system Au–CeO<sub>2</sub> has been found to be remarkably active in the oxidation of CO at low temperatures [338] making it suitable for removing CO in fuel cells.

Another area that is receiving much attention at the moment is the use of Au-CeO<sub>2</sub> in water–gas–shift (WGS) processes [339, 340]. The WGS reaction is an important reaction that plays a key role in the production of high purity H<sub>2</sub> for use in ammonia (NH<sub>3</sub>) production [341]. NH<sub>3</sub> is one of the commercial world’s most important chemicals because of its usefulness in the production of fertilisers. The WGS reaction is



which occurs at approximately 400 °C in the presence of an Fe<sub>3</sub>O<sub>4</sub>–Cr<sub>2</sub>O<sub>3</sub> catalyst [341]. Within the past decade, both Au and Pt WGS catalysts have been studied because of their high activity at low-temperatures (> 200 °C) [340, 342, 343, 344]. Despite the poor chemisorption properties of Au for H<sub>2</sub> at the bulk scale, Au when dispersed as < 5 nm particles or clusters has shown to be remarkably active for CO oxidation [8]. Pt is always active, regardless of size [189] but Burch and co-workers showed that a carefully prepared high dispersion Au catalyst can be at least as active as Pt based catalysts with CeO<sub>2</sub> as the support [345].

Fu et al have argued that the active phase in Au-CeO<sub>2</sub> is not the Au nanoparticles but a rather non-metallic Au species [346]. Their evidence is based on activity measurements in

which they found a similar activity for their as prepared nanoparticle Au-CeO<sub>2</sub> catalysts and leached versions which only contained atomically dispersed Au [346]. They suggest that the species Au<sup>+1</sup> and Au<sup>+3</sup> are the only species present in the leached catalyst (similarly Pt<sup>+2</sup> and Pt<sup>+4</sup>) [346]. They also believe that the presence of Au leads to weakly bound O at the surfaces which are the actual sources of the catalytic activity of the system. DFT calculations by Liu *et al* indicate that the most energetically favourable location of the active Au species is at Ce vacancies leading to an overall negative charge [347]. DFT calculations by Zhang *et al* give the most favourable adsorption energies for the mechanism proposed by Fu *et al* [348] as do surface energy DFT calculations by Tibiletti *et al* [349]. XPS measurements by Wang *et al* also support this [350]. Branda *et al* indicate that the CeO {1 1 1} surfaces may contain a dynamic mixture of Au metal and oxidised species [351].

The precise origin of the activity of Au-CeO<sub>2</sub> catalysts in the WGS context had lead to numerous studies into the practicalities of single atom catalysts. One such single atom system is Au-TiO<sub>2</sub> [180, 352] which has been earmarked as a low temperature CO oxidation catalyst and as an alternate catalyst for the WGS reaction [353]. The studies in [180, 352] have used HAADF-STEM to identify the location of atomic species on the support but only in vacuum at ambient temperature.

More recent HAADF-STEM studies of Au-CeO<sub>2</sub> catalysts have shown extraordinary atomic column intensities on Au-CeO<sub>2</sub> [85]. There have been similar studies on other systems such as Pt-FeO<sub>x</sub> [354]. With Pt-FeO<sub>x</sub> and Au-TiO<sub>2</sub>, the support is composed of light elements where the difference in *Z* between the support material and Au is substantial. The authors [352, 354], attributed the high intensities of certain atomic columns to the presence of single Au atoms on the support surface.

With Au-CeO<sub>2</sub> the atomic number of Au is 79 but Ce is 51, so the *Z*<sup>2</sup> difference is significant but not as remarkable as in the Pt-FeO [354] and Au-TiO<sub>2</sub> [352] systems. Atomic Au species had not been observed until very recently with only nanoparticles and clusters being observed with HAADF-STEM or other methods (see for example [344]). HRTEM has been previously used to image the surfaces of CeO<sub>2</sub> crystals [85, 355] showing that the O surface atoms are unstable under electron irradiation. The movement of O has not been observed using HAADF-STEM.

Abnormal intensities have been observed on Au-CeO<sub>2</sub> HAADF-STEM images taken with the JEOL 2200FS at the York-JEOL Nanocentre [85]. The purpose of that work was to observe Au in a fresh and aged catalyst to deduce the stability of the Au atoms [85].

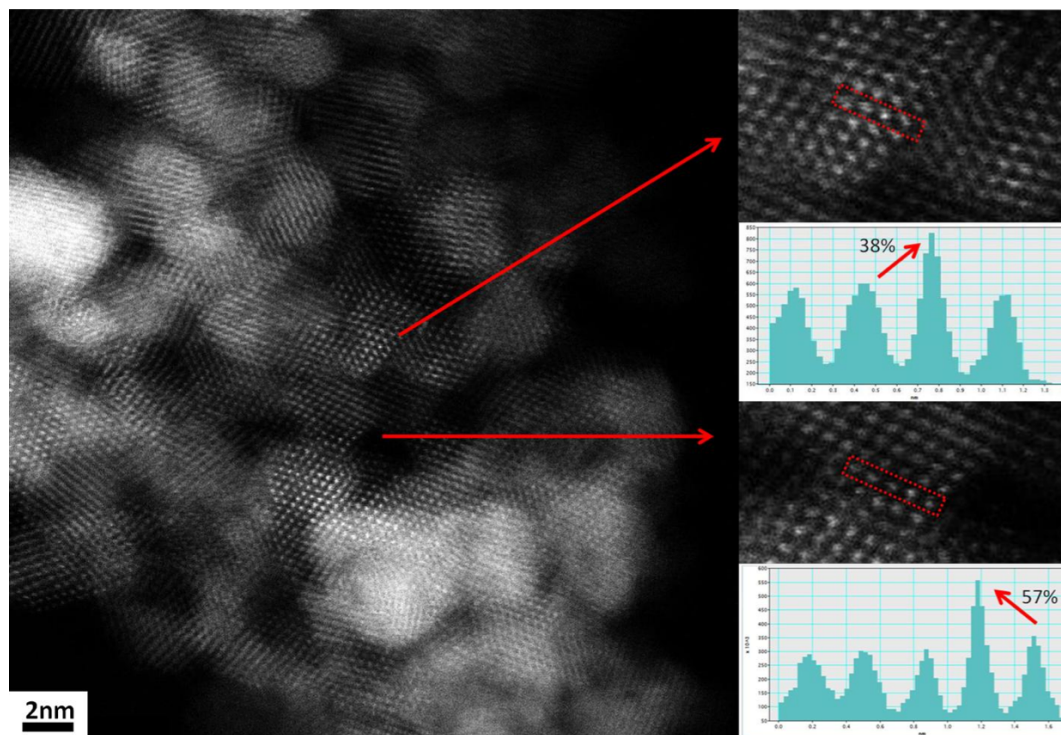


Figure 6.12: A reproduced figure from Mike Walsh's thesis (Figure 7.11, page 122) [85] showing extraordinary intensities on some of the Ce columns of  $\text{CeO}_2$ . The specimen contained small amounts of Au suggesting that these anomalous intensities were caused by Au being substituted into a Ce vacancy [85]. The purpose of the work presented in this thesis section is to verify these intensities using QSTEM HAADF-STEM simulations

One of the images from Mike Walsh's thesis has been reproduced here. Figure 6.12 shows an example of a HAADF-STEM image of the Au- $\text{CeO}_2$  catalyst showing anomalous intensities of some of the atomic columns.

The purpose of this work is to use simulation software to quantify whether the intensity difference can be explained by the presence of single Au atoms. The work is based on the evidence by Fu *et al* [346] that Au is always located at a Ce vacancy. In general,  $\text{CeO}_2$  crystals are faceted with  $\{111\}$  planes, meaning that observations in HAADF-STEM are taken from stepped surfaces, therefore it must be determined whether Au can be distinguished from a Ce atomic step. A quantitative analysis of said intensities will have important implications in the study of single atom catalysts not just being limited to Au- $\text{CeO}_2$ .

### 6.3.2 Creating the Models

The original image is a HAADF-STEM image of a leached Au- $\text{CeO}_2$  crystal in the  $[110]$  zone axis as shown in Figure 6.12. The crystals observed are approximately 10–20 atoms

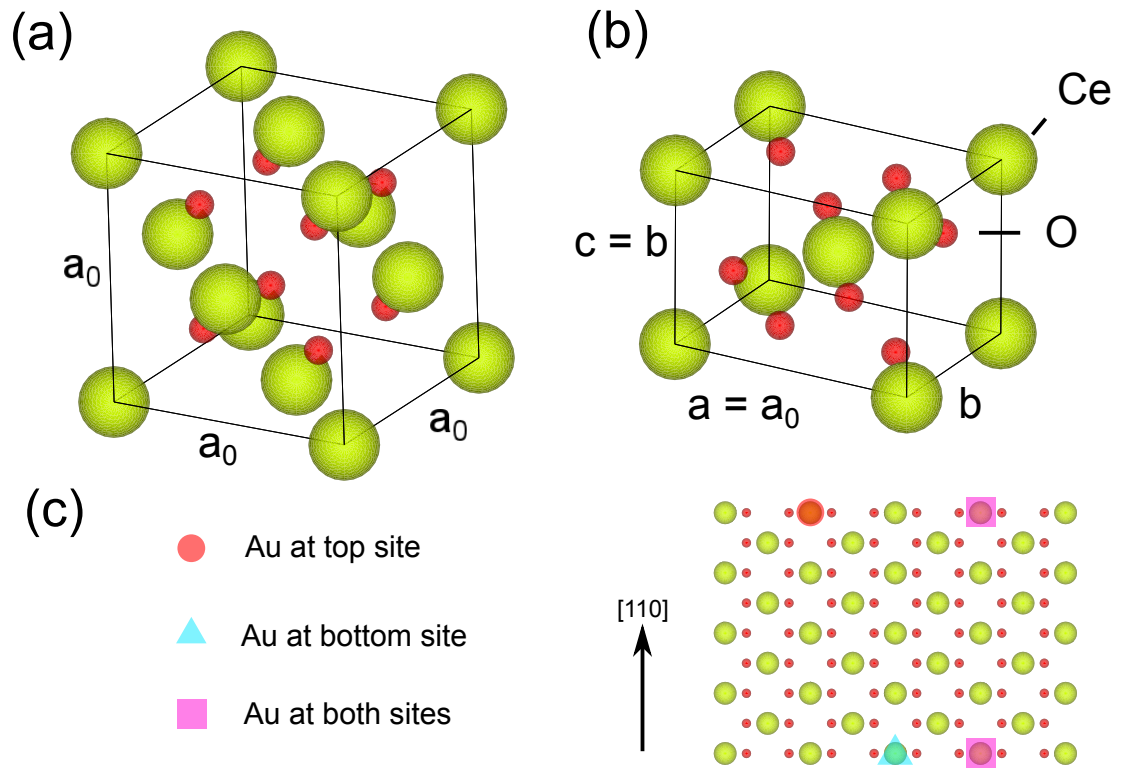


Figure 6.13: Schematic showing (a) the CeO<sub>2</sub> fluorite unit cell, (b) the newly defined tetragonal unit cell and (c) a diagram showing the types of Au capped columns on a CeO<sub>2</sub> slab with  $[1\ 1\ 0]$  facing the electron beam. Note that the  $\{1\ 1\ 0\}$  surface is stepped but only intensities from the taller columns were measured

wide so it has been assumed that the crystals are also about 20 atoms thick at most. The most likely location of the Au atom is a Ce vacancy on the surface of the crystal based on what the literature says [346].

Crystal visualisation programs use standard unit cells. CeO<sub>2</sub> has the fcc fluorite structure and lattice parameter of 0.541 nm. The fluorite CeO<sub>2</sub> unit cell when orientated into a  $[1\ 1\ 0]$  will display a cube viewed edge on. The coordinates of such a system cannot be exported and used to adequately model the CeO<sub>2</sub> crystal with a Au atom at its surface because the boundary conditions would not be preserved. A supercell had to be created.

The supercells were created by redefining the CeO<sub>2</sub> unit cell into an alternative tetragonal unit cell with two vectors lying perpendicular to  $[1\ 1\ 0]$ . This was achieved using a transformation matrix which relates the original lattice parameters  $a, b$  and  $c$  to the new ones  $a', b'$  and  $c'$ , according to the relationship

$$\begin{pmatrix} a' \\ b' \\ c' \end{pmatrix} = \begin{pmatrix} a_x & a_y & a_z \\ b_x & b_y & b_z \\ c_x & c_y & c_z \end{pmatrix} \begin{pmatrix} a \\ b \\ c \end{pmatrix} \quad (6.1)$$

where  $a_x, b_x \dots$  are numbers that define the transformation. The values these need to take

can be understood by looking at Figure 6.13. The vectors  $\mathbf{a}'$  and  $\mathbf{c}'$  are defined in terms of  $\mathbf{a}$  and  $\mathbf{c}$  in Figure 6.13(a). An  $[1\ 1\ 0]$  view of the traditional  $\text{CeO}_2$  unit cell in Figure 6.13(b) shows that  $\mathbf{b}'=\mathbf{b}$ . From these relationships the transformation matrix is then

$$\begin{pmatrix} -\frac{1}{2} & 0 & \frac{1}{2} \\ 0 & 1 & 0 \\ \frac{1}{2} & 0 & \frac{1}{2} \end{pmatrix} \quad (6.2)$$

where the indices are equivalent to those in (6.1). Entering the transformation matrix into JEMs transform unit cell function generates a structure such as the one shown in Figure 6.13(c). The new unit cell is a  $\text{CeO}_2$  slab that corresponds to the original unit cells  $\text{CeO}_2$   $[1\ 1\ 0]$  zone axis. That unit cell was exported as a .cif file and loaded into another crystal visualisation package called VESTA. The unit cell was duplicated by  $5 \times 5 \times n$  times where  $n$  was between 1 and 10 to provide a range of thicknesses. Using VESTA, the duplicated unit cell was exported as an .xyz file where the coordinates are in terms of distances and are volumetric (not fractional). JEMs could only export in fractional coordinates hence the reason for using VESTA. Using a spreadsheet program, empty space around the crystal structure was added to act as a means of ensuring the boundary conditions of the supercell. A .cfg file for use with QSTEM was then created for each model and Ce atoms substituted for Au accordingly. Finally, QSTEM configuration files (.qsc) were made by entering the appropriate parameters described in the next sub-section.

### 6.3.3 Simulation Parameters and Preliminary Simulations

In QSTEM, one enters parameters corresponding to the model of the microscope including  $C_s$ ,  $C_c$  (chromatic aberration) and  $dE$  in addition to the operational parameters  $\Delta f$  and stigmatism,  $A_1$ . Table 6.1 displays the values used in the following simulations as they are entered in QSTEM.  $A_1$  was chosen to be 0 because a good aberration correction can result in an  $A_1$  value of less than 100 pm. The TDS value represents the number of repeated simulations for which a random atomic displacement is applied according to the atom's Debye-Waller factor to account for thermal diffuse scattering. 30 runs were used for each simulation.

An important aspect of QSTEM is the the probe array which samples the atomic potentials and defines the active scattering volume of the specimen. It is shown in Figure 6.14(b) as the pink area. The larger the probe array the more accurate the simulation is because it increases the scattering area in the crystal. Its resolution determines the sampling rate of the atomic potentials and sets the effective maximum scattering angle. In the case here, a supercell is being used to represent a small lone crystal therefore a probe array of similar

Table 6.1: QSTEM simulation parameters excluding  $\Delta f$

Parameter	Value
$A_1$	0 nm
$C_s$	0.001 mm
$C_c$	1.6 mm
$dE$	0.8 eV
Pixel Array	100 x 100 pixels
Probe Array	200 x 200 pixels
Probe Array Resolution	0.04 x 0.04 Å
TDS	30
Inner Detector Angle	70 mrad
Outer Detector Angle	110 mrad

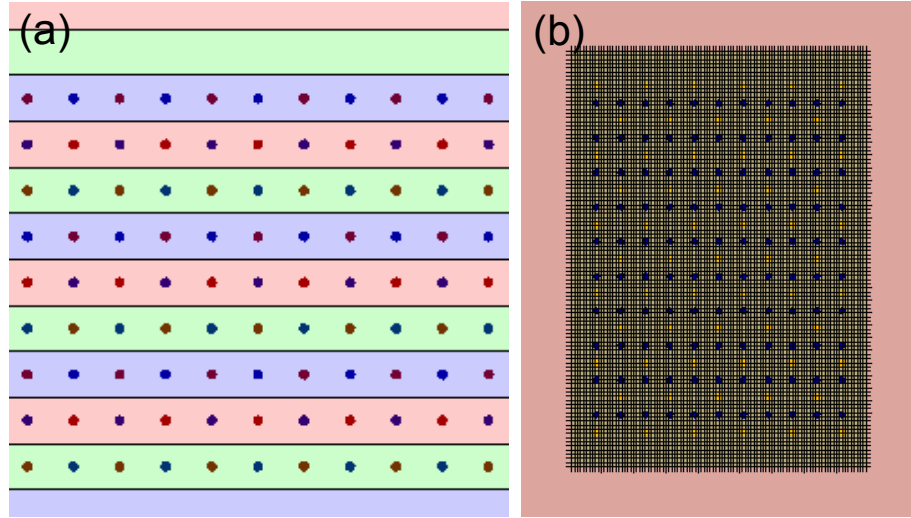


Figure 6.14: Screenshot of the QSTEM Matlab graphical user interface with (a) showing a side view of the crystal showing the slices and (b) a top view showing the pixel array (dark area) and the probe array (dark pink) area. The presence of an extra slice at the top of the model is due to the presence of the buffer zone and the ideal requirement of 1 atom layer per slice but it has no effect on the outcome

size to the supercell crystal with resolution of 0.04 Å x 0.04 Å is sufficient to produce scattering up to and beyond 170 mrad. This value (and the inner angle of 70 mrad) is the known outer angle of the York JEOL 2200FS detector. The pixel array in QSTEM is the region where an image will be computed for and hence it is the output image area. A pixel array of 100x100 was deemed a reasonable quantity to sufficiently image the atomic columns. This size of pixel array was used in all simulations in this thesis.

To investigate the effect of probe array size and the crystal size on the intensities of atomic columns, the supercell was expanded to 10x10 and 20x20 unit cells in addition to the original 5x5 supercell. Each one was 4 tetragonal unit cells thick for testing purposes because thicker cells require more computation time. Probe arrays of 100x100, 200x200,

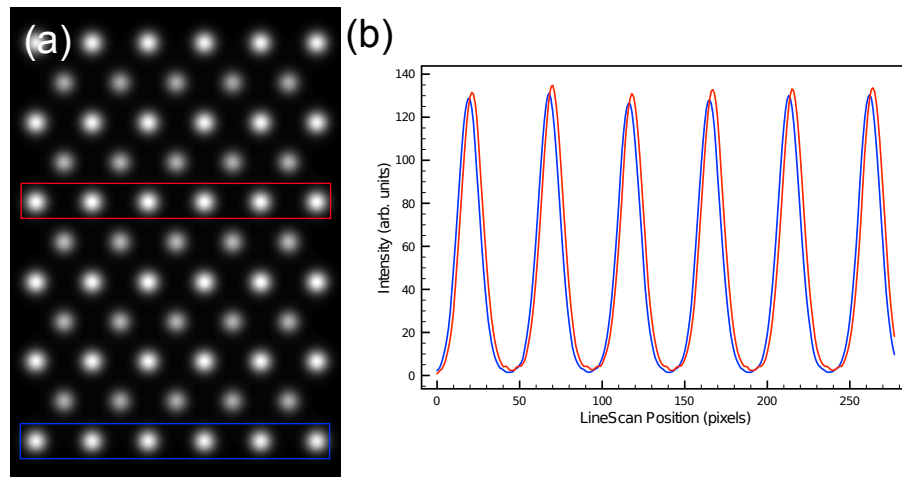


Figure 6.15: (a) QSTEM output image for a plain  $\text{CeO}_2$  slab  $5 \times 5 \times 4$  tetragonal unit cells with a probe array of  $100 \times 100$  and (b) intensity measurements from the columns indicated by colour. Note that the intensity of the central columns are slightly brighter than those near the edge. The slight difference in peak positions is caused by slight differences in the horizontal starting point of the linescans which were done manually

$400 \times 400$  and  $800 \times 800$  were tested. In all instances, plain  $\text{CeO}_2$  supercells were used and a pixel array of  $100 \times 100$  at the same location.

It was found that decreasing the probe array area resulted in slight increases in the intensities of the central columns on the  $5 \times 5 \times 4$  supercell image. Figure 6.15 shows an example of this effect. The intensities of the atomic columns near the bottom of the cell are slightly dimmer than those in the centre. This can be explained on the basis of electron scattering. Essentially the maximum amount of available scattered electrons will scatter into the region because the region around the cell is a vacuum. Similar measurements also applied to the  $10 \times 10$  and  $20 \times 20$  supercell images for probe arrays of  $100 \times 100$ . The likely cause of this is because the probe array, even in the  $20 \times 20$  supercell case does not sample the entire crystal, only the small region in the centre, so there are essentially less electrons at the edge of the crystal compared to the centre.

It was found that the intensities of the columns in the larger cells varied when the probe array size was increased. In the  $20 \times 20$  case using an  $800 \times 800$  probe array, a bright column was followed by a dimmer column in a row. An example of this effect is shown in Figure 6.16. The effect of thermal diffuse scattering in the simulations is done by the frozen phonon model which adds random displacements to all atoms depending on their Debye–Waller factor. The phenomenon of oscillating intensities seen in Figure 6.16 appears periodic but TDS is not periodic so the intensity variations cannot be explained purely by the position of atoms since approximately the same  $Z^2$  contrast rule applies for the same number of atoms in a column. This suggests that the simulation itself may be



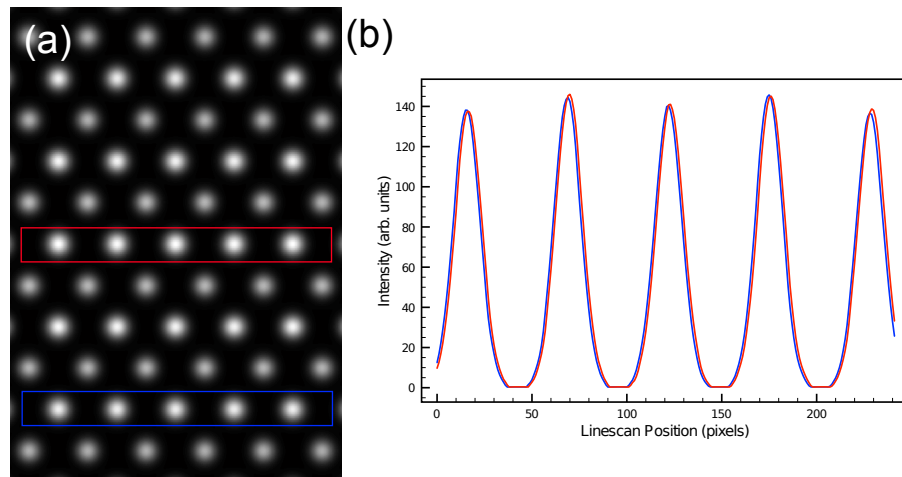


Figure 6.16: a) QSTEM output image for a plain  $\text{CeO}_2$  slab  $20 \times 20 \times 4$  tetragonal unit cells with a probe array of  $800 \times 800$  and (b) intensity measurements from the columns indicated by colour. In this case, the intensity of the atomic columns oscillates from one to another across a row but the overall intensity are similar regardless of which row the intensities are measured across

at fault but in general, the intensity difference between  $\text{CeO}$  columns are very small. In the Au capped column simulations described in the next section, the intensities of five ordinary  $\text{CeO}_2$  were measured in addition to the Au capped ones to take into account of effects of the physical interaction volume implied by Figures 6.15 and 6.16.

It was decided that a probe array of  $200 \times 200$  with resolution of  $0.04 \text{ \AA} \times 0.04 \text{ \AA}$  in the  $x$  and  $y$  plane was sufficient. Table 6.1 summarises the QSTEM input parameters for the simulations in the following section. All simulations were carried out on workstations with dual Intel Xeon E5-2630 CPUs and 64 GB 1600 Mhz DDR3 ECC RAM running 64 bit Linux Ubuntu 12.10. The Linux version of QSTEM was compiled by summer research students in the physics department of York using the QSTEM version 2.16 tarball, the latest release at the time.

### 6.3.4 Au Capped Simulation Results

#### Effect of Convergence Angle

The range of convergence angles available on the 2200FS at the York-JEOL Nanocentre was between 14 mrad and 30 mrad as determined by Leonardo Lari. To explore the effect of convergence angle on the appearance of substitutional Au atoms, the 4 unit cell thick model described before was calculated for a range of convergence angles at a fixed defocus of 0. The result, expressed in terms of the difference in intensity between the Au capped



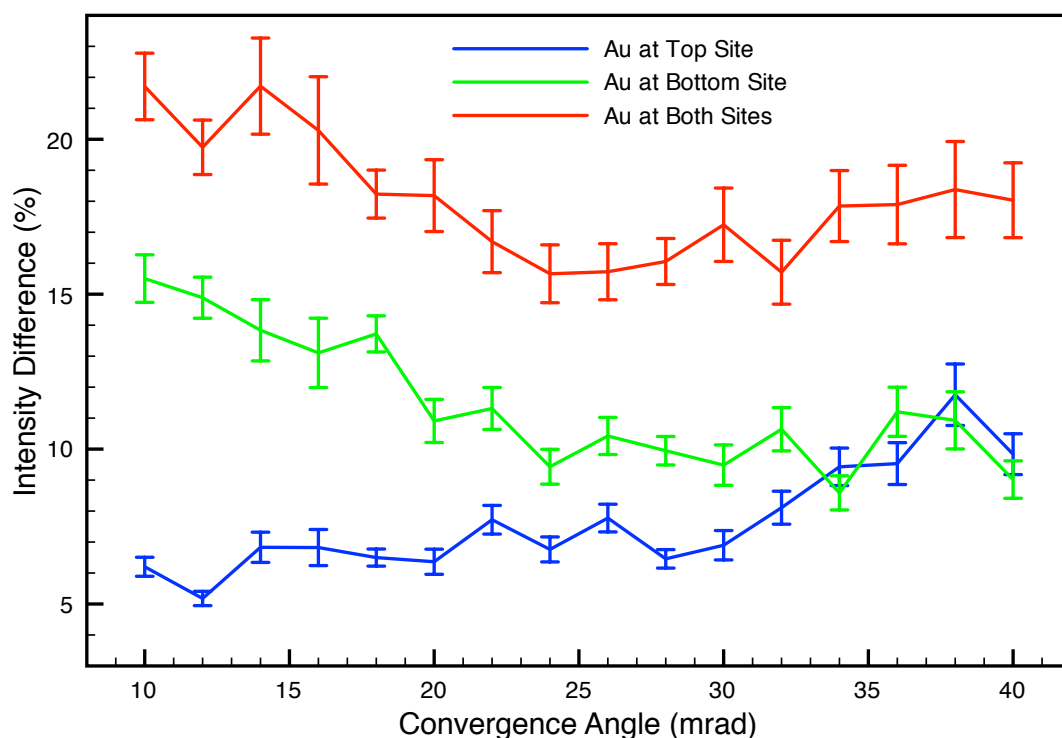


Figure 6.17: Effect of convergence angle on the intensity difference % between top, bottom and both top and bottom Au capped Ce atomic columns compared to normal Ce columns

columns and the normal Ce columns is shown in Figure 6.17. The output images are similar to those in Figure 6.19 and are not shown. The results shown in Figure 6.17 indicate that as the convergence angle is decreased there is a larger difference between the Au capped columns and the ordinary Ce columns. This could be because of increased channelling effects. In practice, the signal received by the HAADF-STEM would be lower for the smaller apertures and this would require the adjusting of the detectors brightness and contrast settings.

### Effect of $dE$

The 4 atom thick model was recalculated using different  $dE$  values including the real value of 0.8 eV. Values used were 0.2 eV to 1.2 eV in 0.2 eV steps. Intensity values of either Ce columns or Au capped columns gave virtually identical results shown graphically in Figure 6.18 suggesting that the  $dE$  values used here are not sufficient to lead to noticeable differences. With the advent of high resolution environmental STEM, the effect of energy loss via the gas medium may be worthy of further study if atomically dispersed catalysts are studied via *in-situ* environmental techniques.

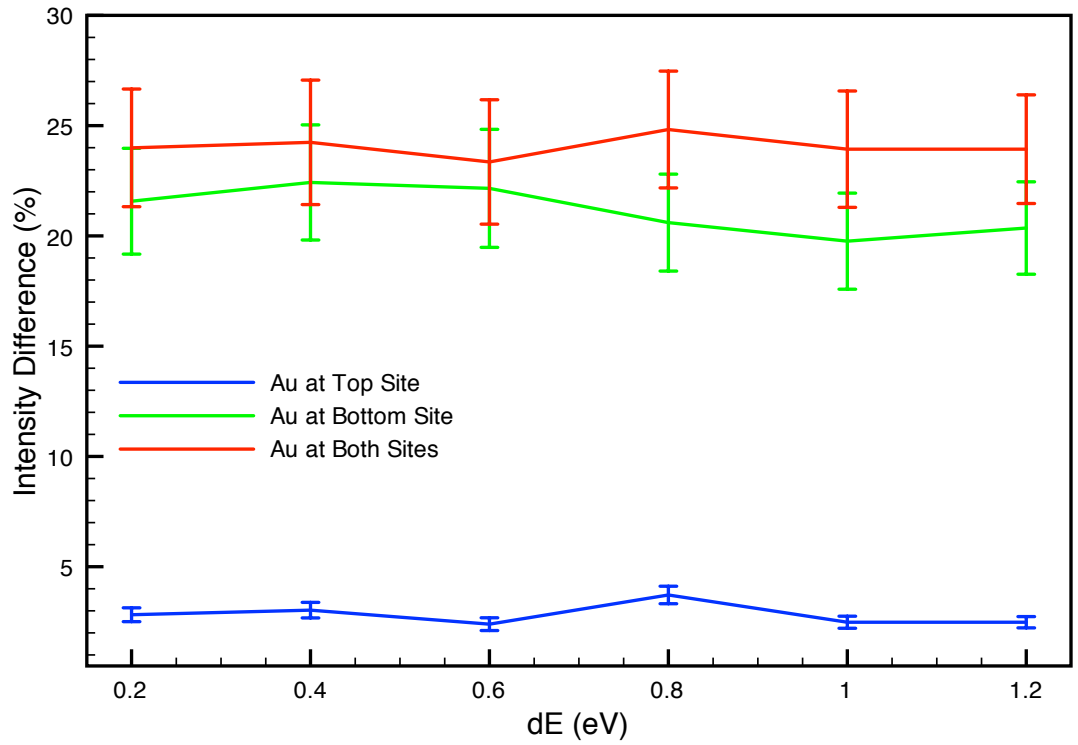


Figure 6.18: Graph showing measured intensity difference on Au terminated columns with different  $dE$  values. The results imply there is virtually no difference in measured intensities

### Effect of Location and Defocus

Initially, to check the effect of atomic location, individual models were created for Au atoms located at the top, bottom and both of the Ce columns. A model that included all three atoms give identical results to the three separate previous models regardless of position. Therefore, the latter model with all three types of Au sites was used to reduce overall simulation and analysis time.

Figure 6.19 shows some examples output images from QSTEM simulations of different  $\Delta f$  (defocus) values and thicknesses. The figures show that at a given  $\Delta f$ , 0, the intensity of the Au terminated columns become increasingly difficult to distinguish from the ordinary Ce columns regardless of where the Au is located. The percentage differences in intensity were measured from the images in Figure 6.19 are shown as graphs in Figure 6.20 which show the effect of thickness and  $\Delta f$  on the intensity differences.

In Figure 6.20, it can be seen that increasing the thickness of the crystal reduces the intensity difference of the Au capped columns relative to the ordinary Ce columns. As the crystal approaches 3 nm thick, equivalent to 5 tetragonal unit cells thick, at  $\Delta f = 0$  the Au

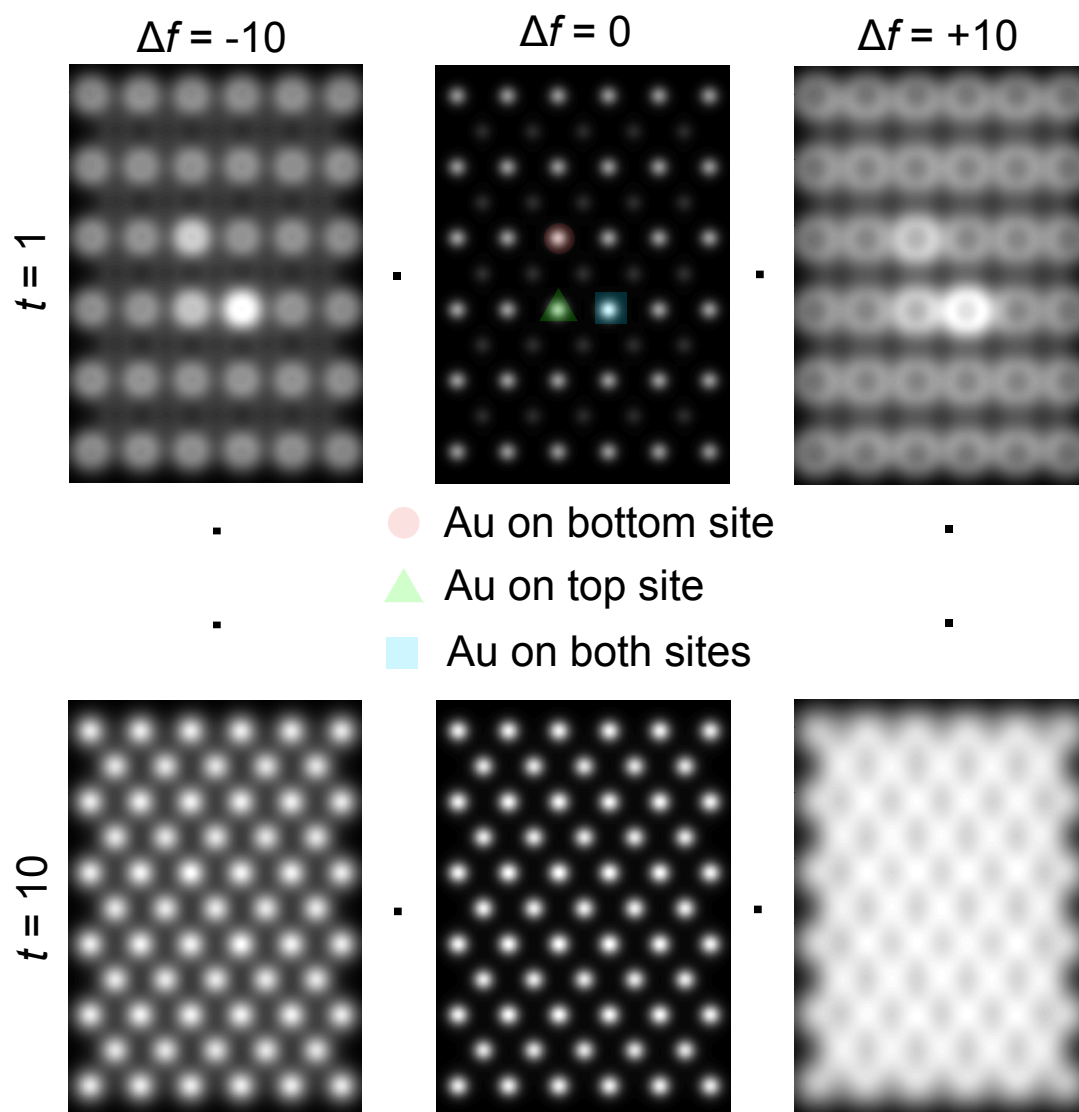


Figure 6.19: Montage of QSTEM output images starting at 1 tetragonal unit cell thick and ending at 10 tetragonal unit cells thick

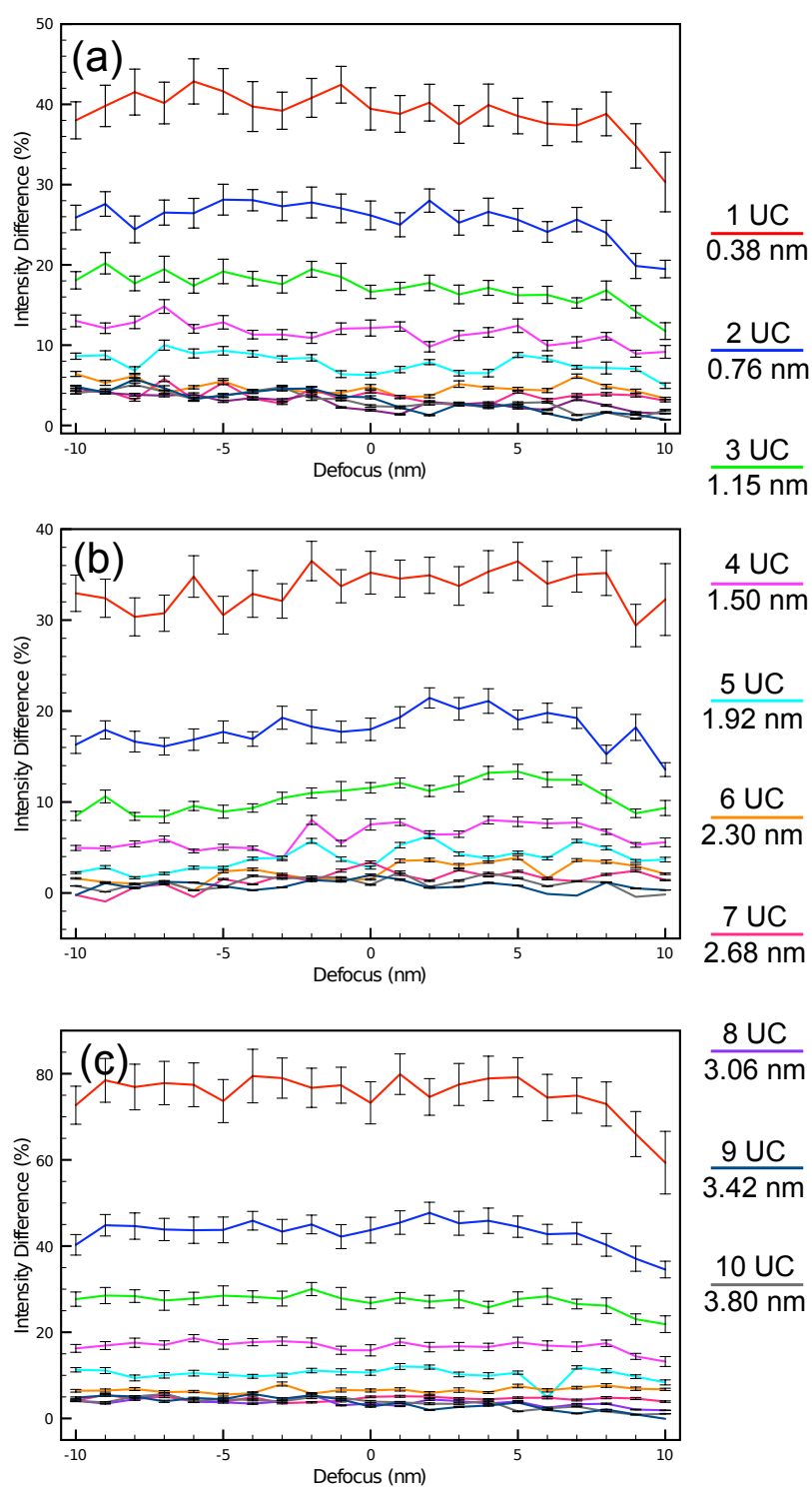


Figure 6.20: Series of graphs showing intensity differences between Ce atomic columns terminated by Au at Ce vacancies located at (a) at the top of the crystal, (b) at the bottom of the crystal and (c) both sites at different defocus,  $\Delta f$  and thickness

column is virtually indistinguishable from the ordinary Ce column regardless if two Au are located on the same column.

The  $\Delta f = 0$  case shows that Au atoms located at the bottom of the crystal appear much brighter than those at the top. At most, the difference is 40 % with the thinnest crystal equivalent to just 0.3 nm thick regardless if the Au is on the bottom or top. If on both, the column is almost 90 % brighter.

Still considering the  $\Delta f = 0$  case it can be seen from Figures 6.20(a), (b) and (c) that as the crystal approaches 6 unit cells thick, which is approximately 3 nm thick, the intensity difference, regardless of position, becomes very small. This makes Au almost indistinguishable from the other columns. The intensity difference drops much quicker for the Au located at the top site suggesting that the beam scatters and spreads more as the amount of atoms it must transverse increases. The imaging of the Au located at the bottom of the crystal may encourage channelling effects due to a sharper probe which penetrates through the crystal.

In all instances, regardless of thickness, the difference in intensities drops when  $\Delta f$  is increased to 8 nm and the general appearance of the crystal appears to become more spread out. The mirror image of the positive defocus values produce different image contrast on the negative side. This is because the 0 defocus position is at the top of the crystal, therefore, the negative defocus probe positions are further away from the crystal.

The defocus adjusts the intensities only slightly by about 5 % at most, even in the case where Au is located at the top. This is presumably because the defocus value adjusts where the beam is focused on. If the beam is centred about the top of the crystal, the beam will diverge by the time it reaches the bottom of the crystal. If focused at the bottom of the crystal the beam will converge through the material so atoms in the column will see a narrower beam which may encourage channeling effects more so than a diverging beam which is focused at the top of the crystal. The intensity difference is greater in the instance where Au is located at the bottom. This is because the beam focused here, despite transversing several other unit cells, will produce the most intense signal from the bottom crystal which goes virtually unhindered into the detector from the crystal exit surface.

## 6.4 Discussion

The results show that increasing the thickness of the crystal beyond 4 nm causes the difference in intensity between Au terminated Ce columns to become virtually indistinguishable. The 40 % difference observed in [85] can only be explained by the presence of Au located at the bottom and top of an atomic column of a crystal less than 4 tetragonal unit cells thick which is about 2 nm.

In all situations, Au located at the top of an atomic column was never as bright as one located at the bottom of the crystal. This could be because by the time the electrons exit the specimen they have re-scattered because of TDS essentially smearing out the original scattering from the top atom.

Although comparisons between the simulations and experimental images have provided some insights, a direct comparison between the two is not possible without a complete understanding of the image processing that occurs with the HAADF-STEM detector. QSTEM images are in absolute intensity, plotted as a function of the initial probe intensity whereas the experimental images have been processed and adjusted using various brightness and contrast settings, some automatic.

## 6.5 Conclusions

Aberration corrected atomic resolution HAADF-STEM with environmental and heating capability has been demonstrated for the first time. Specimens were prepared specifically for purpose and have provided insights into the behaviour of nanoparticles and atoms under the influence of heat and gas with atomic resolution.

The clusters of Pt-Pd were found to be unstable during exposure to the electron beam. Furthermore, atoms were observed to hop to and from nanoparticles, no stable individual atoms on the support were observed. Exposure to gas resulted in contamination becoming an issue, even with additional beam showering but heating the specimen to 300 °C nullified contamination from an imaging point of view.

No difference was detected regarding the shape and size of nanoparticles in H<sub>2</sub> at 300 °C without the electron beam but noticeable effects, primarily in the growth and faceting of clusters was observed at 600 °C without continuous exposure to electrons. This results suggests that the electron beam influences the specimen more so than the gas

and therefore future investigations into similar specimens in gas and under the influence of heat should have their exposure to the electron beam minimised.

Simulations of single atom catalysts, namely Au on CeO<sub>2</sub> have shown that large intensity differences between ordinary Ce columns and Au terminated columns can only be explained if the crystal is thinner than 3 nm.

# Chapter 7

## *In-situ* Co<sub>3</sub>O<sub>4</sub> Reduction in H<sub>2</sub>

### 7.1 Introduction

The reduction of Co<sub>3</sub>O<sub>4</sub> to Co is required for the activation of a Fischer-Tropsch process catalyst. There have been several studies on the reduction process using E-TEM and most of them detect the presence of a distinct intermediate phase in the form of CoO [296, 297, 298]. Despite this, it is not known precisely how Co<sub>3</sub>O<sub>4</sub> transforms to Co and if that transition effects the structural changes of the final catalyst compared to a single step reduction. This chapter contains results an environmental AC-HRTEM H<sub>2</sub> reduction study of model (unsupported) Co<sub>3</sub>O<sub>4</sub> and provides new insights into the transformation mechanism from Co<sub>3</sub>O<sub>4</sub> to CoO.

### 7.2 Specimen Preparation and Characterisation

The Co<sub>3</sub>O<sub>4</sub> material used in this study was Aldrich brand Co<sub>3</sub>O<sub>4</sub> fine powder. For (S)TEM specimen preparation, the powder was added to a small amount of ethanol and underwent ultrasonic treatment for 120 s. For *in-situ* studies, the powder was crushed using pestle and mortar and an empty Ti or Cu grid moved through it.

Figure 7.1 shows a TEM image and selected area diffraction (SAD) pattern of the as prepared Co<sub>3</sub>O<sub>4</sub> specimen on a holey-C grid. The crystals were often found in clumps. Individual crystals had diameters of approximately 50 nm. SAD revealed the presence of a single phase: Co<sub>3</sub>O<sub>4</sub>. The low spatial frequency of the {1 1 1} reflections at 2.15 nm<sup>-1</sup> is a useful characteristic of Co<sub>3</sub>O<sub>4</sub> which enables it's presence to be distinguished from CoO whose {1 1 1} spatial frequencies are similar to Co<sub>3</sub>O<sub>4</sub> {2 2 2}.



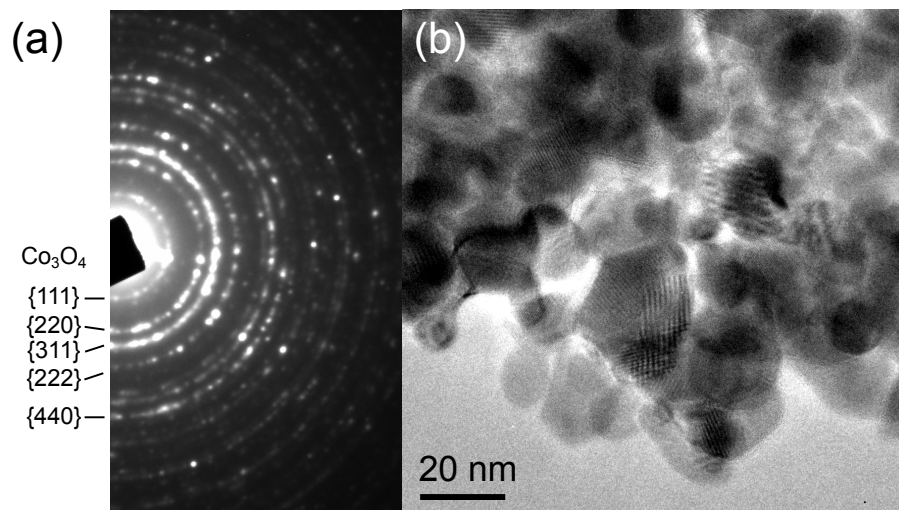


Figure 7.1: SAD pattern (a) and TEM image (b) of a typical region observed in the as prepared  $\text{Co}_3\text{O}_4$  powder catalyst supported on holey-C. The ring diffraction pattern was indexed only as  $\text{Co}_3\text{O}_4$  confirming that other phases of Co oxides are not present

A faint incomplete ring at  $2.50 \text{ nm}^{-1}$  corresponds to  $\text{Co}_3\text{O}_4 \{002\}$  which is a forbidden reflection according to the structure factor. Its presence can be explained by double diffraction of, for example, the  $\{\bar{1}\bar{1}1\}$  and  $\{111\}$  reflections. In Figure 7.1 the  $\{022\}$  and  $\{044\}$  are the brightest as predicted by the structure factor and suggesting that  $\text{Co}_3\text{O}_4$  is high quality with a generally well ordered structure.

### 7.3 HRTEM and Diffraction Reduction Sequences

Figure 7.2 shows a HRTEM image and FFT sequence of a  $\text{Co}_3\text{O}_4$  crystal at different temperatures during exposure to  $\text{H}_2$  *in-situ*.  $\text{Co}_3\text{O}_4$  was easily identified from other phases because of the presence of large  $0.47 \text{ nm } \{111\}$  atomic plane spacing. In the FFT, the 002 reflections are present despite being considered forbidden suggesting double diffraction. The crystal shown in Figure 7.2 at room temperature is rounded at the right side suggesting the presence of low symmetry atomic planes which contain kinks and steps. Kinks and steps are known to act as nucleation sites and encourage the adsorption and breaking of H–H bonds [174]. Potoczna-Petru and Kepinski [298] have also suggested that rounded  $\text{Co}_3\text{O}_4$  crystals (similar but larger to the ones presented here) are more likely to contain defects at the surface. They make reference to the work of Paryjczak *et al* [356] who found that the synthesis temperature of the  $\text{Co}_3\text{O}_4$  crystals had an impact on the onset reduction temperature to CoO because the synthesis temperature correlated to the quality of the crystal facets.

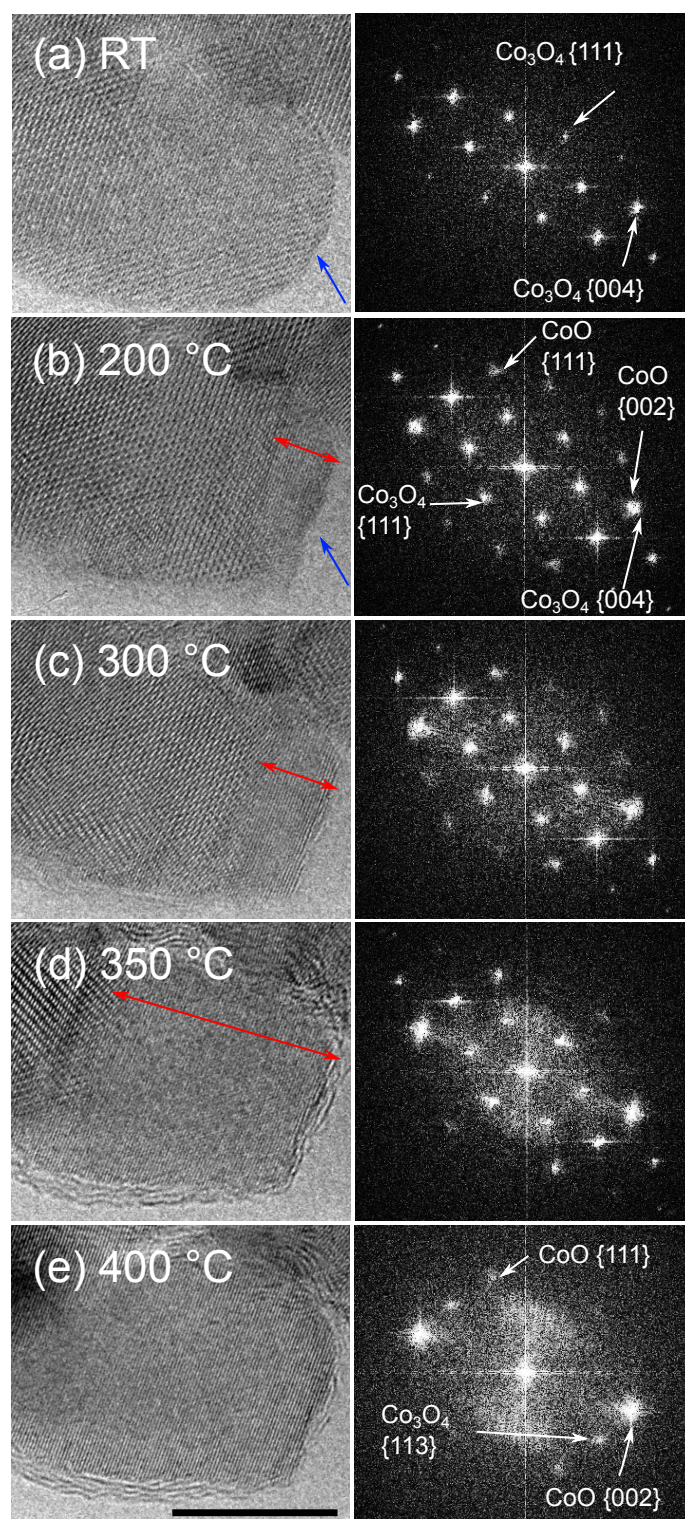


Figure 7.2: *In-situ* HRTEM image sequence with corresponding FFTs of a 20 nm wide  $\text{Co}_3\text{O}_4$  crystal undergoing reduction in  $\text{H}_2$  at the temperatures indicated. Scale bar in (e) is 5 nm and applies to all images. For reference,  $\text{Co}_3\text{O}_4$   $g_{004} = 4.95 \text{ nm}^{-1}$

Increasing the temperature to 150 °C resulted in no structural changes but the Cu grid had buckled slightly leading to a change in orientation of the crystal producing HRTEM images with different contrast. At 200 °C the first signs of structural change were observed. Bulavchenko *et al* [297] also observed the initial signs of transformation at 190 °C. XRD analysis of their as prepared Co<sub>3</sub>O<sub>4</sub> suggested the presence of octahedral vacancies and they believe that at 190 °C, CoO is formed because the crystal will try and fill the vacancies [297].

Figure 7.2(b) shows that the crystal previously with a rounded edge in Figure 7.2 (a) has become faceted at 200 °C. The new surface is terminated by CoO {002} although it is not a perfect surface with some (arrowed) steps remaining. This onset of reduction was observed to occur primarily at stepped surfaces. It could be initiated by the exposure of octahedral vacancies as suggested by Bulavchenko *et al* [297]. Potoczna-Petru and Kepinski also believe this to be true [298]. The FFT shows distorted Co<sub>3</sub>O<sub>4</sub> {002} and {004} reflections. The broadness of the {004} reflection suggests the presence of CoO which has {002} spacings within 1 % of Co<sub>3</sub>O<sub>4</sub> {004}. The CoO region penetrates approximately 3.4 nm into the Co<sub>3</sub>O<sub>4</sub> crystal. This is approximately 6 unit cells of CoO. The FFT implies the lattice parameter varies across this region and it can be seen that there is a grain boundary between the modified edge and the rest of the Co<sub>3</sub>O<sub>4</sub> structure. The 6 % difference between the doubled CoO unit cell and the Co<sub>3</sub>O<sub>4</sub> can be expected to cause strain in this region.

Increasing the temperature up to 300 °C caused the CoO region to spread deeper into the Co<sub>3</sub>O<sub>4</sub> crystal; maintaining an almost perfect epitaxial grain boundary as it did at 200 °C. The distance penetrated into the Co<sub>3</sub>O<sub>4</sub> was 6.1 nm at 300 °C, double what it was at 200 °C. The FFT in Figure 7.2(c) was taken from the region about the boundary but separate FFTs (not shown) confirm the right hand side of the crystal is CoO. At this temperature, it was also observed similar events taking place primarily at the edges of other rounded differently sized crystals. Flat facets (e.g {111} and {200}) on the other hand remained unchanged during the reduction process. There seems to be a correlation between low symmetry faces and the reduction onset temperature which seems to be consistent with Potoczna-Petru and Kepinski's [298] investigation.

At 350 °C there is a dramatic change in the appearance of the crystals. The CoO region has moved further into the Co<sub>3</sub>O<sub>4</sub> crystal with the penetration being 15 nm. On the left hand side of the crystal, dramatic contrast can be observed. The previous images suggest that there are multiple crystals here with slight orientation differences between them. The

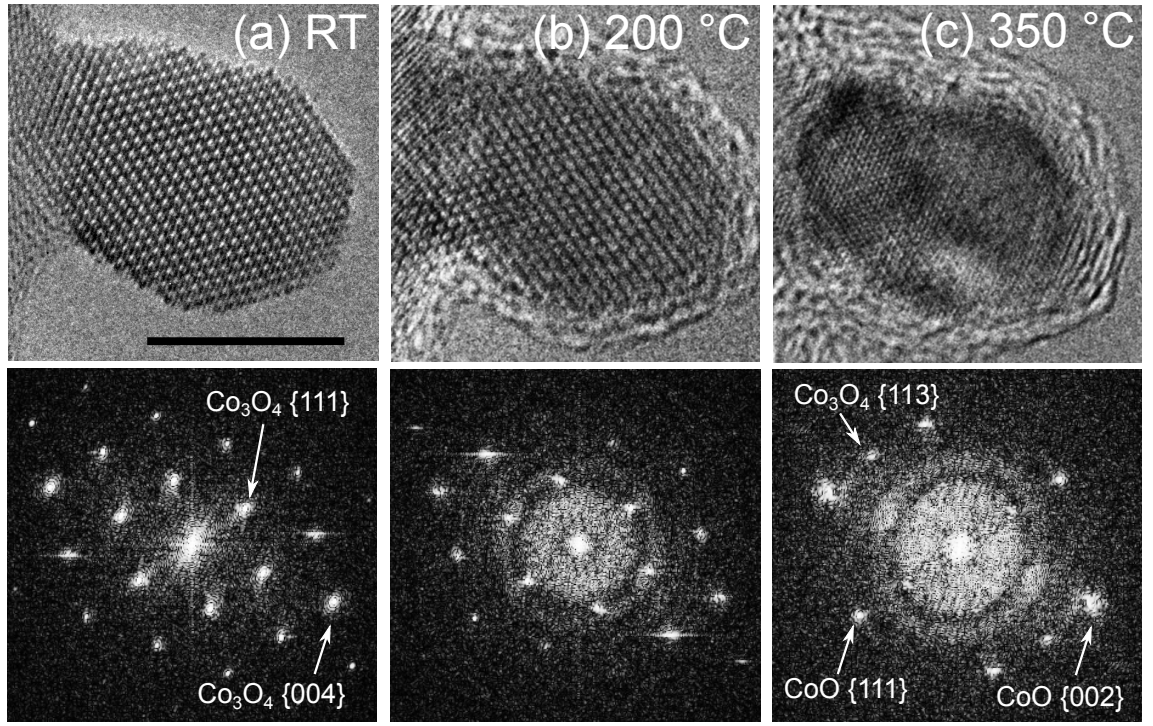


Figure 7.3: *In-situ* HRTEM image sequence with corresponding FFTs of a 12 nm diameter  $\text{Co}_3\text{O}_4$  nanoparticle which reduces to CoO at 350 °C without forming any detectable defects or the interface like structure seen in Figure 7.2

unusual contrast seen on the left hand side (and elsewhere) is due to the presence of Moiré fringes. The FFT shows no unusual spacings which confirms the effects seen are Moiré fringes. Moiré fringe width  $D$  can be calculated using equation (2.10). The Moiré fringes in Figure 7.2(d) produce effects in the  $[1\bar{1}1]$  direction and  $[13\bar{1}]$  direction. The Moiré fringes can be explained by the overlap of the strong CoO  $\{002\}$  planes in the smaller crystal and the  $\text{Co}_3\text{O}_4$   $\{113\}$  planes in the large parent crystal.

At 400 °C, the crystal that was initially  $\text{Co}_3\text{O}_4$  as shown in Figure 7.2(a) is now completely CoO as shown in Figure 7.2(e). The surrounding region is also CoO. Moiré fringe contrast seen at 350 °C was also observed at 400 °C but only in regions greater than 30 nm wide. The larger crystals had structures resembled Figure 7.2(b-d) with CoO located near the edge and  $\text{Co}_3\text{O}_4$  being located near the centre. The resultant overlap produced Moiré fringes in the central regions of crystals larger than 20 nm. It is likely that CoO has formed on the top surfaces which give rise to the Moiré fringes. Potoczna-Petru and Kepinski [298] and Dehghan *et al* also observed similar Moiré fringe effects in most of their nanoparticles larger than 20 nm. Here, Moiré fringes were not observed on smaller crystals because the CoO transformation was much more rapid.

Nanoparticles smaller than 15 nm were observed to reduce completely to CoO at lower

temperatures, namely 350 °C. An example is shown in Figure 7.3, it shows a spherical nanoparticle approximately 12 nm in diameter. The crystal in Figure 7.3 has stepped surfaces but even after reduction the stepped surfaces remain. This occurs because the contribution of edge and corner atoms to the free energy of nanoparticles is significant for smaller nanoparticles. It was found that  $\text{Co}_3\text{O}_4$  particles larger than 20 nm regardless of initial shape became more faceted as they were reduced to CoO.

In Figure 7.4 (a), the TEM image shows the central region of a crystal which has a maximum width of  $\sim 50$  nm. Figures 7.4(b-e) shows a selected area diffraction sequence of Figure 7.4(a) at the temperatures indicated. There are no major changes at temperatures below 300 °C except for a slight change in orientation of the crystal resulting in small differences between the diffracted intensities.

At 300 °C, faint CoO reflections can be identified in the diffraction pattern. The differences in reciprocal lattice vectors is more apparent for the higher order reflections (e.g.  $\text{Co}_3\text{O}_4$   $\{444\}$  and CoO  $\{222\}$ ). As in the previous cases in Figure 7.2 and Figure 7.3, the  $\text{Co}_3\text{O}_4$  and CoO crystallographic directions are epitaxial with no obvious rotation between the two different crystals. i.e.  $\{002\}$  and  $\{111\}$  faces between the two materials was observed to be always parallel to each other.

It can be seen that although there are no major structural changes up until 300 °C, the  $\text{Co}_3\text{O}_4$   $\{111\}$  planes gradually lose their intensity at the expense of the  $\text{Co}_3\text{O}_4$   $\{004\}$  and CoO  $\{002\}$  reflections. It is well known that electron diffraction intensities can vary as a function of crystal thickness but also the tilt of the crystal with respect to the beam. The diffraction patterns shown in Figure 7.4 are approximately between 3 – 5° out of the exact  $[110]$  zone axis. The structure factor for spinel materials predicts that  $\{440\}$  reflections should be the most intense, followed by  $\{400\}$  and  $\{113\}$  reflections. At 300 °C the most intense reflections are  $\{400\}$  followed by  $\{113\}$ . Using JEMs, the diffraction pattern was simulated (see next section) suggesting that any major difference between predicted and observed intensities can be explained by the crystal tilt as opposed to the presence of point defects observed by Casas-Cabanas *et al* [290].

The  $\text{Co}_3\text{O}_4$   $\{004\}$  and  $\{440\}$  reflections become significantly brighter and broader at 400 °C suggesting bulk transformations to CoO have taken place. By 450 °C the transformation is complete and the crystal has orientated itself closer to the CoO  $[110]$  zone axis leading to more typical intensities in the different reflections.

Despite heating the area up to 500 °C no Co formation was observed suggesting that



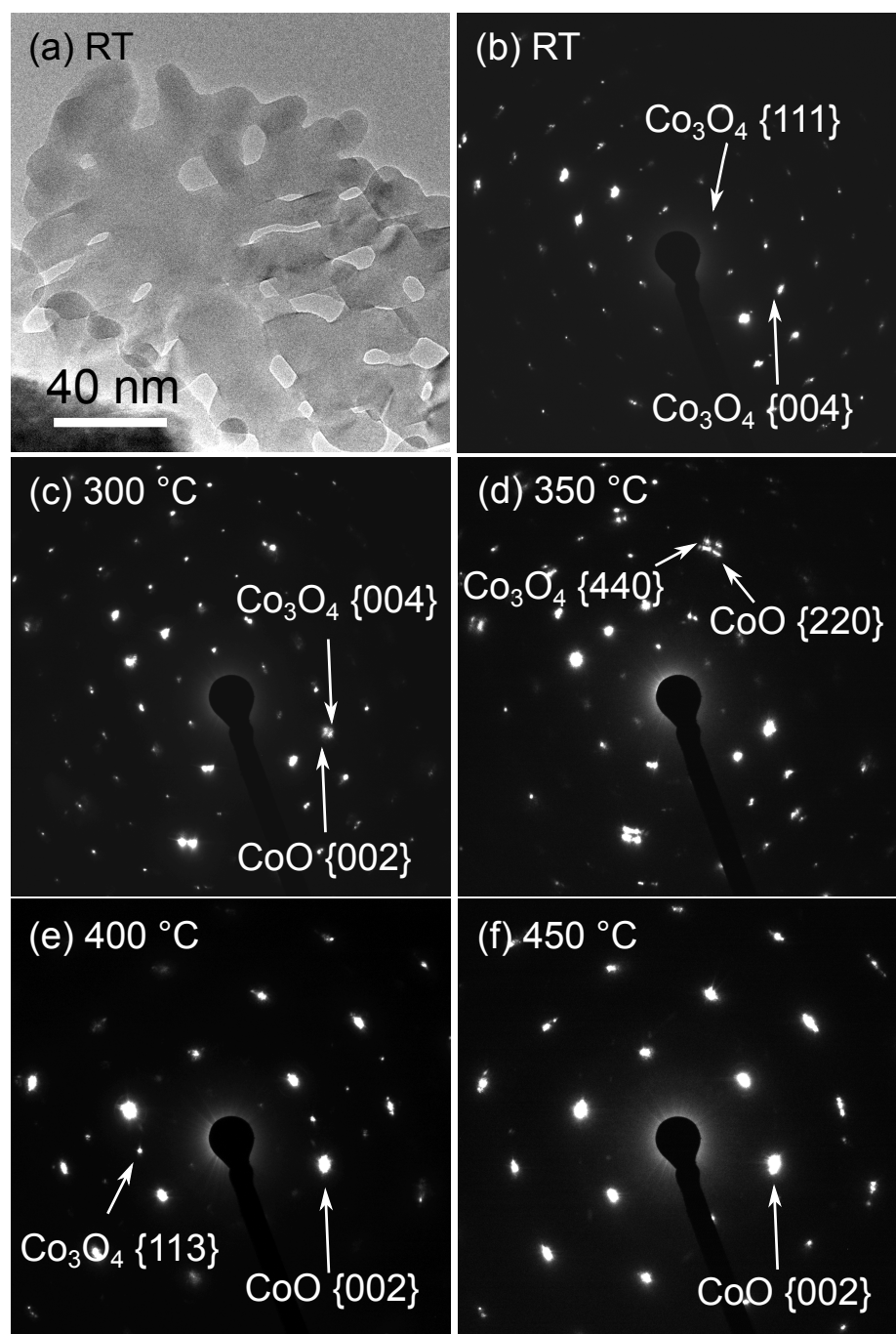


Figure 7.4: *In-situ* SAD sequence of the 50 nm crystal seen in (a). Faint CoO reflections appear at 300 °C and as the temperature increases they become more dominant. Not shown is the 500 °C diffraction pattern because it is virtually identical to the 450 °C shown in (f)

the relatively low  $H_2$  pressure (designed to be increased with further microscope development) is insufficient to facilitate the reduction of CoO. Previous *in-situ* studies using similar low pressure also did not observe the formation of Co. An example of such a study is by Li *et al* [357] who used *in-situ* (1.3 mbar  $H_2/N_2$ ) HAADF-STEM to observe the reduction of Ru promoted  $Co_3O_4$ . Despite the presence of a promotor, they observed the formation of CoO and CoRu particles but never Co on its own [357]. Bulavchenko also observed this trend when using a low  $H_2$  partial pressure mixture of  $H_2$  and  $N_2$  in their *in-situ* experiments [297].

Dehghan *et al* [301] found that after they finished their reduction experiment and reduced the temperature down to room temperature, they noticed that their Co/CoO re-oxidised in  $H_2$ . They found that  $Co_3O_4$  formed after a few minutes suggesting that residual O at the surface (which have not been removed due to the formation of  $H_2O$ ) has re-bonded with Co metal at the surface. Potoczna-Petru and Kepinski's study also observed this trend but it was far more dramatic with core-shell structures being observed [298]. The study in [298] was *ex-situ* so the re-oxidation in air could have enhanced this re-oxidation. There is still some debate over whether re-oxidation is detrimental to the activity of Co Fischer-Tropsch catalysts [287].

## 7.4 Simulations

HRTEM and diffraction simulations were carried out using the JEMs HRTEM simulation package. The purpose of the simulations was twofold: first, determine if the contrast observed in some of the HRTEM images were due to the presence of a defect, such as a stacking fault, or because of defocus/thickness effects; and second, to determine if the thickness/tilt of the crystal could explain the observed intensities of the  $Co_3O_4$   $\{1\ 1\ 3\}$ ,  $\{4\ 0\ 0\}$  and  $\{4\ 4\ 0\}$  reflections in the diffraction patterns.

Using the Laue Circle tool in JEMs, tilt was added before image calculation using  $Co_3O_4$  (ICSD 28158 [358]) and CoO (ICSD 624575)  $[1\ 1\ 0]$  HRTEM images using settings corresponding to the microscope. The width of the crystal varies between 25 nm and 30 nm so these were used as the thicknesses of the crystal for the simulations. The  $Co_3O_4$  and CoO ICSD files were loaded separately into JEMs. Based on HRTEM observations, it was assumed that the crystal thickness for  $Co_3O_4$  was on the order of 30 nm. Microscope parameters were chosen to represent the York-JEOL Nanocentre JEOL 2200FS as closely as possible. These are shown in Table 7.1 as they were entered into JEMs microscope

Table 7.1: JEMs simulation parameters

Parameter	Value
$C_s$	$-0.001$ mm
$C_5$	2 mm
$C_c$	1.6 mm
$dE$	0.8 eV
Accelerating Voltage	200 kV
Lens Stability	1 ppm

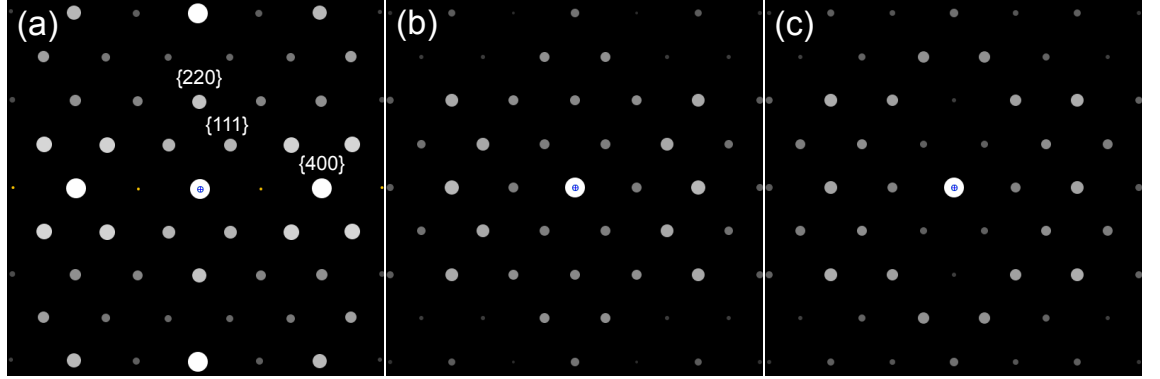


Figure 7.5: Simulated electron diffraction patterns of  $\text{Co}_3\text{O}_4$  using JEMS with different conditions. (a) is the default two-beam case, (b) all beam dynamical calculation for a crystal 15 nm thick and (c) the same as (b) but for a crystal 30 nm thick. Note that double diffraction has been included because most experimental images and diffraction patterns show the forbidden  $\{002\}$  reflections

settings.

Figure 7.5 shows electron diffraction patterns calculated in JEMS. The diffraction pattern in (a) is the default appearance of the diffraction pattern which does not take into account the thickness and uses a two-beam approach. The very small spots in frame (a) are forbidden reflections which are included in the calculation for (b) and (c). Both (b) and (c) are all beam dynamical calculations but the crystal thickness is 15 nm and 30 nm for (b) and (c) respectively. The diffraction patterns in Figure 7.5 demonstrate that as expected intensities in the diffraction pattern change because of the crystal thickness, even before the inclusion of tilt.

Figure 7.6 shows electron diffraction patterns out of the zone axis by (a-c)  $3.80^\circ$  and (d-f)  $4^\circ$  in different directions to replicate the observed intensities shown in Figure 7.4. The same approach was used to replicate the FFTs shown in Figure 7.3 and in general the simulated electron diffraction pattern agrees with the FFTs. The simulated electron diffraction shown in Figure 7.6(a-c) generally agree with the observed intensities in the experimental electron diffraction pattern (Figure 7.4(b)) at room temperature. However, the experimental intensities seen at  $300^\circ\text{C}$  and above in Figure 7.4(c-e) could not be replicated. The



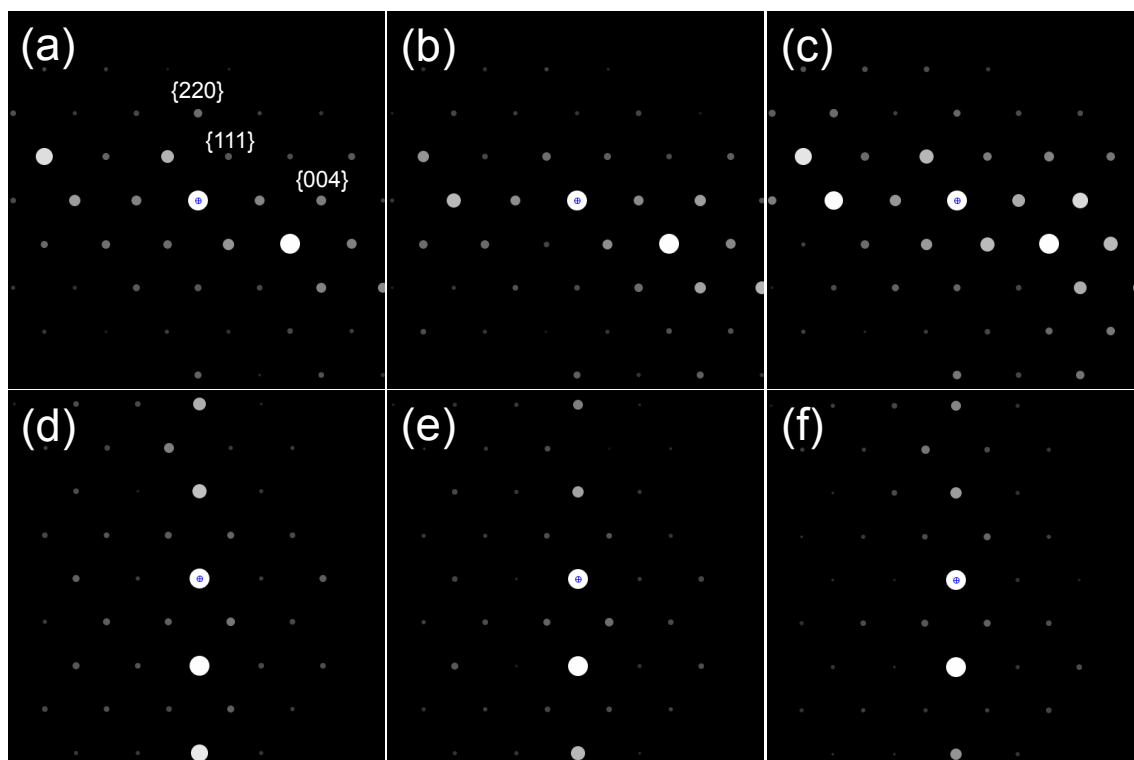


Figure 7.6: Simulated electron diffractions of  $\text{Co}_3\text{O}_4$  using JEMs all using all beam dynamical calculations for (a,d) kinematical conditions and dynamical conditions for (b,e) 15 nm and (c,f) 30 nm thicknesses. The tilt angle in (a-c) is  $3.8^\circ$  away from the  $[110]$  zone axis and is an analogue to Figure 7.4(b). The tilt angle in (d-f) is  $4^\circ$  away from the same zone axis but tilted toward a different direction and is analogous to Figure 7.4c but there are some differences as described in the text

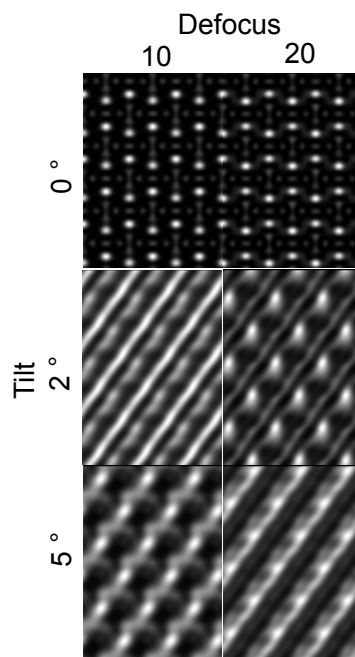


Figure 7.7: Simulated HRTEM images of  $\text{Co}_3\text{O}_4$  using JEMs which demonstrate the effect of crystal tilt on the appearance of  $\text{Co}_3\text{O}_4$  for a crystal approximately 30 nm thick at the defocus values (in nm) and tilts indicated. Extended dark line regions such as those seen in the 20 nm defocus case tilted at  $5^\circ$  imply that similar contrast observed in the experimental images are due to defocus effects as opposed to the presence of planar defects.

strong  $\{004\}$  and  $\{440\}$  reflections seen in the experimental pattern could not be replicated in the simulations just with tilt.

Figure 7.7 shows a selection of simulated HRTEM images of  $\text{Co}_3\text{O}_4$  at different defocus values and  $2^\circ$  and  $5^\circ$  crystal tilts which correspond approximately to the  $[598\ 572\ 23]$  and  $[110\ 99\ 10]$  zone axes respectively. The images in Figure 7.7 show that the appearance of  $\text{Co}_3\text{O}_4$  is very sensitive to crystal tilt. The crystal thickness was set to 30 nm, corresponding to 24  $[1\ 1\ 0]$  zone axis unit cells thick. The appearance of the crystal shown in Figure 7.3 generally matched with the  $5^\circ$  tilt cases although variations in the experimental image contrast imply that the thickness varies. The simulations also do not take into account the presence of CoO on top or on the bottom of  $\text{Co}_3\text{O}_4$ . However, the simulated images show that the contrast effects can be explained in terms of thickness/defocus effects as opposed to the presence of planar defects such as stacking faults.

## 7.5 The $\text{Co}_3\text{O}_4$ –CoO Grain Boundary

During the *in-situ* reduction process, an epitaxial grain boundary was formed between the  $\text{Co}_3\text{O}_4$  and CoO phases in most crystals. Figure 7.8 shows a close-up of such a boundary.

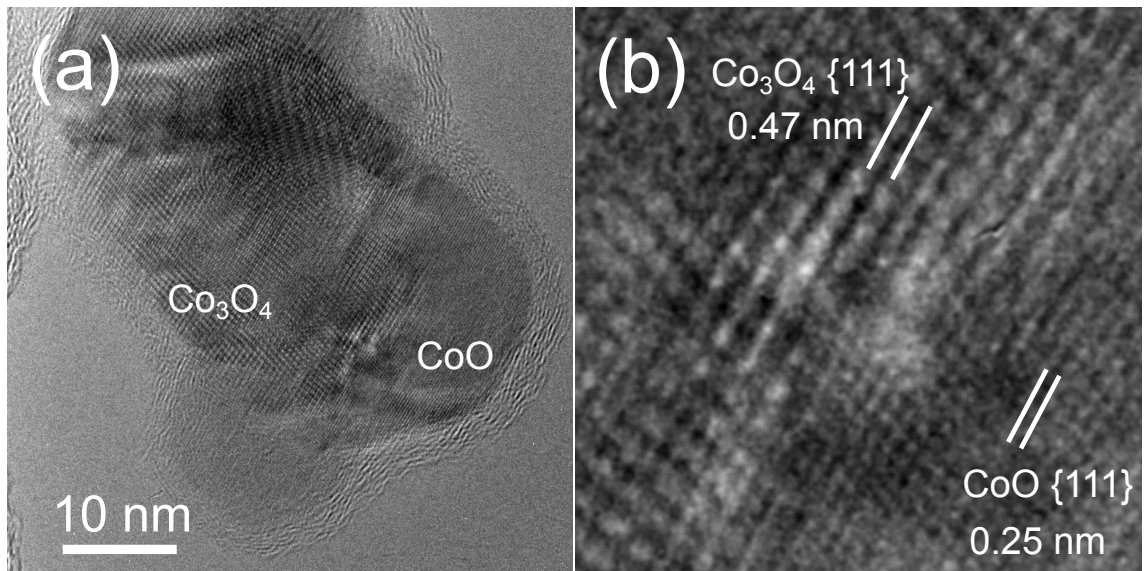


Figure 7.8: HRTEM images from another *in-situ* experiment taken at the same pressure as the previous images at 450 °C. (a) shows the nanoparticle in wider view and (b) shows a close-up of the epitaxial grain boundary between  $\text{Co}_3\text{O}_4$  and  $\text{CoO}$

The crystal shown in Figure 7.8 is out of the  $[1\ 1\ 0]$  zone axis by approximately  $4^\circ$ . The tilt is such that one set the  $\{1\ 1\ 1\}$  reflections are the strongest in the FFT and diffraction pattern hence the domination of the  $\{1\ 1\ 1\}$  planes in the image. Previous studies of the  $\text{Co}_3\text{O}_4$  reduction process observed epitaxy between  $\text{Co}_3\text{O}_4$  and  $\text{CoO}$  [298] but this is the first time a boundary between the two materials has been observed. Bulavchenko *et al* did report the formation of stacking faults by analysing peak broadening in their XRD data [297], these were not observed directly in the images presented here.

At the grain boundary there is a sudden change in contrast moving from the  $\text{CoO}$  region into the  $\text{Co}_3\text{O}_4$  region. Although not resolved atomically in the image, it can be seen that there are defects present near the centre of Figure 7.8(b). Several  $\{1\ 1\ 1\}$  plane fringes near the centre can be seen to merge into fewer  $\{1\ 1\ 1\}$  fringes suggesting the presence of dislocations. The contrast around the grain boundary seen more clearly in Figure 7.8(a) could arise from the strain associated with the presence of such defects. Further work is required to confirm the presence of dislocations and to identify their Burgers vector and whether they are screw or edge dislocations. An *in-situ* HAADF-STEM experiment could yield this information due to HAADF-STEM intensities being more intuitive than HRTEM contrast.

The lattice parameter of  $\text{Co}_3\text{O}_4$  is 0.8084 nm and the lattice parameter of  $\text{CoO}$  is 0.426 nm. When the  $\text{CoO}$  unit cell is doubled, there is still a 6 % mismatch between the locations of Co atoms located at  $\{0\ 0\ 1\}$  faces. There is no detailed information published

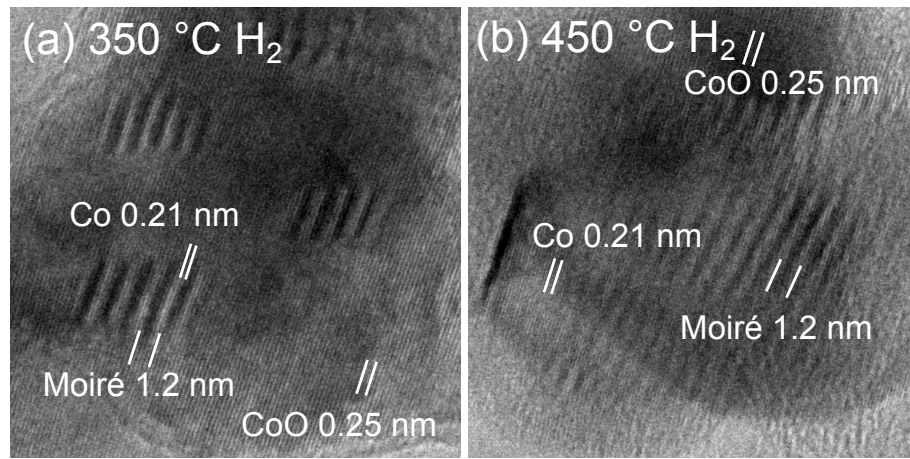


Figure 7.9: *In-situ* HRTEM images taken during an experiment using a pressure of 3 mbar at the readout at (a) 350 °C and (b) 450 °C. The crystal is approximately 10° out of the [1 1 2] zone axis

on the mechanism by which  $\text{Co}_3\text{O}_4$  transforms to CoO and how strain in this system is accommodated. There exists information on interfaces between rocksalt and spinel materials (same structures as CoO and  $\text{Co}_3\text{O}_4$  respectively) such as MgO and  $\text{Fe}_3\text{O}_4$  [359,360] and NiO and  $\text{Fe}_3\text{O}_4$  [361] but in these circumstances the lattice mismatch is less than 1 %.

## 7.6 Formation of Co at Higher Pressure

During a scouting experiment using a higher pressure (3 mbar at readout), the formation of Co metal (fcc) was observed at 450 °C. Figure 7.9 shows HRTEM images from this experiment showing Moiré fringes caused by the overlap of the parallel CoO and Co {1 1 1} planes. In Figure 7.9(a), which is taken at 350 °C, the Co is limited to the Moiré fringe regions as revealed by filtering the image by masking the Co {1 1 1} reflections. The Co metal forms small clusters at the top of the crystals and eventually spreads forming a Co shell. Similar observations were made *in-situ* by Dehghan *et al* [301] and Li *et al* [357]. The Co shell was observed in another crystal shown in Figure 7.9(b) at 450 °C where the Moiré fringes have become more extensive.

Dehghan *et al* used a pressure of 3.4 mbar and observed similar contrast to that seen in Figure 7.9 at 360 °C in their Ru promoted  $\text{Co}_3\text{O}_4$  reduction process. They observed the formation of hcp Co in addition to fcc Co at 360 °C but in the study here, only the fcc phase was observed. It is believed that the fcc phase is more likely to form at temperatures above 350 °C but the presence of a promotor in Dehghans *et al* [301] work could encourage the initial formation of hcp Co. Bulavchenko *et al* observed the formation of

Co at temperatures as low as 260 °C but this was using a much higher pressure of 1 bar (100 kPa). Kitakami *et al* [362] investigated the size dependence on the phase of Co and they found that a pure hcp phase only existed in crystals larger than 40 nm and pure fcc Co phase in crystals smaller than 20 nm. A similar result was found by Owen *et al* [291]. The work performed by Kitakami *et al* and Owen *et al* were not an *in-situ* reduction studies but rather dedicated phase formation (via chemical synthesis) studies.

## 7.7 Conclusions

The onset of reduction of  $\text{Co}_3\text{O}_4$  to CoO was observed at 200 °C but bulk reduction did not occur until 350 °C. This result is similar to work performed on rounded crystals suggesting that vacancies originally in  $\text{Co}_3\text{O}_4$  play a key role in the reduction process [297, 298]. The reduction temperatures of  $\text{Co}_3\text{O}_4$  supported on supports such as  $\text{Al}_2\text{O}_3$  are different, due to support interactions [300].

In this study, Co metal was only produced using higher  $\text{H}_2$  pressures but a single step reduction from  $\text{Co}_3\text{O}_4$  to CoO was not observed. In general, the single step reduction was only observed in high pressure environments [297]. The findings presented here are consistent with previous literature that use lower pressures of  $\text{H}_2$  [297, 298, 301, 357] including other *in-situ* (S)TEM studies [301, 357]. New insights into the reduction mechanism include the formation of a  $\text{Co}_3\text{O}_4$  to CoO grain boundary which gradually moves further into  $\text{Co}_3\text{O}_4$  as the reaction time and temperature is increased. Defects were strongly implied in crystals larger than 20 nm close to  $\text{Co}_3\text{O}_4$ /CoO grain boundaries. The same epitaxial grain boundary was not observed in crystals smaller than 5 nm suggesting that the strain induced by the lattice mismatch between  $\text{Co}_3\text{O}_4$  and CoO can be annulled by strain relaxation in smaller crystals.

Further work is required to resolve the identify of defects in the crystals during reduction. This includes point vacancies in the initial  $\text{Co}_3\text{O}_4$  structure as several groups have pointed out that the presence of O vacancies can reduce the reduction temperature [297, 298]. An atomic resolution *in-situ* HAADF-STEM experiment could yield further information regarding the presence of defects, especially at the interfaces since HAADF-STEM intensity is more intuitive than HRTEM. As the York-JEOL 2200FS continues to be developed, higher pressure runs should encourage the formation of Co at lower temperatures to allow a more detailed investigation into this reduction process.

# Chapter 8

## Model Supported Nanoparticle Systems

### 8.1 Nanostructure of PtPd nanoparticle coated ZnO Tetrapods

#### 8.1.1 Introduction

ZnO is a metal oxide semiconductor. In its wurtzite phase, it has a 3.37 eV direct band gap and an exciton binding energy of 60 meV [363,364,365]. ZnO is of considerable technological interest in optoelectronics, thin film transistors and piezoelectric devices, [366,367] because of the large variety of structures that can be formed at the nanoscale. [365] Structures can range from simple rods and nanoparticles to more complex formations such as belts and flowers [364]. The simplest 3D structure is the tetrapod. [366] A ZnO tetrapod consists of a nucleus from which four tetrahedrally coordinated (separated by around  $107^\circ$ ) wurtzite phase legs extend out. The exact structure of the nucleus for different tetrapod morphologies is still debated. The most explored models are the octa-twin [368], multiple element hexagonal twins [369], four hexagonal twinned grains [370] and the cubic nucleus model [371, 372]. In its hexagonal wurtzite phase, ZnO has lattice parameters  $a = 0.325$  nm and  $c = 0.520$  nm and the arms grow outward from the core in the  $[001]$  direction [366]

The size of tetrapods varies considerably, arm lengths can range from several hundred  $\mu\text{m}$  down to around 100 nm. The size and the morphology of the legs depends on the growth mechanism during synthesis [373] but hexagonal prism leg morphology is the simplest [373]. ZnO tetrapods can be prepared by many methods but the simplest method is the oxidation of pure Zn pellets in an  $\text{O}_2$  rich atmosphere by rapid heating [374]. For certain applications, ZnO tetrapods are beneficial over other nanoscale forms of ZnO be-

cause bulk quantities can be prepared easily [375]. Furthermore, the multiple legs of the tetrapod offers unique applications over rods allowing devices to be constructed using a single tetrapod [363] because multiple contacts can be formed.

In addition, there is growing interest in ZnO composite systems. The presence of metal nanoparticles limits the mobility of charge carriers leading to Au, Pt, Ag and Cu-ZnO composite materials because the electronic properties of the ZnO substrate can be adjusted by this means. It is reported in the literature that ZnO films coated with larger 2.8 nm and 6.4 nm average diameter Pt nanoparticles, the optical bandgap was observed to decrease with increased Pt coverage [376]. Sputtering of larger 5 – 8 nm Pt nanoparticles onto ZnO rods greatly enhanced the bandgap emission [377] as a function of nanoparticle size, possibly due to the population of Pt in O vacancies [377]. The coating of 12 nm Ag nanoparticles onto ZnO rods has indicated that the presence of the nanoparticles decreases the infrared emission of the material [378]. It is thought that such composite systems could lead to new materials for IR optics [378].

The deposition of metal nanoparticles such as Au onto semiconductor nanostructures was found not only to increase the activity of the nanoparticles but also the support [379]. It has been found that 8 – 12 nm Au nanoparticles deposited onto ZnO tetrapods offer the highest activity at room temperature for the oxidation of CO [380] when compared with cylindrical and needle shaped ZnO substrates. Similar composite systems using Pt nanoparticles have shown increased sensitivity to ethanol and hydrogen [381] and Ag nanoparticles have greatly improved the speed of the sensing properties [382]. The nanoparticle systems are also of interest because of their photocatalytic activity. For example, Au-ZnO composites are believed to improve the photocatalytic activity [383]. However in these studies nanoparticles have been generally larger than 2 nm.

The purpose of the work here is to use double aberration corrected (S)TEM to probe the core and surface structure of small tetrapods to deduce their worthiness as substrates for nanoparticles. The interface between deposited nanoparticles and the ZnO surface is also examined using HRTEM. Through knowing the interface structure of nanoparticles on ZnO it may be possible to design more efficient composite systems for a variety of applications including catalysts and gas sensors.

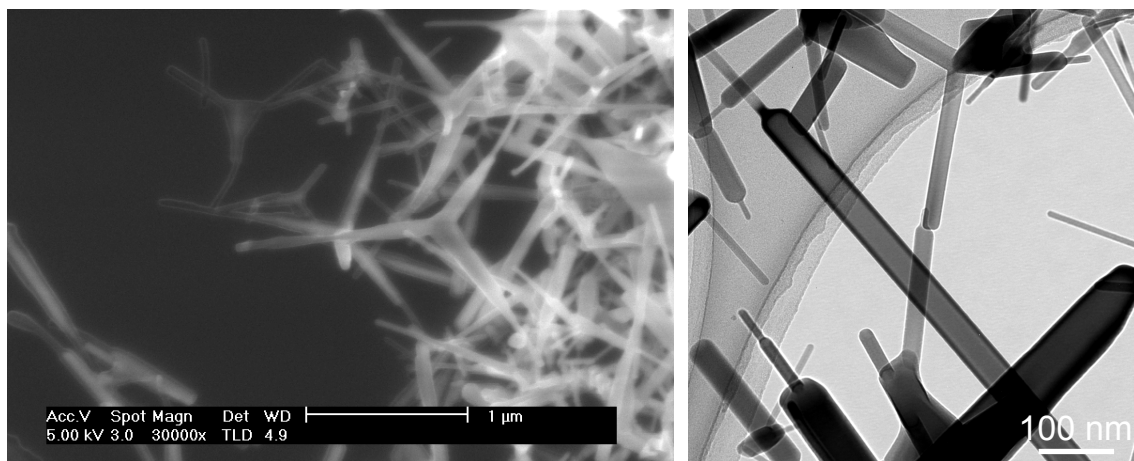


Figure 8.1: A SEM image (a) and TEM image (b) of the as prepared ZnO tetrapod (S)TEM specimen demonstrating the dominant presence of tetrapod like structures

### 8.1.2 Sample Preparation

The ZnO tetrapods were prepared in Japan by Kenta Yoshida and his students at Nagoya University. They synthesised ZnO tetrapods by vaporising 100  $\mu\text{m}$  Zn pellets using electrified W wire which is similar to how Wang *et al* synthesised their materials [374]. The vapour diffuses through the air, partially oxidising. The vapour nucleates onto a series of holey C film coated TEM grids forming ZnO through vapour phase transport. The Zn and ZnO in the air formed nucleation sites on the TEM grids allowing a variety of structures to grow. The resulting specimens contained a wide variety of different shapes but the majority of them were tetrapod like.

Figure 8.1 shows SEM and a low-magnification TEM image of one of the (S)TEM specimens. The images show that most of the structures feature tetrapod legs although their morphologies are varied. For the (S)TEM analysis, only structures clearly identified as tetrapods were studied. The formation of other structures is a consequence of the synthesis method where little control over the growth rate or temperature was available. Pt-Pd (ratio 7:1) nanoparticles were deposited onto the ZnO TEM grids using a JEOL JST-2300 HR coating machine at the York-JEOL Nanocentre. To obtain nanoparticles between 1 – 3 nm, a beam current of 20 mA set to 1 nm nominal coating thickness was used after a series of trials using amorphous carbon TEM grids were coated at a variety of thicknesses.



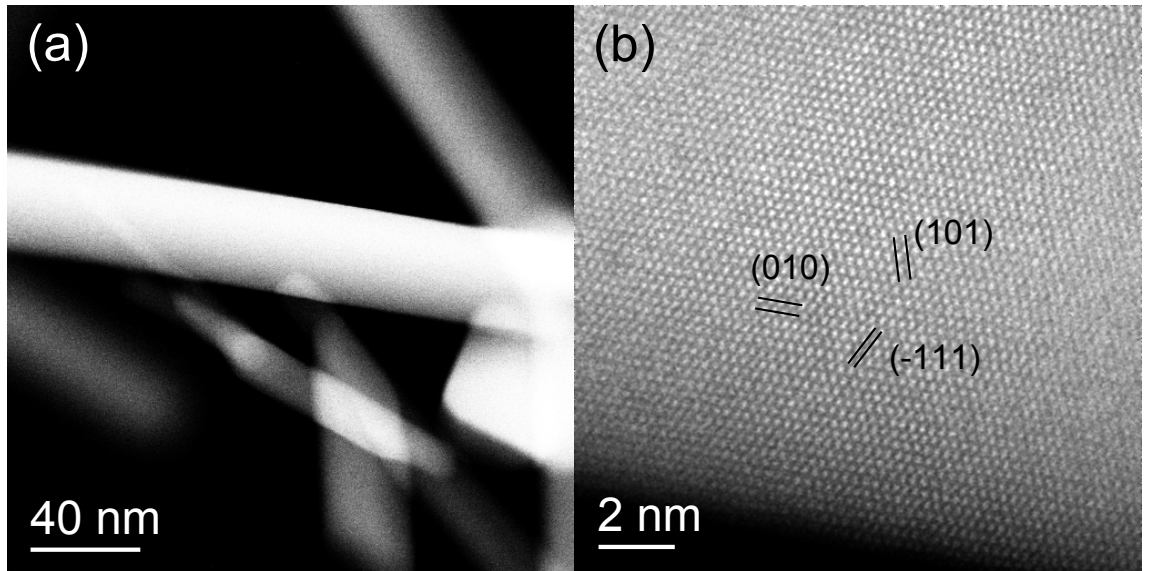


Figure 8.2: HAADF-STEM of a tetrapod leg demonstrating the flat nature of the  $\{1\bar{1}0\}$  planes

### 8.1.3 Leg and Core Structure of Small Tetrapods

Figure 8.2 shows HAADF-STEM images of a tetrapod leg in  $[101]$  showing that the crystal edges formed by the  $(\bar{1}10)$  planes are flat [384]. To verify if small tetrapods synthesised using the method above had core structures consistent with current literature, the structure of several tetrapods with leg lengths less than 100 nm and leg widths of approximately 15 nm were studied using HRTEM. Figure 8.3 shows the HRTEM image of the mentioned tetrapod and corresponding FFT. The FFT reveals that both of the legs are in the  $\langle 110 \rangle$  zone axis. In this zone axis, it can be seen that the legs grow out in  $[001]$  from the core. Atomic steps that can be seen on the tetrapod leg surfaces are believed to arise because of beam damage and they are not necessarily genuine crystal growth features since they were not present on all images taken from the same area.

The interface between the core and the legs reveals that there are defects. These have been identified as stacking faults and dislocations. The FFT of the HRTEM image has been indexed as three separate crystals: two wurtzite  $[110]$  and a zincblende  $[110]$ . The tetrapod legs grow out from the  $\{111\}$  faces of the core. Crystallography reveals that there is a difference between the directions of ZB $[111]$  and WZ $[001]$  which suggests that the stacking faults and dislocations at one side of the leg/core interface adjust the interface to account for the angle discrepancy. The observation here was made at least five times with similarly sized tetrapods. The results support those presented by Shiojiri *et al* [371].

A difficulty in studying ZnO was that it was beam sensitive. To investigate the effects

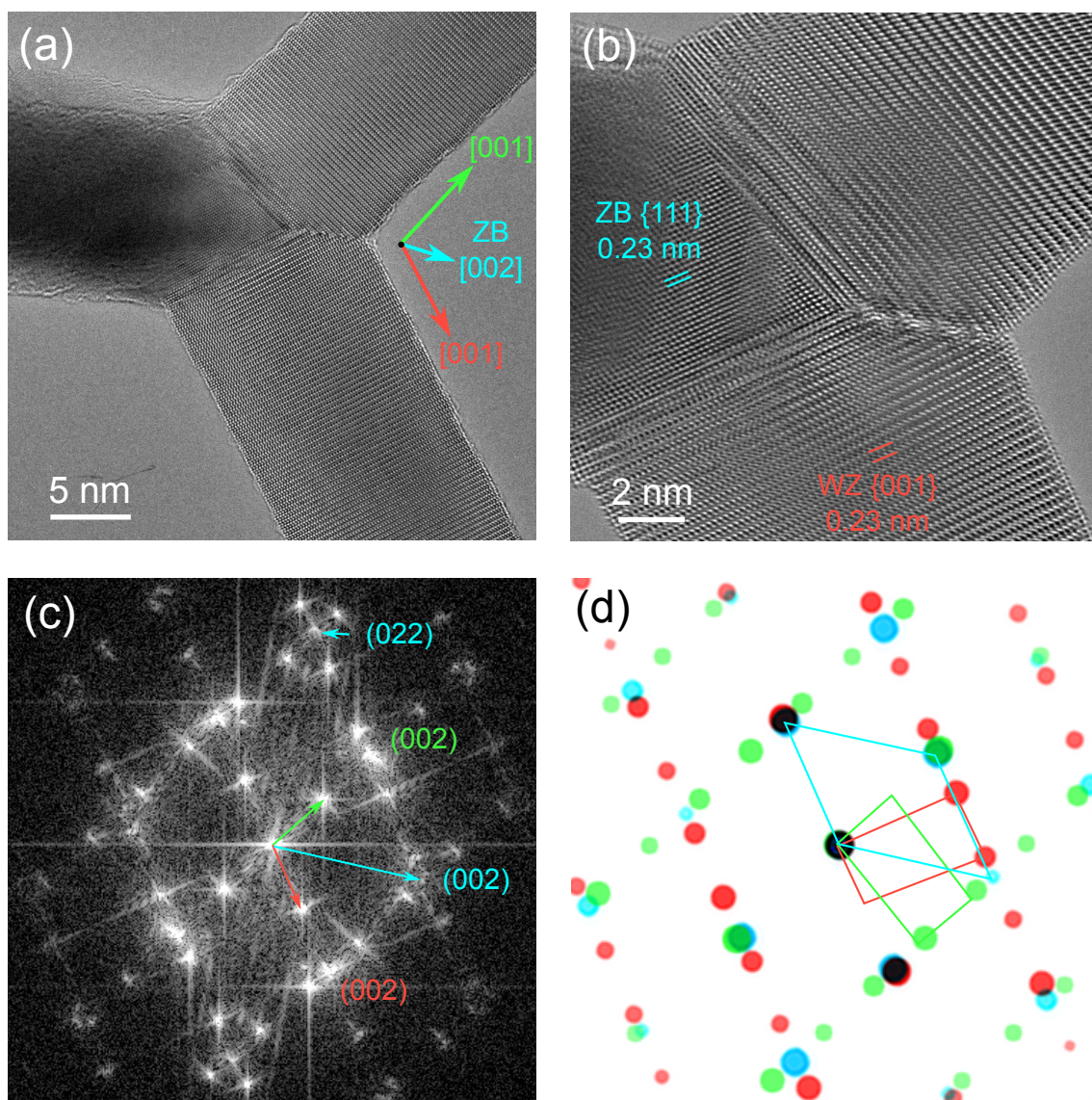


Figure 8.3: HRTEM images of a ZnO tetrapod with (a) showing the tetrapod, (b) core-region and (c) and (d) the FFT of (b) and simulated diffraction pattern respectively. The FFT was analysed as the overlap of three separate crystals: two wurtzite ZnO [1 1 0] and a zincblende ZnO [1 1 0] diffraction pattern with 112° rotation between the former

Table 8.1: Table of Moiré fringe widths and angles

Nanoparticle	Fringe Width nm	Angle°
1	0.56	94
2	0.55	45
3	0.63	40
4	0.63	40
5	0.24	48
6	0.24	50

of extended exposure, tetrapods with approximately the same dimensions as the one in Figure 8.3 was exposed to a  $500 \mu\text{Acm}^{-2}$  beam for 600 s. Figure 8.4 shows two different tetrapods before and after irradiation. Additional faceted features have appeared on the tetrapod surface. Diffraction patterns shown as insets in Figure 8.4(c) and (d) shows only  $\text{ZnO}[110]$  with no Zn detected. To calculate the surface area of the damaged tetrapod, the original area was modified by adding the surface area generated by the appearance of 5 nm cubic modifications the tetrapod legs presumably caused by the removal of material because of knock on damage. The presence of these intrusions do not generate additional surface area on the  $\{1\bar{1}0\}$  faces because its cubic form approximately the same area of this surface. The additional surface area comes from the two additional  $\{001\}$  and four  $\{1\bar{1}0\}$  faces. The surface area was calculated to be approximately double its original surface area. This was achieved by assuming that each intrusion created four additional facets corresponding to the facets of the cubic intrusion. The area of the base of the intrusion was assumed to be the same as the top of the undamaged tetrapod surface. It is important to note that the estimate here does not take into account the role of overlapping voids which are likely at the edges of the  $\{1\bar{1}0\}$  faces.

#### 8.1.4 HAADF-STEM and HRTEM of Coated Tetrapods

Figure 8.5 shows a ZnO tetrapod leg coated in small Pt-Pd nanoparticles. The average particle size was determined to be approximately 2 nm. HAADF-STEM Cryotomography of the coated tetrapods showed that the coating across the tetrapod was consistent on one side [385]. The other side was uncoated.

To investigate whether there was any epitaxy between the nanoparticles and tetrapods the coated tetrapods were studied using HRTEM and diffraction. Figure 8.6 shows a HRTEM image of a coated ZnO tetrapod with the nanoparticles appearing as Moiré fringes. The Moiré fringes were analysed by measuring the fringe widths  $D$  and then comparing them to widths predicted by (2.10).

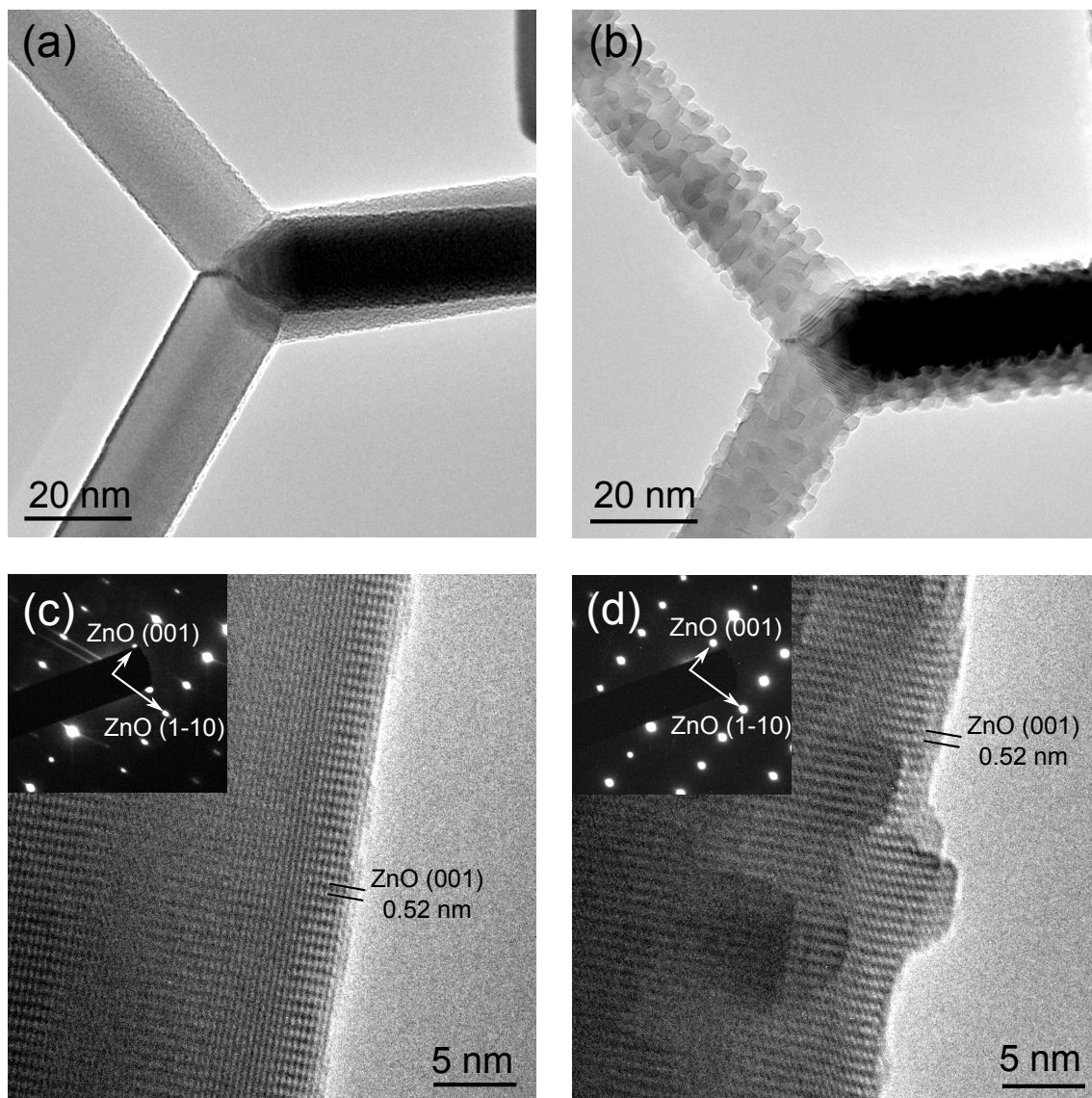


Figure 8.4: TEM image of a tetrapod (a) before extended electron irradiation and (b) after extended electron irradiation. (c) and (d) show the HRTEM and diffraction pattern of another irradiated tetrapod suggesting that ZnO forms additional faceted features but no Zn is formed. The diffraction patterns are both  $[1\ 1\ 0]$  ZnO, note there is a  $30^\circ$  rotation between the image and diffraction pattern

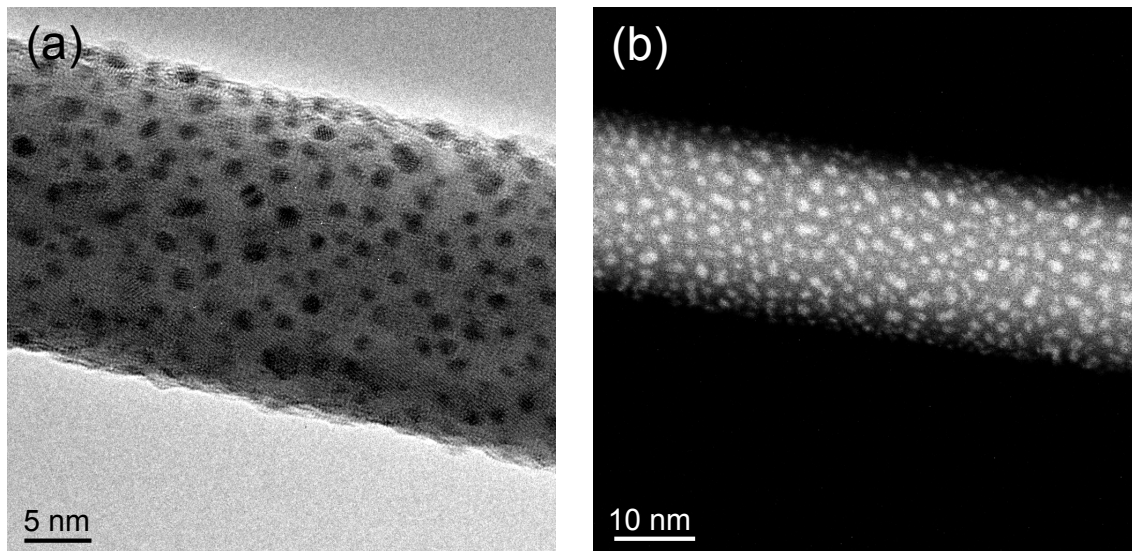


Figure 8.5: Nanoparticle coated tetrapods with (a) being a TEM image and (b) a HAADF-STEM image. The nanoparticles are very thin relative to their diameter as suggested by the ones at the edge

The image FFT shows strong  $\text{ZnO } \{002\}$  reflections and faint  $\text{Pt } \{111\}$  reflections and theory predicts that the aforementioned reflections are the brightest for their respective crystals according to the structure factor (2.6). It was assumed that the  $\text{ZnO } \{002\}$  and  $\text{Pt } \{111\}$  were responsible for the Moiré fringes. Table 8.1 shows the Moiré interference fringe measurements from Figure 8.6(c) as indicated. The measurements show that there is no set epitaxy between the nanoparticles and  $\text{ZnO}$  surfaces. Direct measurements from the nanoparticles in Figure 8.6(a) also do not show any preferential orientation.

### 8.1.5 Conclusions

To summarise, the surfaces of the  $\{1\bar{1}0\}$  surfaces and edges of  $\text{ZnO}$  tetrapods with hexagonal prism leg morphology have been revealed to be atomically flat. To test their suitability as a substrate for catalytically active nanoparticles, which can often modify the tetrapods electronic properties, Pt-Pd nanoparticles were deposited onto the tetrapods. HAADF-STEM and HRTEM showed that the nanoparticles cover the tetrapods uniformly. Their orientation relationship on HRTEM showed that no set epitaxy was achieved as revealed by the analysis of Moiré fringes.



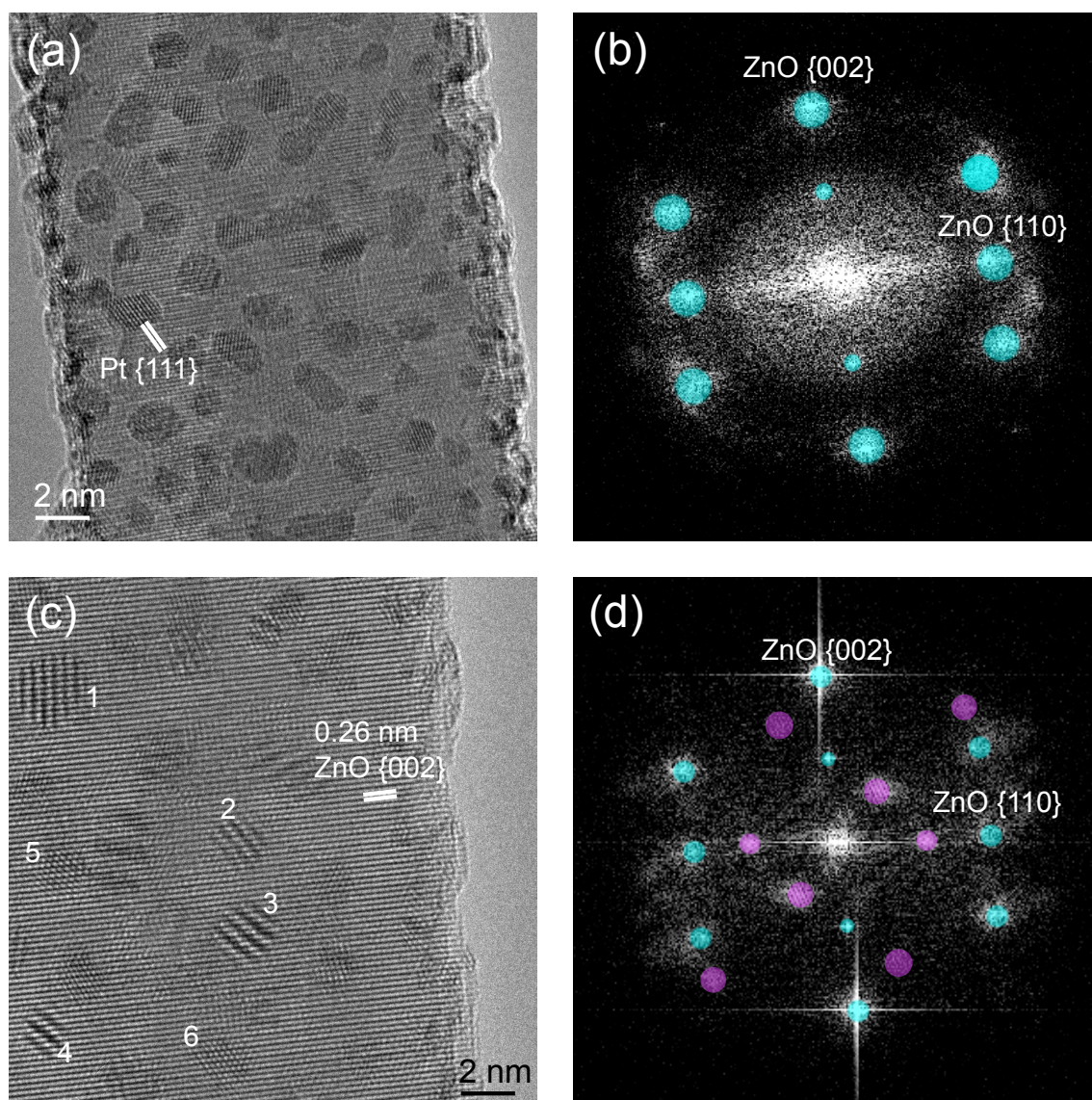


Figure 8.6: HRTEM images with corresponding FFTs of the same nanoparticle coated tetrapod showing (a) no Moiré and (b) Moiré fringes caused by the interference of Pt-Pd nanoparticle and ZnO atomic plane fringes. The blue circles in the FFT highlight ZnO spatial frequencies and the pink ones are Moiré fringes

# Chapter 9

## Summary and Final Remarks

In this work, through the use of HAADF-STEM, HRTEM and electron diffraction, new insights into nanoparticle deactivation and activation mechanisms have been presented.

The segregation of Pt and Pd in the Pt-Pd-Al<sub>2</sub>O<sub>3</sub> DOC involved the Pd enrichment of the nanoparticle's outer layers leaving behind a Pt enriched core. This segregation agrees with previous experimental segregation studies that use similar Al<sub>2</sub>O<sub>3</sub> supports [235, 236, 309], C supports [239], and theoretical studies [238].

The intricacies of the incomplete segregation of Pt and Pd was also detected through EDX and HAADF-STEM, this is the first time such a detailed experiment has been carried out on commercially aged DOCs with previous investigations into this phenomena being done using TEM [193] or using as prepared Pt-Pd catalysts [93]. For the smaller nanoparticles on the Pt-Pd-Al<sub>2</sub>O<sub>3</sub> DOC, no obvious signs of segregation were observed, but perhaps this is because Pd and Pt are less likely to completely segregate in small nanoparticles [237].

Overall, the structures in the Pt-SiO<sub>2</sub> DOC remained spherical despite the increase in nanoparticle size on the aged variant relative to the fresh one. On the other hand, the nanoparticles in the Pt-Pd-Al<sub>2</sub>O<sub>3</sub> DOC were often observed to be faceted and therefore containing fewer low-coordination atoms than spherical nanoparticles.

New insights have been gained into the sintering mechanism through the use of NBD which has revealed interesting diffraction phenomena from sintered nanoparticles. These include the observation of streaking in the diffraction pattern which may be caused by the presence of angled interfaces between different crystals. Further investigations could yield quantitative shape information extracted from shape effects in the diffraction pattern and simultaneous analysis of the nanoparticles and the surrounding support could yield

new insights on the interface between the nanoparticle and support.

On the issue of nanoparticle sintering, there is some debate as to whether very small clusters of Pt are stabilised by the surface defects of  $\gamma$ -Al<sub>2</sub>O<sub>3</sub>. Model Pt-Al<sub>2</sub>O<sub>3</sub> was treated in air for up to 15 h in air to encourage the sintering of Pt nanoparticles. Using HAADF-STEM, no isolated single atoms were observed in the fresh or any catalyst aged for 3 h but the nanoparticles had grown substantially in the catalyst treated at 750 °C. Nano-area diffraction provided some insights into the sintering of large nanoparticles including the formation of a grain boundary between two differently orientated nanoparticles.

Single atoms were observed in the specimens aged for 15 h and appeared to be stabilised by the support in agreement with Bradley et al's work [326]. The clusters observed were estimated to be between 2-5 atoms thick which implies they are a 3D crystal structure as opposed to the 2D raft structure described by others [90,93,142]. The support structure in this catalyst was complex and resembled a commercial catalyst so no nanoparticle-support interactions could be deduced from this study but clusters did appear to be stabilised by the support since they were present on the catalyst aged for 15 h. This new insight needs to be confirmed, but to do so would be very difficult with the inconsistent metal loading and support structure of the catalyst used here.

A model support, in the form of large, flat Al<sub>2</sub>O<sub>3</sub> crystals is needed to deduce accurate nanoparticle-support interactions. Generally, the detailed structure of the complex  $\gamma$ -Al<sub>2</sub>O<sub>3</sub> is not taken into account in previous sintering studies.

A proposed experiment which utilises the recent developments in E(S)TEM at the York-JEOL nano-centre, could be to analyse the stability of atomically dispersed Pt (and nanoparticles) on large, flat Al<sub>2</sub>O<sub>3</sub> supports (perhaps of different phase) that could have different surfaces (e.g. (001) and (111)). The flat support and large crystal size would make it easier to deduce nanoparticle-support interactions either with HRTEM, HAADF-STEM but especially with NBD and SAD. This could potentially have important repercussions on the design of future DOCs and similar catalysts. Analysis of the road aged sample shows the potential to reduce significantly the Pt loading and cost.

In this thesis, new developments in E(S)TEM are presented. The work here shows it is possible to see individual atoms of Pt and Pd at temperatures as high as 600 °C in H<sub>2</sub>. Although environmental HAADF-STEM has been done previously (e.g. [357]) this is the first time atomic resolution *in-situ* HAADF-STEM under both gas and heat has been presented [66].



At room temperature, atoms were observed in O<sub>2</sub>. During these studies, the atoms were observed to move under the influence of the electron beam. This has been done previously [38,57] but further work is required to deduce if it is possible to distinguish between genuine chemistry and other physical effects ( e.g. Ostwald ripening) from electron beam induced effects. Recently, an oxidation resistant heating holder has become available offering the potential to simulate O<sub>2</sub> rich operating conditions at elevated temperature such as in DOCs.

However, the introduction of gas into the electron microscope does present the question: at what point does the gas (and species) influence the performance of the microscope? A possible experiment could involve the use of different gases at different pressures to deduce intensity changes in HAADF-STEM images over a hole *in-situ*. Heavier gases, such as O<sub>2</sub>, at higher pressure could potentially mask the presence of single atoms on heavy supports so it is important to deduce the practical limits of this technique.

The limitations of the HAADF-STEM technique (in vacuum) were explored by the use of QSTEM simulations for heavy atoms located on heavy supports and to investigate claims of extraordinarily bright atomic columns in Au-CeO<sub>2</sub> WGS catalyst [85]. Similar experimental studies have been carried out on Pt-FeO<sub>x</sub> [354] and Au-TiO<sub>2</sub> [352] but it is believed that this investigation through image simulation is the first of its type to quantify these intensities.

The simulations account for the observed intensity difference between the Au terminated Ce atomic column and ordinary Ce atomic column of the same thickness when an atom terminates the top and bottom of the column. Walsh [85] observed intensity differences of approximately 40 %. The simulations replicate that difference only if the crystal is less than 0.38 nm thick with a single Au atom. Au located at the bottom was approximately 10 % brighter compared to Au located at the top. Two Au in the same column were approximately double the intensity difference compared to Au located at the bottom. The results therefore imply that the intensity differences observed by Walsh [85] are unlikely to be caused entirely by the presence of single Au atoms but may be associated with the noise of the HAADF-STEM image formation.

Although the simulations are designed to be quantitative there is still some uncertainty regarding the thickness of the specimen. A useful insight would be what the intensity of a single atom is in HAADF-STEM so that atom counting would be possible but to be truly quantitative the intensity scale of the experimental image needs to be absolute [47]. For example, in chapter 6 and [66], the intensities were calibrated for individual images but

not between images. QSTEM outputs images in an absolute intensity scale in terms of the probe intensity. A direct comparison between the simulations and experimental images requires careful calibration of the image acquisition system at York and this is beyond the scope of the work in this thesis.

In addition to deactivation mechanisms, the activation mechanism of Co catalysts through the reduction of  $\text{Co}_3\text{O}_4$  was carried out in an *in-situ* reduction HRTEM study. New insights into the reduction mechanism have been observed, namely the formation of a grain boundary between  $\text{Co}_3\text{O}_4$  and the intermediate CoO. Further work to the microscope is required to access the higher pressures required for the formation of Co. The development of *in-situ* HAADF-STEM could also benefit this study.

# List of Symbols

$\alpha$	Convergence angle
$\beta$	Divergence angle
$\Gamma$	Skewness
$\gamma$	Surface free energy density
$\Delta f$	Defocus
$\Delta z$	Slice thickness
$\epsilon_d$	d-band centre energy
$\theta$	Angle
$\theta_b$	Bragg angle
$\theta_w$	Contact/Wetting angle
$\lambda$	Wavelegnth
$\mu$	Mean
$\mu(r)$	Chemical potential
$\mu_0$	Bulk checmical potential
$\sigma$	Standard deviation
$\sigma_c$	Interaction constant
$\phi_p(x, y)$	Projected potential
$\chi(u)$	Phase function
$\psi_0$	Electron amplitude
$\psi(r), \psi(x, y)$	Electron wavefunction
$\Omega$	Atomic volume of bulk metal
$A(u)$	Aperture function
$a, b, c$	Lattice parameters
$B$	Full width half maximum
$C_c$	Chromatic aberration coefficient
$C_s$	Spherical aberration coefficient
$D_s$	Diffusion constant for atom
$D_p$	Diffusion constant for particle
$d$	Atomic plane spacing
$d_{av}$	Average particle diameter
$E$	Energy
$E_f$	Fermi energy
$E_{ad}$	Adsorption energy
$E_{tot}$	Sublimation energy
$E_r$	Reaction barrier energy
$E_d$	Desorption energy
$E(u)$	Energy envelope term
$F$	Structure factor
$f_i(\theta)$	Atomic form factor

$G$	Gibbs free energy
$\mathbf{g}$	Reciprocal lattice vector
$G_s$	Bulk shear modulus
$h_i$	Distance from nanoparticle centre to facet
$\{h\ k\ l\}$	Miller indices
$\mathbf{k}$	Incident wavevector
$\mathbf{k}'$	Diffacted wavevector
$\mathbf{K}$	Difference in diffracted and incident wavevectors
$k_b$	Boltzmann constant
$K_{sch}$	Scherrer constant
$L$	Camera length
$m_0$	Electron mass
$n$	Reflection order
$P$	Pressure
$Q$	Activation energy for surface diffusion
$R$	The gas constant
$r$	Nanoparticle radius
$r^*$	Critical nanoparticle radius
$S$	Entropy
$\mathbf{s}$	Excitation error
$T$	Temperature
$T(u)$	Contrast transfer function
$t$	Time
$u$	Spatial frequency
$X_c$	Random walk displacement
$Y$	Distance measured on recorded diffraction pattern
$Z$	Atomic number

# List of Acroynms

AFM	Atomic force microscopy
bcc	Body centre cubic
BF	Bright field
CBD	Covergent beam diffraction
CCD	Charged couple device
CTF	Contrast transfer function
DF	Dark field
DFT	Density functional theory
DOC	Diesel oxidation catalyst
EDX	Energy dispersive X-ray spectroscopy
EELS	Electron energy loss spectroscopy
E(S)TEM	Environmental (scanning) transmission electron microscopy
fcc	face centre cubic
FEG	Field emmision gun
FFT	Fast fourier transform
FT	Fischer-Tropsch
HAADF	High angle annular dark field
GTL	Gas to liquids
hcp	hexagonal close packed
HRTEM	High resolution transmission electron microscopy
LHS	Left hand side
LUT	Look up table
LSW	Lifshitz-Slyozov-Wagner
MTP	Multiply Twinned Particle
NBD	Nano-beam diffraction
RHS	Right hand side
SAD	Selected area diffraction
SEM	Scanning electron microscopy
SMSI	Strong metal support interaction
TPR	Temperature programmed reduction
(S)TEM	(Scanning) transmission electron microscopy
STM	Scanning tunnelling microscopy
TWC	Three way catalyst
WGS	Water gas shift
WPOA	Weak phase approximation
XPS	X-ray photoelectron spectroscopy
XRD	X-ray diffraction

# Bibliography

- [1] H. S. Gandhi, G. W. Graham, and R. W. McCabe, “Automotive exhaust catalysis,” *Journal of Catalysis*, vol. 216, no. 1–2, pp. 433–442, 2003.
- [2] A. Russell and W. S. Epling, “Diesel oxidation catalysts,” *Catalysis Reviews*, vol. 53, no. 4, pp. 337–423, 2011.
- [3] B. C. H. Steele and A. Heinzl, “Materials for fuel-cell technologies,” *Nature*, vol. 414, no. 6861, pp. 345–352, 2001.
- [4] H. Schulz, “Short history and present trends of fischer–tropsch synthesis,” *Applied Catalysis A: General*, vol. 186, no. 1–2, pp. 3 – 12, 1999.
- [5] H. Davy, “Glowing of metals in contact with mixtures of air and combustible gases,” *Philosophical Transactions of the Royal Society of London*, vol. 107, 1820.
- [6] E. Davy, “On some combinations of platinum,” *Philosophical Transactions of the Royal Society of London*, vol. 110, pp. 108–125, 1820.
- [7] B. Lindström and L. J. Pettersson, “A brief history of catalysis,” *CATTECH*, vol. 7, no. 4, pp. 130–138, 2003.
- [8] M. Haruta, T. Kobayashi, H. Sano, and N. Yamada, “Novel gold catalysts for the oxidation of carbon-monoxide at a temperature far below 0 °C,” *Chemistry Letters*, vol. 2, pp. 405–408, 1987.
- [9] M. J. Walsh, K. Yoshida, A. Kuwabara, M. L. Pay, P. L. Gai, and E. D. Boyes, “On the structural origin of the catalytic properties of inherently strained ultrasmall decahedral gold nanoparticles,” *Nano Letters*, vol. 12, no. 4, pp. 2027–2031, 2012.
- [10] M. Faraday, “The bakerian lecture: experimental relations of gold (and other metals) to light,” *Philosophical Transactions of the Royal Society of London*, vol. 147, pp. 145–181, 1847.
- [11] C. Kittel, *Introduction to Solid State Physics*. Wiley, 8 ed., 2005.

- [12] W. L. Bragg, “The diffraction of short electromagnetic waves by a crystal,” *Proceedings of the Cambridge Philosophical Society*, vol. 17, pp. 43–57, 1913.
- [13] B. D. Cullity, *Elements of X-Ray Diffraction*. Addison-Wesley, 1956.
- [14] P. B. Hirsch, A. Howie, R. B. Nicholson, D. W. Pashley, and M. J. Whelan, *Electron Microscopy of Thin Crystals*. Butterworths Scientific Publications, 1965.
- [15] D. B. Williams and C. B. Carter, *Transmission Electron Microscopy: A Textbook for Materials Science*. Springer, 1996.
- [16] V. Y. Shevchenko, A. E. Madison, and Y. I. Smolin, “Specific features of diffraction by nanoparticles,” *Glass Physics and Chemistry*, vol. 28, no. 5, pp. 326–333, 2002.
- [17] J. Cowley, “Electron nanodiffraction,” *Microscopy Research and Technique*, vol. 46, no. 2, pp. 75–97, 1999.
- [18] J. Cowley, “Applications of electron nanodiffraction,” *Micron*, vol. 35, no. 5, pp. 345 – 360, 2004.
- [19] H. He and C. Nelson, “A method of combining stem image with parallel beam diffraction and electron-optical conditions for diffractive imaging,” *Ultramicroscopy*, vol. 107, no. 4–5, pp. 340 – 344, 2007.
- [20] L. D. Marks, “Experimental studies of small particle structures,” *Rep. Prog. Phys.*, vol. 57, pp. 603–649, 1994.
- [21] J. W. Edington, *Practical Transmission Electron Microscopy in Materials Science*. Philips, 1976.
- [22] D. Cherns, “Direct resolution of surface atomic steps by transmission electron microscopy,” *Philosophical Magazine*, vol. 30, no. 3, pp. 549–556, 1974.
- [23] V. Germain, J. Li, D. Inger, Z. L. Wang, and M. P. Pileni, “Stacking faults in formation of silver nanodisks,” *The Journal of Physical Chemistry B*, vol. 107, no. 34, pp. 8717–8720, 2003.
- [24] J. Reyes-Gasga, A. Gómez-Rodríguez, X. Gao, and M. José-Yacamán, “On the interpretation of the forbidden spots observed in the electron diffraction patterns of flat Au triangular nanoparticles,” *Ultramicroscopy*, vol. 108, no. 9, pp. 929 – 936, 2008.

- [25] G. A. Bassett, J. W. Menter, and D. W. Pashley, “Moiré patterns on electron micrographs, and their application to the study of dislocations in metals,” *Proceedings of the Royal Society of London. Series A. Mathematical and Physical Sciences*, vol. 246, no. 1246, pp. 345–368, 1958.
- [26] A. V. Crewe, D. N. Eggenberger, J. Wall, and L. M. Welter, “Electron gun using a field emission source,” *Review of Scientific Instruments*, vol. 39, no. 4, pp. 576–583, 1968.
- [27] G. Y. Fan and M. H. Ellisman, “Digital imaging in transmission electron microscopy,” *Journal of Microscopy*, vol. 200, no. 1, pp. 1–13, 2000.
- [28] J. M. Cowley and A. F. Moodie, “The scattering of electrons by atoms and crystals. I. A new theoretical approach,” *Acta Crystallographica*, vol. 10, pp. 609–619, Oct 1957.
- [29] J. M. Cowley, *Diffraction Physics*. Elsevier, 3rd ed., 1995.
- [30] K. W. Urban, “Studying atomic structures by aberration-corrected transmission electron microscopy,” *Science*, vol. 321, no. 5888, pp. 506–510, 2008.
- [31] K. W. Urban, C.-L. Jia, L. Houben, M. Lentzen, S.-B. Mi, and K. Tillmann, “Negative spherical aberration ultrahigh-resolution imaging in corrected transmission electron microscopy,” *Philosophical Transactions of the Royal Society A: Mathematical, Physical and Engineering Sciences*, vol. 367, no. 1903, pp. 3735–3753, 2009.
- [32] J. Chen, H. Zandbergen, and D. Dyck, “Atomic imaging in aberration-corrected high-resolution transmission electron microscopy,” *Ultramicroscopy*, vol. 98, no. 2–4, pp. 81 – 97, 2004.
- [33] J. Biskupek and U. Kaiser, “Practical considerations on the determination of the accuracy of the lattice parameters measurements from digital recorded diffraction patterns,” *Journal of Electron Microscopy*, vol. 53, pp. 601–610, 12 2004.
- [34] L. Y. Chang, A. S. Barnard, L. C. Gontard, and R. E. Dunin-Borkowski, “Resolving the structure of active sites on platinum catalytic nanoparticles,” *Nano Letters*, vol. 10, no. 8, pp. 3073–3076, 2010.
- [35] W. Qin and P. Fraundorf, “Lattice parameters from direct-space images at two tilts,” *Ultramicroscopy*, vol. 94, pp. 245–262, 4 2003.



- [36] A. V. Crewe, J. Wall, and L. M. Welter, “A high-resolution scanning transmission electron microscope,” *Journal of Applied Physics*, vol. 39, no. 13, pp. 5861–5868, 1968.
- [37] M. Knoll, “Charge potential and secondary emissions of electron irradiated bodies,” *Physikalische Zeitschrift*, vol. 36, pp. 861–869, 1935.
- [38] A. V. Crewe, J. Wall, and J. Langmore, “Visibility of single atoms,” *Science*, vol. 168, no. 3937, pp. 1338–1340, 1970.
- [39] R. Erni, M. D. Rossell, C. Kisielowski, and U. Dahmen, “Atomic-resolution imaging with a sub-50-pm electron probe,” *Physical Review Letters*, vol. 102, no. 9, pp. 096101–, 2009.
- [40] J. Cowley, “Coherent interference effects in SIEM and CBED,” *Ultramicroscopy*, vol. 7, no. 1, pp. 19 – 26, 1981.
- [41] H. Sawada, T. Sannomiya, F. Hosokawa, T. Nakamichi, T. Kaneyama, T. Tomita, Y. Kondo, T. Tanaka, Y. Oshima, Y. Tanishiro, and K. Takayanagi, “Measurement method of aberration from ronchigram by autocorrelation function,” *Ultramicroscopy*, vol. 108, no. 11, pp. 1467 – 1475, 2008.
- [42] P. Nellist and S. Pennycook, “The principles and interpretation of annular dark-field Z-contrast imaging,” vol. 113 of *Advances in Imaging and Electron Physics*, pp. 147 – 203, Elsevier, 2000.
- [43] O. L. Krivanek, M. F. Chisholm, V. Nicolosi, T. J. Pennycook, G. J. Corbin, N. Dellby, M. F. Murfitt, C. S. Own, Z. S. Szilagy, M. P. Oxley, S. T. Pantelides, and S. J. Pennycook, “Atom-by-atom structural and chemical analysis by annular dark-field electron microscopy,” *Nature*, vol. 464, pp. 571–574, 03 2010.
- [44] M. M. J. Treacy, A. Howie, and C. J. Wilson, “Z contrast of platinum and palladium catalysts,” *Philosophical Magazine A*, vol. 38, no. 5, pp. 569–585, 1978.
- [45] J. M. LeBeau and S. Stemmer, “Experimental quantification of annular dark-field images in scanning transmission electron microscopy,” *Ultramicroscopy*, vol. 108, no. 12, pp. 1653 – 1658, 2008.
- [46] J. M. LeBeau, S. D. Findlay, X. Wang, A. J. Jacobson, L. J. Allen, and S. Stemmer, “High-angle scattering of fast electrons from crystals containing heavy elements: Simulation and experiment,” *Physical Review B*, vol. 79, pp. 214110–, 06 2009.

- [47] J. M. LeBeau, S. D. Findlay, L. J. Allen, and S. Stemmer, “Standardless atom counting in scanning transmission electron microscopy,” *Nano Letters*, vol. 11, no. 1, pp. 310–310, 2010.
- [48] V. Grillo, “An advanced study of the response of ADF detector,” *Journal of Physics: Conference Series*, vol. 326, no. 1, p. 012036, 2011.
- [49] H. E. P. D. Nellist, S. Lozano-Perez, and D. Ozkaya, “Quantitative analysis of core-shell catalyst nanoparticles for industrial applications,” *Journal of Physics: Conference Series*, vol. 371, no. 1, p. 012027, 2012.
- [50] H. E. P. D. Nellist, A. J. D’Alfonso, and L. J. Allen, “Quantitative techniques for aberration corrected HAADF STEM of nano-materials,” *Journal of Physics: Conference Series*, vol. 371, no. 1, p. 012054, 2012.
- [51] O. Scherzer, “Ein elektronenoptischer apochromat,” *Zeitschrift Naturforschung Teil A*, vol. 3, p. 544, 1948.
- [52] M. Haider, H. Rose, S. Uhlemann, E. Schwan, B. Kabius, and K. Urban, “A spherical-aberration-corrected 200 kv transmission electron microscope,” *Ultramicroscopy*, vol. 75, no. 1, pp. 53 – 60, 1998.
- [53] M. Haider, S. Uhlemann, E. Schwan, H. Rose, B. Kabius, and K. Urban, “Electron microscopy image enhanced,” *Nature*, vol. 392, pp. 768–769, 04 1998.
- [54] O. Krivanek, G. Corbin, N. Dellby, B. Elston, R. Keyse, M. Murfitt, C. Own, Z. Szilagyi, and J. Woodruff, “An electron microscope for the aberration-corrected era,” *Ultramicroscopy*, vol. 108, no. 3, pp. 179 – 195, 2008.
- [55] L. M. Peng, S. L. Dudarev, and M. J. Whelan, *High Energy Electron Diffraction and Microscopy*. Oxford Science Publications, 2004.
- [56] F. Zemlin, K. Weiss, P. Schiske, W. Kunath, and K.-H. Herrmann, “Coma-free alignment of high resolution electron microscopes with the aid of optical diffractograms,” *Ultramicroscopy*, vol. 3, no. 0, pp. 49 – 60, 1978.
- [57] P. E. Batson, N. Dellby, and O. L. Krivanek, “Sub-angstrom resolution using aberration corrected electron optics,” *Nature*, vol. 418, pp. 617–620, 08 2002.
- [58] O. L. Krivanek and et al, “Towards sub-0.5 Å electron beams,” *Ultramicroscopy*, vol. 96, pp. 229–237, 2003.

- [59] P. D. Nellist, M. F. Chisholm, N. Dellby, O. L. Krivanek, M. F. Murfitt, Z. S. Szi-  
lagyi, A. R. Lupini, A. Borisevich, W. H. Sides, and S. J. Pennycook, “Direct sub-  
angstrom imaging of a crystal lattice,” *Science*, vol. 305, pp. 1741–1741, 09 2004.
- [60] B. J. Duggan and I. P. Jones, “The orientation and position accuracy of electron  
diffraction,” *Texture of Crystalline Solids*, vol. 2, pp. 205–223, 1977.
- [61] A. W. Agar, “Accuracy of selected-area microdiffraction in the electron micro-  
scope,” *British Journal of Applied Physics*, vol. 11, pp. 185–189, May 1960.
- [62] J. Yamasaki, H. Sawada, and N. Tanaka, “First experiments of selected area nano-  
diffraction from semiconductor interfaces using a spherical aberration corrected  
TEM,” *Journal of Electron Microscopy*, vol. 54, pp. 123–126, 04 2005.
- [63] S. J. Pennycook, *Scanning Transmission Electron Microscopy*. Springer, 2011.
- [64] O. Krivanek, N. Dellby, and A. Lupini, “Towards sub- Å electron beams,” *Ultrami-  
croscopy*, vol. 78, no. 1–4, pp. 1 – 11, 1999.
- [65] D. Alloyeau, C. Ricolleau, T. Oikawa, C. Langlois, Y. L. Bouar, and A. Loiseau,  
“STEM nanodiffraction technique for structural analysis of CoPt nanoparticles,”  
*Ultramicroscopy*, vol. 108, no. 7, pp. 656 – 662, 2008.
- [66] E. D. Boyes, M. R. Ward, L. Lari, and P. L. Gai, “ESTEM imaging of single atoms  
under controlled temperature and gas environment conditions in catalyst reaction  
studies,” *Annalen der Physik*, vol. 525, no. 6, pp. 423–429, 2013.
- [67] J. Creemer, S. Helveg, G. Hoveling, S. Ullmann, A. Molenbroek, P. Sarro, and  
H. Zandbergen, “Atomic-scale electron microscopy at ambient pressure,” *Ultrami-  
croscopy*, vol. 108, no. 9, pp. 993 – 998, 2008.
- [68] J. B. Wagner, F. Cavalca, C. D. Damsgaard, L. D. Duchstein, and T. W. Hansen,  
“Exploring the environmental transmission electron microscope,” *Micron*, vol. 43,  
no. 11, pp. 1169 – 1175, 2012.
- [69] H. Hashimoto, T. Naiki, T. Eto, and K. Fujiwara, “High temperature gas reac-  
tion specimen chamber for an electron microscope,” *Japanese Journal of Applied  
Physics*, vol. 7, no. 8, pp. 946–952, 1968.
- [70] R. T. K. Baker and P. S. Harris, “Controlled atmosphere electron microscopy,” *Jour-  
nal of Physics E: Scientific Instruments*, vol. 5, no. 8, p. 793, 1972.

- [71] E. Boyes and P. Gai, “Environmental high resolution electron microscopy and applications to chemical science,” *Ultramicroscopy*, vol. 67, no. 1–4, pp. 219 – 232, 1997.
- [72] P. L. Gai and E. D. Boyes, “Advances in atomic resolution in-situ environmental transmission electron microscopy and 1 Å aberration corrected in-situ electron microscopy,” *Microscopy Research and Technique*, vol. 72, no. 3, pp. 153–164, 2009.
- [73] P. L. Gai and E. D. Boyes, “Angstrom analysis with dynamic in-situ aberration corrected electron microscopy,” *Journal of Physics: Conference Series*, vol. 241, p. 012055, 2010.
- [74] C. A. Schneider, W. S. Rasband, and K. W. Eliceiri, “NIH Image to ImageJ: 25 years of image analysis,” *Nat Meth*, vol. 9, pp. 671–675, 07 2012.
- [75] P. Stadelmann, “EMS - a software package for electron diffraction analysis and HREM image simulation in materials science,” *Ultramicroscopy*, vol. 21, no. 2, pp. 131 – 145, 1987.
- [76] K. Momma and F. Izumi, “VESTA3 for three-dimensional visualization of crystal, volumetric and morphology data,” *Journal of Applied Crystallography*, vol. 44, pp. 1272–1276, Dec 2011.
- [77] C. T. Koch, *Determination of core structure periodicity and point defect density along dislocations*. PhD thesis, Arizona State University, 2002.
- [78] P. Goodman and A. F. Moodie, “Numerical evaluations of  $N$ -beam wave functions in electron scattering by the multi-slice method,” *Acta Crystallographica Section A*, vol. 30, pp. 280–290, Mar 1974.
- [79] P. Rez, C. J. Humphreys, and M. J. Whelan, “The distribution of intensity in electron diffraction patterns due to phonon scattering,” *Philosophical Magazine*, vol. 35, no. 1, pp. 81–96, 1977.
- [80] P. Rez, “Does phonon scattering give high-resolution images?,” *Ultramicroscopy*, vol. 52, no. 3–4, pp. 260 – 266, 1993.
- [81] D. V. Dyck, “Is the frozen phonon model adequate to describe inelastic phonon scattering?,” *Ultramicroscopy*, vol. 109, no. 6, pp. 677 – 682, 2009.
- [82] Z. Wang, “Thermal diffuse scattering in high-resolution electron holography,” *Ultramicroscopy*, vol. 52, no. 3–4, pp. 504 – 511, 1993.

- [83] J. Goldstein, D. E. Newbury, D. C. Joy, C. E. Lyman, P. Echlin, E. Lifshin, L. C. Sawyer, and J. R. Michael, *Scanning Electron Microscopy and X-ray Microanalysis*. Springer, 3rd ed., 2002.
- [84] E. D. Boyes and P. L. Gai, “Environmental high resolution electron microscopy and applications to chemical science,” *Ultramicroscopy*, vol. 67, pp. 219–232, 1996.
- [85] M. J. Walsh, *Aberration Corrected In-Situ Electron Microscopy of Nanoparticle Catalysts*. PhD thesis, University of York, Department of Physics, 2012.
- [86] M. Haider, S. Uhlemann, and J. Zach, “Upper limits for the residual aberrations of a high-resolution aberration-corrected STEM,” *Ultramicroscopy*, vol. 81, no. 3–4, pp. 163 – 175, 2000.
- [87] E. Fermi, *Thermodynamics*. Dover, 2000.
- [88] C. R. Henry, “Morphology of supported nanoparticles,” *Progress in Surface Science*, vol. 80, no. 3–4, pp. 92 – 116, 2005.
- [89] G. Wulff, “Zeitschrift fur kristallographie,” *Mineral*, vol. 25, pp. 449–530, 1901.
- [90] M. Vaarkamp, J. T. Miller, F. S. Modica, and D. C. Koningsberger, “On the relation between particle morphology, structure of the metal-support interface, and catalytic properties of Pt/ $\gamma$ -Al<sub>2</sub>O<sub>3</sub>,” *Journal of Catalysis*, vol. 163, no. 2, pp. 294 – 305, 1996.
- [91] A. Y. Stakheev and L. M. Kustov, “Effects of the support on the morphology and electronic properties of supported metal clusters: modern concepts and progress in 1990s,” *Applied Catalysis A: General*, vol. 188, pp. 3–35, 11 1999.
- [92] J. H. Kwak, J. Hu, D. Mei, C.-W. Yi, D. H. Kim, C. H. F. Peden, L. F. Allard, and J. Szanyi, “Coordinatively unsaturated Al<sup>3+</sup> centers as binding sites for active catalyst phases of platinum on  $\gamma$ -Al<sub>2</sub>O<sub>3</sub>,” *Science*, vol. 325, pp. 1670–1673, 09 2009.
- [93] O. Ezekoye, A. Drews, H.-W. Jen, R. Kudla, R. McCabe, M. Sharma, J. Howe, L. Allard, G. Graham, and X. Pan, “Characterization of alumina-supported Pt and Pt–Pd NO oxidation catalysts with advanced electron microscopy,” *Journal of Catalysis*, vol. 280, no. 1, pp. 125 – 136, 2011.
- [94] N. M. Marković, R. R. Adžić, B. D. Cahan, and E. B. Yeager, “Structural effects in electrocatalysis: oxygen reduction on platinum low index single-crystal surfaces

- in perchloric acid solutions,” *Journal of Electroanalytical Chemistry*, vol. 377, pp. 249–259, 10 1994.
- [95] W. Winterbottom, “Equilibrium shape of a small particle in contact with a foreign substrate,” *Acta Metallurgica*, vol. 15, no. 2, pp. 303 – 310, 1967.
- [96] A. R. Tao, S. Habas, and P. Yang, “Shape control of colloidal metal nanocrystals,” *Small*, vol. 4, no. 3, pp. 310–325, 2008.
- [97] Z. Peng and H. Yang, “Designer platinum nanoparticles: Control of shape, composition in alloy, nanostructure and electrocatalytic property,” *Nano Today*, vol. 4, no. 2, pp. 143 – 164, 2009.
- [98] Y. Xiong and Y. Xia, “Shape-controlled synthesis of metal nanostructures: The case of palladium,” *Advanced Materials*, vol. 19, no. 20, pp. 3385–3391, 2007.
- [99] W. Niu, L. Zhang, and G. Xu, “Shape-controlled synthesis of single-crystalline palladium nanocrystals,” *ACS Nano*, vol. 4, no. 4, pp. 1987–1996, 2010.
- [100] S. Ino, “Epitaxial growth on metals on rocksalt faces cleaved in vacuum. II. orientation and structure of gold particles formed in ultrahigh vacuum,” *Journal of The Physical Society of Japan*, vol. 21, no. 2, 1966.
- [101] C. Y. Yang, “Crystallography of decahedral and icosahedral particles,” *Journal of Crystal Growth*, vol. 47, pp. 274–282, 1979.
- [102] F. Robinson and M. Gillet, “Electron microscopy investigation of structure and morphology of small supported metal particles of palladium,” *Thin Solid Films*, vol. 98, no. 3, pp. 179 – 196, 1982.
- [103] M. José-Yacamán, M. Marín-Almazo, and J. Ascencio, “High resolution tem studies on palladium nanoparticles,” *Journal of Molecular Catalysis A: Chemical*, vol. 173, pp. 61–74, 2001.
- [104] J. L. Elechiguerra, J. Reyes-Gasga, and M. J. Yacaman, “The role of twinning in shape evolution of anisotropic noble metal nanostructures,” *J. Mater. Chem.*, vol. 16, pp. 3906–3919, 2006.
- [105] J. Allpress and J. Sanders, “The structure and orientation of crystals in deposits of metals on mica,” *Surface Science*, vol. 7, no. 1, pp. 1 – 25, 1967.
- [106] C. Y. Yang, M. J. Yacaman, and K. Heinemann, “Crystallography of decahedral and icosahedral particles,” *Journal of Crystal Growth*, vol. 47, pp. 283–290, 1979.

- [107] A. S. Barnard, N. P. Young, A. I. Kirkland, M. A. van Huis, and H. Xu, “Nanogold: A quantitative phase map,” *ACS Nano*, vol. 3, no. 6, pp. 1431–1436, 2009.
- [108] R. V. Chepulskii and S. Curtarolo, “Ab initio insights on the shapes of platinum nanocatalysts,” *ACS Nano*, vol. 5, no. 1, pp. 247–254, 2011.
- [109] S. Maksimuk, X. Teng, and H. Yang, “Roles of twin defects in the formation of platinum multipod nanocrystals,” *The Journal of Physical Chemistry C*, vol. 111, no. 39, pp. 14312–14319, 2007.
- [110] D. Hull and D. J. Bacon, *Introduction to Dislocations*. Elsevier, 2011.
- [111] *Springer Handbook of Crystal Growth*. Springer, 2010.
- [112] X.-Z. Wu, R. Wang, S.-F. Wang, and Q.-Y. Wei, “Ab initio calculations of generalized-stacking-fault energy surfaces and surface energies for fcc metals,” *Applied Surface Science*, vol. 256, pp. 6345–6349, 8 2010.
- [113] J. Cai, F. Wang, C. Lu, and Y. Y. Wang, “Structure and stacking-fault energy in metals Al, Pd, Pt, Ir, and Rh,” *Physical Review B*, vol. 69, pp. 224104–, 06 2004.
- [114] K. Du, F. Ernst, M. Pelsozy, J. Barthel, and K. Tillmann, “Expansion of inter-atomic distances in platinum catalyst nanoparticles,” *Acta Materialia*, vol. 58, no. 3, pp. 836 – 845, 2010.
- [115] C. R. Berry, “Electron diffraction from small crystals,” *Phys. Rev.*, vol. 88, pp. 596–599, Nov 1952.
- [116] H. Wasserman and J. Vermaak, “On the determination of a lattice contraction in very small silver particles,” *Surface Science*, vol. 22, no. 1, pp. 164 – 172, 1970.
- [117] P. Montano, J. Zhao, M. Ramanathan, G. Shenoy, W. Schulze, and J. Urban, “Structure of silver microclusters,” *Chemical Physics Letters*, vol. 164, no. 2–3, pp. 126 – 130, 1989.
- [118] C. Mays, J. Vermaak, and D. Kuhlmann-Wilsdorf, “On surface stress and surface tension: II. determination of the surface stress of gold,” *Surface Science*, vol. 12, no. 2, pp. 134 – 140, 1968.
- [119] C. Solliard and M. Flueli, “Surface stress and size effect on the lattice parameter in small particles of gold and platinum,” *Surface Science*, vol. 156, Part 1, no. 0, pp. 487 – 494, 1985.

- [120] H. Wasserman and J. Vermaak, “On the determination of the surface stress of copper and platinum,” *Surface Science*, vol. 32, no. 1, pp. 168 – 174, 1972.
- [121] K. Heinemann and H. Poppa, “In-situ TEM evidence of lattice expansion of very small supported palladium particles,” *Surface Science*, vol. 156, Part 1, no. 0, pp. 265 – 274, 1985.
- [122] S. Giorgio, C. Henry, C. Chapon, and J. Penisson, “Structure and morphology of small palladium particles (2–6 nm) supported on MgO micro-cubes,” *Journal of Crystal Growth*, vol. 100, no. 1–2, pp. 254 – 260, 1990.
- [123] J. Vermaak, C. Mays, and D. Kuhlmann-Wilsdorf, “On surface stress and surface tension: I. theoretical considerations,” *Surface Science*, vol. 12, no. 2, pp. 128 – 133, 1968.
- [124] R. Lamber, S. Wetjen, and N. I. Jaeger, “Size dependence of the lattice parameter of small palladium particles,” *Phys. Rev. B*, vol. 51, pp. 10968–10971, Apr 1995.
- [125] W.-H. Li, S. Y. Wu, C. C. Yang, S. K. Lai, K. C. Lee, L. Huang, H. and D. Yang, H. “Thermal contraction of Au nanoparticles,” *Phys. Rev. Lett.*, vol. 89, p. 135504, Sep 2002.
- [126] W. H. Qi, M. P. Wang, and Y. C. Su, “Size effect on the lattice parameters of nanoparticles,” *Journal of Materials Science Letters*, vol. 21, no. 11, pp. 877–878, 2002.
- [127] Z. Wei, T. Xia, J. Ma, W. Feng, J. Dai, Q. Wang, and P. Yan, “Investigation of the lattice expansion for Ni nanoparticles,” *Materials Characterization*, vol. 58, no. 10, pp. 1019 – 1024, 2007.
- [128] N. Toshima and T. Yonezawa, “Bimetallic nanoparticles-novel materials for chemical and physical applications,” *New J. Chem.*, vol. 22, pp. 1179–1201, 1998.
- [129] D. Alloyeau, R. Ricolleau, C. Mottet, T. Oikawa, C. Langlois, Y. L. Bouar, N. Braidy, and A. Loiseau, “Size and shape effects on the order-disorder phase transition in CoPt nanoparticles,” *Nature Materials*, vol. 8, pp. 940–946, 2009.
- [130] A. R. Denton and N. W. Ashcroft, “Vegard’s law,” *Phys. Rev. A*, vol. 43, pp. 3161–3164, Mar 1991.
- [131] S. C. Y. Tsen, P. A. Crozier, and J. Liu, “Lattice measurements and alloy compositions in metal and bimetallic nanoparticles,” *Ultramicroscopy*, vol. 98, pp. 63–72, 2003.



- [132] Y. Sun, L. Zhuang, J. Lu, X. Hong, and P. Liu, "Collapse in crystalline structure and decline in catalytic activity of Pt nanoparticles on reducing particle size to 1 nm," *Journal of the American Chemical Society*, vol. 129, no. 50, pp. 15465–15467, 2007.
- [133] N. V. Long, M. Ohtaki, M. Uchida, R. Jalem, H. Hirata, N. D. Chien, and M. Nogami, "Synthesis and characterization of polyhedral Pt nanoparticles: Their catalytic property, surface attachment, self-aggregation and assembly," *Journal of Colloid and Interface Science*, vol. 359, no. 2, pp. 339 – 350, 2011.
- [134] L. M. Molina and B. Hammer, "Active role of oxide support during CO oxidation at Au/MgO," *Phys. Rev. Lett.*, vol. 90, p. 206102, May 2003.
- [135] J.-D. Grunwaldt, C. Kiener, C. Wögerbauer, and A. Baiker, "Preparation of supported gold catalysts for low-temperature CO oxidation via "size-controlled" gold colloids," *Journal of Catalysis*, vol. 181, no. 2, pp. 223 – 232, 1999.
- [136] T. H. Fleisch, R. F. Hicks, and A. T. Bell, "An XPS study of metal-support interactions on Pd–SiO<sub>2</sub> and Pd–La<sub>2</sub>O<sub>3</sub>," *Journal of Catalysis*, vol. 87, no. 2, pp. 398 – 413, 1984.
- [137] K. Hayek, M. Fuchs, B. Klötzer, W. Reichl, and G. Rupprechter, "Studies of metal–support interactions with "real" and "inverted" model systems: reactions of CO and small hydrocarbons with hydrogen on noble metals in contact with oxides," *Topics in Catalysis*, vol. 13, pp. 55–66, 2000.
- [138] R. Baker, E. Prestidge, and G. McVicker, "The interaction of palladium with alumina and titanium oxide supports," *Journal of Catalysis*, vol. 89, no. 2, pp. 422 – 432, 1984.
- [139] S. J. Tauster, "Strong metal-support interactions," *Accounts of Chemical Research*, vol. 20, no. 11, pp. 389–394, 1987.
- [140] Q. Fu and T. Wagner, "Interaction of nanostructured metal overlayers with oxide surfaces," *Surface Science Reports*, vol. 62, no. 11, pp. 431 – 498, 2007.
- [141] K. Sun, J. Liu, N. Nag, and N. Browning, "Studying the metal-support interaction in Pd/ $\gamma$ -Al<sub>2</sub>O<sub>3</sub> catalysts by atomic-resolution electron energy-loss spectroscopy," *Catalysis Letters*, vol. 84, pp. 193–199, 2002. 10.1023/A:1021428003587.
- [142] P. D. Nellist and S. J. Pennycook, "Direct imaging of the atomic configuration of ultradispersed catalysts," *Science*, vol. 274, pp. 413–415, 10 1996.

- [143] K. Sohlberg, S. Rashkeev, A. Y. Borisevich, S. J. Pennycook, and S. T. Pantelides, "Origin of anomalous Pt–Pt distances in the Pt/alumina catalytic system," *ChemPhysChem*, vol. 5, no. 12, pp. 1893–1897, 2004.
- [144] K. C. Taylor, "Nitric oxide catalysis in automotive exhaust systems," *Catalysis Reviews*, vol. 35, no. 4, pp. 457–481, 1993.
- [145] B. C. Gates, "Supported metal clusters: Synthesis, structure, and catalysis," *Chemical Reviews*, vol. 95, no. 3, pp. 511–522, 1995.
- [146] M. Che and C. O. Bennett, "The influence of particle size on the catalytic properties of supported metals," vol. 36 of *Advances in Catalysis*, pp. 55 – 172, Academic Press, 1989.
- [147] B. Shi and B. Davis, "Alcohol dehydration: Mechanism of ether formation using an alumina catalyst," *Journal of Catalysis*, vol. 157, no. 2, pp. 359 – 367, 1995.
- [148] J. M. McHale, A. Navrotsky, and A. J. Perrotta, "Effects of increased surface area and chemisorbed H<sub>2</sub>O on the relative stability of nanocrystalline  $\gamma$ -Al<sub>2</sub>O<sub>3</sub> and  $\alpha$ -Al<sub>2</sub>O<sub>3</sub>," *The Journal of Physical Chemistry B*, vol. 101, no. 4, pp. 603–613, 1997.
- [149] J. M. McHale, A. Auroux, A. J. Perrotta, and A. Navrotsky, "Surface energies and thermodynamic phase stability in nanocrystalline aluminas," *Science*, vol. 277, no. 5327, pp. 788–791, 1997.
- [150] I. Levin and D. Brandon, "Metastable alumina polymorphs: Crystal structures and transition sequences," *Journal of the American Ceramic Society*, vol. 81, no. 8, pp. 1995–2012, 1998.
- [151] P. S. Santos, H. S. Santos, and S. Toledo, "Standard transition aluminas. electron microscopy studies," *Materials Research*, vol. 3, pp. 104 – 114, 10 2000.
- [152] R.-S. Zhou and R. L. Snyder, "Structures and transformation mechanisms of the  $\eta$ ,  $\gamma$  and  $\theta$  transition aluminas," *Acta Crystallographica Section B*, vol. 47, pp. 617–630, Oct 1991.
- [153] B. C. Lippens and J. H. de Boer, "Study of phase transformations during calcination of aluminum hydroxides by selected area electron diffraction," *Acta Crystallographica*, vol. 17, pp. 1312–1321, Oct 1964.
- [154] S. Wilson and J. M. Connell, "A kinetic study of the system  $\gamma$ -AlOOH/Al<sub>2</sub>O<sub>3</sub>," *Journal of Solid State Chemistry*, vol. 34, no. 3, pp. 315 – 322, 1980.

- [155] G. Paglia, C. E. Buckley, A. L. Rohl, B. A. Hunter, R. D. Hart, J. V. Hanna, and L. T. Byrne, “Tetragonal structure model for boehmite-derived  $\gamma$ -alumina,” *Phys. Rev. B*, vol. 68, p. 144110, Oct 2003.
- [156] V. Jayaram and C. Levi, “The structure of  $\gamma$ -alumina evolved from the melt and the  $\gamma$   $\delta$  transformation,” *Acta Metallurgica*, vol. 37, no. 2, pp. 569 – 578, 1989.
- [157] G. Paglia, C. E. Buckley, A. L. Rohl, R. D. Hart, K. Winter, A. J. Studer, B. A. Hunter, and J. V. Hanna, “Boehmite derived  $\gamma$ -alumina system. 1. structural evolution with temperature, with the identification and structural determination of a new transition phase,  $\gamma'$ -alumina,” *Chemistry of Materials*, vol. 16, no. 2, pp. 220–236, 2003.
- [158] S.-D. Mo, Y.-N. Xu, and W.-Y. Ching, “Electronic and structural properties of bulk  $\gamma$ - $\text{Al}_2\text{O}_3$ ,” *Journal of the American Ceramic Society*, vol. 80, no. 5, pp. 1193–1197, 1997.
- [159] G. Kryukova, D. Klenov, A. Ivanova, and S. Tsybulya, “Vacancy ordering in the structure of  $\gamma$ - $\text{Al}_2\text{O}_3$ ,” *Journal of the European Ceramic Society*, vol. 20, no. 8, pp. 1187 – 1189, 2000.
- [160] Y. G. Wang, P. M. Bronsveld, J. T. M. DeHosson, B. Djuričić, D. McGarry, and S. Pickering, “Ordering of octahedral vacancies in transition aluminas,” *Journal of the American Ceramic Society*, vol. 81, no. 6, pp. 1655–1660, 1998.
- [161] J. A. Wang, X. Bokhimi, A. Morales, O. Novaro, T. López, and R. Gómez, “Aluminum local environment and defects in the crystalline structure of solgel alumina catalyst,” *The Journal of Physical Chemistry B*, vol. 103, no. 2, pp. 299–303, 1999.
- [162] C. Pecharromán, I. Sobrados, J. E. Iglesias, T. González-Carreño, and J. Sanz, “Thermal evolution of transitional aluminas followed by NMR and IR spectroscopies,” *The Journal of Physical Chemistry B*, vol. 103, no. 30, pp. 6160–6170, 1999.
- [163] G. Paglia, E. S. Božin, and S. J. L. Billinge, “Fine-scale nanostructure in  $\gamma$ - $\text{Al}_2\text{O}_3$ ,” *Chemistry of Materials*, vol. 18, no. 14, pp. 3242–3248, 2006.
- [164] Y. Rozita, R. Brydson, and A. J. Scott, “An investigation of commercial gamma- $\text{Al}_2\text{O}_3$  nanoparticles,” *Journal of Physics: Conference Series*, vol. 241, no. 1, p. 012096, 2010.

- [165] P. Atkins and J. de Paula, *Atkins' Physical Chemistry*. OUP Oxford, 9 ed., 2009.
- [166] C. Doornkamp and V. Ponec, "The universal character of the mars and van krevelen mechanism," *Journal of Molecular Catalysis A: Chemical*, vol. 162, no. 1–2, pp. 19 – 32, 2000.
- [167] I. E. Beck, V. I. Bukhtiyarov, I. Y. Pakharukov, V. I. Zaikovsky, V. V. Kriventsov, and V. N. Parmon, "Platinum nanoparticles on  $\text{Al}_2\text{O}_3$ : Correlation between the particle size and activity in total methane oxidation," *Journal of Catalysis*, vol. 268, no. 1, pp. 60 – 67, 2009.
- [168] R. Narayanan and M. A. El-Sayed, "Shape-dependent catalytic activity of platinum nanoparticles in colloidal solution," *Nano Letters*, vol. 4, no. 7, pp. 1343–1348, 2004.
- [169] S. Mostafa, F. Behafarid, J. R. Croy, L. K. Ono, L. Li, J. C. Yang, A. I. Frenkel, and B. R. Cuenya, "Shape-dependent catalytic properties of Pt nanoparticles," *Journal of the American Chemical Society*, vol. 132, no. 44, pp. 15714–15719, 2010.
- [170] R. Wang, H. He, L.-C. Liu, H.-X. Dai, and Z. Zhao, "Shape-dependent catalytic activity of palladium nanocrystals for the oxidation of carbon monoxide," *Catal. Sci. Technol.*, vol. 2, pp. 575–580, 2012.
- [171] O. M. Wilson, M. R. Knecht, J. C. Garcia-Martinez, and R. M. Crooks, "Effect of Pd nanoparticle size on the catalytic hydrogenation of allyl alcohol," *Journal of the American Chemical Society*, vol. 128, no. 14, pp. 4510–4511, 2006.
- [172] J. M. Domínguez and M. J. Yacamán, "On the catalytic properties and structure of small platinum particles supported on graphite," *Journal of Catalysis*, vol. 64, pp. 223–227, 1980.
- [173] R. van Hardeveld and A. van Montfoort, "The influence of crystallite size on the adsorption of molecular nitrogen on nickel, palladium and platinum: An infrared and electron-microscopic study," *Surface Science*, vol. 4, no. 4, pp. 396 – 430, 1966.
- [174] G. A. Somorjai and D. W. Blakely, "Mechanism of catalysis of hydrocarbon reactions by platinum surfaces," *Nature*, vol. 258, pp. 580–583, 12 1975.
- [175] Y. Li, E. Boone, and M. A. El-Sayed, "Size effects of PVP-Pd nanoparticles on the catalytic suzuki reactions in aqueous solution," *Langmuir*, vol. 18, no. 12, pp. 4921–4925, 2002.

- [176] A. Benedetti, G. Fagherazzi, F. Pinna, G. Rampazzo, M. Selva, and G. Strukul, "The influence of a second metal component (Cu, Sn, Fe) on Pd/SiO<sub>2</sub> activity in the hydrogenation of 2,4-dinitrotoluene," *Catalysis Letters*, vol. 10, pp. 215–223, 1991.
- [177] R. L. Augustine and S. T. O'Leary, "Heterogeneous catalysis in organic chemistry. part 10. effect of the catalyst support on the regiochemistry of the heck arylation reaction," *Journal of Molecular Catalysis A: Chemical*, vol. 95, no. 3, pp. 277 – 285, 1995.
- [178] M. Grass, Y. Zhang, D. Butcher, J. Park, Y. Li, H. Bluhm, K. Bratlie, T. Zhang, and G. Somorjai, "A reactive oxide overlayer on rhodium nanoparticles during CO oxidation and its size dependence studied by in-situ ambient-pressure X-ray photoelectron spectroscopy," *Angewandte Chemie International Edition*, vol. 47, no. 46, pp. 8893–8896, 2008.
- [179] S. H. Joo, J. Y. Park, J. R. Renzas, D. R. Butcher, W. Huang, and G. A. Somorjai, "Size effect of ruthenium nanoparticles in catalytic carbon monoxide oxidation," *Nano Letters*, vol. 10, no. 7, pp. 2709–2713, 2010.
- [180] N. Lopez, T. Janssens, B. Clausen, Y. Xu, M. Mavrikakis, T. Bligaard, and J. Nørskov, "On the origin of the catalytic activity of gold nanoparticles for low-temperature CO oxidation," *Journal of Catalysis*, vol. 223, no. 1, pp. 232 – 235, 2004.
- [181] B. Hammer, O. Nielsen, and J. Nørskov, "Structure sensitivity in adsorption: CO interaction with stepped and reconstructed Pt surfaces," *Catalysis Letters*, vol. 46, pp. 31–35, 1997.
- [182] B. Hammer and J. Nørskov, "Electronic factors determining the reactivity of metal surfaces," *Surface Science*, vol. 343, no. 3, pp. 211 – 220, 1995.
- [183] M. Gsell, P. Jakob, and D. Menzel, "Effect of substrate strain on adsorption," *Science*, vol. 280, no. 5364, pp. 717–720, 1998.
- [184] M. Mavrikakis, B. Hammer, and J. K. Nørskov, "Effect of strain on the reactivity of metal surfaces," *Phys. Rev. Lett.*, vol. 81, pp. 2819–2822, Sep 1998.
- [185] L. A. Kibler, A. M. El-Aziz, R. Hoyer, and D. M. Kolb, "Tuning reaction rates by lateral strain in a palladium monolayer," *Angewandte Chemie International Edition*, vol. 44, no. 14, pp. 2080–2084, 2005.

- [186] A. Schlapka, M. Lischka, A. Groß, U. Käsberger, and P. Jakob, “Surface strain versus substrate interaction in heteroepitaxial metal layers: Pt on ru(0001),” *Phys. Rev. Lett.*, vol. 91, p. 016101, Jun 2003.
- [187] J. Greeley, W. P. Krekelberg, and M. Mavrikakis, “Strain-induced formation of sub-surface species in transition metals,” *Angewandte Chemie International Edition*, vol. 43, no. 33, pp. 4296–4300, 2004.
- [188] T. Bligaard, J. K. Nørskov, S. Dahl, J. Matthiesen, C. H. Christensen, and J. Sehested, “The brønsted–evans–polanyi relation and the volcano curve in heterogeneous catalysis,” *Journal of Catalysis*, vol. 224, pp. 206–217, 5 2004.
- [189] S. N. Rashkeev, A. R. Lupini, S. H. Overbury, S. J. Pennycook, and S. T. Pantelides, “Role of the nanoscale in catalytic CO oxidation by supported Au and Pt nanostructures,” *Phys. Rev. B*, vol. 76, p. 035438, Jul 2007.
- [190] B. Hvolbæk, T. V. W. Janssens, B. S. Clausen, H. Falsig, C. H. Christensen, and J. K. Nørskov, “Catalytic activity of Au nanoparticles,” *Nano Today*, vol. 2, pp. 14–18, 8 2007.
- [191] S. E. Golunski, “Why use platinum in catalytic converters?,” *Platinum Metals Review*, vol. 51, p. 162, 2007.
- [192] A. Winkler, D. Ferri, and M. Aguirre, “The influence of chemical and thermal aging on the catalytic activity of a monolithic diesel oxidation catalyst,” *Applied Catalysis B: Environmental*, vol. 93, no. 1–2, pp. 177 – 184, 2009.
- [193] M. H. Wiebenga, C. H. Kim, S. J. Schmieg, S. H. Oh, D. B. Brown, D. H. Kim, J.-H. Lee, and C. H. Peden, “Deactivation mechanisms of Pt/Pd-based diesel oxidation catalysts,” *Catalysis Today*, vol. 184, no. 1, pp. 197–204, 2011.
- [194] J. Libuda, “Molecular beams and model catalysis: Activity and selectivity of specific reaction centers on supported nanoparticles,” *ChemPhysChem*, vol. 5, no. 5, pp. 625–631, 2004.
- [195] R. Finsy, “On the critical radius in ostwald ripening.,” *Langmuir*, vol. 20, pp. 2975–2976, March 2004.
- [196] C. T. Campbell, S. C. Parker, and D. E. Starr, “The effect of size-dependent nanoparticle energetics on catalyst sintering,” *Science*, vol. 298, no. 5594, pp. 811–814, 2002.

- [197] E. R. Lewis, “The effect of surface tension (kelvin effect) on the equilibrium radius of a hygroscopic aqueous aerosol particle,” *Aerosol Science*, vol. 37, no. 1605-1617, 2006.
- [198] P. Wynblatt and N. Gjostein, “Particle growth in model supported metal catalysts—i. theory,” *Acta Metallurgica*, vol. 24, no. 12, pp. 1165 – 1174, 1976.
- [199] B. Chakraverty, “Grain size distribution in thin films—1. conservative systems,” *Journal of Physics and Chemistry of Solids*, vol. 28, no. 12, pp. 2401 – 2412, 1967.
- [200] P. Wynblatt and N. Gjostein, “Supported metal crystallites,” *Progress in Solid State Chemistry*, vol. 9, no. 0, pp. 21 – 58, 1975.
- [201] T. J. Lee and Y. G. Kim, “Redispersion of supported platinum catalysts,” *Journal of Catalysis*, vol. 90, no. 2, pp. 279 – 291, 1984.
- [202] P. J. F. Harris, “Growth and structure of supported metal catalyst particles,” *International Materials Reviews*, vol. 40, no. 3, pp. 97–115, 1995.
- [203] S. B. Simonsen, I. Chorkendorff, S. Dahl, M. Skoglundh, J. Sehested, and S. Helveg, “Direct observations of oxygen-induced platinum nanoparticle ripening studied by in situ TEM,” *Journal of the American Chemical Society*, vol. 132, no. 23, pp. 7968–7975, 2010.
- [204] S. B. Simonsen, I. Chorkendorff, S. Dahl, M. Skoglundh, J. Sehested, and S. Helveg, “Ostwald ripening in a Pt/SiO<sub>2</sub> model catalyst studied by in situ TEM,” *Journal of Catalysis*, vol. 281, no. 1, pp. 147 – 155, 2011.
- [205] S. B. Simonsen, I. Chorkendorff, S. Dahl, M. Skoglundh, K. Meinander, T. N. Jensen, J. V. Lauritsen, and S. Helveg, “Effect of particle morphology on the ripening of supported Pt nanoparticles,” *The Journal of Physical Chemistry C*, vol. 116, no. 9, pp. 5646–5653, 2012.
- [206] K. Morgenstern, G. Rosenfeld, and G. Comsa, “Local correlation during ostwald ripening of two-dimensional islands on Ag(111),” *Surface Science*, vol. 441, no. 2–3, pp. 289 – 300, 1999.
- [207] R.-J. Liu, P. Crozier, C. Smith, D. Hucul, J. Blackson, and G. Salaita, “Metal sintering mechanisms and regeneration of palladium/alumina hydrogenation catalysts,” *Applied Catalysis A: General*, vol. 282, no. 1–2, pp. 111 – 121, 2005.

- [208] K. Okumura, S.-a. Hyodo, and S. Noda, "Growth of Pt crystallites supported on  $\gamma$ -Al<sub>2</sub>O<sub>3</sub> studied by atomic force microscopy," *The Journal of Physical Chemistry B*, vol. 105, no. 35, pp. 8345–8349, 2001.
- [209] R. Baker, C. Thomas, and R. Thomas, "Continuous observation of the particle size behavior of platinum on alumina," *Journal of Catalysis*, vol. 38, no. 1–3, pp. 510 – 513, 1975.
- [210] M. Chen and L. Schmidt, "Morphology and sintering of pt crystallites on amorphous sio<sub>2</sub>," *Journal of Catalysis*, vol. 55, no. 3, pp. 348 – 360, 1978.
- [211] P. C. Flynn and S. E. Wanke, "A model of supported metal catalyst sintering: I. development of model," *Journal of Catalysis*, vol. 34, no. 3, pp. 390 – 399, 1974.
- [212] F. A. Nichols and W. W. Mullins, "Morphological changes of a surface of revolution due to capillarity-induced surface diffusion," *Journal of Applied Physics*, vol. 36, no. 6, pp. 1826–1835, 1965.
- [213] S. Arcidiacono, N. Bieri, D. Poulikakos, and C. Grigoropoulos, "On the coalescence of gold nanoparticles," *International Journal of Multiphase Flow*, vol. 30, no. 7–8, pp. 979 – 994, 2004.
- [214] P. Buffat and J.-P. Borel, "Size effect on the melting temperature of gold particles," *Phys. Rev. A*, vol. 13, pp. 2287–2298, Jun 1976.
- [215] C. Q. Sun, Y. Wang, B. K. Tay, S. Li, H. Huang, and Y. B. Zhang, "Correlation between the melting point of a nanosolid and the cohesive energy of a surface atom," *The Journal of Physical Chemistry B*, vol. 106, no. 41, pp. 10701–10705, 2002.
- [216] C. Q. Sun, B. K. Tay, X. T. Zeng, S. Li, T. P. Chen, J. Zhou, H. L. Bai, and E. Y. Jiang, "Bond-order–bond-length–bond-strength (bond-OLS) correlation mechanism for the shape-and-size dependence of a nanosolid," *Journal of Physics: Condensed Matter*, vol. 14, no. 34, p. 7781, 2002.
- [217] R. Theissmann, M. Fendrich, R. Zinetullin, G. Guenther, G. Schierning, and D. E. Wolf, "Crystallographic reorientation and nanoparticle coalescence," *Physical Review B*, vol. 78, pp. 205413–, 11 2008.
- [218] K. E. J. Lehtinen and M. R. Zachariah, "Effect of coalescence energy release on the temporal shape evolution of nanoparticles," *Phys. Rev. B*, vol. 63, p. 205402, Apr 2001.



- [219] K. E. Lehtinen, R. S. Windeler, and S. K. Friedlander, “A note on the growth of primary particles in agglomerate structures by coalescence,” *Journal of Colloid and Interface Science*, vol. 182, no. 2, pp. 606 – 608, 1996.
- [220] M. R. Zachariah and M. J. Carrier, “Molecular dynamics computation of gas-phase nanoparticle sintering: a comparison with phenomenological models,” *Journal of Aerosol Science*, vol. 30, no. 9, pp. 1139 – 1151, 1999.
- [221] M. José-Yacamán, C. Gutierrez-Wing, M. Miki, D.-Q. Yang, K. N. Piyakis, and E. Sacher, “Surface diffusion and coalescence of mobile metal nanoparticles,” *The Journal of Physical Chemistry B*, vol. 109, no. 19, pp. 9703–9711, 2005.
- [222] M. Kaneeda, H. Iizuka, T. Hiratsuka, N. Shinotsuka, and M. Arai, “Improvement of thermal stability of NO oxidation Pt/Al<sub>2</sub>O<sub>3</sub> catalyst by addition of Pd,” *Applied Catalysis B: Environmental*, vol. 90, no. 3-4, pp. 564 – 569, 2009.
- [223] P. Gélin, L. Urfels, M. Primet, and E. Tena, “Complete oxidation of methane at low temperature over Pt and Pd catalysts for the abatement of lean-burn natural gas fuelled vehicles emissions: influence of water and sulphur containing compounds,” *Catalysis Today*, vol. 83, pp. 45–57, 8 2003.
- [224] E. E. Gruber, “Calculated size distributions for gas bubble migration and coalescence in solids,” *Journal of Applied Physics*, vol. 38, no. 1, pp. 243–250, 1967.
- [225] L. E. Willertz and P. G. Shewmon, “Diffusion of helium gas bubbles in gold and copper foils,” *Metallurgical Transactions*, vol. 1, no. 8, pp. 2217–2223, 1970.
- [226] F. A. Nichols, “Coalescence of two spheres by surface diffusion,” *Journal of Applied Physics*, vol. 37, no. 7, pp. 2805–2808, 1966.
- [227] C. Herring, “Effect of change of scale on sintering phenomena,” *Journal of Applied Physics*, vol. 21, no. 4, pp. 301–303, 1950.
- [228] M. A. Asoro, D. Kovar, Y. Shao-Horn, L. F. Allard, and P. J. Ferreira, “Coalescence and sintering of Pt nanoparticles: in situ observation by aberration-corrected HAADF STEM,” *Nanotechnology*, vol. 21, no. 2, p. 025701, 2010.
- [229] P. Harris, “The sintering of platinum particles in an alumina-supported catalyst: Further transmission electron microscopy studies,” *Journal of Catalysis*, vol. 97, no. 2, pp. 527 – 542, 1986.

- [230] R. Baker, P. Harris, and R. Thomas, "Direct observation of particle mobility on a surface in a gaseous environment," *Surface Science*, vol. 46, no. 1, pp. 311 – 316, 1974.
- [231] S. C. Parker and C. T. Campbell, "Kinetic model for sintering of supported metal particles with improved size-dependent energetics and applications to Au on TiO<sub>2</sub>(110)," *Physical Review B*, vol. 75, pp. 035430–, 01 2007.
- [232] C. G. Granqvist and R. A. Burhman, "Reply to "comments on the sintering mechanism of supported metal catalysts"," *Journal of Catalysis*, vol. 46, pp. 238–242, 2 1977.
- [233] A. K. Datye, Q. Xu, K. C. Kharas, and J. M. McCarty, "Particle size distributions in heterogeneous catalysts: What do they tell us about the sintering mechanism?," *Catalysis Today*, vol. 111, pp. 59–67, 1 2006.
- [234] S. E. Wanke, "Comments on the sintering mechanism of supported metal catalysts," *Journal of Catalysis*, vol. 46, no. 2, pp. 234 – 237, 1977.
- [235] M. Chen and L. Schmidt, "Morphology and composition of Pt–Pd alloy crystallites on SiO<sub>2</sub> in reactive atmospheres," *Journal of Catalysis*, vol. 56, no. 2, pp. 198 – 218, 1979.
- [236] A. Morlang, U. Neuhausen, K. Klementiev, F.-W. Schütze, G. Mieke, H. Fuess, and E. Lox, "Bimetallic Pt/Pd diesel oxidation catalysts: Structural characterisation and catalytic behaviour," *Applied Catalysis B: Environmental*, vol. 60, no. 3–4, pp. 191 – 199, 2005.
- [237] G. Barcaro, A. Fortunelli, M. Polak, and L. Rubinovich, "Patchy multishell segregation in Pd-Pt alloy nanoparticles," *Nano Letters*, vol. 11, no. 4, pp. 1766–1769, 2011.
- [238] F. Tao, M. E. Grass, Y. Zhang, D. R. Butcher, J. R. Renzas, Z. Liu, J. Y. Chung, B. S. Mun, M. Salmeron, and G. A. Somorjai, "Reaction-driven restructuring of Rh-Pd and Pt-Pd core-shell nanoparticles," *Science*, vol. 322, no. 5903, pp. 932–934, 2008.
- [239] L. C. A. van den Oetelaar, O. W. Nooij, S. Oerlemans, A. W. Denier van der Gon, H. H. Brongersma, L. Lefferts, A. G. Roosenbrand, and J. A. R. van Veen, "Surface segregation in supported PdPt nanoclusters and alloys," *The Journal of Physical Chemistry B*, vol. 102, no. 18, pp. 3445–3455, 1998.

- [240] K. Persson, K. Jansson, and S. G. Järås, "Characterisation and microstructure of Pd and bimetallic Pd–Pt catalysts during methane oxidation," *Journal of Catalysis*, vol. 245, no. 2, pp. 401 – 414, 2007.
- [241] M. R. Ward, T. Hyde, E. D. Boyes, and P. L. Gai, "Nanostructural studies of fresh and road-aged practical Pt/SiO<sub>2</sub> and Pt-Pd/Al<sub>2</sub>O<sub>3</sub> diesel oxidation catalysts by using aberration-corrected (scanning) transmission electron microscopy," *ChemCatChem*, vol. 4, no. 10, pp. 1622–1631, 2012.
- [242] T. R. Johns, J. R. Gaudet, E. J. Peterson, J. T. Miller, E. A. Stach, C. H. Kim, M. P. Balogh, and A. K. Datye, "Microstructure of bimetallic Pt-Pd catalysts under oxidizing conditions," *ChemCatChem*, vol. 5, no. 9, pp. 2636–2645, 2013.
- [243] W. J. Moore and L. Pauling, "The crystal structures of the tetragonal monoxides of lead, tin, palladium, and platinum," *Journal of the American Chemical Society*, vol. 63, no. 5, pp. 1392–1394, 1941.
- [244] J. Waser, H. A. Levy, and S. W. Peterson, "The structure of PdO," *Acta Crystallographica*, vol. 6, pp. 661–663, Jul 1953.
- [245] J. Kumar and R. Saxena, "Formation of NaCl- and Cu<sub>2</sub>O-type oxides of platinum and palladium on carbon and alumina support films," *Journal of the Less Common Metals*, vol. 147, no. 1, pp. 59 – 71, 1989.
- [246] T. Orent and S. Bader, "Leed and els study of the initial oxidation of Pd(100)," *Surface Science*, vol. 115, no. 2, pp. 323 – 334, 1982.
- [247] N. Rodriguez, S. Oh, R. Dallabetta, and R. Baker, "In-situ electron microscopy studies of palladium supported on Al<sub>2</sub>O<sub>3</sub>, SiO<sub>2</sub>, and ZrO<sub>2</sub> in oxygen," *Journal of Catalysis*, vol. 157, no. 2, pp. 676 – 686, 1995.
- [248] J. J. Chen and E. Ruckenstein, "Role of interfacial phenomena in the behavior of alumina-supported palladium crystallites in oxygen," *The Journal of Physical Chemistry*, vol. 85, no. 11, pp. 1606–1612, 1981.
- [249] R. J. Farrauto, J. K. Lampert, M. C. Hobson, and E. M. Waterman, "Thermal decomposition and reformation of PdO catalysts; support effects," *Applied Catalysis B: Environmental*, vol. 6, no. 3, pp. 263 – 270, 1995.
- [250] A. K. Datye, J. Bravo, T. R. Nelson, P. Atanasova, M. Lyubovsky, and L. Pfefferle, "Catalyst microstructure and methane oxidation reactivity during the Pd↔PdO

- transformation on alumina supports,” *Applied Catalysis A: General*, vol. 198, no. 1-2, pp. 179 – 196, 2000.
- [251] H. Graoui, S. Giorgio, and C. R. Henry, “Shape variations of Pd particles under oxygen adsorption,” *Surface Science*, vol. 417, pp. 350–360, 11 1998.
- [252] S. Penner, D. Wang, B. Jenewein, H. Gabasch, B. Klotzer, A. Knop-Gericke, R. Schlogl, and K. Hayek, “Growth and decomposition of aligned and ordered PdO nanoparticles,” *The Journal of Chemical Physics*, vol. 125, no. 9, p. 094703, 2006.
- [253] T. Baldwin and R. Burch, “Catalytic combustion of methane over supported palladium catalysts: I. alumina supported catalysts,” *Applied Catalysis*, vol. 66, no. 1, pp. 337 – 358, 1990.
- [254] J. T. Hirvi, T.-J. J. Kinnunen, M. Suvanto, T. A. Pakkanen, and J. K. Norskov, “CO oxidation on PdO surfaces,” *The Journal of Chemical Physics*, vol. 133, no. 8, p. 084704, 2010.
- [255] E. E. Galloni and J. Angel E. Roffo, “The crystalline structure of  $\text{Pt}_3\text{O}_4$ ,” *The Journal of Chemical Physics*, vol. 9, no. 12, pp. 875–877, 1941.
- [256] J. Waser and J. Edwin D. McClanahan, “The crystal structure of  $\text{NaPt}_3\text{O}_4$ ,” *The Journal of Chemical Physics*, vol. 19, no. 4, pp. 413–416, 1951.
- [257] E. E. Galloni and R. H. Busch, “The structure of platinum oxides,” *The Journal of Chemical Physics*, vol. 20, no. 1, pp. 198–199, 1952.
- [258] O. Muller and R. Roy, “Formation and stability of the platinum and rhodium oxides at high oxygen pressures and the structures of  $\text{Pt}_3\text{O}_4$ ,  $\beta\text{-PtO}_2$  and  $\text{RhO}_2$ ,” *Journal of the Less Common Metals*, vol. 16, pp. 129–146, 10 1968.
- [259] R. D. Shannon, “Synthesis and properties of two new members of the rutile family  $\text{RhO}_2$  and  $\text{PtO}_2$ ,” *Solid State Communications*, vol. 6, pp. 139–143, 3 1968.
- [260] M. Fernandez and B. Chamberland, “A new high pressure form of  $\text{PtO}_2$ ,” *Journal of the Less Common Metals*, vol. 99, no. 1, pp. 99 – 105, 1984.
- [261] N. Seriani, W. Pompe, and L. C. Ciacchi, “Catalytic oxidation activity of  $\text{Pt}_3\text{O}_4$  surfaces and thin films,” *The Journal of Physical Chemistry B*, vol. 110, no. 30, pp. 14860–14869, 2006.
- [262] T. M. Pedersen, W. Xue Li, and B. Hammer, “Structure and activity of oxidized Pt(110) and  $\alpha\text{-PtO}_2$ ,” *Phys. Chem. Chem. Phys.*, vol. 8, pp. 1566–1574, 2006.

- [263] B. L. M. Hendriksen and J. W. M. Frenken, "CO oxidation on Pt(110): Scanning tunneling microscopy inside a high-pressure flow reactor," *Phys. Rev. Lett.*, vol. 89, p. 046101, Jul 2002.
- [264] L. Maya, L. Riester, T. Thundat, and C. S. Yust, "Characterization of sputtered amorphous platinum dioxide films," *Journal of Applied Physics*, vol. 84, no. 11, pp. 6382–6386, 1998.
- [265] M. Hecq, A. Hecq, J. Delrue, and T. Robert, "Sputtering deposition, XPS and X-ray diffraction characterization of oxygen-platinum compounds," *Journal of the Less Common Metals*, vol. 64, no. 2, pp. P25 – P37, 1979.
- [266] J. R. McBride, G. W. Graham, C. R. Peters, and W. H. Weber, "Growth and characterization of reactively sputtered thin-film platinum oxides," *Journal of Applied Physics*, vol. 69, no. 3, pp. 1596–1604, 1991.
- [267] K. G. Kreider, M. J. Tarlov, and J. P. Cline, "Sputtered thin-film pH electrodes of platinum, palladium, ruthenium, and iridium oxides," *Sensors and Actuators B: Chemical*, vol. 28, no. 3, pp. 167 – 172, 1995.
- [268] J. Zhensheng, X. Chanjuan, Z. Qingmei, Y. Feng, Z. Jiazheng, and X. Jinzhen, "Catalytic behavior of nanoparticle  $\alpha$ -PtO<sub>2</sub> for ethanol oxidation," *Journal of Molecular Catalysis A: Chemical*, vol. 191, no. 1, pp. 61 – 66, 2003.
- [269] P. V. McKinney, "The reduction of platinum oxide by carbon monoxide and catalysis of the reaction between carbon monoxide and oxygen," *Journal of the American Chemical Society*, vol. 56, no. 12, pp. 2577–2580, 1934.
- [270] F. Bernardi, M. C. M. Alves, and J. Morais, "Monitoring of Pt nanoparticle formation by H<sub>2</sub> reduction of PtO<sub>2</sub>: An in situ dispersive X-ray absorption spectroscopy study," *The Journal of Physical Chemistry C*, vol. 114, no. 49, pp. 21434–21438, 2010.
- [271] A. Dianat, N. Seriani, M. Bobeth, W. Pompe, and L. C. Ciacchi, "DFT study of the thermodynamic stability of Pd-Pt bulk oxide phases," *The Journal of Physical Chemistry C*, vol. 112, no. 35, pp. 13623–13628, 2008.
- [272] C. K. Rofer-DePoorter, "A comprehensive mechanism for the fischer-tropsch synthesis," *Chemical Reviews*, vol. 81, no. 5, pp. 447–474, 1981.

- [273] A. Y. Khodakov, "Fischer–tropsch synthesis: Relations between structure of cobalt catalysts and their catalytic performance," *Catalysis Today*, vol. 144, no. 3–4, pp. 251 – 257, 2009.
- [274] A. Steynberg, R. Espinoza, B. Jager, and A. Vosloo, "High temperature fischer–tropsch synthesis in commercial practice," *Applied Catalysis A: General*, vol. 186, no. 1–2, pp. 41 – 54, 1999.
- [275] E. Iglesia, S. L. Soled, and R. A. Fiato, "Fischer–tropsch synthesis on cobalt and ruthenium. metal dispersion and support effects on reaction rate and selectivity," *Journal of Catalysis*, vol. 137, no. 1, pp. 212 – 224, 1992.
- [276] E. Iglesia, "Design, synthesis, and use of cobalt-based fischer-tropsch synthesis catalysts," *Applied Catalysis A: General*, vol. 161, no. 1–2, pp. 59 – 78, 1997.
- [277] E. Iglesia, S. C. Reyes, R. J. Madon, and S. L. Soled, "Selectivity control and catalyst design in the fischer-tropsch synthesis: Sites, pellets, and reactors," vol. 39 of *Advances in Catalysis*, pp. 221 – 302, Academic Press, 1993.
- [278] S. L. Soled, E. Iglesia, R. A. Fiato, J. E. Baumgartner, H. Vroman, and S. Miseo, "Control of metal dispersion and structure by changes in the solid-state chemistry of supported cobalt fischer–tropsch catalysts," *Topics in Catalysis*, vol. 26, pp. 101–109, 2003.
- [279] R. Oukaci, A. H. Singleton, and J. G. G. Jr., "Comparison of patented Co F-T catalysts using fixed-bed and slurry bubble column reactors," *Applied Catalysis A: General*, vol. 186, no. 1–2, pp. 129 – 144, 1999.
- [280] G. J. Haddad, B. Chen, J. G. Goodwin, and Jr., "Effect of  $\text{La}^{3+}$  promotion of  $\text{Co/SiO}_2$  on CO hydrogenation," *Journal of Catalysis*, vol. 161, no. 1, pp. 274 – 281, 1996.
- [281] M. Rothaemel, K. F. Hanssen, E. A. Blekkan, D. Schanke, and A. Holmen, "The effect of water on cobalt fischer-tropsch catalysts studied by steady-state isotopic transient kinetic analysis (SSITKA)," *Catalysis Today*, vol. 38, no. 1, pp. 79 – 84, 1997.
- [282] F. Rohr, O. Lindvåg, A. Holmen, and E. Blekkan, "Fischer–tropsch synthesis over cobalt catalysts supported on zirconia-modified alumina," *Catalysis Today*, vol. 58, no. 4, pp. 247 – 254, 2000.

- [283] G. L. Bezemer, J. H. Bitter, H. P. C. E. Kuipers, H. Oosterbeek, J. E. Holewijn, X. Xu, F. Kapteijn, A. J. van Dillen, and K. P. de Jong, "Cobalt particle size effects in the fischer-tropsch reaction studied with carbon nanofiber supported catalysts," *Journal of the American Chemical Society*, vol. 128, no. 12, pp. 3956–3964, 2006.
- [284] G. L. Bezemer, U. Falke, A. J. van Dillen, and K. P. de Jong, "Cobalt on carbon nanofiber catalysts: auspicious system for study of manganese promotion in fischer-tropsch catalysis," *Chem. Commun.*, pp. 731–733, 2005.
- [285] P. van Berge, J. van de Loosdrecht, S. Barradas, and A. van der Kraan, "Oxidation of cobalt based fischer–tropsch catalysts as a deactivation mechanism," *Catalysis Today*, vol. 58, no. 4, pp. 321 – 334, 2000.
- [286] M. Bremaud, P. Fongarland, J. Anfray, S. Jallais, D. Schweich, and A. Khodakov, "Influence of syngas composition on the transient behavior of a fischer–tropsch continuous slurry reactor," *Catalysis Today*, vol. 106, no. 1–4, pp. 137 – 142, 2005.
- [287] J. van de Loosdrecht, B. Balzhinimaev, J.-A. Dalmon, J. Niemantsverdriet, S. Tsybulya, A. Saib, P. van Berge, and J. Visagie, "Cobalt fischer-tropsch synthesis: Deactivation by oxidation?," *Catalysis Today*, vol. 123, no. 1–4, pp. 293 – 302, 2007.
- [288] E. van Steen, M. Claeys, M. E. Dry, J. van de Loosdrecht, E. L. Viljoen, and J. L. Visagie, "Stability of nanocrystals: thermodynamic analysis of oxidation and re-reduction of cobalt in water/hydrogen mixtures," *The Journal of Physical Chemistry B*, vol. 109, no. 8, pp. 3575–3577, 2005.
- [289] S. E. Colley, R. G. Copperthwaite, G. J. Hutchings, S. P. Terblanche, and M. M. Thackeray, "Identification of body-centred cubic cobalt and its importance in CO hydrogenation," *Nature*, vol. 339, pp. 129–130, 05 1989.
- [290] M. Casas-Cabanas, G. Binotto, D. Larcher, A. Lecup, V. Giordani, and J.-M. Tarascon, "Defect chemistry and catalytic activity of nanosized  $\text{Co}_3\text{O}_4$ ," *Chemistry of Materials*, vol. 21, no. 9, pp. 1939–1947, 2009.
- [291] E. A. Owen and D. M. Jones, "Effect of grain size on the crystal structure of cobalt," *Proceedings of the Physical Society. Section B*, vol. 67, no. 6, p. 456, 1954.
- [292] R. W. Grimes and K. P. D. Lagerlöf, "Polymorphs of cobalt oxide," *Journal of the American Ceramic Society*, vol. 74, no. 2, pp. 270–273, 1991.

- [293] J. F. Liu, S. Yin, H. P. Wu, Y. W. Zeng, X. R. Hu, Y. W. Wang, G. L. Lv, and J. Z. Jiang, “Wurtzite-to-rocksalt structural transformation in nanocrystalline CoO,” *The Journal of Physical Chemistry B*, vol. 110, no. 43, pp. 21588–21592, 2006.
- [294] D. P. Dinega and M. G. Bawendi, “A solution-phase chemical approach to a new crystal structure of cobalt,” *Angewandte Chemie International Edition*, vol. 38, no. 12, pp. 1788–1791, 1999.
- [295] V. F. Puentes, K. M. Krishnan, and A. P. Alivisatos, “Colloidal nanocrystal shape and size control: The case of cobalt,” *Science*, vol. 291, no. 5511, pp. 2115–2117, 2001.
- [296] H.-Y. Lin and Y.-W. Chen, “The mechanism of reduction of cobalt by hydrogen,” *Materials Chemistry and Physics*, vol. 85, no. 1, pp. 171 – 175, 2004.
- [297] O. Bulavchenko, S. Cherepanova, V. Malakhov, L. Dovlitova, A. Ishchenko, and S. Tsybulya, “In situ XRD study of nanocrystalline cobalt oxide reduction,” *Kinetics and Catalysis*, vol. 50, pp. 192–198, 2009.
- [298] D. Potoczna-Petru and L. Kępiński, “Reduction study of Co<sub>3</sub>O<sub>4</sub> model catalyst by electron microscopy,” *Catalysis Letters*, vol. 73, pp. 41–46, 2001.
- [299] R. Dieckmann, “Point defects and transport properties of binary and ternary oxides,” *Solid State Ionics*, vol. 12, no. 0, pp. 1 – 22, 1984.
- [300] G. Jacobs, T. K. Das, Y. Zhang, J. Li, G. Racoillet, and B. H. Davis, “Fischer–tropsch synthesis: support, loading, and promoter effects on the reducibility of cobalt catalysts,” *Applied Catalysis A: General*, vol. 233, no. 1–2, pp. 263 – 281, 2002.
- [301] R. Dehghan, T. Hansen, J. Wagner, A. Holmen, E. Rytter, Ø. Borg, and J. Walmsley, “In-situ reduction of promoted cobalt oxide supported on alumina by environmental transmission electron microscopy,” *Catalysis Letters*, vol. 141, no. 6, pp. 754–761, 2011.
- [302] A. M. Venezia, L. F. Liotta, G. Pantaleo, V. La Parola, G. Deganello, A. Beck, Z. Koppány, K. Frey, D. Horváth, and L. Guzzi, “Activity of SiO<sub>2</sub> supported gold–palladium catalysts in CO oxidation,” *Applied Catalysis A: General*, vol. 251, pp. 359–368, 9 2003.
- [303] A. Ivanova, E. Slavinskaya, R. Gulyaev, V. Zaikovskii, . Stonkus, I. Danilova, L. Plyasova, I. Polukhina, and A. Boronin, “Metal–support interactions in Pt/Al<sub>2</sub>O<sub>3</sub>



- and Pd/Al<sub>2</sub>O<sub>3</sub> catalysts for co oxidation,” *Applied Catalysis B: Environmental*, vol. 97, no. 1–2, pp. 57 – 71, 2010.
- [304] R. J. Farrauto and K. E. Voss, “Monolithic diesel oxidation catalysts,” *Applied Catalysis B: Environmental*, vol. 10, no. 1–3, pp. 29 – 51, 1996.
- [305] T. Boger, A. K. Heibel, and C. M. Sorensen, “Monolithic catalysts for the chemical industry,” *Industrial Engineering Chemistry Research*, vol. 43, no. 16, pp. 4602–4611, 2004.
- [306] T. A. Nijhuis, A. E. W. Beers, T. Vergunst, I. Hoek, F. Kapteijn, and J. A. Moulijn, “Preparation of monolithic catalysts,” *Catalysis Reviews*, vol. 43, no. 4, pp. 345–380, 2001.
- [307] E. Ringe, R. P. Van Duyne, and L. D. Marks, “Wulff construction for alloy nanoparticles,” *Nano Letters*, vol. 11, no. 8, pp. 3399–3403, 2011.
- [308] D. Van Dyck, G. Van Tendeloo, and S. Amelinckx, “Diffraction effects due to a single translation interface in a small crystal,” *Ultramicroscopy*, vol. 15, no. 4, pp. 357–370, 1984.
- [309] P. L. Hansen, A. M. Molenbroek, and A. V. Ruban, “Alloy formation and surface segregation in zeolite-supported Pt-Pd bimetallic catalysts,” *The Journal of Physical Chemistry B*, vol. 101, no. 10, pp. 1861–1868, 1997.
- [310] Y. Ding, F. Fan, Z. Tian, and Z. L. Wang, “Atomic structure of Au-Pd bimetallic alloyed nanoparticles,” *Journal of the American Chemical Society*, vol. 132, no. 35, pp. 12480–12486, 2010.
- [311] J. Sarkany and R. D. Gonzalez, “Support and dispersion effects on silica- and alumina-supported platinum catalysts: II. effect on the CO-O<sub>2</sub> reaction,” *Applied Catalysis*, vol. 5, pp. 85–97, 1 1983.
- [312] M. J. Walsh, K. Yoshida, M. L. Pay, P. L. Gai, and E. D. Boyes, “On the effect of atomic structure on the activity and deactivation of catalytic gold nanoparticles,” *ChemCatChem*, vol. 4, no. 10, pp. 1638–1644, 2012.
- [313] E. Slavinskaya, O. Stonkus, R. Gulyaev, A. Ivanova, V. Zaikovskii, P. Kuznetsov, and A. Boronin, “Structural and chemical states of palladium in Pd/Al<sub>2</sub>O<sub>3</sub> catalysts under self-sustained oscillations in reaction of CO oxidation,” *Applied Catalysis A: General*, vol. 401, no. 1–2, pp. 83 – 97, 2011.

- [314] M. Shao, T. Yu, J. H. Odell, M. Jin, and Y. Xia, "Structural dependence of oxygen reduction reaction on palladium nanocrystals," *Chem. Commun.*, vol. 47, pp. 6566–6568, 2011.
- [315] P. L. Gai, *Electron Microscopy in Heterogeneous Catalysis*. Taylor & Francis, 2003.
- [316] H. Gabasch, A. Knop-Gericke, R. Schlögl, M. Borasio, C. Weilach, G. Rupprechter, S. Penner, B. Jenewein, K. Hayek, and B. Klotzer, "Comparison of the reactivity of different Pd-O species in CO oxidation," *Phys. Chem. Chem. Phys.*, vol. 9, pp. 533–540, 2007.
- [317] J. Rickard, L. Genovese, A. Moata, and S. Nitsche, "Redispersion of platinum on Pt/Al<sub>2</sub>O<sub>3</sub> model catalyst in oxygen studied by transmission electron microscopy," *Journal of Catalysis*, vol. 121, no. 1, pp. 141 – 152, 1990.
- [318] Z. Zhang, *Model study of platinum nanoparticle interactions with  $\gamma$ -alumina single crystal supports*. PhD thesis, University of Pittsburgh, 2012.
- [319] T. Mang, B. Breitscheldel, P. Polanek, and H. Knözinger, "Adsorption of platinum complexes on silica and alumina: Preparation of non-uniform metal distributions within support pellets," *Applied Catalysis A: General*, vol. 106, no. 2, pp. 239 – 258, 1993.
- [320] R. Ferrando, J. Jellinek, and R. L. Johnston, "Nanoalloys: From theory to applications of alloy clusters and nanoparticles," *Chemical Reviews*, vol. 108, no. 3, pp. 845–910, 2008.
- [321] B. Tilley, David and A. Eggleton, Richard, "The natural occurrence of eta-alumina ( $\eta$ -Al<sub>2</sub>O<sub>3</sub>) in bauxite," *Clays and Clay Minerals*, vol. 44, no. 5, pp. 658–664, 1996.
- [322] S. Giorgio, C. R. Henry, B. Pauwels, and G. Van Tendeloo, "Au particles supported on (1 1 0) anatase-TiO<sub>2</sub>," *Materials Science and Engineering: A*, vol. 297, pp. 197–202, 1 2001.
- [323] A. Y. Borisevich, A. R. Lupini, and S. J. Pennycook, "Depth sectioning with the aberration-corrected scanning transmission electron microscope," *Proceedings of the National Academy of Sciences of the United States of America*, vol. 103, pp. 3044–3048, 02 2006.
- [324] L. K. Ono, B. Yuan, H. Heinrich, and B. R. Cuenya, "Formation and thermal stability of platinum oxides on size-selected platinum nanoparticles: Support effects," *The Journal of Physical Chemistry C*, vol. 114, no. 50, pp. 22119–22133, 2010.

- [325] L. K. Ono, J. R. Croy, H. Heinrich, and B. Roldan Cuenya, "Oxygen chemisorption, formation, and thermal stability of Pt oxides on Pt nanoparticles supported on SiO<sub>2</sub>/Si(001): Size effects," *The Journal of Physical Chemistry C*, vol. 115, no. 34, pp. 16856–16866, 2011.
- [326] S. Bradley, W. Sinkler, D. Blom, W. Bigelow, P. Voyles, and L. Allard, "Behavior of Pt atoms on oxide supports during reduction treatments at elevated temperatures, characterized by aberration corrected stem imaging," *Catalysis Letters*, vol. 142, no. 2, pp. 176–182, 2012.
- [327] P. Harris, "Carbonaceous contaminants on support films for transmission electron microscopy," *Carbon*, vol. 39, no. 6, pp. 909 – 913, 2001.
- [328] P. J. F. Harris, "Carbon nanotubes and other graphitic structures as contaminants on evaporated carbon films," *Journal of Microscopy*, vol. 186, no. 1, pp. 88–90, 1997.
- [329] R. F. Klie, D. Ciuparu, L. Pfefferle, and Y. Zhu, "Multi-walled carbon nanotubes on amorphous carbon films," *Carbon*, vol. 42, no. 10, pp. 1953–1957, 2004.
- [330] R. Egerton, P. Li, and M. Malac, "Radiation damage in the TEM and SEM," *Micron*, vol. 35, no. 6, pp. 399 – 409, 2004.
- [331] C. M. McGilvery, A. E. Goode, M. S. Shaffer, and D. W. McComb, "Contamination of holey/lacey carbon films in STEM," *Micron*, vol. 43, no. 2–3, pp. 450 – 455, 2012.
- [332] J. Mitchell, *The structure and growth direction of ErSi<sub>2-x</sub> nanowires on Si(0 0 1)*. PhD thesis, University of York, 2012.
- [333] P. E. Batson, "Motion of gold atoms on carbon in the aberration-corrected STEM," *Microscopy and Microanalysis*, vol. null, pp. 89–97, 2 2008.
- [334] M. Isaacson, D. Kopf, M. Utlaut, N. W. Parker, and A. V. Crewe, "Direct observations of atomic diffusion by scanning transmission electron microscopy," *Proceedings of the National Academy of Sciences*, vol. 74, no. 5, pp. 1802–1806, 1977.
- [335] S. Bals, S. Van Aert, C. P. Romero, K. Lauwaet, M. J. Van Bael, B. Schoeters, B. Partoens, E. Yücelen, P. Lievens, and G. Van Tendeloo, "Atomic scale dynamics of ultrasmall germanium clusters," *Nat Commun*, vol. 3, p. 897, 06 2012.
- [336] J. Kaspar, P. Fornasiero, and M. Graziani, "Use of CeO<sub>2</sub>-based oxides in the three-way catalysis," *Catalysis Today*, vol. 50, pp. 285–298, 1999.

- [337] R. D. Monte and J. Kašpar, “On the role of oxygen storage in three-way catalysis,” *Topics in Catalysis*, vol. 28, pp. 47–57, 2004.
- [338] S. Carrettin, P. Concepción, A. Corma, J. M. López Nieto, and V. F. Puentes, “Nanocrystalline CeO<sub>2</sub> increases the activity of Au for CO oxidation by two orders of magnitude,” *Angewandte Chemie International Edition*, vol. 43, no. 19, pp. 2538–2540, 2004.
- [339] Q. Fu, A. Weber, and M. Flytzani-Stephanopoulos, “Nanostructured Au-CeO<sub>2</sub> catalysts for low-temperature water–gas shift,” *Catalysis Letters*, vol. 77, pp. 87–95, 2001.
- [340] D. Andreeva, V. Idakiev, T. Tabakova, L. Ilieva, P. Falaras, A. Bourlinos, and A. Travlos, “Low-temperature water-gas shift reaction over Au/CeO<sub>2</sub> catalysts,” *Catalysis Today*, vol. 72, no. 1–2, pp. 51 – 57, 2002.
- [341] D. Mendes, A. Mendes, L. M. Madeira, A. Iulianelli, J. M. Sousa, and A. Basile, “The water-gas shift reaction: from conventional catalytic systems to Pd-based membrane reactors—a review,” *Asia-Pacific Journal of Chemical Engineering*, vol. 5, no. 1, pp. 111–137, 2010.
- [342] T. Bunluesin, R. Gorte, and G. Graham, “Studies of the water-gas-shift reaction on ceria-supported Pt, Pd, and Rh: Implications for oxygen-storage properties,” *Applied Catalysis B: Environmental*, vol. 15, no. 1–2, pp. 107 – 114, 1998.
- [343] R. Gorte and S. Zhao, “Studies of the water-gas-shift reaction with ceria-supported precious metals,” *Catalysis Today*, vol. 104, no. 1, pp. 18 – 24, 2005.
- [344] H. Sakurai, T. Akita, S. Tsubota, M. Kiuchi, and M. Haruta, “Low-temperature activity of Au/CeO<sub>2</sub> for water gas shift reaction, and characterization by ADF-STEM, temperature-programmed reaction, and pulse reaction,” *Applied Catalysis A: General*, vol. 291, no. 1–2, pp. 179 – 187, 2005.
- [345] R. Burch, “Gold catalysts for pure hydrogen production in the water-gas shift reaction: activity, structure and reaction mechanism,” *Physical Chemistry Chemical Physics*, vol. 8, no. 47, pp. 5483–5500, 2006.
- [346] Q. Fu, H. Saltsburg, and M. Flytzani-Stephanopoulos, “Active nonmetallic Au and Pt species on ceria-based water-gas shift catalysts,” *Science*, vol. 301, no. 5635, pp. 935–938, 2003.

- [347] Z.-P. Liu, S. J. Jenkins, and D. A. King, "Origin and activity of oxidized gold in water-gas-shift catalysis," *Phys. Rev. Lett.*, vol. 94, p. 196102, May 2005.
- [348] C. Zhang, A. Michaelides, D. A. King, and S. J. Jenkins, "Structure of gold atoms on stoichiometric and defective ceria surfaces," *The Journal of Chemical Physics*, vol. 129, no. 19, p. 194708, 2008.
- [349] D. Tibiletti, A. A. Fonseca, R. Burch, Y. Chen, J. M. Fisher, A. Goguet, C. Hardacre, P. Hu, and D. Thompsett, "DFT and in situ EXAFS investigation of gold/ceria-zirconia low-temperature water gas shift catalysts: identification of the nature of the active form of gold," *The Journal of Physical Chemistry B*, vol. 109, no. 47, pp. 22553–22559, 2005.
- [350] X. Wang, J. A. Rodriguez, J. C. Hanson, M. Perez, and J. Evans, "In situ time-resolved characterization of Au–CeO and AuO<sub>x</sub>–CeO<sub>2</sub> catalysts during the water-gas shift reaction: Presence of Au and O vacancies in the active phase," *The Journal of Chemical Physics*, vol. 123, no. 22, p. 221101, 2005.
- [351] M. M. Branda, N. J. Castellani, R. Grau-Crespo, N. H. de Leeuw, N. C. Hernandez, J. F. Sanz, K. M. Neyman, and F. Illas, "On the difficulties of present theoretical models to predict the oxidation state of atomic Au adsorbed on regular sites of CeO(111)," *The Journal of Chemical Physics*, vol. 131, no. 9, p. 094702, 2009.
- [352] L. M. Molina, M. D. Rasmussen, and B. Hammer, "Adsorption of O<sub>2</sub> and oxidation of CO at Au nanoparticles supported by TiO<sub>2</sub>(110)," *The Journal of Chemical Physics*, vol. 120, no. 16, pp. 7673–7680, 2004.
- [353] D. S. Newsome, "The water-gas shift reaction," *Catalysis Reviews*, vol. 21, no. 2, pp. 275–318, 1980.
- [354] B. Qiao, A. Wang, X. Yang, L. F. Allard, Z. Jiang, Y. Cui, J. Liu, J. Li, and T. Zhang, "Single-atom catalysis of CO oxidation using Pt<sub>1</sub>/FeO<sub>x</sub>," *Nat Chem*, vol. 3, pp. 634–641, 08 2011.
- [355] S. J. Haigh, N. P. Young, H. Sawada, K. Takayanagi, and A. I. Kirkland, "Imaging the active surfaces of cerium dioxide nanoparticles," *ChemPhysChem*, vol. 12, no. 13, pp. 2397–2399, 2011.
- [356] T. Paryjczak, J. Rynkowski, and S. Karski, "Thermoprogrammed reduction of cobalt oxide catalysts," *Journal of Chromatography A*, vol. 188, pp. 254–256, 1 1980.

- [357] P. Li, J. Liu, N. Nag, and P. Crozier, “In situ synthesis and characterization of Ru promoted Co/Al<sub>2</sub>O<sub>3</sub> fischer–tropsch catalysts,” *Applied Catalysis A: General*, vol. 307, no. 2, pp. 212 – 221, 2006.
- [358] W. L. Smith and A. D. Hobson, “The structure of cobalt oxide, Co<sub>3</sub>O<sub>4</sub>,” *Acta Crystallographica Section B*, vol. 29, pp. 362–363, Feb 1973.
- [359] V. K. Lazarov, M. Weinert, S. A. Chambers, and M. Gajdardziska-Josifovska, “Atomic and electronic structure of the Fe<sub>3</sub>O<sub>4</sub>(111)MgO(111) model polar oxide interface,” *Physical Review B*, vol. 72, pp. 195401–, 11 2005.
- [360] S. K. Arora, R. G. S. Sofin, I. V. Shvets, and M. Luysberg, “Anomalous strain relaxation behavior of Fe<sub>3</sub>O<sub>4</sub>/MgO (100) heteroepitaxial system grown using molecular beam epitaxy,” *Journal of Applied Physics*, vol. 100, no. 7, p. 073908, 2006.
- [361] A. Rečnik, D. L. Carroll, K. A. Shaw, D. M. Lind, and M. Rühle, “Structural characterization of Fe<sub>3</sub>O<sub>4</sub>-NiO superlattices using high-resolution transmission electron microscopy,” *Journal of Materials Research*, vol. null, pp. 2143–2151, 8 1997.
- [362] O. Kitakami, H. Sato, Y. Shimada, F. Sato, and M. Tanaka, “Size effect on the crystal phase of cobalt fine particles,” *Phys. Rev. B*, vol. 56, pp. 13849–13854, Dec 1997.
- [363] O. Lupan, L. Chow, and G. Chai, “A single ZnO tetrapod-based sensor,” *Sensors and Actuators B: Chemical*, vol. 141, no. 2, pp. 511 – 517, 2009.
- [364] Z. L. Wang, “Zinc oxide nanostructures: growth, properties and applications,” *Journal of Physics: Condensed Matter*, vol. 16, no. 25, p. R829, 2004.
- [365] Z. Fan and J. G. Lu, “Zinc Oxide Nanostructures: Synthesis and Properties,” *Journal of Nanoscience and Nanotechnology*, vol. 5, pp. 1561–1573, Oct. 2005.
- [366] M. C. Newton and P. A. Warburton, “ZnO tetrapod nanocrystals,” *Materials Today*, vol. 10, no. 5, pp. 50 – 54, 2007.
- [367] U. Özgür, D. Hofstetter, and H. Morkoç, “ZnO devices and applications: A review of current status and future prospects,” *Proceedings of the IEEE*, vol. 98, no. 7, pp. 1255–1268, July 2010.
- [368] M. Fujii, H. Iwanaga, M. Ichihara, and S. Takeuchi, “Structure of tetrapod-like ZnO crystals,” *Journal of Crystal Growth*, vol. 128, pp. 1095–1098, 3 1993.

- [369] K. Nishio, T. Isshiki, M. Kitano, and M. Shiojiri, "Structure and growth mechanism of tetrapod-like ZnO particles," *Philosophical Magazine A*, vol. 76, pp. 889–904, 2013/06/11 1997.
- [370] C. Ronning, N. G. Shang, I. Gerhards, H. Hofsass, and M. Seibt, "Nucleation mechanism of the seed of tetrapod ZnO nanostructures," *Journal of Applied Physics*, vol. 98, pp. 034307–5, 08 2005.
- [371] M. Shiojiri and C. Kaito, "Structure and growth of ZnO smoke particles prepared by gas evaporation technique," *Journal of Crystal Growth*, vol. 52, Part 1, no. 0, pp. 173 – 177, 1981.
- [372] Y. Wu, X.-H. Zhang, F. Xu, L.-S. Zheng, and J. Kang, "A hierarchical lattice structure and formation mechanism of ZnO nano-tetrapods," *Nanotechnology*, vol. 20, no. 32, p. 325709, 2009.
- [373] L. Shen, H. Zhang, and S. Guo, "Control on the morphologies of tetrapod ZnO nanocrystals," *Materials Chemistry and Physics*, vol. 114, no. 2–3, pp. 580 – 583, 2009.
- [374] F. Wang, Z. Ye, D. Ma, L. Zhu, and F. Zhuge, "Novel morphologies of ZnO nanotetrapods," *Materials Letters*, vol. 59, no. 5, pp. 560 – 563, 2005.
- [375] D. Calestani, M. Zha, R. Mosca, A. Zappettini, M. Carotta, V. D. Natale, and L. Zanotti, "Growth of ZnO tetrapods for nanostructure-based gas sensors," *Sensors and Actuators B: Chemical*, vol. 144, no. 2, pp. 472 – 478, 2010.
- [376] U. Pal, J. García-Serrano, G. Casarrubias-Segura, N. Koshizaki, T. Sasaki, and S. Terahuchi, "Structure and optical properties of M/ZnO (M=Au, Cu, Pt) nanocomposites," *Solar Energy Materials and Solar Cells*, vol. 81, no. 3, pp. 339 – 348, 2004.
- [377] J. M. Lin, H. Y. Lin, C. L. Cheng, and Y. F. Chen, "Giant enhancement of bandgap emission of ZnO nanorods by platinum nanoparticles," *Nanotechnology*, vol. 17, no. 17, p. 4391, 2006.
- [378] X. Ye, Y. Zhou, J. Chen, Y. Sun, and Z. Wang, "Coating of ZnO nanorods with nanosized silver particles by electroless plating process," *Materials Letters*, vol. 62, no. 4–5, pp. 666 – 669, 2008.

- [379] M.-C. Daniel and D. Astruc, “Gold Nanoparticles: Assembly, Supramolecular Chemistry, Quantum-Size-Related Properties, and Applications toward Biology, Catalysis, and Nanotechnology,” *Chemical Reviews*, vol. 104, pp. 293–346, 2004.
- [380] S. Carabineiro, B. Machado, R. Bacsa, P. Serp, G. Dražić, J. Faria, and J. Figueiredo, “Catalytic performance of Au/ZnO nanocatalysts for CO oxidation,” *Journal of Catalysis*, vol. 273, no. 2, pp. 191 – 198, 2010.
- [381] C. S. Rout, S. H. Krishna, S. Vivekchand, A. Govindaraj, and C. Rao, “Hydrogen and ethanol sensors based on ZnO nanorods, nanowires and nanotubes,” *Chemical Physics Letters*, vol. 418, no. 4–6, pp. 586 – 590, 2006.
- [382] Q. Xiang, G. Meng, Y. Zhang, J. Xu, P. Xu, Q. Pan, and W. Yu, “Ag nanoparticle embedded-ZnO nanorods synthesized via a photochemical method and its gas-sensing properties,” *Sensors and Actuators B: Chemical*, vol. 143, no. 2, pp. 635 – 640, 2010.
- [383] P. Pawinrat, O. Mekasuwandumrong, and J. Panpranot, “Synthesis of Au–ZnO and Pt–ZnO nanocomposites by one-step flame spray pyrolysis and its application for photocatalytic degradation of dyes,” *Catalysis Communications*, vol. 10, no. 10, pp. 1380 – 1385, 2009.
- [384] P. L. Gai, K. Yoshida, C. Shute, X. Jia, M. Walsh, M. Ward, M. S. Dresselhaus, J. R. Weertman, and E. D. Boyes, “Probing structures of nanomaterials using advanced electron microscopy methods, including aberration-corrected electron microscopy at the angstrom scale,” *Microscopy Research and Technique*, vol. 74, no. 7, pp. 664–670, 2011.
- [385] M. R. Ward, H. Sugiura, K. Yoshida, N. Tanaka, P. L. Gai, and E. D. Boyes, “Aberration corrected and 3D cryo-tomography HAADF-STEM surface studies of ZnO tetrapods,” *Journal of Physics: Conference Series*, vol. 371, no. 1, p. 012073, 2012.